Mineral Potential Mapping with Mathematical Geological Models

Alok Kumar Porwal

International Institute for Geo-information Science and
Earth Observation, Enschede, The Netherlands

University of Utrecht

Cover designed by Alok Porwal
Printed by ITC Printing Department

Mineral Potential Mapping with Mathematical Geological Models

Potentiële aanwezigheid van mineralen in kaart gebracht met
wiskundig geologische modellen
(met een samenvatting in het Nederlands)

PROEFSCHRIFT

ter verkrijging van de graad van doctor aan de Universiteit Utrecht
op gezag van de Rector Magnificus, Prof. Dr. W.H. Gispen,
ingevolge het besluit van het College voor Promoties
in het openbaar te verdedigen
op woensdag 1 februari 2006 des middags te 12.45

door

ALOK KUMAR PORWAL

geboren op 30 juni 1964 te Udaipur, India

Promotor: Prof. Dr. M. Hale, Faculty of Geosciences, Utrecht University and ITC

Co-promotor: Dr. E.J.M. Carranza, ITC

Dedicated to my parents and wife

Acknowledgements

It is a pleasure to thank the many people who made this thesis possible.

I cannot overstate my gratitude to Professor Dr. Martin Hale who accepted me as his promovendus and guided me from the very first stage of formulating the research proposal to the final stage of compiling this thesis. He encouraged me to think for myself and gave me complete freedom to develop the research, but ensured that the research moved forward and not in circles. I must have sorely tried his patience by long periods of inactivity due to my job commitments, nevertheless, his unbridled support was forthcoming during the entire tenure of my research. I thank Dr. John Carranza, my good friend and co-supervisor, who took over at a particularly-difficult phase of my research and helped me steer through with much dexterity. I am grateful to Dr. Edmund Sides (now at GE Smallworld) for guiding me in the initial phase of my research at ITC, Delft. I thank Dr. Donald Singer, Dr. Graeme Bonham-Carter, Dr. Gary Raines, Dr. R.B. McCammon and several anonymous referees, who reviewed and accepted for publication the papers that I submitted to various journals and offered insightful comments for improving them. In particular, Dr. Singer took immense personal interest in my work, pointed out several deficiencies and gave valuable advice for improving the research. I am indebted to Mr. Lalit Gurjar and Dr. S.K. Haldar (now retired) of Hindustan Zinc Ltd., Udaipur, India, for sharing without reserve their professional experience of base metal exploration and insights into base metal deposits of the Aravalli province.

I am grateful to Professor Alfred Stein for translating to dutch the summary of this thesis. I thank Dr. Elisabeth Kosters, Ms. Ineke Theussing and Ms. Loes Colenbrander for administrative support, Henk Wilbrink and Aiko Mulder for computer hardware/software support and Barnette Stern and Carla Gerritsen for library support. I thank Bish Kewaldaar for facility support and his elder-brotherly care during my stay in Delft. I fondly remember Frank van

Contents

List of Figures

List of Tables

Chapter 1

Introduction

1.1   Background to the Research

Optimization of land use is a major policy objective in most countries. However, for making decisions about allocating land use in the face of competing demands from different sectors, reliable information on natural resources is an important prerequisite because it enables decision-making agencies to estimate prospective benefits from different uses of the land and prioritize them based on the social and economic needs of the society. Several natural resources such as forest, surface water and soil are generally exposed on the surface, and, hence they are directly mapped using ground and aerospace survey data. Other natural resources including mineral deposits, occur below the land surface and cannot, therefore, be mapped directly. However, it is possible to map mineral potential.

1.1.1   Mineral Potential

The term 'mineral deposits,' as used here, refers to accumulations or concentrations of one or more useful substances that are generally sparsely distributed in the earth's crust (Bateman, 1951a), which include large and small mineral deposits, mineral occurrences and mineral prospects. The term 'mineralization' refers to the collective geological processes that lead to the formation of mineral deposits (Bateman, 1951b). The term 'mineral potential' describes the possibility of the presence of mineral deposits or mineralization. Mineral potential does not take into account economic factors such as deposit grade, tonnage, physical, chemical and mineralogical characteristics, nature and thickness of

overburden, availability of man power and technology, market demand, etc., as these are typically unknown during mineral potential mapping.

Mineral potential mapping of an area involves demarcation of potentially-mineralized zones based on geologic features that exhibit significant spatial association with target mineral deposits. These features, which are termed recognition criteria, are spatial features indicative of various genetic earth processes that acted conjunctively to form the deposits in the area. Recognition criteria are sometimes directly observable; more often, their presence is inferred from their responses in various spatial datasets, which are appropriately processed to enhance and extract the recognition criteria to obtain evidential or predictor maps.

1.1.2 Mathematical geological modeling of mineral potential

In traditional approaches to mineral potential mapping, the predictor maps are interpreted, either individually or conjunctively using manual overlay, to demarcate potentially-mineralized zones. In recent years, use of geographic information systems (GIS) for digital overlay of predictive maps has supplanted these traditional approaches. However, naive applications of GIS, which involve, for example, simple overlay or Boolean operations to combine predictor maps, are usually unsuitable for mineral potential mapping because they tend to give equal importance to all recognition criteria. Given the complexity of earth systems that form mineral deposits, it is too naive to assume that all earth processes that were involved in the formation of the target mineral deposits made equal contributions and, hence, all recognition criteria have equal importance as indicators of the target mineral deposits.

It is pragmatic to assume that the process of mineralization responds to random (or stochastic) spatial controls on localization of mineral deposits. Stochastic processes are readily modeled by the application of mathematics (for example, Agterberg, 1974; Alberti and Uhlmann, 1982; Nelson, 1995). It is possible to use appropriate mathematical geological models of the relation between recognition criteria and target mineral deposits for mineral potential mapping. What is important is the selection of appropriate mathematical geological model(s).

Although a variety of models and their applications to map mineral potential are documented in the published literature (for references, see succeeding chapters), a comprehensive study involving applications of several models to the same area is lacking. Such a study can help to establish strengths and lim-

itations of different modeling techniques and, therefore, can facilitate selecting appropriate model(s) for mapping mineral potential of geologically comparable areas.

1.2 Main Research Question

A mathematical geological model for mineral potential mapping can be defined as a highly-simplified mathematical representation of the relation between recognition criteria (generally represented by predictor maps) and the target mineral deposits. A generalized mathematical geological model can be empirically represented as below (see also Bonham-Carter, 1994):

$$MPM = \{f(x_{ij}), P_k\}, \tag{1.1}$$

where MPM is a mineral potential map, x_{ij} is the jth ($j = 1$ to L) pattern on the ith predictor map X_i ($i = 1$ to N), P_k is the kth ($k = 1$ to K) parameter of the mathematical function f, L is the total number patterns on X_i, N is the total number of predictor maps and K is the total number of parameters of the function f.

Based on whether the relationship is hypothesized to be linear or non-linear, a variety of linear and non-linear functions can be used to approximate the relationship between recognition criteria and mineral deposits. The main problem in spatial-mathematical-model-based approaches to mineral potential mapping is the selection of appropriate functions that can effectively approximate the relation between the target mineral deposits and recognition criteria as well as account for dependencies amongst the recognition criteria. Therefore, a key research question is:

- which mathematical function(s) can be used most effectively to approximate the relationship between a set of recognition criteria (or predictor maps) and the target mineral deposits?

1.3 Main Research Objectives

In this research, a variety of linear and non-linear mathematical functions are investigated in the framework of mathematical geological models using the available regional-scale geoscientific database of a study area in the Aravalli metallogenic province of India with the following objectives:

- to identify and map important regional-scale recognition criteria for base-metal deposits of the Aravalli province,

- to evaluate a series of mathematical functions for capturing approximately spatial relationships between predictor maps and target mineral deposits and, if required, develop procedures to implement them in a GIS-environment,

- to evaluate mathematical geological models for regional-scale base-metal potential mapping of the study area, and

- to identify major strengths and limitations of various models.

1.4 Modeling Assumptions

Every model is based on certain assumptions, which the modeler assumes to be true in order to build the model. The mathematical geological models described in this thesis are based on the following assumptions:

- the geology of the target area has been mapped and studied, and there exist basic data (predictor maps) for modeling;

- the data are reliable; and

- the genetic characters of at least some of the deposits in the area are known, or can be extrapolated from deposits occurring in similar geological environments elsewhere.

The above-mentioned basic assumptions pertain to a model that uses only conceptual knowledge for estimating model parameters. The following assumption is added for a model that uses empirical data (or both empirical data and conceptual knowledge) for estimating model parameters:

- a sufficient number of known mineral deposits occur in the area, and they have been well-studied and documented.

1.5 Research Methodology

A flow chart of the generalized methodology used in this research for spatial-mathematical-model-based mineral potential mapping is shown in Fig. 1.1.

The research is implemented in the following sequential steps.
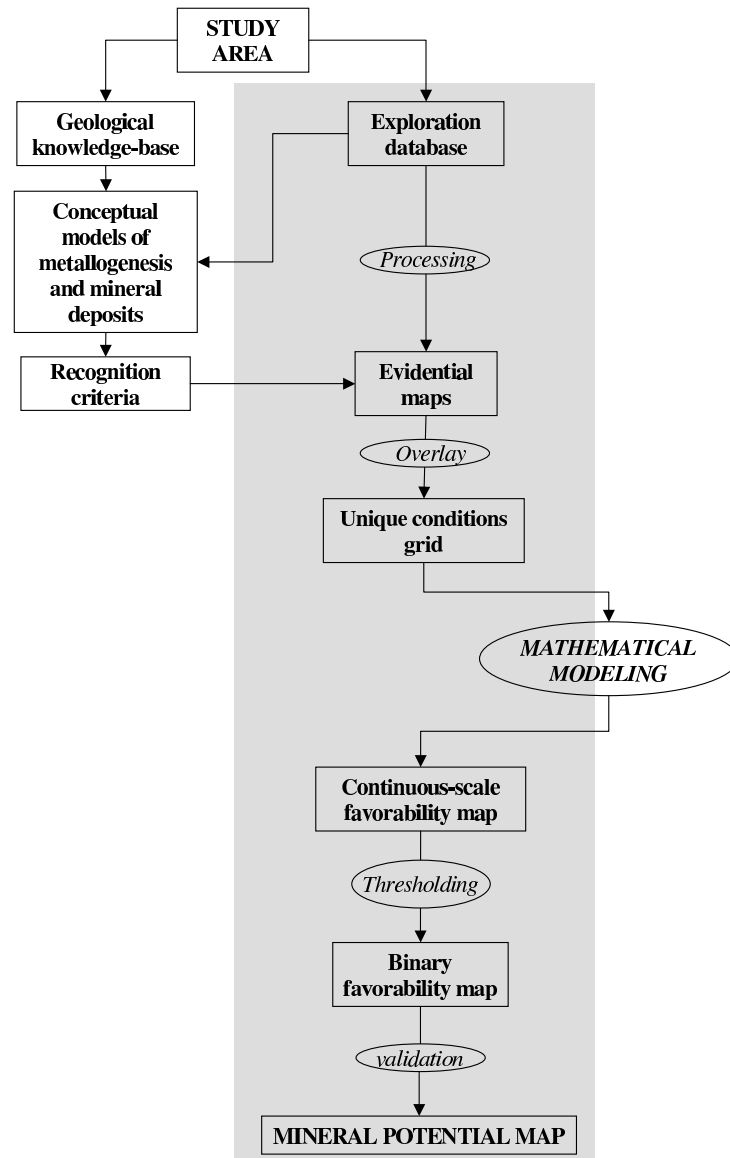
Figure 1.1: Flowchart of generalized procedures used for mineral potential mapping. Small rectangular boxes contain objects created at various stages and small elliptical boxes contain processes used for creating the objects. Shaded area represents GIS environment and contains objects and processes that were, respectively, created and implemented within the GIS. Mathematical modeling was implemented, depending on the model, both inside and outside the GIS and so lies partially inside the shaded area.

- Step 1: Base-metal deposit recognition criteria in the study area were identified and then represented as predictor maps.

- Step 2: The predictor maps were digitally superposed in the GIS to generate a unique conditions grid.

- Step 3: The unique conditions grid was processed using the mathematical geological models either inside or outside the GIS.

- Step 4: The outputs of the mathematical geological models were mapped to generate continuous-scale favorability maps.

- Step 5: The continuous-scale favorability maps were reclassified to generate binary favorability maps.

- Step 6: Binary favorability maps were validated to derive mineral potential maps.

Step 1: Identification of base-metal deposit recognition criteria

In this research, a conceptual approach (Hodgson and Troop, 1988) was used for identifying regional-scale (1:250,000) recognition criteria for base-metal deposits in the study area and representing them as predictor maps for inputting to the mathematical geological models. The approach was implemented in the following steps:

- A conceptual model of base-metal metallogenesis in the framework of overall tectono-stratigraphic evolution of the study area was selected based on published studies coupled with a new interpretive syntheses of regional-scale exploration data.

- Controls on mineralization and recognition criteria for base metal deposits in the study area were identified based on the conceptual model.

- Predictor maps representing the recognition criteria were generated by processing, interpretation and reclassification of the exploration datasets.

Step 2: Generation of unique conditions grid

A 'unique conditions grid map' was generated by combining predictor maps in the GIS. It is defined as "an integer grid formed by the combination of two or more predictor maps, in which the class values represent uniquely-occurring

combinations of the classes of the input themes" (Kemp *et al.*, 1999). An attribute table associated with a unique conditions grid map (unique conditions table) contains one record per unique condition class and one field for each predictor map. The predictor maps were input to the mathematical geological models in the form of a unique conditions grid.

Step 3: Mathematical geological modeling

The mathematical geological models were implemented either inside the GIS or outside the GIS using specialized computer programs, depending on the software resources required to implement their parameter-learning algorithms. Similarly, procedures used for implementing each mathematical geological model depend on the specific requirements of the model, and are described in detail in relevant chapters of this thesis.

In general, all mathematical geological models were implemented in the following two steps.

- Each model was first trained by estimating the model parameters either heuristically from conceptual knowledge or algorithmically from training data.

- The trained model was then used to process the unique conditions grid. The output for each unique condition was stored in a new field in the unique conditions table.

Step 4: Generation of continuous-scale favorability maps

The outputs of each mathematical geological model for the unique conditions were mapped in the GIS to generate a continuous-scale favorability map (if the modeling was implemented outside the GIS, the processed unique conditions grid was imported back into the GIS). For each unique condition, the output of the mathematical geological model, irrespective of its form, was interpreted as a relative favorability value.

Step 5: Generation of binary favorability maps

Continuous-scale favorability maps are cumbersome to interpret for demarcating areas of mineral potential because they represent favorability in a continuous scale from 0 (minimum) to 1 (maximum). Thresholding the favorability values based on some objective criteria facilitates the demarcation of mineral

potential zones. In this research, a graphical procedure based on the hypothesis that mineral-bearing areas occupy a very small proportion of the total area of a metallogenic province (Boleneus *et al.*, 2001) was used to identify threshold favorability values, which were then used to reclassify the continuous-scale favorability maps into binary favorability maps.

Step 6: Validation of binary favorability maps

The binary favorability maps were validated by overlaying locations of known deposits chosen for validation on the binary favorability maps. After the validation, the binary favorability maps could be used as base-metal potential maps of the study area.

1.6 Organization of the Thesis

This thesis is a compilation of the results of research work carried out to apply and evaluate a number of mathematical geological models, based on different linear and non-linear mathematical functions, for mineral potential mapping. With the exception of this introductory chapter and the concluding chapter, each chapter of the thesis has been published in a peer-reviewed international journal. The contents of the papers, however, have been edited to avoid repetition and to underscore the essential continuity between different chapters. The relation between different chapters is summarized in Fig. 1.2.

Chapter 2 introduces the reader to the geology of the study area and the exploration datasets used in the research. It applies a conceptual model of base-metal metallogenesis in the study area to identify deposit recognition criteria, which are represented as predictor maps, validated using empirical spatial analyses, and subsequently used as inputs in applications of the mathematical geological models. Portions of this chapter have been published as "Knowledge-driven and Data-driven Fuzzy Models for Predictive Mineral Potential Mapping" (Porwal *et al.*, 2003a) and "Tectonostratigraphy and base-metal mineralization controls, Aravalli province (western India): new interpretations from geophysical data" (Porwal *et al.*, 2006b).

Chapter 3 develops new "Knowledge-driven and Data-driven Fuzzy Models for Predictive Mineral Potential Mapping" (Porwal *et al.*, 2003a). For deriving fuzzy membership values of input predictor maps, the knowledge-driven fuzzy model uses a logistic membership function, whereas the data-driven model uses a piece-wise linear function. In both models, a multi-stage

RECOGNITION CRITERIA
(Chapter 2)

BAYESIAN PROBABILISTIC APPROACH

FUZZY APPROACH

NEURAL NETWORK APPROACH

Extended Weights-of-Evidence Model
(Chapter 4)

Fuzzy Models
(Chapter 3)

Neural Network Model
(Chapter 6)

Hybrid Fuzzy Weights-of-Evidence Model
(Chapter 5)

Hybrid Neuro-Fuzzy Model
(Chapter 7)

Bayesian Network Classifier Models
(Chapter 8)
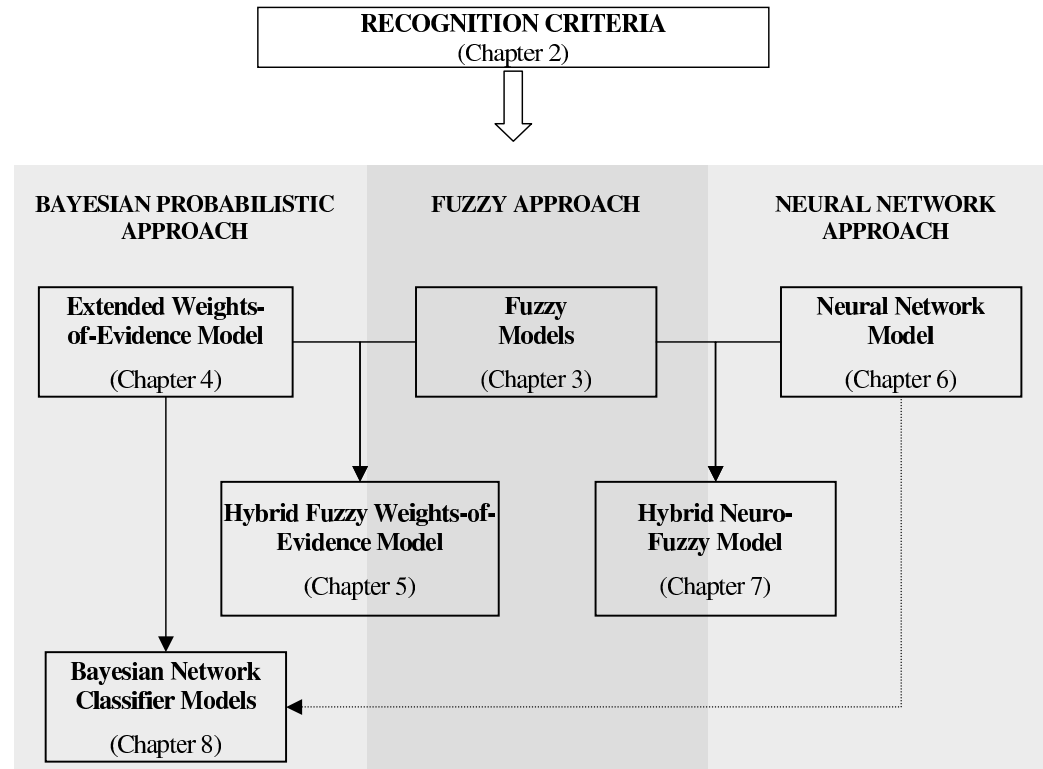
Figure 1.2: Relation of different chapters in this thesis; solid and dashed connector lines represent, respectively, direct and indirect linkages.

inference engine is used to combine the predictor patterns. A graphical defuzzification procedure is used in both models for the generating mineral potential maps.

Chapter 4 describes "Extended Weights-of-Evidence Modeling for Predictive Mapping of Base Metal Deposit Potential in Aravalli Province, Western India" (Porwal *et al.*, 2003b). The model applies the Bayesian equation in a log-linear form to model multi-class predictor maps for mineral potential mapping in an attempt to maximize mineral potential information.

Chapter 5 implements a hybrid fuzzy weights-of-evidence model by introducing fuzzy modeling procedures in the framework of an extended weights-of-evidence model. This chapter is based on a paper titled "A Hybrid Fuzzy Weights of Evidence Model for Mineral Potential Mapping"(Porwal *et al.*, 2006c).

Chapter 6 applies an artificial neural network based on radial basis functions to mineral potential mapping. The learning algorithms for estimating the parameters of the neural network required specialized computer programs and, therefore, are implemented outside the GIS. The chapter has been published as "Artificial Neural Networks for Mineral Potential Mapping: A Case Study from Aravalli Province, Western India" (Porwal *et al.*, 2003c).

Chapter 7 describes "A Hybrid Neuro-Fuzzy Model for Mineral Potential Mapping"(Porwal *et al.*, 2004a). By implementing a fuzzy model in the framework of an adaptive neural network, this hybrid model seeks to optimize the estimation of parameters of the fuzzy model. The hybrid parameter-learning algorithms are implemented outside the GIS.

Chapter 8 investigates an augmented naive Bayesian classifier that uses the non-linear Bayesian equation without any simplification and thus recognizes and accounts for conditional dependencies amongst input predictor patterns. The chapter also examines the effects of violations of the conditional independence assumption in Bayesian approaches to mineral potential mapping. The parameter-learning algorithms are implemented outside GIS. The chapter has been published as "Bayesian Network Classifiers for Mineral Potential Mapping" (Porwal *et al.*, 2006a).

In Chapter 9, the mathematical geological models and their applications to base-metal potential mapping in the study area are reviewed vis-à-vis the research objectives and, based on the reviews, conclusions regarding their respective strengths and limitations are drawn. The chapter also outlines some recommendations for future research on mathematical geological modeling.

Chapter 2

Base-Metal Potential Recognition Criteria in Study Area

This chapter describes the application of a conceptual model of base-metal metallogenesis in the study area to identify deposit recognition criteria, which are represented as predictor maps, validated using empirical spatial analyses and subsequently used as inputs in evaluation applications of GIS-based mathematical geological models described in this research. First, tectono-stratigraphy and base-metal mineralizations of the study area are described. Then, exploration data inputs to a GIS of the study area are described. Conjunctive interpretations of processed exploration data are described next. Then, a conceptual model of base-metal metallogenesis in the framework of overall tectono-stratigraphic evolution of the study area is used to identify mineralization controls and recognition criteria for base-metal deposits. Finally, empirical models are used to validate spatial association of base-metal deposits and the recognition criteria. Portions of this chapter have been published as "Knowledge-driven and Data-driven Fuzzy Models for Predictive Mineral Potential Mapping" (Porwal *et al.*, 2003a) and "Tectonostratigraphy and base-metal mineralization controls, Aravalli province (western India): new interpretations from geophysical data" (Porwal *et al.*, 2006b).

2.1 Study Area

The Aravalli province (Fig.2.1), which is located in the state of Rajasthan, India, constitutes the most important metallogenic province for base-metal deposits in India and hosts the entire economically-viable lead-zinc resource-base of the country. The economically-viable reserves of lead and zinc in the province stand at 130 million tonnes with average grades of 2.2% Pb and 9.2% Zn; possible resources in producing mines and deposits under detailed exploration amount to 30 million tonnes (Paliwal, *et al.*, 1986; Kala, 2001; Haldar, 2001). The province is characterized by an Archaean basement overlain by thick successions of intensely deformed and metamorphosed volcanic and sedimentary rocks. Eastern parts of the province comprise flat and largely soil-covered peneplains occupied by Archaean basement rocks. Central parts of the province comprise the NNE-SSW trending and 700-km-long Aravalli Mountain Chain, which is composed of Palaeo- to Meso-Proterozoic meta-volcano-sedimentary rocks. Western parts of the province blend into the Great Thar Desert and are occupied by Neo-Proterozoic magmatic rocks.

A block (about 50,000 km^2) of the Aravalli province between latitudes 23°30' N and 26° N and longitudes 73° E and 75° E (Fig. 2.2) was selected and used in this research as a study area for demonstrating the applications of various mathematical geological models to mineral potential mapping. The study area contains more than 90% of the province's base-metal deposits plus several base-metal prospects, occurrences and abandoned mining pits, which have made it a prime exploration target area for base metals. It has been relatively well explored by different governmental agencies. Significant amounts of reliable and public domain data are available, largely generated by the Geological Survey of India. Moreover, genetic attributes of most of the major deposits in the study area are documented in published literature. Therefore, the study area meets all the assumptions stated in chapter 1 for applying spatial-mathematical-model-based approaches to mineral potential mapping.

2.1.1 Previous geological work in study area

The broad tectono-stratigraphic framework of the study area was first defined by Heron (1917, 1939, 1953). Since then, several field and laboratory studies have contributed to a much better understanding of the tectono-stratigraphy of the study area (Roy, 1988a; Gupta *et al.*, 1997; Roy and Kataria, 1999; Sinha-Roy *et al.*, 1998; Deb, 2000a). Similarly, larger base-metal deposits in the
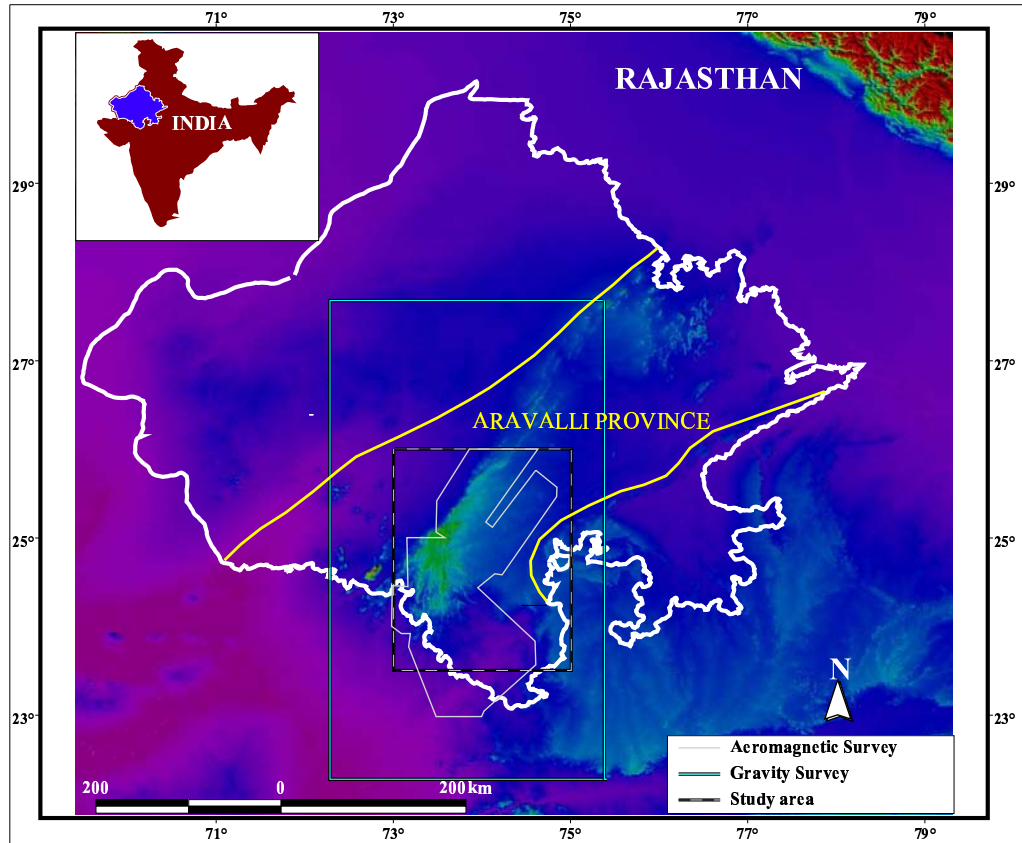
Figure 2.1: Location of study area showing boundaries of aeromagnetic and gravity surveys. Shaded-relief image of digital elevation model of Rajasthan in background is created from 90-m resolution SRTM (Shuttle Radar Topography Mission) data.
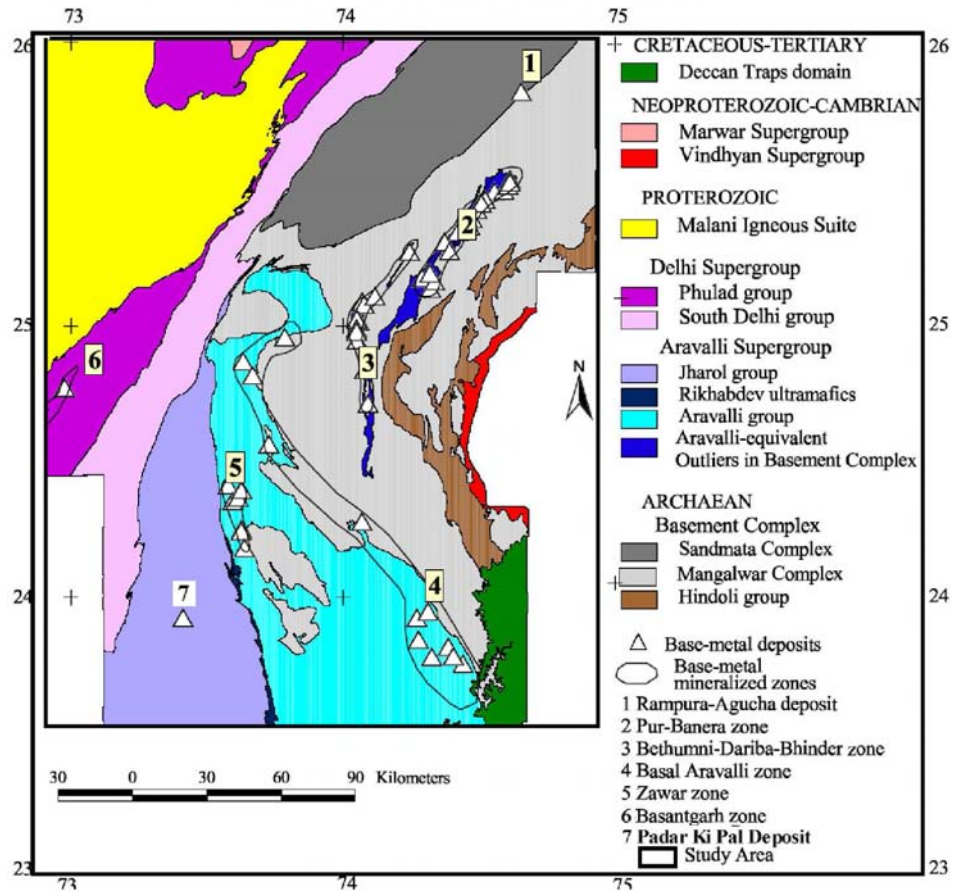
Figure 2.2: Generalized geological map of study area showing important base-metal mineralized belts and deposits (After Sinha-Roy *et al.*, 1998).

study area are well studied and documented (e.g., Mookherjee, 1964a, 1964b, 1965; Poddar, 1965; Straczec and Srikant, 1967; Chauhan, 1977; Gandhi *et al.*, 1984; Deb, 1986, 1990; Deb and Bhattacharya, 1980; Deb *et al.* 1989; Ranawat *et al.*, 1988; Sarkar, 2000; Gandhi, 2001; Haldar and Deb, 2001; Roy, 2001) and, thus, much is fairly well known about major controls on base-metal mineralizations in the study area.

The study area is generally divided into three major tectono-stratigraphic units (Heron, 1953; Gupta *et al.*, 1980, 1997; Roy, 1988b).

Bhilwara supergroup. This Archaean supergroup (Raja Rao *et al.*, 1971; Gupta *et al.*, 1980, 1997; Fig. 2.3A), comprising largely a heterogeneous complex of granite and granodioritic gneisses, migmatites, ampbhibolites and granulites, constitutes the basement of the study area. It also contains enclaves of meta-volcanic-sedimentary rocks (Gupta *et al.*, 1980, 1997). Several workers have reported remnants of greenstone sequences from the basement complex (Sinha-Roy, 1985; Sahu and Mathur, 1991; Upadhyaya *et al.*, 1992). The spatial distribution of basement rocks in central parts of the study area (Figs. 2.3 and 2.4) is ill defined and widely debated (see below). Consequently, it is referred to by various names in the literature, viz., Mewar Gneiss (Roy, 1988b, 1990; Roy and Kroner, 1996; Fig. 2.3B), Banded Gneissic Complex (Heron, 1953; Sharma, 1988; Sugden *et al.*, 1990; Bose, 2000; Deb and Thorpe, 2001; Fig. 2.4A) and Basement Complex (Sinha-Roy *et al.*, 1998; Fig. 2.4B). In spite of several commonalities, each name has a different spatial connotation (Figs. 2.3 and 2.4).

Aravalli supergroup. This Palaeo- to Meso-Proterozoic supergroup (Figs. 2.3 and 2.4) exhibits an inverted V-shaped geometry. It is bisected roughly along its long axis by a narrow, linearly-disposed suite of ultramafic rocks that separate a shallow-water shelf association of (predominantly dolomitic) carbonates and a variety of clastic sedimentary rocks in the east from a carbonate-free deep-water association of pelitic sediments intercalated by thin bands of quartzites in the west (Roy and Paliwal, 1981). In southern parts of the study area, this supergroup is separated from the basement by a profound erosional unconformity (Roy and Paliwal, 1981; Roy *et al.*, 1988) but, in the central parts, the boundary between the two is blurred by a pervasive migmatization and soil cover. The central parts comprise several linear belts of base-metal-bearing metasedimentary sequences (outlined in black in Figs. 2.3 and 2.4) sep-

15

arated by wide tracts of gneisses and migmatites or soil cover. These metasedimentary sequences host some of the largest Pb-Zn deposits of the country. The central parts have been variously classified en bloc into the Archaean Bhilwara supergroup (Gupta *et al.*, 1980, 1997; Fig. 2.3A), into the Proterozoic Aravalli supergroup (Roy, 1988b; Roy *et al.*, 1993; Roy and Kataria, 1999; Fig. 2.3B), or into a separate group called 'Bhilwara belt' of Proterozoic age (Sugden *et al.*, 1990; Fig. 2.4A). Sinha-Roy *et al.* (1998) separate these base-metal-bearing metasedimentary enclaves from surrounding gneisses and migmatites and consider the latter as parts of Archaean basement and the former as Aravalli-equivalent Proterozoic outliers (Fig. 2.4B). The tectono-stratigraphic status of the Hindoli volcano-sedimentary sequences along the eastern margin of the study area (outlined in white in Figs. 2.3 and 2.4) is also unresolved. They have been variously classified into the Archaean Bhilwara Supergroup (Gupta *et al.*, 1980; 1997; Fig. 2.3A), into the Proterozoic Aravalli supergroup (Roy, 1988b; Roy and Kataria, 1999; Fig. 2.3B), into the Proterozoic Bhilwara belt (Sugden *et al.*, 1990; Fig. 2.4A) and into the Archaean Basement Complex (Sinha-Roy, 1988; Sinha-Roy *et al.*, 1998; Fig. 2.4B).

Delhi supergroup. Flanking the Aravalli supergroup in the west with a well-defined unconformity (Figs. 2.3 and 2.4), this Meso- to Neo-Proterozoic supergroup comprises an arenite-dominated assemblage in the east and a pelite-dominated assemblage in the west. Metavolcanic rocks have much wider temporal and spatial distributions in the Delhi supergroup than in the Aravalli supergroup. Along its western margin, the Delhi supergroup includes a suite of base-metal-bearing volcano-sedimentary rocks (Heron, 1953; Gupta *et al.*, 1980; 1997; Sinha-Roy *et al.*, 1998; Roy and Kataria, 1999) and rocks showing ophiolitic affinity (Phulad ophiolites, cf. Gupta *et al.*, 1980, 1997; Sugden *et al.*, 1990). This suite of rocks has been identified as a separate tectonic terrane by Deb *et al.* (2001).

In addition to the above major tectonostratigraphic units, the study area also contains largely undeformed and unmetamorphosed sedimentary sequences of Neo-Proterozoic to Lower Cambrian age (Marwar and Vindhyan supergroups; Fig. 2.2). The western parts of the study area comprise the Neo-Proterozoic Malani Igneous Suite (Fig. 2.2), which represents a major period of anorogenic magmatism (A-type) in the Aravalli province and forms the third largest felsic magmatic terrane in the world (Kochar, 2000). This suite

comprises a variety of granites and cogenetic acidic volcanic rocks showing spectacular ring structures and radial dykes.

Base-metal mineralizations in study area

Base-metal deposits in the study area are hosted by supracrustal rocks of the Aravalli supergroup and Delhi supergroup (Fig. 2.2). Major concentrations of base-metal mineralization in the Aravalli supergroup occur in the Rampura-Agucha deposit and in the Pur-Banera, Bethumni-Dariba-Bhinder and Zawar mineralized zones (Fig. 2.2). Rampura-Agucha is a world-class Zn-Pb-(Ag) deposit with the highest combined metal grade (about 15%) among base-metal deposits in India. In the Bethumni-Dariba-Bhinder zone, Zn-Pb-(Cu) deposits are located in a 17 km long belt running from Bethumni in north to Dariba in south, with a pyrite zone further south around Bhinder. Pur-Banera is a low-grade polymetallic zone with several small deposits/prospects. Middle Aravalli sequences host Zn-Pb deposits in the Zawar zone. In addition, low-grade Cu(-Pb-Zn) mineralizations occur in basal sequences of the Aravalli supergroup (Fig. 2.2). The Delhi supergroup hosts smaller deposits of Cu-Zn and Zn-Pb-Cu in the Basantgarh zone. Table 2.1 summarizes the available geological information on important mineralized zones in the study area.

Base-metal mineralization in the study area shows systemic variation in time and space. Broadly, the following phases of base-metal metallogeny can be recognized.

The oldest phase is represented by low-grade dolomite-hosted Cu-(Pb-Zn) deposits in basal sequences of the Aravalli group (Fig. 2.2). The deposits show close spatial association with metamorphosed mafic volcanic rocks. Detailed genetic studies on this phase of base-metal mineralization are not available. The age of this phase of mineralization can be constrained at ca. 2000 Ma by extrapolating available geochronological data from basal volcanic rocks (Deb and Thorpe, 2001).

The second phase of base-metal mineralization, which has been dated at ca. 1800 Ma (Deb and Thorpe, 2001), is represented by large SEDEX-type Zn-Pb deposits (Menzie and Mossier, 1986; Goodfellow, 2001; Fig. 2.9B) at Rampura-Agucha and in the Pur-Banera, Bethumni-Dariba-Bhinder and Zawar zone of the Aravalli supergroup. Base-metal sulphide deposits in the Aravalli-equivalent outliers (Fig. 2.2) were formed by convective seawater circulation in zones of crustal extension (Deb, 1986; Deb and Sarkar, 1990). Metal content of exhalative brines was precipitated in second-order troughs with high
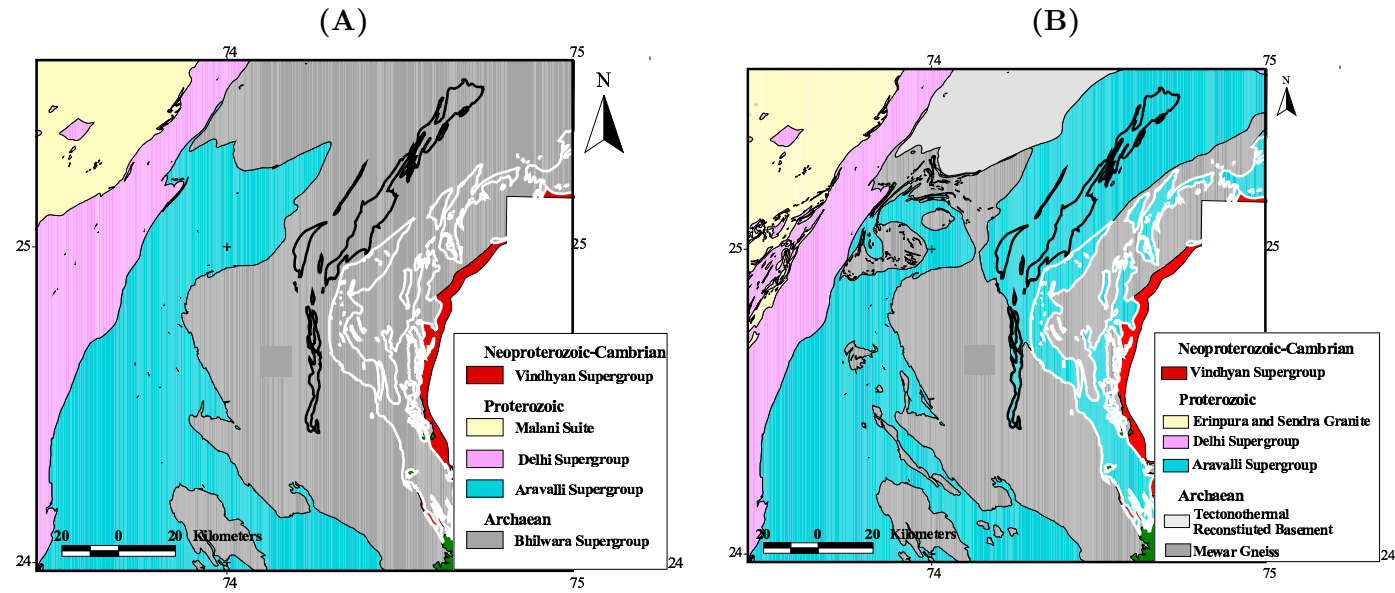
Figure 2.3: Tectonostratigraphic interpretations of south-central parts of Aravalli province: (A) after Gupta *et al.* (1997) and (B) after Roy (1988b). Areas demarcated by black and white lines are, respectively, base-metal bearing metasedimentary enclaves of Bhilwara area and low-grade meta-volcano-sedimentary sequences of Hindoli area.
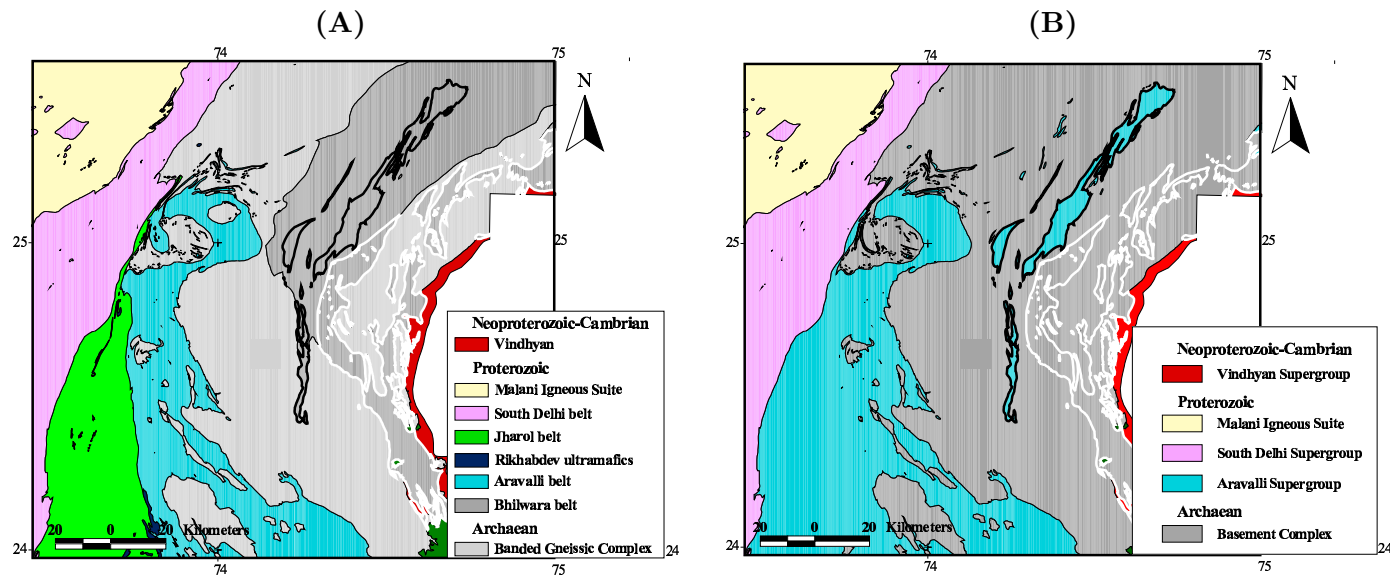
Figure 2.4: Tectonostratigraphic interpretations of south-central parts of Aravalli province: (A) after Sugden *et al.* (1990) and (B) after Sinha-Roy *et al.* (1998). Areas demarcated by black and white lines are, respectively, base-metal bearing metasedimentary enclaves of Bhilwara area and low-grade meta-volcano-sedimentary sequences of Hindoli area.

Table 2.1: Summary of available information on important mineralized zones in study area

	Rampura Agucha Deposit	Rajpura Dariba Zone	Pur-Banera Zone	Zawar Basantgarh Zone	Zone
Age	$\sim$ 1800Ma	$\sim$ 1800 Ma	$\sim$ 1800 Ma	$\sim$ 1700 Ma	$\sim$ 1000 Ma
Reserves(MT)	60	261	64	8	
Combined metal grade (Wt%)	15.5	2.6-7.38	Low grade	6.7	9.8
Type	SEDEX	SEDEX	SEDEX	SEDEX	VMS
Host lithology	Graphitic mica schist with sillimanite	Recrystallized siliceous dolomite; carbonaceous chert; graphitic mica schists	Fine grained, grey dolomite, commonly gritty/arkosic	Calc-silicates; associated banded magnetite quartzite	Hornblende schists; Anthophyllite-chlorite schists
Geological setting	Isolated metasedimentary enclave within the basement; geological sequence comprises striped amphibolite, diopside-garnet amphibolite, graphite-garnet-mica-sillimanite gneisses, aplite, feldspathic, arkosic quartzite, pegmatite	Linear intracratonic basins within basement; geological sequence comprises calc biotite schist grading to recrystallized cross bedded dolomite with conformable amphibolite, siliceous carbonate rock, carbonaceous chert, graphite mica, banded magnetite quartzite, ferrugineous breccia in ore zone	Second order basins close to a basement inlier; geological sequence comprises conglomerate, grit, quartzite (often arkosic), phyllite and greywacke, impure dolomite	Linear intracratonic basins within basement; geological sequence comprises calc-silicates, hornblende schists, graphite mica schists, banded magnetite quartzite	Linear belts of volcanic rocks; geological sequence comprises metamorphosed and altered volcanic rocks (hornblende-biotite-quartz schist, cordierite-anthophyllite-sericite-quartz schist, amphibolite etc.

Table 2.1 Continued

	Rampura Agucha Deposit	Rajpura Dariba Zone	Pur-Banera Zone	Zawar Zone	Basantgarh Zone
Volcanics	Amphibolite (mafic volcanics)	Amphibolites (mafic volcanics?) in footwall argillites and tuffaceous layers in graphite mica schist	Hornblende schist	None represented	Metamorphosed and altered mafic and bimodal volcanics
Organic association	Ubiquitous graphite	Carbonaceous matter intimately associated with Pb-Zn	Graphite associated with host rocks	Host rocks carbonaceous at places	None represented
Metamorphism	Upper Amphibolite facies (Max temperature: 650 C Max pressure : 6 kbar)	Amphibolite; (Max pressure: 5.4 kbar, Max temperature: 555 C)	Amphibolite; ubiquitous evidence of remobilization	Green schist; ubiquitous evidence of remobilization	Amphibolite(?)
References	Gandhi *et al.* (1984), Ranawat *et al.* (1988), Deb *et al.* (1989), Deb and Sarkar (1990), Ranawat and Sharma (1990), Deb and Thrope (2001), Haldar (2001), Roy (2001)	Poddar (1974), Chauhan (1977), Deb and Kumar (1982), Deb (1986), Deb *et al.* (1989), Deb and Sarkar (1990), Deb and Thrope (2001), Haldar (2001)	Raghunandan *et al.* (1981); Deb and Thorpe (2001)	Straczec and Srikant (1962); Deb *et al.* (1989), Deb and Sarkar (1990), Deb and Thorpe (2001)	Raghunandan *et al.* (1981), Deb (1999, 2000b)

biological activity. It must be mentioned here that the Rampura-Agucha deposit does not show all characteristics that are typical of SEDEX deposits (Gandhi, 2001), mainly because it has undergone high-grade metamorphism (700°) that has obliterated most of the pre-metamorphic features of the deposit. The deposit is geologically similar to the Broken Hill deposit of Australia for which the SEDEX model has been questioned by several authors (for example, Plimer, 1986; Beeson, 1990; Pongratz and Davidson, 1996; Large *et al.*, 1996). However, Gandhi (2001) convincingly argues in favor of a SEDEX origin of the deposit on the basis of its mineralogical composition, form and mode of occurrence, host rock lithology and geotectonic environment. The Zn-Pb deposits of the Aravalli group (Fig. 2.2) were formed close to a basement inlier, in second-order basins with biological activity, by hydrothermal fluids convecting through a heterogeneous source (Deb *et al.*, 1989; Deb and Sarkar, 1990).

The third phase of base-metal mineralization is represented by the Zn-Pb-Cu and Cu-Zn deposits in the Basantgarh zone of the Delhi supergroup (Fig. 2.2). These deposits, which are associated with metamorphosed and altered low-K tholeiites and calc-alkaline basalts, show affinity to VMS-type deposits (Deb, 2000b). Deb and Thorpe (2001) have dated this phase of mineralization at ca. 1000 Ma.

2.1.2 Data requirements for further tectonostratigraphic studies

Since the pioneering works of Heron (1917, 1939, 1953), significant progress has been made in understanding the tectono-stratigraphy of the study area. However, as the foregoing discussion shows, the following questions (amongst others) remain unresolved.

- Are the Hindoli sequences parts of the basement?

- What is the tectono-stratigraphic status of base-metal-bearing metasedimentary enclaves in central parts of the study area?

- Do base-metal-bearing meta-volcanic-sedimentary sequences along the western margin of the Delhi supergroup constitute a separate tectono-stratigraphic domain?

Until very recently, most tectonostratigraphic studies in the study area relied entirely on structural, lithological and lithogeochemical data, with very

little consideration of geophysical data. Certain geophysical data provide information about the 3-dimensional structure of the lithosphere and can thus provide insights into unresolved tectono-stratigraphic issues in the study area. For example, recent deep seismic reflectivity and gravity studies over the 400-km long Nagaur-Jhalawar transect across central parts of the Aravalli province, carried out by the National Geophysical Research Institute (NGRI) of India, provided a better understanding of crustal structure and tectonic evolution of the province (Tewari *et al.*, 1995, 1997a, 1997b, 1998, 2000; Rajendra Prasad *et al.*, 1998, 1999; Mishra *et al.*, 1998, 2000; Vijaya Rao *et al.*, 2000; Satyavani *et al.*, 2001).

Variations in the geomagnetic field, or magnetic anomalies, are caused by variations in content of magnetite and other ferromagnetic minerals in crustal rocks formed at temperatures above the Curie point ($\sim$50 km below earth's surface). Magnetic anomalies thus reflect compositional and geometric variations of outcropping and concealed crustal rocks. Similarly, lateral variations in the Earth's gravitational field, or gravity anomalies, are essentially caused by lateral variations of subsurface mass distribution and, therefore, reflect subsurface density variations. Bouguer gravity anomalies, which are determined by applying free-air, Bouguer and terrane corrections to observed gravitational field values (in order to eliminate effects of latitude, elevation and topography), reflect lateral variations in density of subsurface rocks. In addition, Bouguer gravity anomalies are, in general, useful for modeling subsurface mass distributions (Bott and Hinze, 1995). Therefore, magnetic and Bouguer gravity anomalies can provide useful insights into tectonics of a province, especially when interpreted in conjunction with surface geological data.

In this research, conjunctive interpretations of total magnetic field intensity data, Bouguer gravity data and other exploration data with the aid of a geographic information system (GIS) are used to address the above unresolved tectono-stratigraphic issues in the study area.

2.2 Exploration Database and Geophysical Data Processing

Available public domain multi-disciplinary spatial data were digitized to create a consistent regional-scale GIS of the study area that could be digitally processed to generate (a) relevant thematic maps for conjunctive tectono-stratigraphic and metallogenetic interpretations and (b) predictor maps for rep-

Table 2.2: Exploration datasets input to GIS

S.No.	Dataset	Scale	Source	Format
1.	Lithostratigraphic data	1:250000	Gupta *et al.* (1995a).	Hard copy (4 sheets)
2.	Structural data	1:250000	Gupta *et al.* (1995b).	Hard copy (4 sheets)
3.	Base-metal deposits data	1:250000	Raghunandan *et al.*, (1981); DMGR (1990); In-house reports of DMGR.	Published and unpublished technical reports
4.	Geochronological data	-	Vinogradov *et al.* (1964); Crawford (1970); Sivaraman and Odom (1982); Chodhary *et al.* (1984); Sarkar *et al.* (1992); Deb *et al.* (1989); Wiedenbeck and Goswami (1994); Roy and Kroner (1996); Fareeduddin and Kroner (1998); Wiedenbeck *et al.* (1996); Deb *et al.* (2001); Deb and Thorpe (2001).	Published research literature.
5.	Total magnetic field intensity data	1:250000	GSI (1981).	Hard copy (4 sheets of contour maps)
6.	Bouguer gravity data	1:1000000	Reddi and Ramakrishna (1988a).	Hard copy (1 sheet of contour map)

resenting recognition criteria and inputting to mathematical geological models.

Datasets input to the GIS (Table 2.2) include lithostratigraphic data (Gupta *et al.*, 1995a), structural data (Gupta *et al.*, 1995b), base-metal deposit/occurrence data (from various sources), geochronological data (from various sources), total magnetic field intensity maps (GSI, 1981) and a Bouguer gravity map (Reddi and Ramakrishna, 1988a). Because the datasets come from diverse sources, they were all georeferenced to the same Universal Transverse Mercator (UTM) projection for accurate spatial data overlay.

Lithostratigraphic data

Lithostratigraphic data of the study area are available in the form of a hard-copy or analog map (in 4 sheets on 1:250,000 scale) published by the Geological Survey of India (Gupta *et al.*, 1995a). The lithostratigraphic map was synthesized from a number of regional-scale maps and relevant geological data

produced by teams of geologists belonging to the Geological Survey of India over decades of systematic field mapping in the study area. In the map, various lithostratigraphic units are classified up to the level of formation. The rationale for the lithostratigraphic classifications are given by Gupta *et al.* (1997).

To input the lithostratigraphic data into the GIS, each lithological unit on the map was manually digitized as a polygonal feature using the UTM projection and its lithological and stratigraphic attributes (lithotype, formation, group and supergroup) were recorded in an associated attribute table.

Structural data

Gupta *et al.* (1995b) compiled a synthesized structural map from a number of regional-scale structural maps and relevant structural data produced by teams of geologists of the Geological Survey of India over decades of systematic structural mapping in the study area. The structural map has been published by the Geological Survey of India in 4 sheets on 1:250,000 scale. By interpreting the structural data in terms of the overall tectonostratigraphic evolution of the study area, Gupta *et al.* (1995b) defined several phases and cycles of deformation in the study area and classified each structural feature into a phase and a cycle of deformation. The rationale for the classifications is given by Gupta *et al.* (1997).

To input the structural data into the GIS, each feature on the structural map was manually digitized as a polyline and its attributes (nature, type, phase and cycle of deformation) were recorded in an associated attribute table. The digitization was carried out using the UTM projection.

Base-metal deposit/occurrence data

Raghunandan *et al.* (1981) compiled detailed information on location, geology, mineralization, reserves and status of exploration of all base-metal deposits of India. Information pertaining to base-metal deposits in the study area was extracted from their compilation to create a base-metal deposit/occurrence data-base, which was updated using mineral information available in the Rajasthan State Department of Mines and Geology. The updated data-base contained information on 54 known base-metal deposits in the study area.

The location of each base-metal deposit or occurrence was manually digitized as a point in the GIS using the UTM projection and its attributes (ore minerals, host rocks, reserves and grade) were recorded in an associated at-

tribute table.

Geochronological data

The geochronological data of radioactively-dated rocks and their locations in the study area are available in published research literature (Vinogradov *et al.*, 1964; Crawford, 1970; Sivaraman and Odom, 1982; Chodhary *et al.*, 1984; Sarkar *et al.*, 1989; Deb *et al.*, 1989; Wiedenbeck and Goswami, 1994; Roy and Kroner, 1996; Fareeduddin and Kroner, 1998; Wiedenbeck *et al.* 1996; Deb *et al.*, 2001; Deb and Thorpe, 2001). Deb and Thorpe (2001) give a detailed synthesis and analysis of the geochronological data of the study area. The above literature was used to create a geochronological data-base of the study area containing locality and age data of radioactively-dated rocks.

The location of each radioactively-dated rock was manually digitized as a point in the GIS using the UTM projection and its age was recorded in an associated attribute table.

Total magnetic field intensity data

A large portion of the study area (Fig. 2.1) was covered by two adjacent multi-sensor airborne magnetic surveys carried out by the United States Agency for International Development (USAID) and the Bureau de Recherches Geologiques et Minieres/Compagnie Generale de Geophysique (BRGM/CCG). The average flightline spacing and flight height in the case of the USAID survey were, respectively, 400 m and 60 m. The average flightline spacing and flight height in the case of the BRGM/CCG survey were, respectively, 400 m and 130 m. Raw data from the two surveys were processed and published by the Geological Survey of India in two sets of total magnetic field intensity contour maps (2 sheets for each set of data) with 10-nT contour interval (GSI, 1981).

The intersections of contours and flightlines on the total magnetic field intensity maps were manually digitized into the GIS as points using the UTM projection and the total magnetic field intensity value at each intersection point was stored in an associated attribute table. The two sets of total magnetic field intensity data were exported in two ASCII files using a xyz format (x and y define a co-ordinate pair for digitized magnetic value z) for processing outside the GIS using digital techniques (see below). Images of processed total magnetic field intensity data were input into the GIS as additional thematic layers.

26

Bouguer gravity data

Bouguer gravity data of the Aravalli province are available in the form of a contour map, with a 5 mgal contour interval, published by Geological Survey of India (Reddi and Ramakrishna, 1988a). Areal coverage of the Bouguer gravity data is shown in Fig. 2.1. The data are based on gravity surveys along roads and tracks at station intervals of 2 km with elevation accuracy of 2 m (Ramakrishna and Bhaskara Rao, 1981). The data are, therefore, regional in nature with an overall accuracy of 1-2 mgal (Ramakrishna and Bhaskara Rao, 1981; Reddi and Ramakrishna, 1988b; Mishra *et al.*, 2000).

The contours on the Bouguer gravity map were manually digitized into the GIS as polylines using the UTM projection and the Bouguer gravity value of each contour was stored in an associated attribute table. The Bouguer gravity contours were then converted into point features and exported in ASCII files using a xyz format (x and y define a co-ordinate pair for each Bouguer gravity value z) for processing outside the GIS using digital techniques (see below). Images of digitally processed Bouguer gravity data were input into the GIS as additional thematic layers.

2.2.1 Geophysical data processing

The geophysical data were processed outside the GIS using specialized software systems (mainly, Oasis Montaj and GM-SYS), as described below.

Total magnetic field intensity data

The two sets of total magnetic field intensity data, which were exported from the GIS in xyz format (see above), were gridded using the minimum curvature method (Briggs, 1974; Swain, 1976) and a cell size of 250 m. Resulting grids were contoured automatically and then compared with original contour maps to determine the accuracy of digital data capture. Original contour maps and computer-generated contours maps were very similar. Subsequently, the two grids were reduced to a common datum by upward-continuing the USAID grid to the level at which the BRGM/CGG data was acquired.

Noise reduction. The International Geomagnetic Reference Field (IGRF) values were removed from the grids to minimize the effect of regional magnetic field. Images of residual grids show several high-frequency anomalies that appear unrelated to probable geological sources. In addition, the USAID

grid shows distinct NW-SE trending flightline-related noise. High-frequency anomalies in the BRGM/CCG grid were filtered using a low-pass Butterworth filter ($k_0 = 0.0005$). High-frequency anomalies and flightline-related noise in the USAID grid were suppressed by applying a combination of high-pass Butterworth ($k_0 = 0.0005$) and directional cosine filters (Minty, 1991). Filtering was performed in the wavenumber domain by transforming gridded data to wavenumbers using Fourier analysis. After filtering, the data were transformed back to the spatial domain. The two grids were then merged and re-gridded using the minimum curvature method and a cell size of 250 m.

Processing and visualization. To re-position magnetic anomalies over their crustal sources, total magnetic field intensity is generally reduced to the pole. However, at low magnetic latitudes, this process results in undesirable amplification of N-S trending anomalies (MacLeod *et al.*, 1993). Amplitude of a 3D analytical signal of total magnetic field produces maxima over a magnetic source, irrespective of direction of magnetization and, therefore, an anomaly is re-positioned over its magnetic source without being affected by magnetic latitude (Roest *et al.*, 1992; MacLeod *et al.*, 1993). Due to the low magnetic latitude of the area, 3-D analytical signals were calculated instead of reducing total magnetic field intensity data to the pole. A first vertical derivative (FVD) filter was applied to enhance short wavelength (near-surface) anomalies and then the filtered data were upward-continued to various heights ranging from 2 to 8 km to enhance long wavelength (deep-seated) anomalies. Subsequently, all processed magnetic grids were displayed as shaded-relief images and then imported into the GIS to facilitate interpretation in conjunction with the other datasets.

Bouguer gravity data

The Bouguer gravity data, which were exported from the GIS in xyz format (see above), were gridded using the minimum curvature method and a cell size of 2 km. The same procedure, as described above to capture aeromagnetic data, was used to verify the accuracy of digital data capture.

Processing and visualization. The gravity data were upward-continued to various heights ranging from 1 km to 20 km to enhance long wavelength (deep-seated) anomalies. Using the method described by Boyce and Morris (2002), the residual field was separated from the regional field by subtracting

the gravity data upward-continued to 500 m from the original gravity data. A FVD filter was then applied to the residual gravity data in order to enhance near-surface anomalies. The processed gravity grids were displayed as shaded-relief images to enhance anomaly features and then imported into the GIS.

2.3 Conjunctive Interpretations of Processed Data

The images of the digitally-processed geophysical data were interpreted in conjunction with surface geological data with the aid of GIS-based overlay techniques to gain insights into the tectono-stratigraphy of the study area.

Regional lineaments

Thematic layers created from the geophysical datasets show prominent regional-scale lineaments comprising (a) composite linear to curvilinear features having distinct characteristics from adjacent features or (b) boundaries between crustal domains having distinct characteristics. Regional lineaments are particularly well-defined on the total magnetic field intensity image (Fig. 2.5A) and on the FVD residual gravity image (Fig. 2.6A). Lineaments were digitized from each shaded-relief image (Figs. 2.5B and 2.6B), resulting in two new thematic layers. Magnetic lineaments show northwesterly to northeasterly trends and, except lineaments M6, M7 and M12, extend for more than 50 km (Fig. 2.5B). Most magnetic lineaments are discernible in the FVD residual gravity image (Fig. 2.6A), although most are indiscernible in the Bouguer gravity image (Fig. 2.7A), perhaps due to lower resolution of the gravity data. The FVD residual gravity image (Fig. 2.6A) shows that magnetic lineament M15 (Fig. 2.5B) extends much further towards northeast and southwest before changing its trend (gravity lineament G7 on Fig. 2.6B). The lineament coincides with the western boundary of the central gravity high in the Bouguer gravity image (Fig. 2.7A). Similarly, magnetic lineament M13 (Fig. 2.5B), which coincides with gravity lineament G5 (Fig. 2.6B), extends further southwards, swings anticlockwise and continues further east with an ENE-WSW trend. The southern section of the lineament is discernible in the Bouguer gravity image (Fig. 2.7A). Magnetic lineament M10 (Fig. 2.5B) is also traceable in the FVD residual gravity image (Fig. 2.6A; G4 in Fig. 2.6B). The eastern boundary of the central gravity high in the Bouguer gravity image (Fig. 2.7A) forms a well-defined lineament in the FVD residual gravity image (Fig. 2.6A; G1 in Fig. 2.6B).
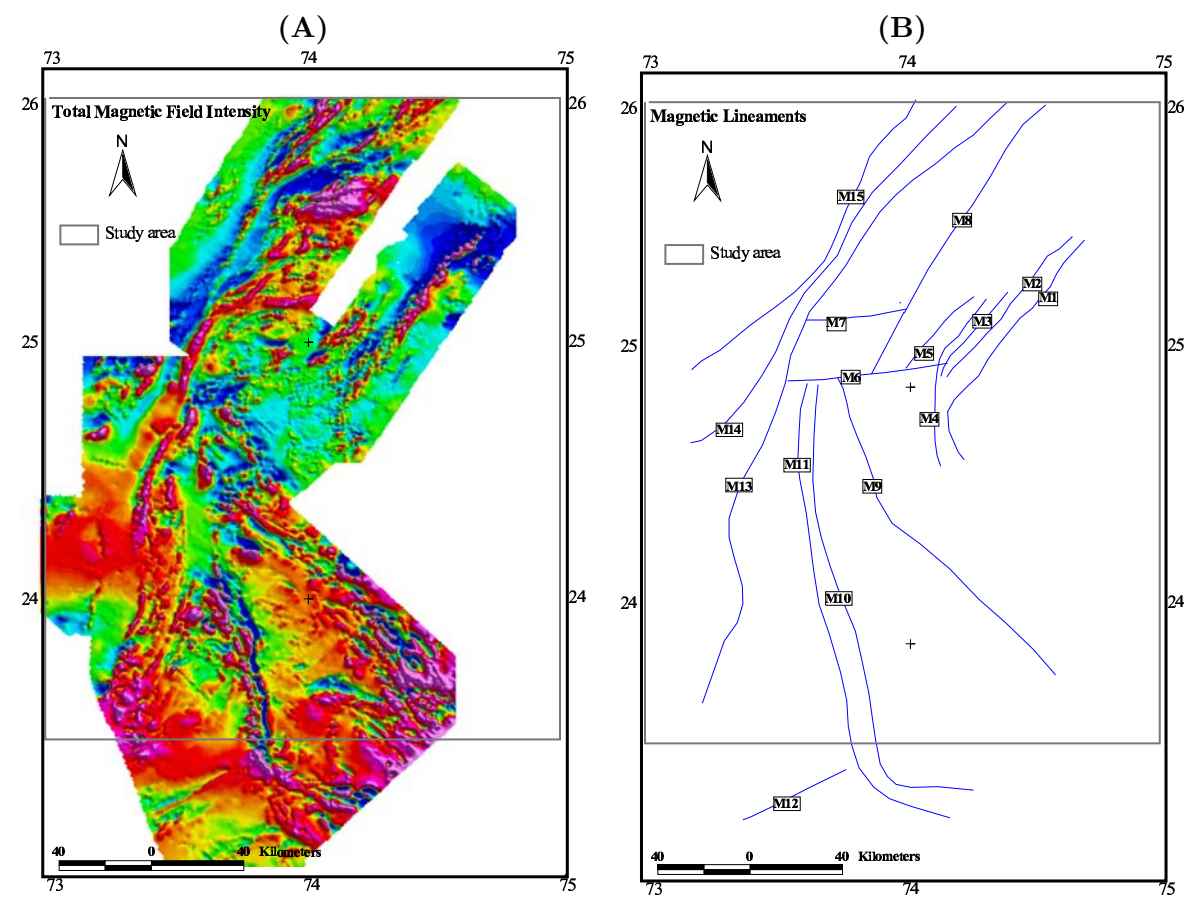
Figure 2.5: (A) Shaded-relief image of total magnetic field intensity and (B) interpreted lineaments.
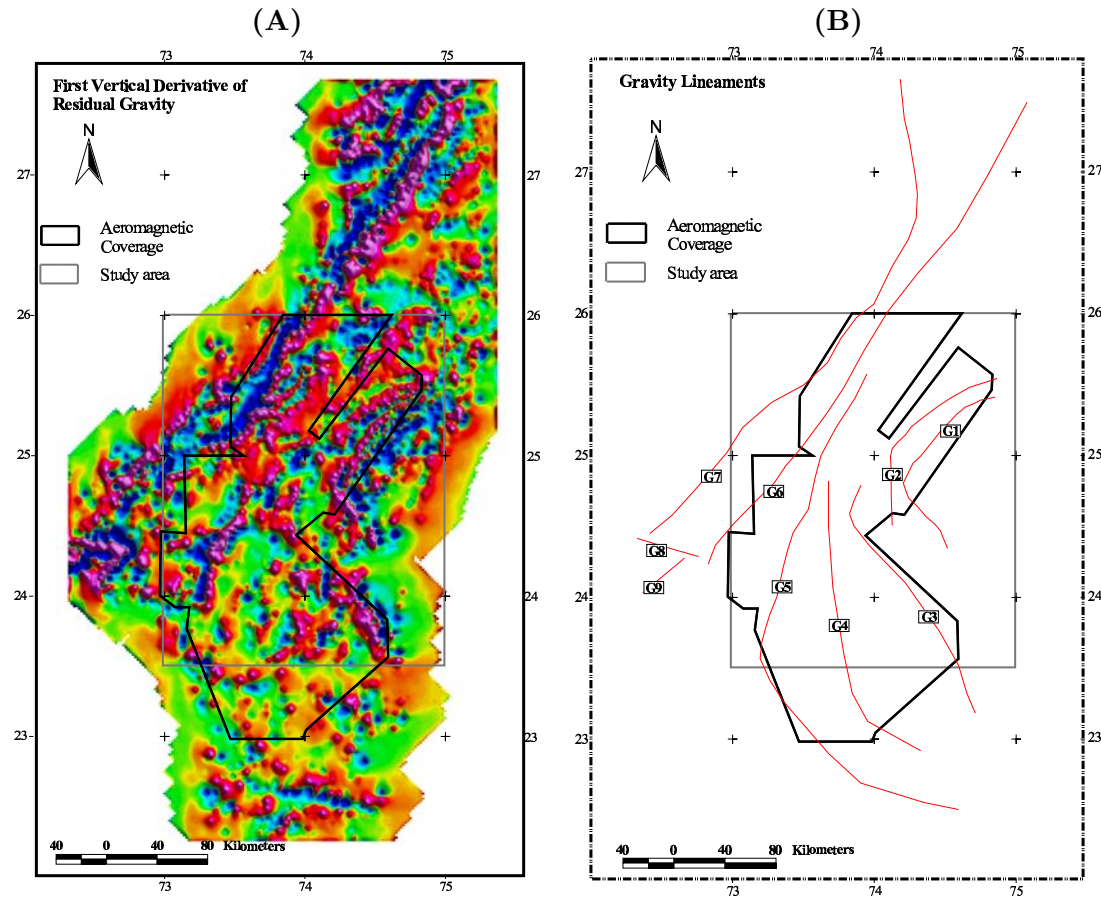
Figure 2.6: (A) Shaded-relief image of first vertical derivative of residual gravity and (B) interpreted lineaments. Crustal section along transect AA' is modeled in Fig. 2.10.
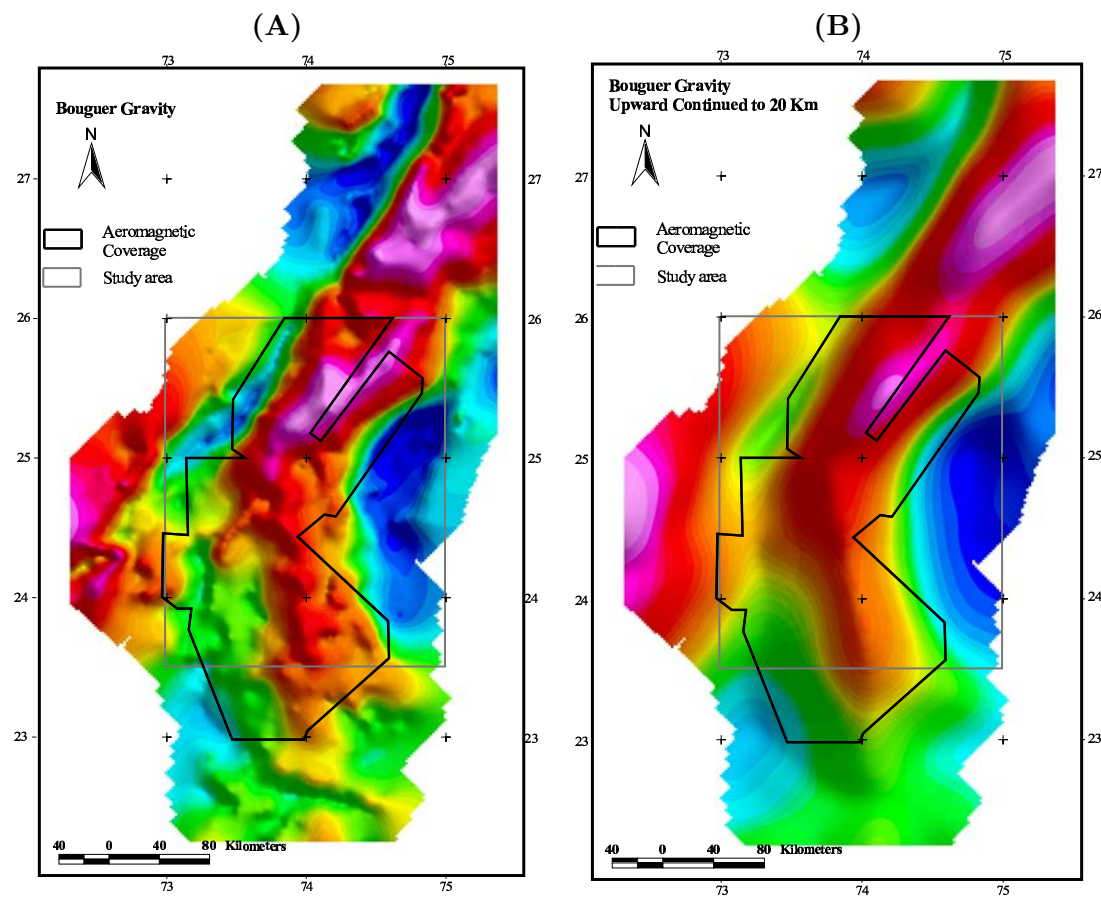
Figure 2.7: Shaded-relief images of (A) Bouguer gravity data and (B) Bouguer gravity upward-continued to 20 km.

Mafic magmatic rocks

By overlaying the lithological layer on the 3-D analytical signals layer (Fig. 2.8A), it was found that high analytical signals coincide spatially with mapped mafic magmatic rocks. As compared to metasedimentary and acidic magmatic rocks, mafic magmatic rocks contain much higher concentrations of magnetite and ferromagnesian minerals and, thus, generate stronger analytical signals. Moreover, analytical signal anomalies are positioned directly above their crustal causative bodies. The analytical signals image (Fig. 2.8A) was thus used to interpret presence of other (i.e., unmapped) mafic magmatic bodies in the area. The interpreted mafic magmatic bodies show good spatial coincidence with mafic magmatic bodies mapped by Gupta *et al.* (1995a). However, the interpreted mafic magmatic bodies have wider areal extents than respective mapped mafic magmatic bodies, which indicates wider subsurface extensions of these bodies below weakly magnetic metasedimentary rocks. Based on available information about mapped (Gupta *et al.*, 1995a) and unmapped (Gupta *et al.*, 1997) mafic magmatic bodies, interpreted mafic magmatic bodies were classified as: (a) mafic metavolcanic rocks, (b) serpentinites, (c) basic granulites, (d) norite, (e) amphibolite and (f) unclassified mafic rocks (Fig. 2.8B).

Tectonic domains

For a qualitative tectonic interpretation, the most important characteristics of magnetic anomalies are their trends, relative amplitudes and wavelengths. Trends of anomalies depend on orientations of magnetic sources, which, in turn, are tectonically controlled. Wavelengths and relative amplitudes of anomalies indicate, respectively, lateral extent and a combination of vertical extent and relative magnetic susceptibilities of causative bodies. Together, such characteristics of magnetic anomalies reflect the tectonic character of a crustal domain. The magnetic image (Fig. 2.5A) was interpreted, based on anomaly characteristics mentioned above, with the objective of dividing the area into a number of tectonic domains (Fig. 2.9A). Due to incomplete aeromagnetic coverage, domains in eastern parts of the area were demarcated based on the FVD residual gravity image and on available tectono-stratigraphic information. The tectonic domains show linear dispositions, occur as parallel or sub-parallel belts having distinctive features in most thematic layers and show good spatial coincidence with major lithostratigraphic belts identified by Sugden *et al.* (1990) and Sinha-Roy *et al.* (1998).
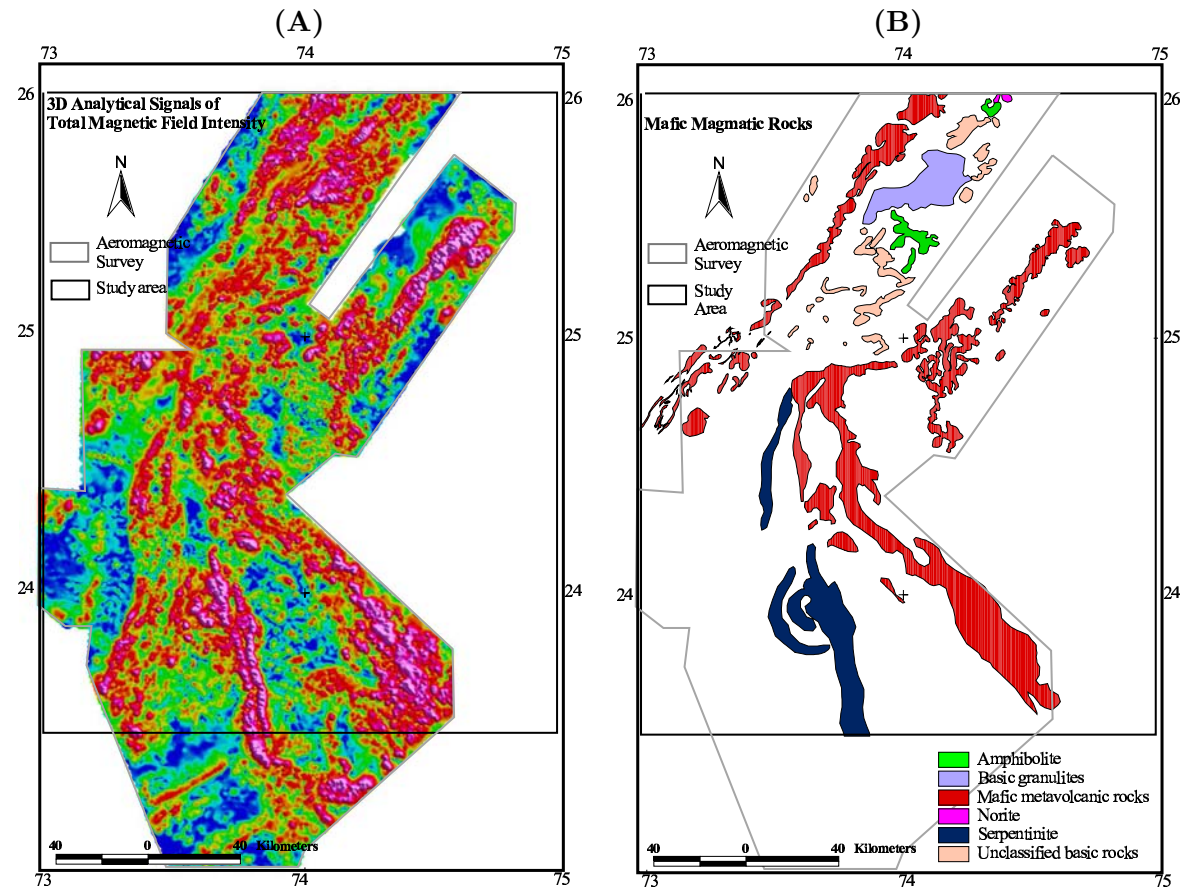
Figure 2.8: (A) Shaded-relief image of 3D analytical signals of total magnetic field intensity and (B) interpreted mafic magmatic bodies.
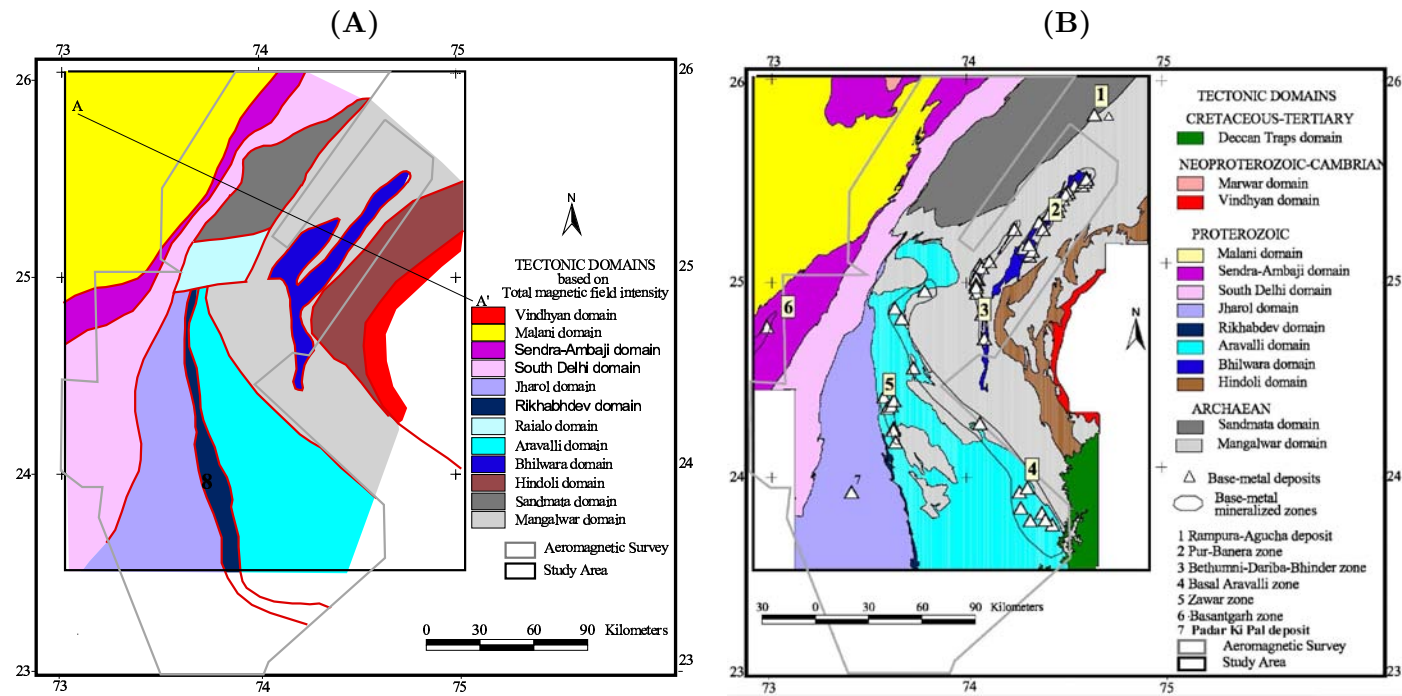
Figure 2.9: Tectonic domains (A) based on interpretations of magnetic data and (B) derived from geological literature. Crustal section along transect AA' is modeled in Fig. 2.10.

Crustal structure

The Bouguer gravity image (Fig. 2.7A) shows a prominent and broad N-S to NNE-SSW trending gravity high flanked by gravity lows along boundaries characterized by steep gradients. The amplitude of the central gravity high and gradients of peripheral gravity lows show a decline from north to south. The pattern is enhanced in upward-continued gravity images (e.g., Fig. 2.7B). However, the pattern is faintly discernible in the FVD residual gravity image (Fig. 2.6A), in which the central gravity high is replaced by a largely low-residual gravity matrix ingrained with bands of high residual gravity, especially in the Sandmata domain (Figs. 2.6A and 2.9A). Because upward-continuation and FVD filters enhance long wavelength (deep-seated) and short wavelength (near-surface) anomalies, respectively, two explanations can be advocated for the central gravity high. First, the source of the central gravity high is a southward-plunging high-density body at deeper crustal levels. Second, near-surface sources do not contribute significantly to the central gravity high except in the Sandmata domain, where high residual gravity bands that correlate broadly with exposed high-density granulitic intrusions indicate presence of a granulitic body emplaced in upper crustal levels.

There is broad correlation between the FVD residual gravity image and the Bouguer gravity image with respect to the peripheral gravity lows (Figs 2.6A and 2.7A). However, the FVD residual gravity image reveals the presence of a narrow linear residual gravity high along the eastern edge of the western peripheral low (Fig. 2.6A), which appears to be the response of exposed high-density mafic rocks of ophiolitic affinity (Gupta *et al.*, 1980; 1997) comprising the Sendra-Ambaji domain (Fig. 2.9). The western margin of the eastern peripheral low is similarly delimited by a narrow residual gravity high (Fig. 2.6A).

A 2D forward gravity modeling procedure was applied to model observed Bouguer gravity values across a section of central parts of the area (line AA' on Figs. 2.6B and 2.9A) using regional magnetic/gravity lineaments as boundaries between different crustal blocks (Fig. 2.10). Modeling is constrained by deep seismic reflectivity data along the Nagaur-Jhalawar transect (about 100 km north of AA'; Tewari *et al.*, 1995) and draws on published gravity models along this transect (Rajendra Prasad *et al.*, 1998; Mishra *et al.*, 2000). The FVD residual gravity image (Fig. 2.6A) and the Bouguer gravity image (Fig. 2.7A) show that main features of the cross-section model (Fig. 2.10), including the presence of a high-density body in the lower crust and a narrow high-density body at the contact between the Malani domain and the South Delhi domain,

are characteristic of the entire Aravalli crust (see also, Mishra *et al.*, 2000). The westerly dipping moderately low-density body below the Hindoli domain (Fig. 2.10), imaged as a bunch of westerly-dipping reflections on the deep seismic reflectivity profile along the Nagaur-Jhalawar transect, is interpreted as a crustal-scale thrust (Jahazpur Thrust) originating from the Moho (Tewari *et al.*, 1998; Rajendra Prasad *et al.*, 1998; Vijaya Rao *et al.*, 2000). Tewari *et al.* (1998) suggest that the Jahazpur Thrust may have served as a channel for transportation of high-density mafic materials to the near surface. This is supported by the FVD residual gravity image (Fig. 2.6A), which shows a narrow near-surface high-density body along the contact between the Hindoli domain and the Mangalwar domain (gravity lineament G1 in Fig. 2.6B).

2.3.1 Constitution and spatial distribution of tectonic domains

Sugden *et al.* (1990) and Deb and Sarkar (1990) used lithological and structural criteria to divide the study area into sub-parallel tectonic belts from east to west (Fig. 2.4A): (a) the Banded Gneissic Complex (BGC) (b) the Bhilwara belt (c) the Aravalli belt (d) the Jharol belt, (e) the South Delhi belt and (f) the Erinpura granites (Malani Igneous suite). Although these belts broadly correlate with tectonic domains interpreted from the geophysical data (Fig. 2.9), their constitution and spatial distribution are quite different from some of the tectonic domains.

The geophysical data indicate that the Bhilwara belt as defined by Sugden *et al.* (1990; Fig. 2.4A) possibly comprises three tectonic domains, viz., the Hindoli domain, the Mangalwar Domain and the Bhilwara domain (Fig. 2.9), which are delimited by crustal scale regional gravity or magnetic lineaments (M1 to M5 and G1 in Figs. 2.5B and 2.6B, respectively). The Hindoli domain comprises bimodal volcanic and turbidite sequences characterized by low-grade greenschist facies metamorphism, whereas the Mangalwar domain comprises gneisses and migmatites characterized by high-grade amphibolite facies metamorphism. Several deep seismic reflectivity studies (Tewari *et al.*, 1998; Rajendra Prasad *et al.*, 1998; Vijaya Rao *et al.*, 2000) have shown that the Hindoli and Mangalwar domains, which are separated by the deep-seated Jahazpur Thrust (marked by gravity lineament G1; Fig. 2.6B), have different crustal characteristics. Similarly, the Bhilwara domain, which comprises linearly-disposed enclaves of base-metal-bearing clastic metasediments and carbonates with associated mafic metavolcanics, are separated from the surrounding Mangalwar domain by prominent magnetic lineaments (M1 to M5 in Fig. 2.5B).
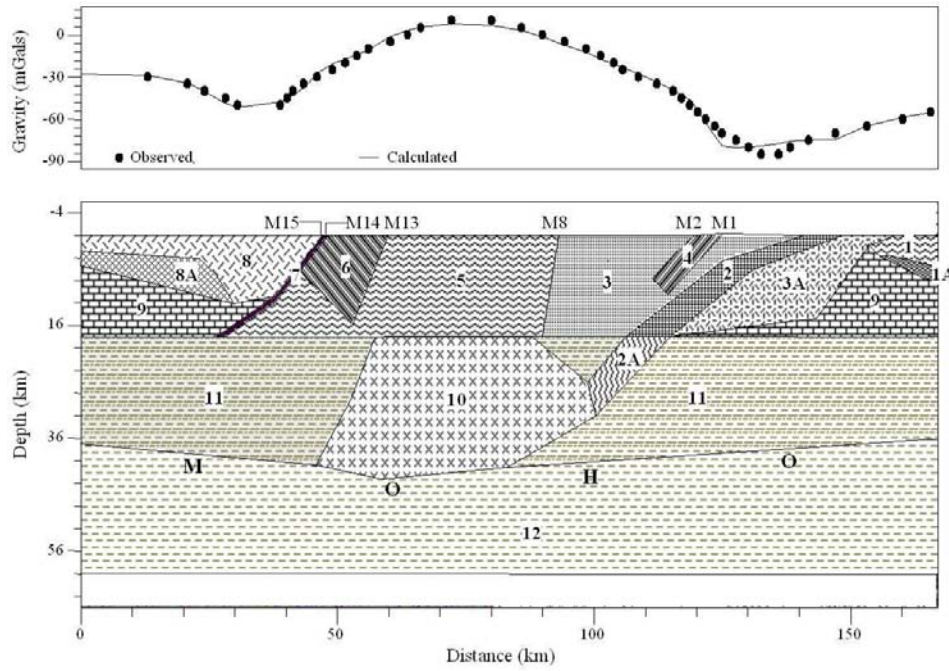
Figure 2.10: Model of crustal section along transect AA' (Figs. 2.6B and 2.9B) based on Bouguer gravity data. Causative sources and densities (in parenthesis; in gm/cc): 1 - Vindhyan domain (2.56); 1A - high density body below Vindhyan domain (2.9); 2 - Hindoli domain (2.65); 2A - high density body below Hindoli domain (2.85); 3 - Mangalwar domain (2.75); 3A - Berach granite (intrusive in Mangalwar domain) (2.62); 4 - Bhilwara domain (2.72); 5 - Sandmata domain (2.76); 6 - South Delhi domain (2.72); 7 - Sendra-Ambaji domain (2.9); 8 - Malani domain (2.62); 8A - high density body below Malani domain (2.9); 9 - Upper Crust (2.7); 10 - high density body within Lower Crust (3.04); 11 - Lower Crust (2.9); 12-Mantle (3.3). Crustal structure is constrained by deep seismic reflectivity data along Nagaur-Jhalawar transect (about 100 km north of AA'; Tewari et al., 1997). Densities of various blocks are from published gravity models along Nagaur-Jhalawar transect (Rajendra Prasad et al., 1998; Mishra et al., 2000). M1, M2, M8, M13 to 15 are magnetic lineaments (Fig. 2.5B.

Difference in tectonic constitution of the Bhilwara and Mangalwar domains is reflected in the magnetic data (Fig. 2.5A): the Bhilwara domain is characterized by pronounced high-amplitude, short-wavelength, NW-SE trending linear anomalies; whereas the Mangalwar domain is characterized by flat and subdued anomalies. Significantly, the difference between magnetic responses of the Bhilwara and Mangalwar domains persists even in upward-continued magnetic data, which indicates that they may have fundamentally different tectonic constitutions. Based on detailed structural and lithological considerations, Sinha-Roy (1988; 1989) and Sinha-Roy and Chore (1991) separate the base-metal-bearing metasedimentary enclaves of the Bhilwara domain from the gneisses and migmatites of the Mangalwar domain.

The geophysical data indicate that the Delhi supergroup comprises two distinct tectonic domains (Fig. 2.9) - the South Delhi domain to the east and the Sendra-Ambaji domain (cf. Deb *et al.*, 2001) to the west - separated by conspicuous magnetic lineament (M14 on Fig. 2.5B). The South Delhi domain, on one hand, is composed largely of arenaceous and calcareous metasediments with subsidiary volcanic rocks. The Sendra-Ambaji domain, on the other hand, is composed predominantly of volcanic-sedimentary sequences with higher proportions of magmatic rocks consisting of bimodal volcanics, a complex petrological association of metamorphosed low-K tholeiites with well-preserved relict pillows, small bodies of pyroxenites, layered gabbros and serpentinites (Phulad ophiolite suite; Gupta *et al.*, 1980; 1997; Sugden *et al.*, 1990). Based on extensive geochronological studies, Deb *et al.* (2001) conclude that rock assemblages of the Sendra-Ambaji domain constitute a distinct tectonic terrane and should be separate from the Delhi supergroup. Difference in tectonic constitution of the South Delhi and Sendra-Ambaji domains is reflected in their contrasting magnetic response: the South Delhi domain is characterized by a flat and subdued magnetic response; whereas the Sendra-Ambaji domain is characterized by NE-SW trending high amplitude anomalies (Fig. 2.5A). The crustal section modeled using the Bouguer gravity data (Fig. 2.10) also shows the Sendra-Ambaji domain as a westerly dipping zone of high density along the western fringe of the South Delhi domain (Rajendra Prasad, 1998).

2.3.2 Stratigraphic correlations

The available geochronological, structural and petrological data suggest that the Sandmata and Mangalwar domains comprise the Archaean basement in the area (Gupta *et al.*, 1997). Although no incontrovertible Archaean dates have

been reported from the Sandmata domain, structural and petrological considerations suggest that it is a basement block that has undergone tectono-thermal reconstitution resulting from emplacement of granulites during the Proterozoic (Sharma, 1988; Sinha-Roy, 1988; 2001; Roy and Kataria, 1999; Bose, 2000). In the case of the Mangalwar domain, undoubted Archaean ages have been reported from its southern parts (MacDougall *et al.*, 1983 1984; Gopalan *et al.*, 1990; Weidenbeck and Goswami, 1994; Roy and Kroener, 1996). However, stratigraphic equivalence of southern parts with other parts of the Mangalwar domain has been questioned strongly by Roy (1988b) and Roy and Kataria (1999), who consider southern parts of the Mangalwar domain (∼Mewar gneiss; cf. Roy, 1988b) as Archaean and other parts (mapped as Bhilwara belt by Sugden *et al.*, 1990; Fig. 2.4A) as Proterozoic. Nevertheless, based on the geophysical data, there seems to be absence of a definitive discontinuity between southern and other parts of the Mangalwar domain (Figs. 2.5A, 2.6A, 2.7A and 2.7B) and therefore the interpretation of Sinha-Roy (1988) that the Mangalwar domain is a single block of Archaean basement rocks seems plausible. It is pointed out, however, that the issue can only be resolved through detailed geochronological studies.

The geochronological data indicate that the Aravalli, Bhilwara and Hindoli domains are Palaeo-Proterozoic and stratigraphically coeval. The age of the Aravalli domain is constrained between ca. 2075 Ma and 2150 Ma for its basal sequences (Deb and Thorpe, 2001) and between ca. 1690 Ma and 1710 Ma for its middle sequences (Deb *et al.*, 1989; Deb and Thorpe, 2001); no specific age constraints are available for its upper sequences. However, based on indirect evidence, Sinha-Roy (2001) constrains closure of Aravalli basins between 1500 and 1600 Ma (see also, Roy and Kataria, 1999; Deb and Thorpe, 2001). Deb and Thorpe (2001) have dated the basal sequences of the Hindoli domain at 1854±7 Ma. The age of the Bhilwara domain is constrained at ca. 1800 Ma based on Pb isotope data from syngenetic base-metal deposits (Deb *et al.*, 1989). No geochronological data are available from the Raialo domain. Most authors consider metasedimentary rocks of the Raialo domain as Palaeo-Proterozoic and stratigraphically equivalent to lower Aravalli sequences (Gupta *et al.*, 1980, 1995a, 1997; Roy *et al.*, 1988; Sinha-Roy, 2001). However, Sinha-Roy *et al.* (1993) suggested a possibility that the Raialo rocks are parts of the Archaean basement and are separated from the Aravalli rocks by the Banas lineament (M6 on Fig. 2.5B), which has a strong topographic expression as well. The Banas lineament possibly does not have a deep-seated origin because

(a) there is evidence of physical continuation of litho-units as well as magnetic anomalies across it and (b) it does not persist in upward-continued magnetic data. Therefore, it seems likely that the Raialo domain is Palaeo-Proterozoic and stratigraphically coeval with the Aravalli domain.

Geochronological data are unavailable for the Jharol domain. Its stratigraphic status is constrained mainly by field relations, which indicate that it stratigraphically overlies the Aravalli domain (Gupta *et al.*, 1980; 1997; Roy *et al.*, 1988; Sinha-Roy *et al.*, 1998). The age of the Delhi domain is also poorly constrained. Deb and Thorpe (2001) indicate an age of ca. 1800 Ma for initialization of Delhi sedimentation, while Sinha-Roy (2001) suggests a much younger age (ca. 1500). Similarly, the age of closure of Delhi basins has been constrained variously at ca. 1400 Ma (Chodhary *et al.*, 1984; Roy and Das, 1985), ca. 1500 (Deb and Thorpe, 2001) and at ca. 900 Ma (Sinha-Roy, 2001). The age of the Sendra-Ambaji domain is constrained at ca. 1000 Ma by Deb *et al.* (2001). Age data of the Malani domain cluster around 850 Ma.

2.4 Conceptual Model of Tectonostratigraphy and Metallogenesis

2.4.1 Evolution of tectonic domains and base-metal mineralization

Sinha-Roy (1985, 1988, 2001) and Sinha-Roy *et al.* (1995) postulate tectonic evolution of Aravalli province in the framework of near-orderly Proterozoic Wilson cycles (see also Deb and Sarkar, 1990; Sugden *et al*, 1990). They hypothesized that recurrent phases of extensional and compressional tectonics of the province in Proterozoic resulted in sequential opening and closing of intracratonic rifts. Sinha-Roy (2000, 2001) described a conceptual model of metallogenesis in the Aravalli province in the framework of the above Proterozoic cycles. Based on his model, evolution of the main tectonic domains and associated base-metal mineralizations in the study area can be envisaged in the framework of Proterozoic tectonic events as follows (Fig. 2.11).

1. At ca. 2500 Ma, the basement complex comprising the Mangalwar and Sandmata domains was cratonized.

2. At ca. 2000 Ma, the Aravalli rift opened and, possibly through a second phase of rifting at ca. 1800 Ma, evolved into an ocean that closed at ca.
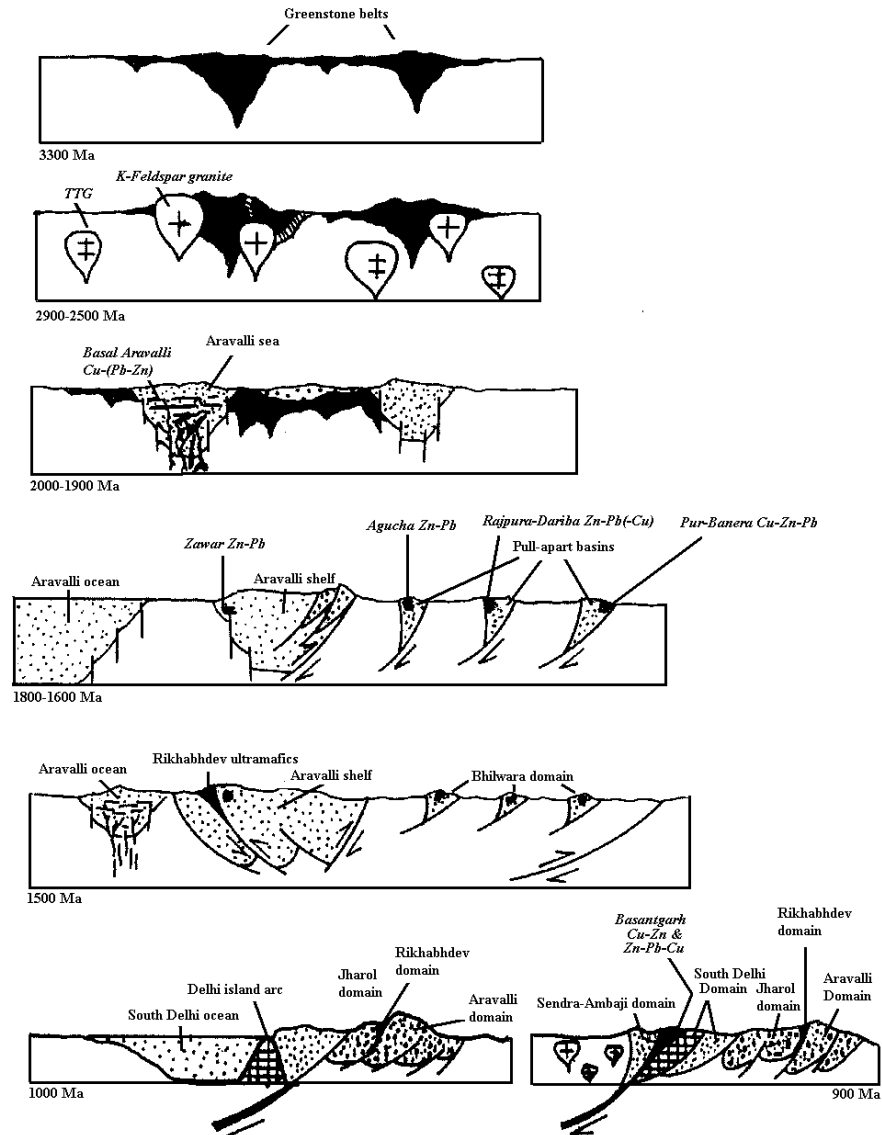
Figure 2.11: Plate tectonic cartoon showing the linkage between crustal evolution and metallogeny in study area (from Sinha-Roy, 2001).

1500 Ma (Sinha-Roy, 2001). Synsedimentary mafic volcanics and near-shore sediments deposited on the shelf of the Aravalli ocean constitute the Aravalli domain, while deep-sea sediments deposited in the Aravalli ocean constitute the Jharol domain. The Rikhabhdev domain, which comprises highly tectonized serpentinites, minor meta-gabbro, meta-basalt and chert ('Rikhabhdev ultramafics'), possibly represents an ophiolite assemblage obducted due to closing of the Aravalli ocean (Sinha-Roy, 1984, 1988, 2000; Sugden *et al.*, 1990; Deb and Sarkar, 1990). The first phase of the rifting was accompanied by minor Cu(-Pb-Zn) mineralization, while the second phase of the rifting was accompanied by a major SEDEX-type stratabound Zn-Pb mineralization event in the Zawar zone. The Zawar deposits were formed close to a basement inlier, in second-order basins with biological activity, by hydrothermal fluids convecting through a heterogeneous source comprising various sediments (Deb *et al.*, 1989; Deb and Sarkar, 1990).

3. At ca. 1800 Ma, several rifts opened in the Mangalwar domain accompanied by mafic volcanism, possibly as pull-apart basins due to large-scale wrench faulting associated with distensional tectonics related to the second stage of the Aravalli rifting (Sinha-Roy, 1989; Sinha-Roy and Chore, 1991; Sinha-Roy, 2000). These narrow rifts were, however, aborted. They are represented by linear metasedimentary enclaves in the Mangalwar domain and constitute the Bhilwara domain. These aborted rifts provided favorable locales for massive SEDEX type stratabound and stratiform Zn-Pb and Zn-Pb-Cu mineralizations at Rampura-Agucha and in the Bethumni-Dariba-Bhinder and Pur-Banera belts, which were formed by convective seawater circulation in zones of crustal extension (Deb, 1986; Deb and Sarkar, 1990). Metal content of exhalative brines was precipitated in second-order troughs with high biological activity.

4. At ca. 1500 Ma, the Delhi rift opened and developed into an ocean, which was subsequently closed following subduction of Delhi ocean crust at ca. 1000 Ma (Sinha-Roy, 2001). This resulted in formation of an island arc along western margin of Delhi ocean, which contained VMS-type Zn-Pb-Cu in Deri area. Subsequent closure of the back-arc basin (floored by oceanic crust; Sinha-Roy, 2001), possibly due to a second stage of subduction at ca. 900 Ma, resulted in obduction and emplacement of an ophiolite melange accompanied by VMS-type Cu-Zn mineralizations

in the Basantgarh zone. Sediments deposited in the Delhi rift constitute the Delhi domain, while the back-arc and island arc sequences, including the ophiolite melange, constitute the Sendra-Ambaji domain.

The magnetic lineaments show consistent spatial association with linear belts of mafic magmatic bodies (Fig. 2.12). The tectonic domains delimited by these lineaments have distinctive lithological, metamorphic and metallogenic characteristics, which suggest that these lineaments possibly represent crustal-scale discontinuities. This is further supported by (a) spatial coincidence of at least some of these lineaments with established tectono-stratigraphic discontinuities in the area (b) persistence of these lineaments (except Banas lineament) in upward-continued magnetic data. In the framework of the tectonic evolution outlined above, the magnetic lineaments are interpreted as traces of the margins of Proterozoic crustal segments (represented by tectonic domains) and, by implication, boundaries of intracratonic rifts (the Aravalli, Bhilwara and South Delhi domains) or subduction zones (the Sendra-Ambaji domain). As boundaries of intracratonic rifts are generally marked by crustal scale extensional faults, lineaments M1 to M5, M9 and M13 (Fig. 2.5B), which mark boundaries of the Bhilwara, Aravalli and Delhi domains, respectively, can be interpreted as crustal scale extensional faults. Similarly, lineaments M14 and M15 (Fig. 2.5B), which delimit the Sendra-Ambaji domain, can be interpreted as crustal scale (compressional?) faults.

2.4.2 Generalized geological setting of base-metal mineralizations

The conceptual model outlined above indicates that major SEDEX-type base-metal mineralization in the study area is linked to the extensional tectonic event at ca. 1800 Ma that resulted in (a) formation of the (aborted) Bhilwara intracratonic rifts and (b) a second stage of rifting in the Aravalli intracratonic rifts that led to deepening of the Aravalli ocean. The settings of the SEDEX mineralization in the study area are similar to the following generalized setting of SEDEX deposits (after Goodfellow, 2001, see also Fig. 2.13).

- Most SEDEX deposits are hosted by basinal sediments deposited within failed intracratonic rifts or fault-bounded grabens or rifted continental margins and are formed during reactivation of extensional structures.
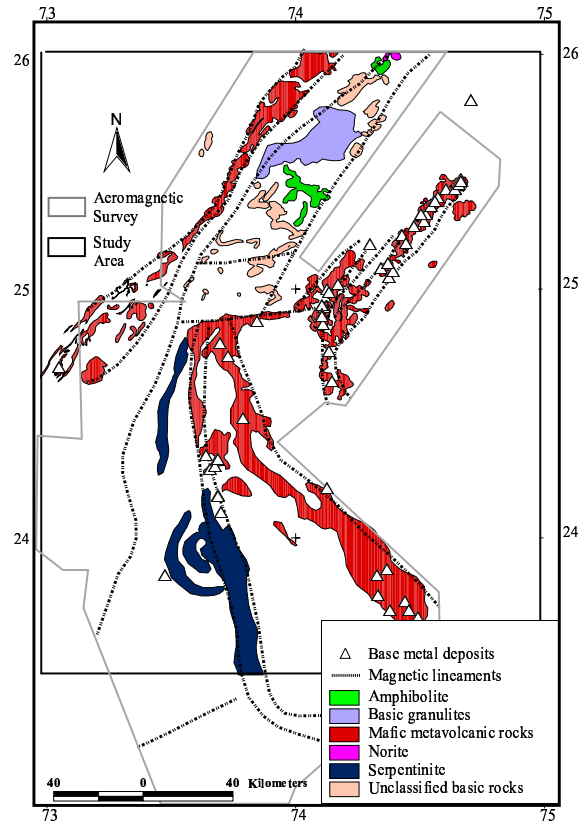
Figure 2.12: Map overlay of mafic igneous rocks, magnetic lineaments and base-metal deposits.

- There is a close temporal and spatial relationship between SEDEX deposits and mafic magmatic rocks, which indicates that magma injection into the lithosphere may have played an essential role in establishing the heat necessary to generate metalliferous hydrothermal fluids and associated SEDEX deposits.

- The ambient sedimentary rocks for SEDEX deposits comprise carbonaceous chert, shale, siltstone and coarser clastics, sedimentary breccias and carbonate rocks.

- There is a close correlation between anoxic conditions and SEDEX deposits, and a similarity in $\delta^{34}S$ trends of hydrothermal and ambient sedimentary sulfides, which indicate that most of the reduced sulfur in many deposits was derived from the ambient water column and that a reduc-

45
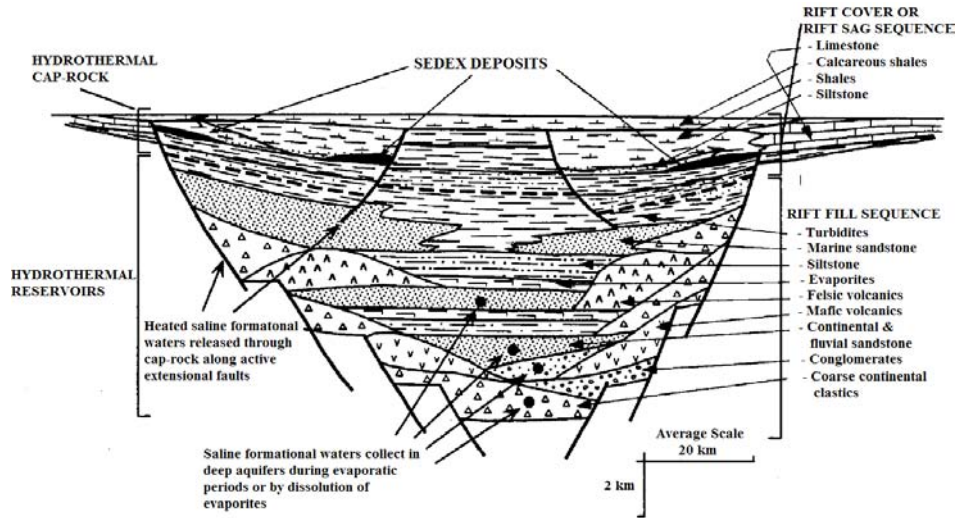
Figure 2.13: Schematic section through a rift-controlled sedimentary basin showing idealized setting of SEDEX deposits. SEDEX deposits are hosted by the cover sequence to an intracratonic rift system filled by continental clastics, marine clastics and rift-related volcanic rocks. The rift cover sequence acts as hydrothermal cap rocks (base marked by bold dashed line) to brines during their heating by deep magmatism or burial. Geopressured heated brines flow to the contemporaneous surface of the cover sequence when the cap rock is ruptured by renewed extensional tectonism. (From Lydon, 1996, 2001).

ing environment may have been essential to the formation of SEDEX deposits.

- Sedimentary textures (for example, graded and cross-laminated beds) and other evidence suggest that most of the sulfides were deposited as sediments on the sea floor.

The VMS-type mineralization in the Basantgarh zone of the Sendra-Ambaji domain, on the other hand, appears to be related to compressional tectonic events at ca. 1000, that led to the closure of Delhi rifts.

2.4.3 Mineralization controls and deposit recognition criteria

Most deposits/prospects in basal sequences of the Aravalli domain are confined to specific stratigraphic horizons and associated with metavolcanic-dolomite-phyllite assemblages. This indicates prominent lithological and stratigraphic control on the first phase of base-metal mineralization. Presence of mafic

metavolcanic (amphibolite) rocks in the host-rock assemblage indicates a possible heat-source control for generation and circulation of metalliferous fluids.

The stratigraphically-controlled stratiform-to-stratabound nature of the large sediment-hosted SEDEX-type base-metal deposits of Rampura-Agucha and in Pur-Banera, Bethumni-Dariba-Bhinder and Zawar zones indicate lithology, stratigraphy and (palaeo-)sedimentary environment as primary regional controls on the second phase of base-metal mineralization. However, presence of mafic metavolcanic rocks (amphibolite) in the host-lithological assemblages (Table 2.1) indicates a possible heat-source control for generation and circulation of metalliferous fluids. Field evidence of widespread post-genetic remobilization and translocation along regional fold axes, especially in the Zawar and Pur-Banera mineralized zones (Raghunandan, 1981; Singh, 1988), suggests that regional folding also constitutes an important control on mineralization.

The smaller VMS-type deposits in the Sendra-Ambaji domain are, according to Deb (2000b), associated with: (a) metamorphosed bimodal volcanic rocks (Ambaji and Deri deposits, which fall outside the study area); and (b) metamorphosed mafic volcanic rocks (Basantgarh deposit). These associations indicate strong magmatic control on mineralization. The mineralization also shows a regional stratigraphic control, as indicated by occurrences of deposits/prospects only in specific stratigraphic horizons.

From the foregoing description of the generalized geological setting of SEDEX deposits and the base-metal deposit settings in the study area, it can be inferred that lithology, stratigraphy, sedimentary environment, heat source, tectonic setting and structure constitute the most important regional controls on base-metal mineralizations in the study area. Accordingly, the following are considered as the most significant recognition criteria for base-metal deposits in the study area (Porwal *et al.*, 2003a):

1. host rock lithology,

2. stratigraphic position,

3. (palaeo-)sedimentary environment,

4. association of mafic volcanic rocks,

5. proximity to favorable structures.

The first three criteria are based on the stratigraphically-controlled synsedimentational nature of the mineralization. The fourth criterion is based on the

suggestion of Deb (1999) and Goodfellow (2001) that mafic volcanic rocks in ore environments provided the heat necessary for the generation and circulation of exhalative brines in the case of SEDEX deposits and form a significant source of metals in the case of VMS deposits. The fifth criterion is based on the following considerations. The extensional/compressional faults, which mark the boundaries of the tectonic domains, could have provided structural permeability for migration of metalliferous hydrothermal fluids. These faults could also have focussed magmatic fluids, which, in turn, could have provided heat-source controls for convection of hydrothermal fluids, as evidenced by their close spatial association with mafic volcanic rocks. Furthermore, there is a strong evidence of extensive post-genetic remobilization and relocation of ores during subsequent deformation, especially in the Zawar and Pur-Banera zones (Raghunandan, 1981; Singh, 1988).

It may be noticed that the recognition criteria were identified from the SEDEX deposits, but there is some overlap of the recognition criteria of the SEDEX and VMS type base-metal deposits (for example, association of mafic volcanic rocks, proximity to favorable structures etc.) in the study area. As a result, several of the mathematical models applied in this research predict base-metal potential zones in the Sendra-Ambaji domain, which is tectonically favorable for VMS-type base-metal mineralization (Section 2.4.1).

2.5   Empirical Models of Spatial Association of Recognition Criteria with Known Base-Metal Deposits

Recognition criteria for base-metal deposits in the study area were represented as predictor maps by processing, interpreting and/or reclassifying the exploration data enumerated in Table 2.2. The procedures used are described in the following sections. The x and y dimensions of each of the predictor map shown in the following sections are 200 km and 275 km, respectively.

Recognition criterion 1: Host rock lithology

The lithostratigraphic map (Gupta *et al.*, 1995a) was used to generate an evidential map for the recognition criterion 'host rock lithology.' Irrespective of their stratigraphic positions, all lithologies on the map were extracted to create a map containing 136 classes of lithologies, most of which differed only in respect of textures and/or metamorphic grades. Because this large number

of classes would result in prohibitively large dimensionality of input data, the map was simplified by merging the classes with similar lithological compositions. The simplified map was analyzed and classes considered unrelated to base-metal mineralizations, such as intrusive granites, trap basalt etc, were merged to create a new class comprising lithologies unrelated to base-metal mineralization. The reclassified map, to be used as a predictor map representing the recognition criterion 'host rock lithology,' is shown in Fig. 2.14A.

Recognition criterion 2: Stratigraphic position

The lithostratigraphic map (Gupta *et al.*, 1995a) was reclassified to create an evidential map for the recognition criterion 'stratigraphic position.' All stratigraphic formations and their stratigraphic attributes (groups and supergroups) were extracted to create a stratigraphic map of the study area. However, the map contained 103 classes of stratigraphic formations, which would lead to undesirably large dimensionality of input data (see above). Therefore the map was generalized by merging stratigraphic formations based on their stratigraphic groups. The simplified map was analyzed and stratigraphic groups considered unrelated to base-metal mineralizations, for example, the Vindhyan group, Malani igneous suite, Deccan Traps, etc., were merged to create a new class comprising stratigraphic groups not related to base-metal mineralizations. The reclassified stratigraphic map, to be used as a predictor map representing the recognition criterion 'stratigraphic position,' is shown in Fig. 2.14B.

Recognition criterion 3: (Palaeo-)sedimentary environment

A (palaeo-)sedimentary environment map of the study area is not available. However, Gupta *et al.* (1997) give detailed information on mineralogy, texture, structure and interpreted depositional conditions of constituent metasedimentary rocks for each stratigraphic formation. Based on this information, the sedimentary environment of each stratigraphic formation was deduced to generate a map representing the recognition criterion '(palaeo-)sedimentary environment' (Fig. 2.15A), which is to be used as one of the input predictor maps. Although the number of stratigraphic formations is large, the number of classes in the map of sedimentary environments is small because many stratigraphic formations have the same interpreted sedimentary environment.

(A)

(B)

Basic rocks
Calc-silicates
Dolomite/dolomitic marble
Magnetite quartzite
Calc-schist/gneiss
Quartzite/Arkose/Conglomerate
Graphitic meta-pelites
Migmatites; gneisses
Unrelated to base metals

Phulad
Jharol
Nathdwara
Udaipur
Debari
Pur-Banera
Rajpura-Dariba
Sanmata Complex
mangalwar Complex
Unrelated to base metals
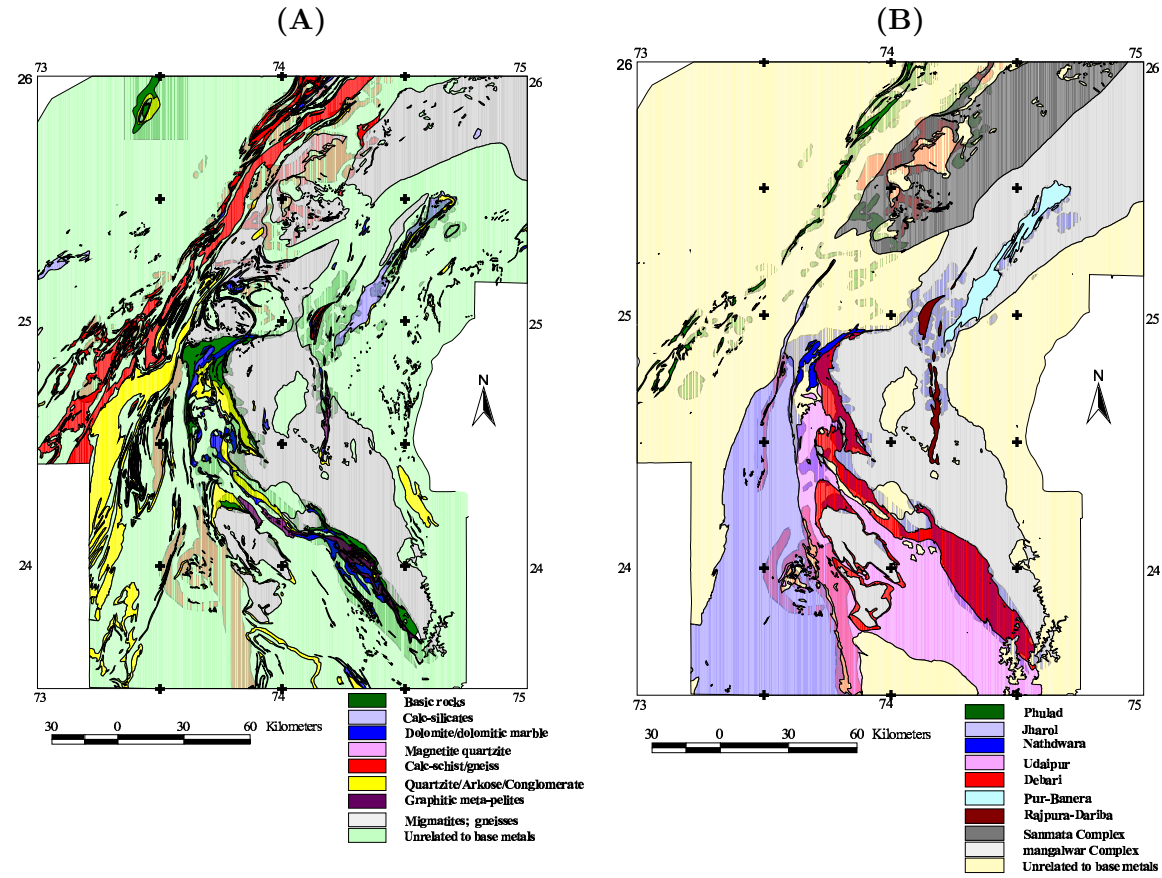
Figure 2.14: Predictor map of (A) lithologies and (B) stratigraphic groups.

Recognition criterion 4: Association of mafic volcanic rocks

An evidential map for the recognition criterion 'association of mafic volcanic rocks' was generated by reclassifying the map of mafic magmatic rocks (Fig. 2.8B), which was interpreted from total magnetic field intensity data. With the exception of the class 'mafic meta-volcanic rocks,' all classes on the map were merged to create a new class comprising all mafic rocks that are not related to base-metal mineralization in the study area. The resulting binary map of mafic magmatic rocks, to be used as a predictor map for the recognition criterion 'association of mafic volcanic rocks,' is shown in Fig. 2.15B.

Recognition criterion 5: Proximity to favorable structures

As discussed in Section 2.4.3, crustal-scale faults could have played significant role in localizing base-metal mineralizations and comprise favorable structural locales for base-metal deposits in the study area. Because the regional magnetic lineaments are interpreted as defining traces of crustal-scale faults (see Section 2.4.1), they were dilated and used as one of the predictor maps for the recognition criteria 'proximity to favorable structures.' The dilation was carried out by creating five buffer zones around the lineaments, each 2 km wide, up to a distance of 10 km. A sixth zone comprising parts of the study area at a distance greater than 10 km from the lineaments was added to generate a predictor map of buffered distances from regional lineaments (Fig. 2.18A).

In order to identify favorable structural trends that might have controlled localization of base-metal deposits, Fry analysis (Fry, 1979), which uses a geometrical method of spatial autocorrelation for point data, was performed using the procedure described by Vearncombe and Vearncombe (1999). For n points there are $n^2 - n$ spatial relationships and, because of the square function, the method yields interpretable results with small as well as large data sets.

Fry plot translations of point locations of all base metal deposits in the study area and the corresponding rose diagram of orientations of point-to-point translations indicate a predominant north-east trend and less dominant north-west trend (Fig. 2.16). Figure 2.17 shows that the north-east trend is defined by the major SEDEX-type base-metal deposits that formed in the second phase of mineralization in the study area ($\sim$ 1800 Ma metallogenetic episode), while the north-west trend is defined by smaller deposits that formed in the first phase of mineralization ($\sim$ 2000 Ma metallogenetic episode).

(A)

(B)
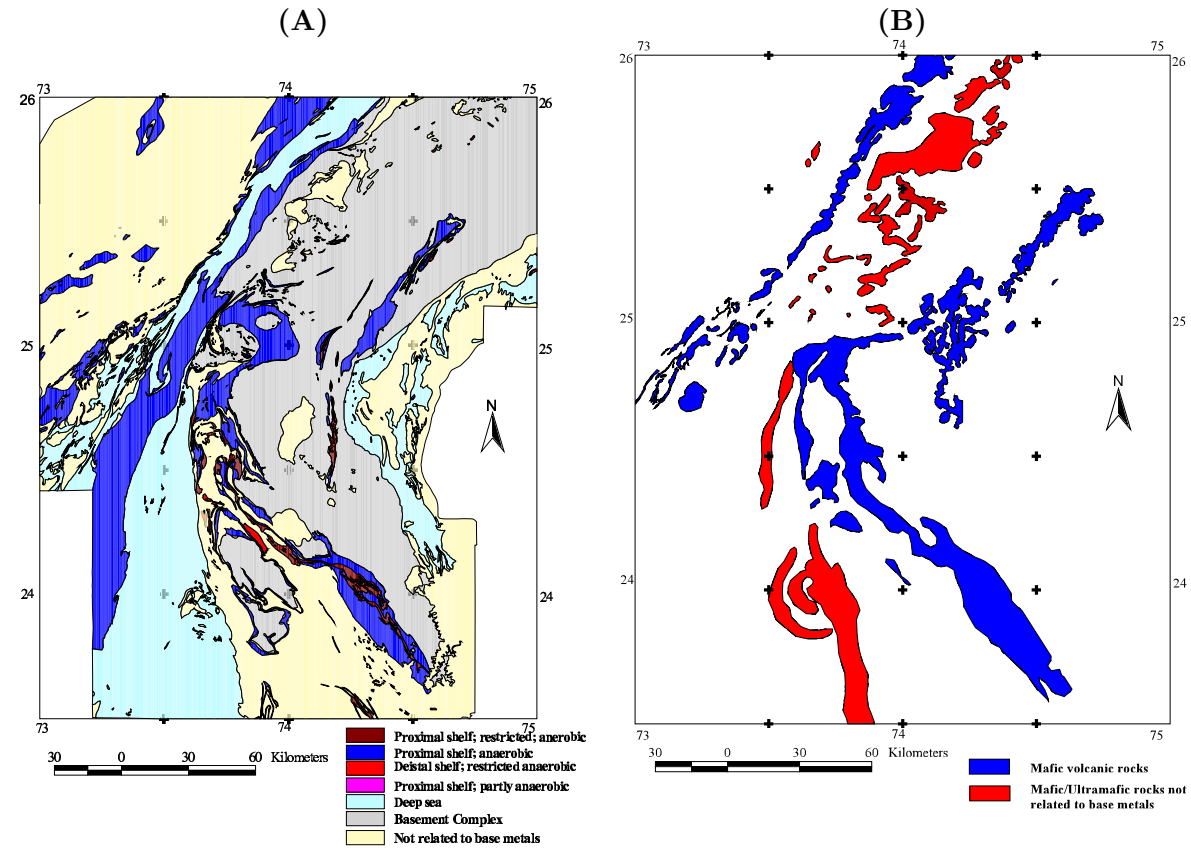
Figure 2.15: Predictor map of (A) sedimentary environments and (B) mafic magmatic rocks.

The third phase of mineralization is represented by just one deposit in the study area, and therefore a Fry analysis of this phase was not applicable. Vearncombe and Vearncombe (1999) show that trends identified in Fry analysis can be used to identify the favorable structural trends for mineralization. The above results therefore indicate that north-east and north-west are the two favorable trends of base-metal mineralization in the study area. As discussed in previous sections, the primary controls on base-metal mineralizations in the study area are lithostratigraphic. Therefore, the favorable trends identified by the Fry analysis are interpreted to indicate favorable structural trends of base-metal-hosting lithostratigraphic units. Because trends of magnetic anomalies reflect trends of source lithostratigraphic units, the trends of anomalies on the shaded-relief image of the total magnetic field intensity data (Fig. 2.5A) were mapped. A rose diagram of the lineaments thus obtained indicated four preferred orientations, viz., NE-SW, NW-SE, E-W and N-S. Based on the results of the Fry analysis described above, the NE- and NW-trending lineaments were extracted as separate maps and each set of lineaments was dilated by buffering into 5 zones, each 1.5 km wide, up to a distance of 7.5 km. To these was added a sixth zone comprising parts of the study area at a distance greater than 7.5 km from the lineaments. In this way two more predictor maps, namely, a map of buffered distances from NE-trending lineaments (Fig. 2.18B) and a map of NW-trending lineaments (Fig. 2.19A), were generated to represent the recognition criterion 'proximity to favorable structures.'

A fourth predictor map was generated by extracting regional fold axes from the structural map of the study area (Gupta *et al.*, 1995b). Well-documented evidence of post-genetic remobilization and translocation of ore lenses along regional fold axes, especially in Zawar deposits and Pur-Banera mineralized zones, indicate that regional fold axes form favorable structural locales for post-genetic concentration of base-metals in the study area (Raghunandan *et al.*, 1981; Singh, 1988; Roy, 2001). The regional fold axes were dilated by buffering into ten zones, each 500 m wide, up to a distance of 5 km. Parts of the study area at a distance greater than 5 km from the fold axes were classified as the eleventh zone to generate the evidential map of buffered distances from fold axes (Fig. 2.19B), which was used as an additional predictor map for the recognition criterion 'proximity to favorable structures.'

53
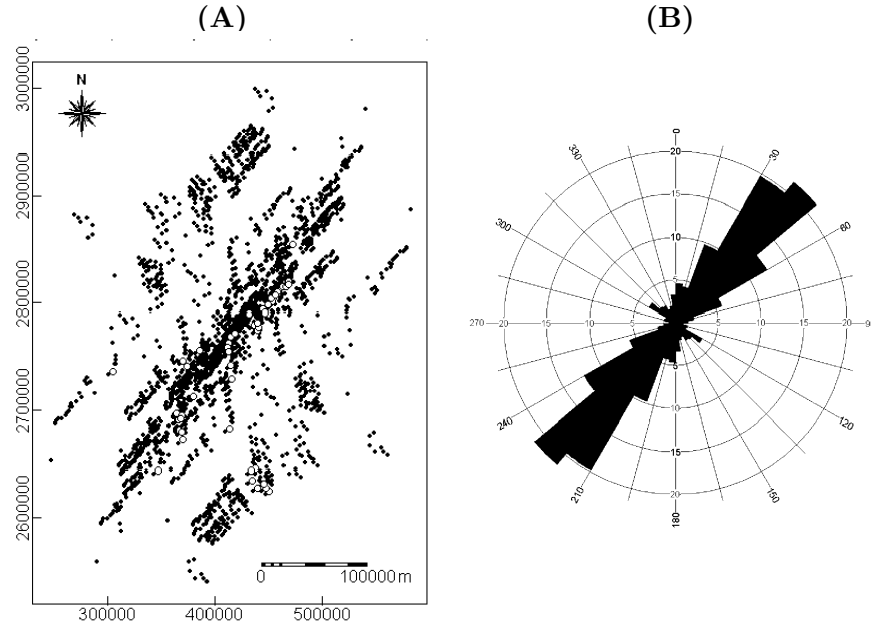
Figure 2.16: (A) Fry plot translations (black dots) of point locations of base metal deposits (white dots) in study area and (B) corresponding rose diagram of orientations of point-to-point translations. Map coordinates are in meters (UTM zone 43). Petal units of rose diagram are measured in relative frequency of orientations.

2.5.1 Spatial association with polygonal geological features

Spatial associations of known base-metal deposits and the four sets of polygonal geological predictor maps, namely, lithologies, stratigraphic groups, sedimentary environment and mafic volcanic rocks, were tested empirically by estimating the ratio of percentage of known deposits in a polygonal feature to percentage of the study area occupied by the polygonal feature. This ratio is indicative of conditional probability of occurrence of a base-metal deposit/occurrence, given the presence of a polygonal feature.

The results (Table 2.3) indicate that base-metal deposits have strong spatial associations with particular lithologies (dolomite, graphitic meta-pelites, calc-silicates and magnetite quartzite) and weak spatial associations with other rocks. Similarly, strong spatial associations are indicated between base-metal deposits and certain stratigraphic groups (Rajpura-Dariba, Pur-Banera, Debari and Nathdwara groups). Shelf sedimentary environments, especially if characterized anaerobic conditions, show strong spatial associations with base-metal deposits. The results also indicate a strong spatial association between

54
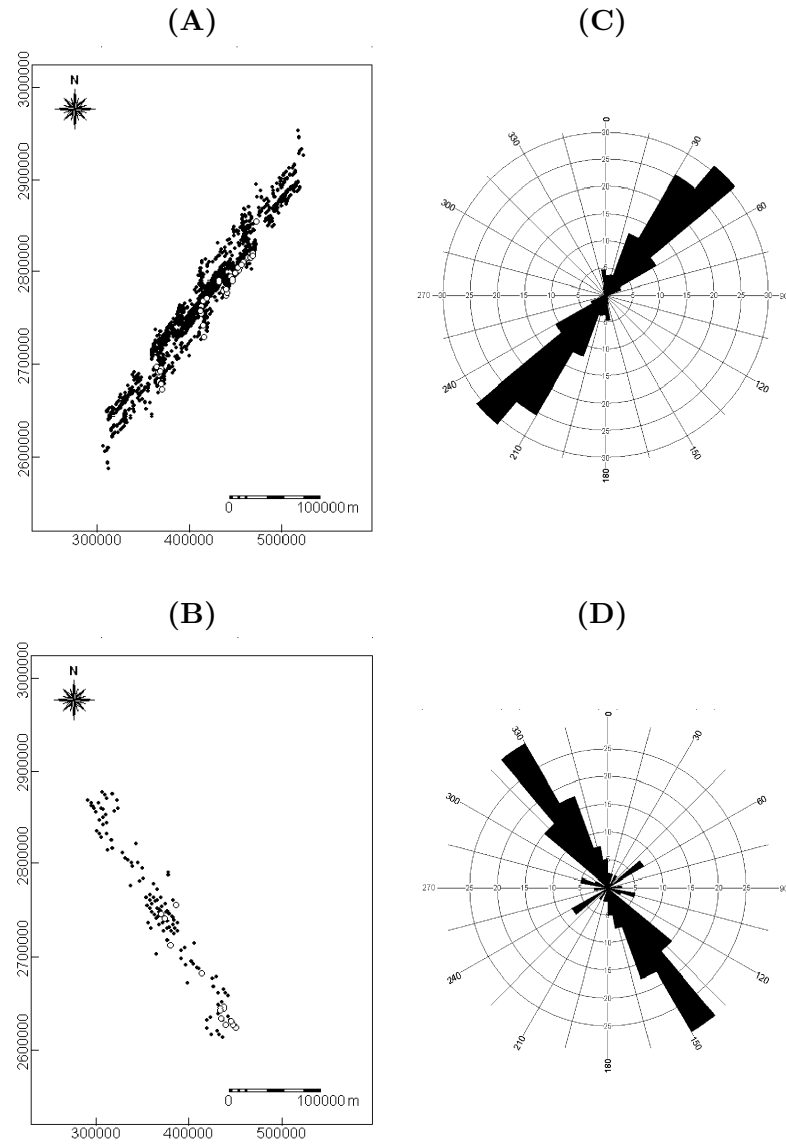
Figure 2.17: Fry plot translations (black dots) of point locations of base metal deposits (white dots) of (A) 1800 Ma metallogenic event and (B) 2000 Ma metallogenic event, and rose diagram of orientations of point-to-point translations for (C) 1800 Ma metallogenic event and (D) 2000 Ma metallogenic event. Map coordinates are in meters (UTM zone 43). Petal units of rose diagram are measured in relative frequency of orientations.

Table 2.3: Spatial association of known base metal deposits and polygonal predictor features

	Predictor map pattern	$\frac{\% \ deposits \ in \ feature}{\% \ area \ in \ feature}$
Predictor map of lithologies		
1	Dolomite/dolomitic Marble	20.90
2	Calc-silicates	26.20
3	Graphic meta-pelites	28.28
4	Magnetite quartzite	60.96
5	Calc-schist/calc-gneiss	0.59
6	Quartzite/Arkose/Conglomerate	0.30
7	Migmatite/Gneisses	0.10
8	Not related to base metals	0.00
Predictor map of stratigraphic groups		
1	Rajpura-Dariba group	62.33
2	Pur-Banera group	43.56
3	Debari groups	6.24
4	Nathdwara group	7.21
5	Phulad group	3.14
6	Udaipur group	1.36
7	Jharol group	0.17
8	Sandmata Complex	0.25
9	Mangalwar Complex	0.09
10	Not related to base metals	0.00
Predictor map of sedimentary environments		
1	Proximal shelf; restricted; anaerobic	22.16
2	Proximal shelf; anaerobic	4.23
3	Distal shelf; restricted; anaerobic	44.11
4	Proximal shelf; partly anaerobic	57.41
5	Deep sea	0.10
6	Basement Complex	0.06
7	Not related to base metals	0.00
Predictor map of mafic igneous rocks		
1	Mafic volcanic rocks	99.55
2	Not related to base metals	2.41

base-metal deposits and mafic volcanic rocks.

The above results validate the interpretation based on a conceptual model of base-metal metallogenesis that host rock lithology, stratigraphic position, (palaeo-)sedimentary environment and association of mafic volcanic rocks are important recognition criteria for base-metal deposits in the study area.

2.5.2 Spatial association with linear geological features

Using the procedures described by Bonham-Carter (1994), proximity analyses were performed to test spatial associations of known base-metal deposits and the four sets of predictor curvilinear features described above, namely, regional lineaments, NE-trending lineaments, NW-trending lineaments and regional
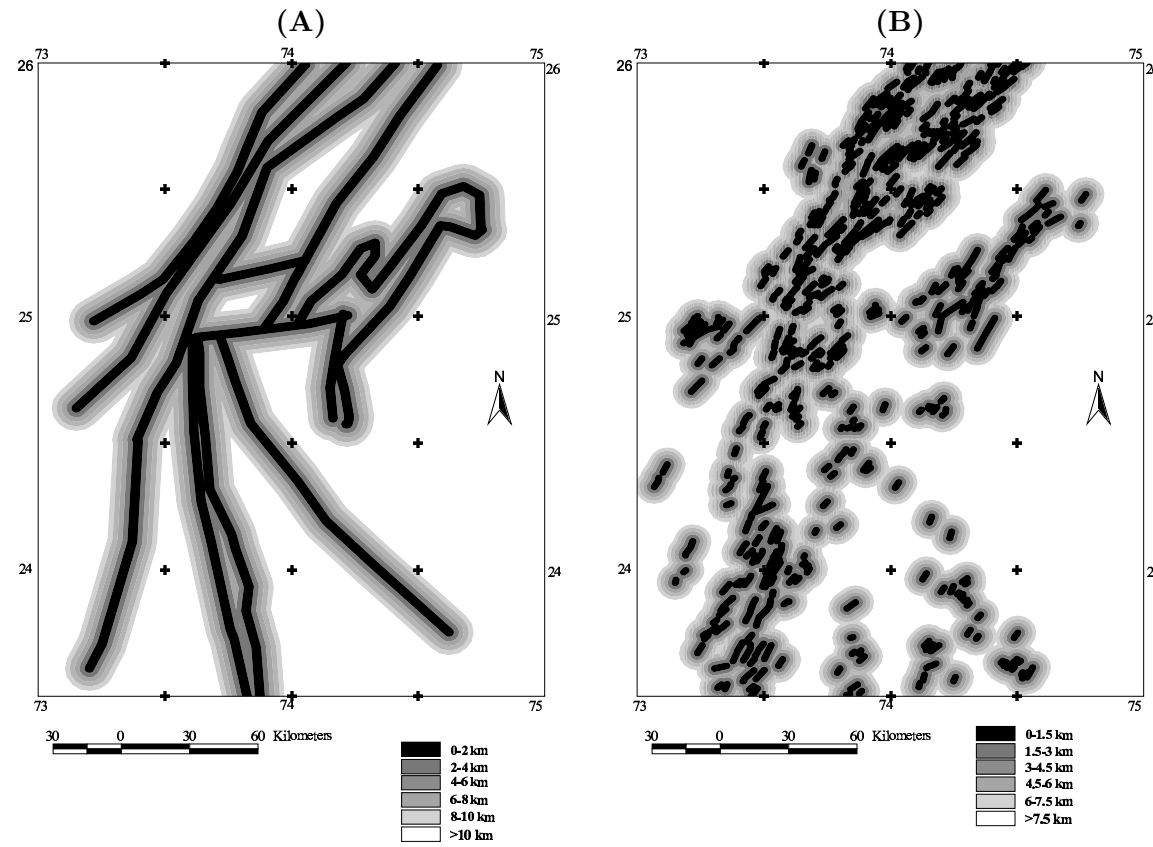
Figure 2.18: Predictor map of buffered distances from (A) regional lineaments and (B) NE-trending lineaments.

(A) **(B)**
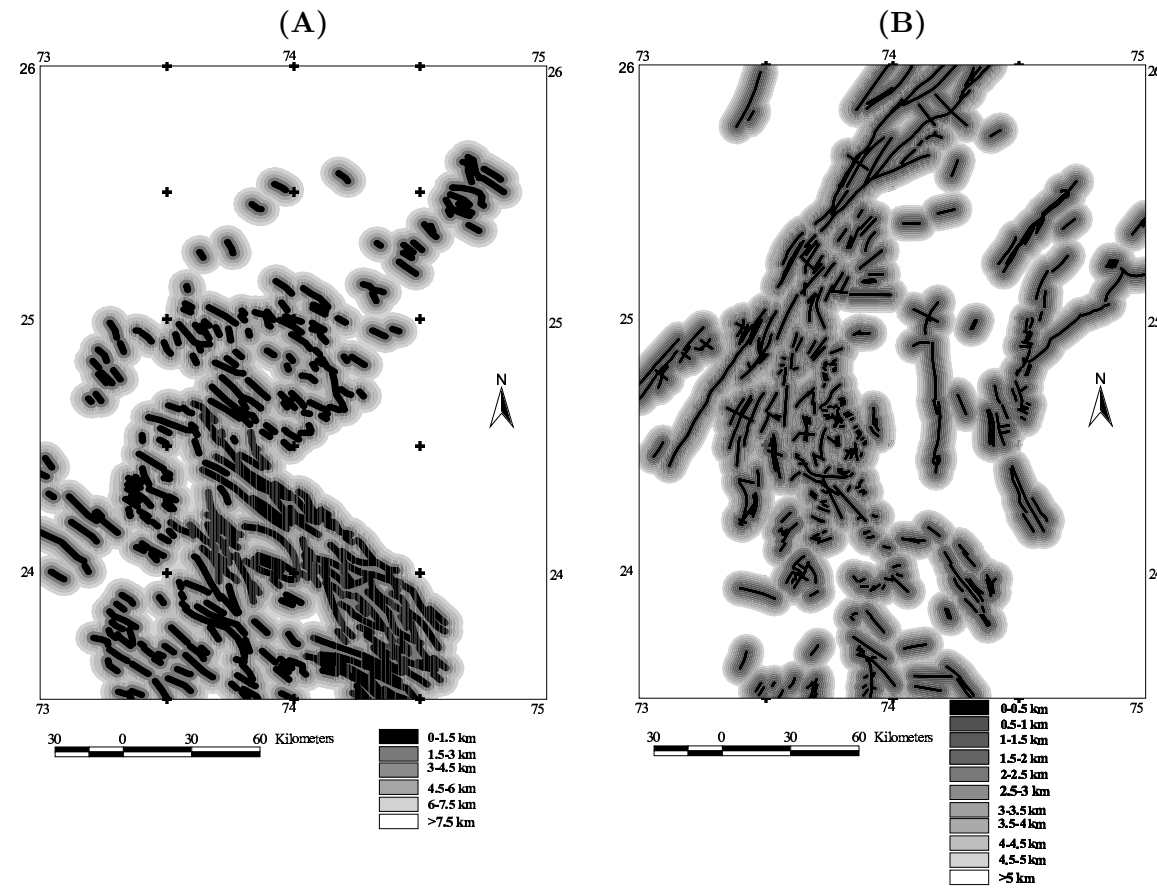
Figure 2.19: Predictor map of buffered distances from (A) NW-trending lineaments and (B) fold axes.

fold axes. Figure 2.20 shows plots of cumulative percentage of pixels in distance corridors around the linear features and cumulative percentage of base-metal deposit pixels in the distance corridors. The former represent random (probability) distribution of occurrence of points (that could be occupied by base-metal deposits) around the linear features, whilst the latter represent observed distribution of base-metal deposit/occurrence points around the linear features. Plots of the observed distribution of base-metal occurrence points are higher than the plots of random distribution of points around the linear feature in each case, which indicates that the probability of base-metal occurrence around the linear features is higher than would be expected due to chance. The plots further indicate that base-metal deposits have a positive spatial association with each set of linear features. The distance to linear features in which there is highest separation between the plots represents the distance of optimal positive spatial between base-metal occurrences and linear geological features. Thus, the positive spatial association between base-metal occurrences and regional lineaments is maximum at 6 km (Fig. 2.20A), the positive spatial association between base-metal occurrences and NE-trending lineaments is maximum at 7 km (Fig. 2.20B), the positive spatial association between base-metal occurrences and NW-trending lineaments is maximum at 3 km (Fig. 2.20C) and the positive spatial association between base-metal occurrences and regional fold axes is optimal at 2 km (Fig. 2.20D). These optimal distances of positive spatial associations depict zones around linear geological features in which there is the highest probability for occurrence of base-metal deposits.

The above results validate the interpretation based on a conceptual model of base-metal metallogenesis that proximity to favorable structures forms an important recognition criteria for base-metal deposits in the study area.

2.6   Concluding Remarks

Analysis of conjunctive interpretations of geological and geophysical datasets vis-á-vis a review of tectono-stratigraphic studies in Aravalli province indicate that interpreted tectonic domains, based on magnetic anomalies, have distinct crustal, lithological, metamorphic and metallogenic characteristics and correlate broadly with lithostratigraphic belts identified by several earlier workers. The analyses contribute the following new or revised interpretations to those of earlier workers. First, Hindoli sequences probably constitute an independent
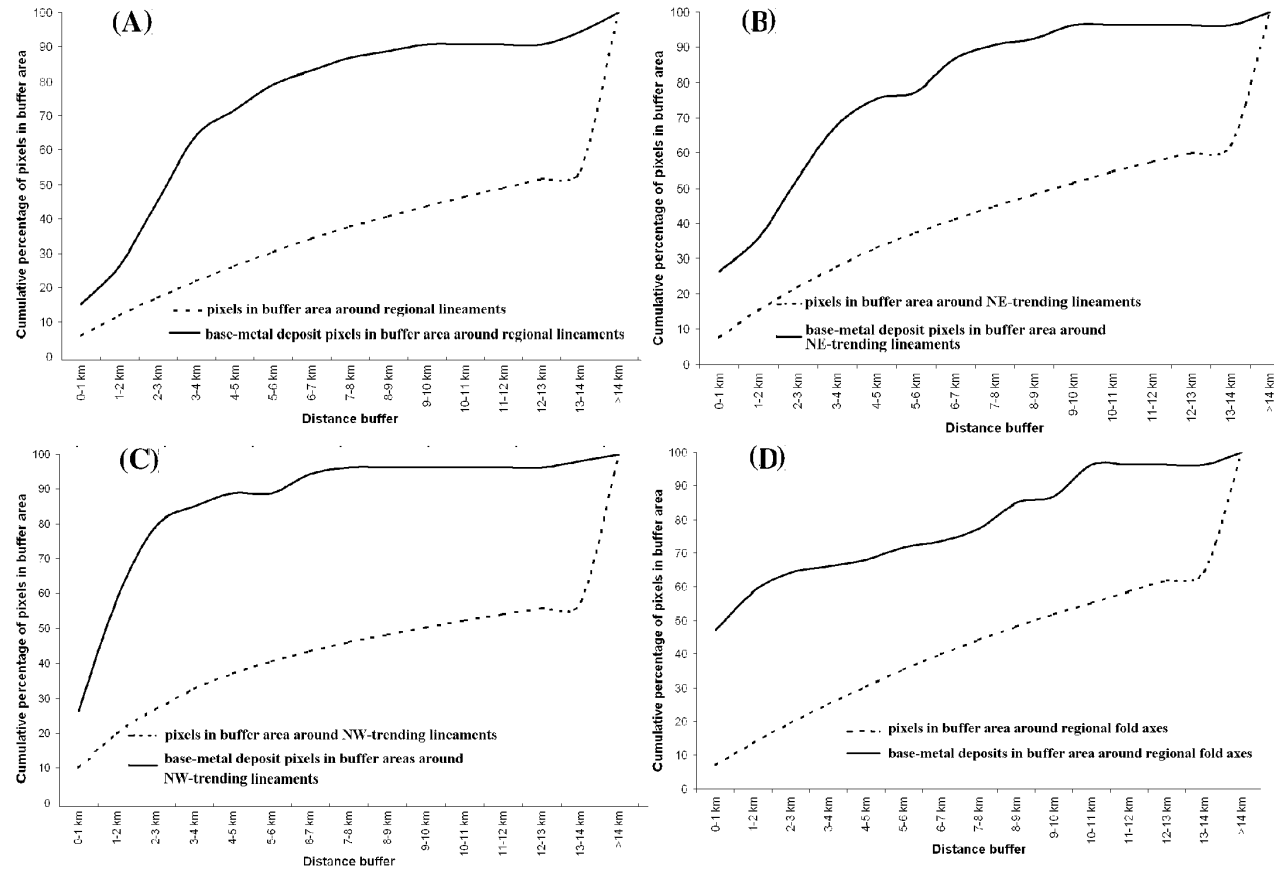
Figure 2.20: Plots of cumulative percentage of pixels in distance corridors around linear features and cumulative percentage of base-metal occurrence pixels in distance corridors for (A) regional lineaments, (B) NE-trending lineaments, (C) NW-trending lineaments and (D) regional fold axes.

Palaeo-Proterozoic tectonic domain and do not form part of Archaean basement complex. Second, base-metal-bearing metasedimentary enclaves in central parts of the area also constitute an independent Palaeo-Proterozoic tectonic domain, quite distinct from surrounding (basement complex?) rocks. Third, base-metal-bearing meta-volcanic-sedimentary sequences along western margins of Delhi supergroup constitute an independent Neo-Proterozoic tectonic domain.

Based on the conceptual model of base-metal metallogenesis in the study area and generalized geological setting of SEDEX deposits, host rock lithology, stratigraphic position, (palaeo-)sedimentary environment, association of mafic volcanic rocks, proximity to favorable structures are identified as significant regional-scale recognition criteria for base-metal deposits in the study area. Empirical modeling of spatial associations indicates strong spatial associations between the known base-metal deposits and each recognition criterion (represented as one or more predictor maps). The empirical modeling therefore validates the recognition criteria that were identified by conceptual modeling.

The results of the simple empirical models of spatial associations between known base-metal deposits and each of the recognition criteria described in this chapter can be useful in ranking or weighting the relative importance of each predictor pattern as an indicator of base-metal deposits in the study area. Note, however, that the simple empirical associations of known base-metal deposits with polygonal predictor features and with linear predictor features were quantified in different ways. In addition, the simple empirical models presented in this chapter do not depict spatial relationships amongst recognition criteria with respect to the base-metal deposits. Predictive mapping of mineral potential requires (a) uniform representation of spatial associations between target mineral deposits and recognition criteria, (b) quantitative representation of spatial relationships amongst recognition criteria with respect to target mineral deposits and (c) a systematic way of combining predictor patterns that is hypothesized to be representative of the complex process of mineral deposit formation. These requirements can be met through complex mathematical geological modeling. In the succeeding chapters, different mathematical geological models for weighting and combining predictor maps are developed and evaluated by applications to base-metal potential mapping in the study area.

Chapter 3

Knowledge-driven and Data-driven Fuzzy Models

This chapter describes "Knowledge-driven and Data-driven Fuzzy Models for Predictive Mineral Potential Mapping" (Porwal *et al.*, 2003a). The knowledge-driven fuzzy model uses a logistic membership function for deriving fuzzy membership values of input predictor maps, whereas the data-driven model uses a piece-wise linear function based on quantified spatial associations between predictor patterns and known mineral deposits for deriving fuzzy membership values of input predictor maps. A graphical defuzzification procedure is used in both models for the interpretation of output fuzzy favorability maps. The models are demonstrated for mapping base metal deposit potential in the study area.

3.1   Introduction

Although real-world geodata are invariably multi-class or continuous in nature, several quantitative models for mineral potential mapping, for example, weights-of-evidence models (Agterberg, 1989; Agterberg *et al.*, 1990; Bonham-Carter and Agterberg, 1990) use binary predictor maps. The generalization and reclassification of geodata into binary maps, however, may result in distortion and possible loss of valuable information. Moreover, reclassification rules are based on available information and these rules may change as more information becomes available. A preferred predictive model is one that (a) accommodates the multi-class and/or continuous nature of geodata and (b) is sufficiently robust to assimilate 'informational fuzziness' (Zimmermann, 1991)

that is inherent in most geodata. Predictive models based on the theory of fuzzy sets fulfill both these criteria. Although the weights-of-evidence method can be adapted for modeling multi-class and continuous data (e.g., Porwal and Hale, 2000; Porwal *et al.*, 2003b; *also see* Chapter 4 of this thesis), the application of fuzzy set theory provides a better theoretical framework for dealing with the complexity of modeling multi-class data in a flexible and yet consistent way. Moreover, the weights-of-evidence method generally requires large amounts of training data in order to minimize uncertainty and hence is applied to relatively well-explored provinces. In contrast, fuzzy models are equally efficacious in both poorly- and well-explored provinces.

Variables of fuzzy models for mineral potential mapping consist of the recognition criteria for the target mineralization. These are selected by using either (a) empirical methods based on a statistical (or heuristic) evaluation of geological characteristics of known mineral deposits or (b) an appropriate genetic mineral deposit model. Spatial data sets that provide evidence for the recognition criteria are then processed to generate multi-class predictor maps for modeling. The most significant procedures in approaches to fuzzy modeling are the definition of fuzzy membership values of multi-class predictor maps and the selection of appropriate inference network and fuzzy set operators for combining the predictor maps. In a knowledge-driven approach, fuzzy membership values are assigned subjectively by the modeler based on his knowledge and exploration experience. In a data-driven approach, fuzzy membership values are calculated from exploration data. The fuzzified predictor maps are then combined through a single- or multi-stage inference network using appropriate fuzzy set operators to generate fuzzy favorability maps. Finally, the fuzzy favorability maps are defuzzified for demarcating exploration targets. Most of the published studies document the knowledge-driven approach, although in recent years attempts have been made to incorporate the data-driven approach in fuzzy modeling.

3.1.1 Previous work

An *et al.* (1991) used a number of multi-class geophysical and geological maps to build a fuzzy model for predictive mapping of base metal and iron deposits in the Farley Lake mining area, Canada. They assigned fuzzy membership values to the predictor maps based on expert knowledge and combined them through a single-stage inference network using the fuzzy γ operator. Gettings and Bultman (1993) applied the fuzzy set theory to map favorability for

quartz-carbonate vein deposits in southeastern Arizona, USA. They assigned fuzzy membership values to predictor maps subjectively and combined them through a single-stage inference network using the fuzzy intersection operator to generate a fuzzy favorability map. Porwal and Sides (2000) developed a knowledge-driven fuzzy model for mapping potential for SEDEX-type base-metal deposits in the Aravalli Province, Western India. They used a single-stage inference network based on the fuzzy γ operator to combine predictor maps. Carranza and Hale (2001) used quantified spatial association of known gold deposits and geological features in the Baguio district of the Philippines to guide assignment of fuzzy membership values to predictor maps, which they combined through a two-stage inference network using a variety of fuzzy set operators.

Cheng and Agterberg (1999) proposed a fuzzy weights-of-evidence model, which generalizes the weights-of-evidence model (Agterberg, 1989; Agterberg and Bonham-Carter, 1990; Bonham-Carter, 1994) to include multi-class predictor maps. They defined 'fuzzy probability' in terms of fuzzy membership values and used it to calculate 'fuzzy weights of evidence' of all patterns in input predictor maps and combined them using a log linear function under an assumption of conditional independence of the predictor maps to derive 'fuzzy posterior probability' of mineral deposits. The model, as much probabilistic as fuzzy, uses a data-driven approach for calculating fuzzy membership values.

Knox-Robinson (2000) introduced the application of vector algebra in fuzzy modeling. He represented favorability as a vector, whose direction and magnitude are defined by fuzzified prospectivity and confidence values, respectively. The former value is the conventional fuzzy membership value of a predictor pattern, while the latter value is a measure of the modeler's confidence in a prospectivity value. The confidence value is assigned subjectively taking into consideration (a) the significance of a factor (i.e., predictor pattern) in the genesis of the target mineralization and (b) the precision with which it has been mapped (low for inferred features and 0 for 'no data' areas). The favorability vectors at each location are combined by calculating the resultant vector, whose direction and magnitude represent the combined favorability and confidence, respectively.

3.2 Fuzzy Model

Real-world models of complex natural phenomena are marked by two kinds of uncertainties, viz., the stochastic and the systemic uncertainties. The stochastic uncertainties arise out of lack of complete information, and can be dealt with appropriately by statistical and probabilistic means, under the assumption that the phenomena and model parameters are well-defined. The systemic uncertainties, on the other hand, are non-statistical and are intrinsically associated with the models. These can have several sources; but arise mainly from the fact that natural phenomena are seldom deterministic and crisp and therefore there is always a semantic or informational fuzziness associated with them. These uncertainties, which arise from vagueness (or 'fuzziness') in the definition of the phenomena and their parameters, are best treated using the concepts of fuzzy sets and fuzzy mathematics (Zadeh, 1965; Zimmerman, 1991; Robinson, 2003).

3.2.1 Fuzzy set theory

If X is a collection of objects denoted generically by x, then a fuzzy set $\tilde{A}$, in X, is a set of ordered pairs:

$$\tilde{A} = \left\{ \left(x, \mu_{\tilde{A}}(x) \right) \mid x \in X \right\}, \tag{3.1}$$

where $\mu_{\tilde{A}}$ is called the membership function or grade of membership (also degree of compatibility or degree of truth) of x in $\tilde{A}$, which maps X to the membership space M (Zimmermann, 1991). When M contains only two points 0 and 1, $\tilde{A}$ is non-fuzzy and $\mu_{\tilde{A}}$ is identical to the characteristic function of a classical set.

For combining fuzzy sets, Zadeh (1965) and Zimmermann (1991) define a number of set operators based on fuzzy mathematics. The most commonly-used operators in fuzzy modeling are the intersection, the union, the complement, the algebraic sum, the algebraic product and the γ operator (Bonham-Carter, 1994). The fuzzy γ operator is defined in terms of the algebraic sum and the algebraic product as follows (Zimmermann and Zysno, 1980; Bonham-Carter, 1994):

$$\mu_{combination} = (1 - \prod_{i=1}^{n}(1 - \mu_i))^\gamma \cdot (\prod_{i=1}^{n} \mu_i)^{1-\gamma}, \tag{3.2}$$

where $\mu_{\tilde{A}_i}$ is the fuzzy membership function for the ith fuzzy set ($i =1$ to n), n is the total number of fuzzy sets to be combined, and γ is a parameter chosen in the range (0,1). The first term in the right hand side of the above equation is the fuzzy algebraic sum and second term is the fuzzy algebraic product. When $\gamma = 1$, the combination is the same as the fuzzy algebraic sum; and when $\gamma = 0$, the combination equals the fuzzy algebraic product. Judicious selection of the value of γ produces output values that ensure flexible compromise between the "increasive" tendencies of the fuzzy algebraic sum and the "decreasive" effects of the fuzzy algebraic product, as shown by Bonham-Carter (1994, p. 297).

3.2.2 Fuzzy modeling procedures

Typically, a fuzzy model comprises the following feedforward modules (Fig. 3.1):

1. a fuzzifier (encoder);

2. an inference engine (processor); and

3. a defuzzifier (decoder).

Fuzzifier

A fuzzifier has the function of converting (or encoding) input categorical or numeric data (crisp values) into fuzzy values. Because these values propagate through a model and ultimately determine the output, fuzzification is the most crucial procedure in fuzzy modeling. Fuzzification of input data always relates to a fuzzy proposition and is carried out by means of a membership function ($\mu_{\tilde{A}}$ in Equation 3.1), which can be derived either from *a priori* knowledge of a system or by using input data (both categorical and numeric). Thole *et al.* (1979) and Zimmerman (1991) describe various membership functions that can be used for fuzzification.
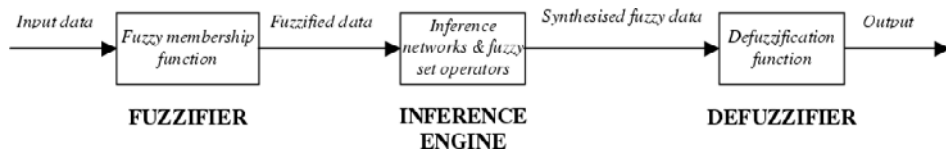
Figure 3.1: Architecture of a typical fuzzy model.

Inference engine

An inference engine is the mind of a fuzzy model. Its function is to filter out informational noise and create a synthesized fuzzy set from the individual fuzzy sets transmitted by the fuzzifier. It constitutes a number of parallel and/or serial networks that sequentially combine fuzzy sets through fuzzy set operators. There are no general guidelines for designing an inference engine except that it should simulate the human decision-making process.

Defuzzifier

A defuzzifier transforms the synthesized fuzzy set back to a crisp set, which expresses the result of modeling. It can be a mathematical function or a subjectively- or objectively-defined threshold fuzzy value. Hellendoorn and Thomas (1993) describe a number of criteria that an ideal defuzzification procedure should satisfy. The most important criterion is that a small change in inputs of a fuzzy model should not cause a significant change in output.

3.3 Fuzzy Models for Mineral Potential Mapping

A generalized fuzzy model for predictive mineral mapping can be defined as follows. If X is a set of n predictor maps X_i (i=1 to n) with r patterns (or classes) denoted generically by x_{ij} (j=1 to r), then n fuzzy sets $\tilde{A}_i$ (i=1 to n) in X, containing 'favorable indicators for the target mineral deposit-type', can be defined as follows:

$$\tilde{A}_i = \left\{ \left(x_{ij}, \mu_{\tilde{A}_i}(x_{ij}) \right) \mid x_{ij} \in X_i \right\}, \tag{3.3}$$

where $\mu_{\tilde{A}_i}$ is the membership function for estimating the fuzzy membership value of x_{ij} in the fuzzy set $\tilde{A}_i$.

The membership function $\mu_{\tilde{A}_i}$ has following properties:

1. $0 \leq \mu_{\tilde{A}_i}(x_{ij}) \leq 1$;

2. $0.5 < \mu_{\tilde{A}_i}(x_{ij}) \leq 1$ if x_{ij} is a positive indicator of target mineral deposit-type;

3. $\mu_{\tilde{A}_i}(x_{ij}) = 0.5$ if, and only if, x_{ij} is a neutral indicator of target mineral deposit-type; and

4. $0 \leq \mu_{\tilde{A}_i}(x_{ij}) < 0.5$ if x_{ij} is a negative indicator of target mineral deposit-type.

The n fuzzy sets $\tilde{A}_i$ so obtained can be combined using one or more of the fuzzy set operators described by Zimmermann (1991) to generate a synthesized fuzzy set $\tilde{F}$:

$$\tilde{F} = \sum_{i=0}^{n} \tilde{A}_i, \tag{3.4}$$

where $\sum$ denotes fuzzy set operations. The synthesized set $\tilde{F}$ can be defined as a fuzzy set containing 'favorable exploration targets'. However, as the result of modeling should be well-defined and, therefore, crisp, the synthesized fuzzy set $\tilde{F}$ is transformed back to a crisp binary set, F, which also is a set of 'favorable exploration targets', but its membership is confined to 0 or 1. A given spatial unit can have a membership value of either 1 (favorable target) or 0 (unfavorable target) in this set.

3.3.1 Knowledge-driven fuzzy Model

The knowledge-driven model is described below in terms of the three constituent modules of a fuzzy model, viz., a fuzzifier, an inference engine and a defuzzifier.

Fuzzifier

The following logistic membership function is used for fuzzification of multi-class predictor maps in a knowledge-driven approach (after Zimmermann, 1991):

$$\mu_{\tilde{A}_i}(x_{ij}) = \frac{1}{1 + e^{-a(cs_{ij}-b)}}, \tag{3.5}$$

where b is the inflexion point, a is the slope of the function and cs_{ij}, the *class score* of x_{ij}, is calculated using the following equation:

$$cs_{ij} = w_i \times w_{ij}, \tag{3.6}$$

where w_i is the *map weight* of the ith predictor map and w_{ij} is the *class weight* of the jth pattern on the ith predictor map.

Based on their subjectively-assessed favorability, all patterns on a predictor map are ranked on a scale of 1 to 10 in a reverse direction, i.e., the most favorable pattern is ranked 10, and the least favorable pattern is ranked 1.

69

Table 3.1: Variation of output fuzzy membership values with parameters of logistic membership function for a synthetic dataset

Predictor map pattern (x_{ij})	Class score cs_{ij}	Fuzzy membership value		
		$a = 0.1$ $b = 50$	$a = 0.2$ $b = 10$	$a = 0.05$ $b = 25$
x_{11}	0	0.01	0.00	0.08
x_{12}	10	0.02	0.00	0.12
x_{13}	20	0.05	0.00	0.18
x_{14}	30	0.12	0.02	0.27
x_{15}	40	0.27	0.12	0.38
x_{16}	50	0.50	0.50	0.50
x_{17}	60	0.73	0.88	0.62
x_{18}	70	0.88	0.98	0.73
x_{19}	80	0.95	1.00	0.82
x_{110}	100	0.99	1.00	0.92

Note: a and b are, respectively, slope and inflexion point of the logistic membership function

In this scheme, the rank of a pattern is its weight. As much as possible, the patterns are ranked at equal intervals. This method of allotting weights by ranking is simple and objective, as most experts would agree upon the rank of a pattern, although each might come up with a different value if asked to assign weight to it.

Similarly, based on the importance of their respective recognition criteria and the confidence in their fidelity and precision, predictor maps are assigned weights in a procedure similar to the one described above for predictor patterns.

The parameters b and a, which represent the inflexion point and the slope of the logistic function, determine the shape of the function and, hence, the output of the fuzzifier. As illustrated by Table 3.1 and Fig. 3.2 for a synthetic dataset, depending on the values of the parameters b and a, the logistic membership function returns different fuzzy values for a given input predictor pattern. The parameters b and a are chosen heuristically based on a subjective assessment of favorability of various predictor patterns.

Inference engine

The design of an inference engine to create a synthesized fuzzy favorability map depends upon the nature of mineralization and types of available predictor maps. The nature of a mineral deposit is the end-result of a complex interplay of several earth processes that leave behind their signatures in form of geologic features associated with the mineral deposit. These features (or recognition criteria) are characterized by their responses in geodata sets, which are used

Curve	Parameters	
	a	*b*
A	0.10	50
B	0.20	10
C	0.05	25
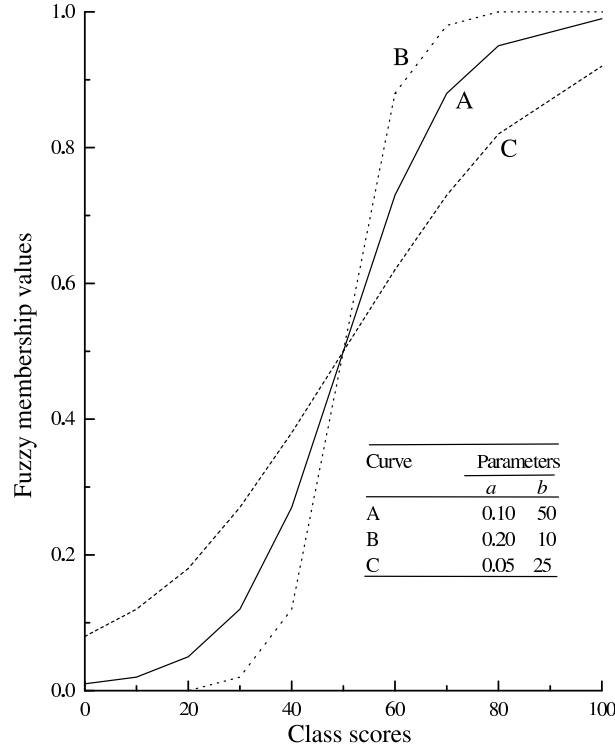
Figure 3.2: Variation of output fuzzy membership values with parameters of logistic membership function for a synthetic dataset.

as predictor maps in mineral exploration. A single predictor map can indicate presence of more than one recognition criteria and several predictor maps can indicate the presence of a single recognition criterion. Because an inference engine seeks to generate a synthesized fuzzy favorability map by combining individual fuzzified predictor maps its design should reflect the subtle relationships among genetic processes, recognition criteria and predictor maps. In fact it is possible for a single model to have several valid inference engines based on different inference networks and fuzzy operators. For example, Carranza and Hale (2001) give a detailed analysis of various inference engines used by them in fuzzy modeling of the epithermal gold potential of the Baguio district, The Philippines. The selection of appropriate fuzzy set operators is particularly important in designing an inference engine. Knox-Robinson (2000) gives a critical review of various fuzzy operators that are used for combining fuzzified predictor maps into a synthesized fuzzy favorability map.

Defuzzifier

The synthesized fuzzy favorability map cannot be interpreted objectively for demarcating specific exploration target areas, as it shows favorability in a continuous scale from the most unfavorable (lowest fuzzy membership value) to the most favorable (highest fuzzy membership value). The following graphical procedure is thus used to defuzzify the synthesized fuzzy favorability map into a binary favorability map. The cumulative fuzzy membership values of the synthesized favorability map are plotted against the cumulative area, which yields a rounded Γ-shaped curve. Initially, the slope of the curve is very steep (close to 90°), which falls down to less than 45° in the middle, and finally becomes close to 0°, signifying that the rate of increase of the cumulative membership values falls as the area increases. In spatial terms, the curve implies that the cumulative (search) area becomes progressively larger without corresponding gain in terms of increase in the cumulative favorability. The point at which there is the sharpest fall in the slope of the curve is determined by visual inspection. The fuzzy membership value corresponding to this point is taken as the threshold value for defuzzifying (i.e., reclassifying) the synthesized fuzzy favorability map into a binary favorability map, provided that this value is greater than 0.5 on the basis of the properties of the fuzzy membership function defined further above. If it is less than 0.5, the design of the model is revised to increase combined fuzzy membership values. This can be achieved by (a) adjusting values of the parameters of the logistic membership function (a and b in Equation 3.5) and/or (b) using additive operators or by increasing the values of the fuzzy γ operator in the inference networks. The process is repeated until a threshold fuzzy membership value greater than 0.5 is obtained.

3.3.2 Data-driven fuzzy model

A data-driven fuzzy model differs from the knowledge-driven model only in respect of the fuzzifier module. The other two modules remain the same. Therefore, only the fuzzifier module of the proposed data-driven model is described here.

The following piece-wise linear membership function based on the *contrast* (C) value (Bonham-Carter, 1994, p. 255) is used as a fuzzifier in the proposed data-driven model:

$$\mu_{\tilde{A}_i}(x_{ij}) = \left\{ \begin{array}{lll} 0.01 & \text{if} & C_{ij} = C_{min} \ \& \ C_{min} < 0 \\ 0.5 - \frac{C_{ij}}{2 \times C_{min}} & \text{if} & C_{min} < C_{ij} \leq 0 \\ 0.5 + \frac{C_{ij}}{2 \times C_{max}} & \text{if} & 0 \leq C_{ij} \leq C_{max} \end{array} \right\} \quad (3.7)$$

where $\mu_{\tilde{A}_i}$ is the fuzzy membership function defining the membership value of x_{ij} in the fuzzy set $\tilde{A}_i$ (Equation 3.3), C_{ij} is the contrast value of x_{ij}, C_{min} and C_{max} are the minimum and maximum contrast values, respectively, in the complete data set.

The following relationship determines C_{ij} (Bonham-Carter, 1994):

$$C_{ij} = W_{ij}^+ - W_{ij}^-, \quad (3.8)$$

where W_{ij}^+ and W_{ij}^- are, respectively, positive and negative weights of evidence of the jth pattern on the ith predictor map. The weights of evidence are calculated using the following equations:

$$W_{ij}^+ = \log_e \frac{P(x_{ij}/D)}{P(x_{ij}/\overline{D})} \quad (3.9)$$

and

$$W_{ij}^- = \log_e \frac{P(\overline{x}_{ij}/D)}{P(\overline{x}_{ij}/\overline{D})}, \quad (3.10)$$

where x_{ij} and $\overline{x}_{ij}$ denote, respectively, the presence and absence of the predictor pattern x_{ij}, and D and $\overline{D}$ denote, respectively, the presence and absence of the target mineral deposit-type.

Equation 3.9 and 3.10 basically quantify the spatial association between a set of predictor patterns and a set of mineral deposits. Two weights, W_{ij}^+ and W_{ij}^- are calculated for each predictor pattern x_{ij}. W_{ij}^+ quantifies the positive association (the probability of the occurrence of the mineral deposit-type, given the presence of x_{ij}), and W_{ij}^- measures the negative correlation (probability of occurrence of the mineral deposit-type, given the absence of x_{ij}). The contrast (C_i), measures the overall spatial association between the predictor pattern x_{ij} and the mineral deposit-type D. Studentized contrast, $s(C)$, is a measure of certainty with which a contrast value is known and therefore provides a more reliable measure of spatial association (Bonham-Carter, 1994, p. 323). It is

73

defined as follows:

$$s(C) = C/\sigma_C, \tag{3.11}$$

where σ_C is the standard deviation of contrast.

The studentized contrast is, therefore, a robust measure of favorability of x_{ij}, and can be also be used in Equation 3.7 for calculating the fuzzy membership value of a predictor pattern in the fuzzy set 'favorable indicators of target mineral deposit-type'.

3.3.3   Conditional independence

An assumption of conditional independence amongst the predictor maps was not made for the proposed fuzzy models. Theoretically, the fuzzy set theory does not require conditional independence for various set operations. However, conditional dependence may create problems in complex fuzzy operations, like combining maps using fuzzy algebraic product, fuzzy algebraic sum or fuzzy γ operator, where the additive effect of conditionally-dependent maps may result in erroneous values. However, because conditional dependence amongst maps is generally because of one of the following two reasons, (1) the maps represent the same recognition criterion or (2) there is possibly a genetic link between the recognition criteria represented by them, appropriate inference network can be designed to combine possible conditionally-dependent maps, using operators like the fuzzy AND or the fuzzy OR.

3.4   Application to Base-Metal Potential Mapping in Aravalli Province

3.4.1   Data preprocessing

Because the two parameters of the gaussian fuzzy membership function, namely, the inflexion point and the slope (b and a, respectively in Equation 3.5), are estimated heuristically, there is no possibility of over-fitting in the estimation of these parameters because of dimensionality of input data (see Chapter 7, p. 191, for a discussion of problems related to dimensionality of input data in the estimation of the parameters of fuzzy membership functions). Consequently, all of the predictor maps, namely, the maps of lithologies, stratigraphic groups, sedimentary environments, mafic igneous rocks, buffered distances from regional lineaments, buffered distances from NW-trending lineaments, buffered

distances from NE-trending lineaments and buffered distances from fold axes, were used as such without any processing or reclassification in the fuzzy models.

Training and validation deposits. A subset of 30 deposits, regarded as 'discovered' and randomly selected from the known base-metal deposits, was used to train the data-driven fuzzy model. The remaining 24 deposits were regarded as 'undiscovered' and used to validate the data-driven model.

3.4.2 Knowledge-driven fuzzy modeling

Fuzzifier

The eight multi-class predictor maps mentioned above were fuzzified using the membership function defined in Equation 3.5. The values of the parameters b and a were taken as 50 and 0.1, respectively, which yield a curve that is symmetrical about the inflexion point (Curve A in Fig. 3.2). The function returns a fuzzy membership value of 0.5 for a class score of 50. The class scores for predictor patterns were calculated from class weights and map weights (Equation 3.6), which were assigned subjectively using the procedure described in Section 3.3.1. The class weights, map weights, class scores and knowledge-driven fuzzy membership values for the predictor maps are given in Table 3.2.

The predictor maps and patterns were ranked on the basis of experience of base-metal exploration in the province, informal discussions with mining geologists of M/s Hindustan Zinc Ltd., which owns most of the large base-metal deposits in the area, and recommendations of various authors, especially Deb (1999) and Sarkar (2000).

Amongst the eight predictor maps, the lithological map was ranked 10, as the base-metal mineralization in the province is controlled primarily by host rock lithology. Among various lithologies, high ranks were assigned on both theoretical grounds and actual field observations to dolomite, calc-silicates (metamorphosed siliceous dolomite) and graphitic meta-pelites. Moderately-high ranks were assigned to magnetite quartzites, which forms a common host rock in Pur-Banera zone and meta-basites, which host VMS-type sulfide deposits of Basantgarh area in the South Delhi belt. Calc-schists/gneisses and quartzite (and associated rocks like arkose and conglomerate) were assigned moderately-low ranks, while migmatites and gneisses, which form the bulk of the basement complex, were assigned low ranks. Other lithologies like granite, trap basalt etc., which have no relation whatsoever with the base-metal

75

mineralization in the province were ranked the lowest.

Sedimentary environment is a significant factor in the formation of SEDEX-type base-metal deposits. However, the sedimentary environment map was ranked 9, lower than the lithological map, because the sedimentary environments were *inferred* and not directly mapped. A majority of the base-metal deposits in the Aravalli province are hosted by rift-cover sequences consisting of proximal shelf (shallow water) sedimentary facies, which were deposited in restricted basins with anaerobic conditions. Consequently, high ranks were assigned to proximal shelf environments especially when characterized by restricted basins conditions with an anaerobic environment. The restricted basin conditions in distal shelf with an anaerobic environment and proximal shelf conditions with a partly anaerobic environment were assigned moderately-high and moderately-low rank, respectively. The deep sea environment was assigned a low rank. The sedimentary environment of the basement complex could not be established and moreover it does not host any significant base-metal deposit. Therefore the basement complex along with several other extrusive and intrusive igneous environments that are not related to base-metal mineralization were assigned the lowest ranks.

The map of stratigraphic groups was also ranked 9 in view of the stratigraphically-controlled distribution of the base-metal deposits in the Aravalli province (Deb, 1999; Deb and Thorpe, 2001). Deb and Thorpe (2001) have established two prominent metallogenic epochs in the province at Ca. 1.8 Ga and Ca. 1.0 Ga, which gave rise to the SEDEX-type deposits of the Aravalli and Bhilwara belts and the VMS-type deposits of the Sendra-Ambaji belt, respectively. However, as absolute ages are meagerly available, stratigraphic proximity to the groups of rocks with known mineral deposits was used for assigning ranks to various groups of rocks in the province. Stratigraphic groups with known base-metal deposits and their stratigraphically-equivalent groups were assigned high ranks, while the stratigraphically-closer groups were assigned moderately-high ranks. Those groups that are stratigraphically-farther apart were assigned moderately-low ranks, while those that are stratigraphically-farthest apart were assigned low ranks. Finally, a number of stratigraphic groups, which have no relationship with the base-metal mineralization were assigned the lowest rank. These groups include younger stratigraphic units comprising extrusive and intrusive igneous or sedimentary rocks.

There are only two patterns on the predictor map of mafic igneous rocks, namely, mafic metavolcanic rocks and other basic rocks that do not have any

Table 3.2: Data-driven and knowledge-driven fuzzy membership values for predictor maps

	Predictor map Pattern	Class Weight	Class Score	Knowledge-driven Fuzzy Membership	Studentized Contrast	Data-driven Fuzzy Membership
	(x_{ij})	(w_j)	(cs_{ij})		$(s(C_i))$	
Predictor map of lithologies (Map weight - 10)						
1	Dolomite/dolomitic Marble	10	100	0.99	9.4232	0.98
2	Calc-silicates	9	90	0.98	7.9338	0.91
3	Graphic meta-pelites	8	80	0.95	6.8287	0.85
4	Magnetite quartzite	7	70	0.88	4.8071	0.75
5	Calc-schist/calc-gneiss	5	50	0.50	0.0088	0.50
6	Quartzite/Arkose/ Conglomerate	4	40	0.27	-0.6942	0.41
7	Migmatite/Gneisses	2	20	0.05	-1.9292	0.26
8	Not related to base-metals	1	10	0.02	ND	0.01
Predictor map of stratigraphic groups (Map weight - 9)						
1	Rajpura-Dariba group	10	90	0.98	8.3418	0.93
2	Pur-Banera group	9	81	0.96	9.7947	1.00
3	Debari groups	8	72	0.90	5.9451	0.80
4	Nathdwara group	7	63	0.79	2.5476	0.63
5	Udaipur group	5	45	0.38	-0.0276	0.50
6	Jharol group	4	36	0.20	-1.2360	0.34
7	Sandmata Complex	3	27	0.09	-0.8217	0.40
8	Mangalwar Complex	2	18	0.04	-1.9389	0.25
9	Not related to base-metals	1	9	0.02	ND	0.01
Predictor map of sedimentary environments (Map weight - 9)						
1	Prox. shelf; restricted; anaerobic	10	90	0.98	7.2055	0.87
2	Prox. shelf; anaerobic	8	72	0.90	6.5347	0.83
3	Distal shelf; restricted; anaerobic	6	54	0.60	4.7974	0.74
4	Prox. shelf; partly anaerobic	4	36	0.20	4.8071	0.75
5	Deep sea	2	18	0.04	-1.8585	0.27
6	Basement Complex	1	9	0.02	-2.4594	0.19
7	Not related to base-metals	1	9	0.02	ND	0.01
Predictor map of mafic igneous rocks (Map weight - 8)						
1	Mafic volcanic rocks	10	80	0.95	8.4795	0.93
2	Not related to base-metals	1	8	0.01	-8.4795	0.01
Predictor map of buffered distances from regional lineaments (Map weight - 8)						
1	0-2 Km	10	80	0.95	2.9348	0.65
2	2-4 Km	8	64	0.80	3.8098	0.69
3	4-6 Km	6	48	0.45	0.9251	0.55
4	6-8 Km	4	32	0.14	-0.0984	0.49
5	8-10 Km	2	16	0.03	-0.6125	0.42
6	>10 Km	1	8	0.01	-3.9548	0.01

(Table 3.2 Contd.)

	Predictor map Pattern (x_{ij})	Class Weight (w_j)	Class Score (cs_{ij})	Knowledge-driven Fuzzy Membership	Studentized Contrast $(s(C_i))$	Data-driven Fuzzy Membership
Predictor map of buffered distances from NE-trending lineaments (Map weight - 6)						
1	0-1.5 Km	10	60	0.73	2.9668	0.65
2	1.5-3 Km	8	48	0.45	2.2137	0.61
3	3-4.5 Km	6	36	0.20	1.5264	0.58
4	4.5-6 Km	4	24	0.07	-0.0555	0.49
5	6-7.5 Km	2	12	0.02	0.2043	0.51
6	>7.5 Km	1	6	0.01	-3.8227	0.02
Predictor map of buffered distances from NW-trending lineaments (Map weight - 6)						
1	0-1.5 Km	10	60	0.73	4.2870	0.72
2	1.5-3 Km	8	48	0.45	2.9002	0.65
3	3-4.5 Km	6	36	0.20	-0.2657	0.47
4	4.5-6 Km	4	24	0.07	0.2324	0.51
5	6-7.5 Km	2	12	0.02	-0.2641	0.47
6	>7.5 Km	1	6	0.01	-3.8645	0.01
Predictor map of buffered distances from fold axes (Map weight - 7)						
1	0-0.5 Km	10	70	0.88	5.9265	0.80
2	0.5-1 Km	9	63	0.79	2.5534	0.63
3	1-1.5 Km	8	56	0.65	1.5165	0.58
4	1.5-2 Km	7	49	0.48	-0.5360	0.43
5	2-2.5 Km	6	42	0.31	ND	0.01
6	2.5-3 Km	5	35	0.18	ND	0.01
7	3-3.5 Km	4	28	0.10	ND	0.01
8	3.5-4 Km	3	21	0.05	ND	0.01
9	4-4.5 Km	2	14	0.03	ND	0.01
10	4.5-5 Km	1	7	0.01	ND	0.01
11	>5 Km	1	7	0.01	-2.9505	0.13

ND: Not Determinable.

relation with base metal mineralization (e.g., the serpentinites, mafic granulites etc.). The former were assigned the highest rank, while the latter were assigned the lowest rank. The map was ranked high at 8, although lower than the lithological, stratigraphic and the sedimentary environment maps because (a) there is an undeniable spatial association of these rocks with some of the largest base-metal deposits in the province, although the genetic relationship of the SEDEX-type base-metal mineralization with mafic metavolcanic rocks is not as well-established as it is with lithology, stratigraphy and sedimentary environment and (b) the map was interpreted from the total magnetic field intensity data and is therefore an *inferred* map.

The regional lineaments, which provide evidence for the crustal-scale faults in the Aravalli province, have a positive spatial association with the base-metal deposits. However, because the lineaments were interpreted from the total magnetic field intensity data, the map of regional lineaments was assigned a map rank of 8. The buffer zones were ranked in the reverse order of their

distances from the lineaments.

The predictor map of buffered distances from fold axes was assigned a rank of 7 in view of the specific evidence of post genetic remobilization and relocation of ores during polyphase deformation of the province. In many areas, the hinges of the folds form the preferred sites for concentration. The buffer zones were ranked in the reverse order of their distances from the fold axes.

The two predictor maps of buffered distances from NE-trending and NW-trending lineaments were ranked 6 each, lower than the predictor map of buffered distances from fold axes. It is because the lineaments were interpreted from the total magnetic field intensity data and therefore these are *inferred* maps. The ranks to buffer zones were assigned in the reverse order of their distances from lineaments.

Inference engine

The two-stage inference engine used here (Fig. 3.3) comprises four parallel networks that sequentially combine collateral fuzzy predictor maps transmitted by the fuzzifier through the fuzzy OR and fuzzy AND operators to yield four intermediate fuzzy predictor maps in the first stage, which are combined in the second stage using the fuzzy γ operator to generate the synthesized fuzzy favorability map.

The first parallel network combines the two fuzzy predictor maps of buffered distances from NE-trending and NW-trending lineaments using the fuzzy AND operator to yield a combined fuzzy predictor map of buffered distances from both sets of lineaments, which, in turn, is combined with the fuzzy predictor map of buffered distances from fold axes using the fuzzy OR operator to yield an intermediate fuzzy predictor map of favorable structural features for post-genetic concentration of ore. The second parallel network combines the fuzzy predictor map of the mafic igneous rocks with the fuzzy predictor map of buffered distances from regional lineaments using the fuzzy OR operator to generate an intermediate fuzzy predictor map of favorable heat sources. The third parallel network combines the fuzzy predictor map of lithologies and the fuzzy predictor map of sedimentary environments using fuzzy AND to yield an intermediate fuzzy predictor map showing the favorable base-metal hosting environments. The fourth parallel network transmits the fuzzy predictor map of stratigraphic groups as such to the second stage. The intermediate fuzzy predictor map showing favorable stratigraphic groups is therefore the same as the one transmitted by the fuzzifier.
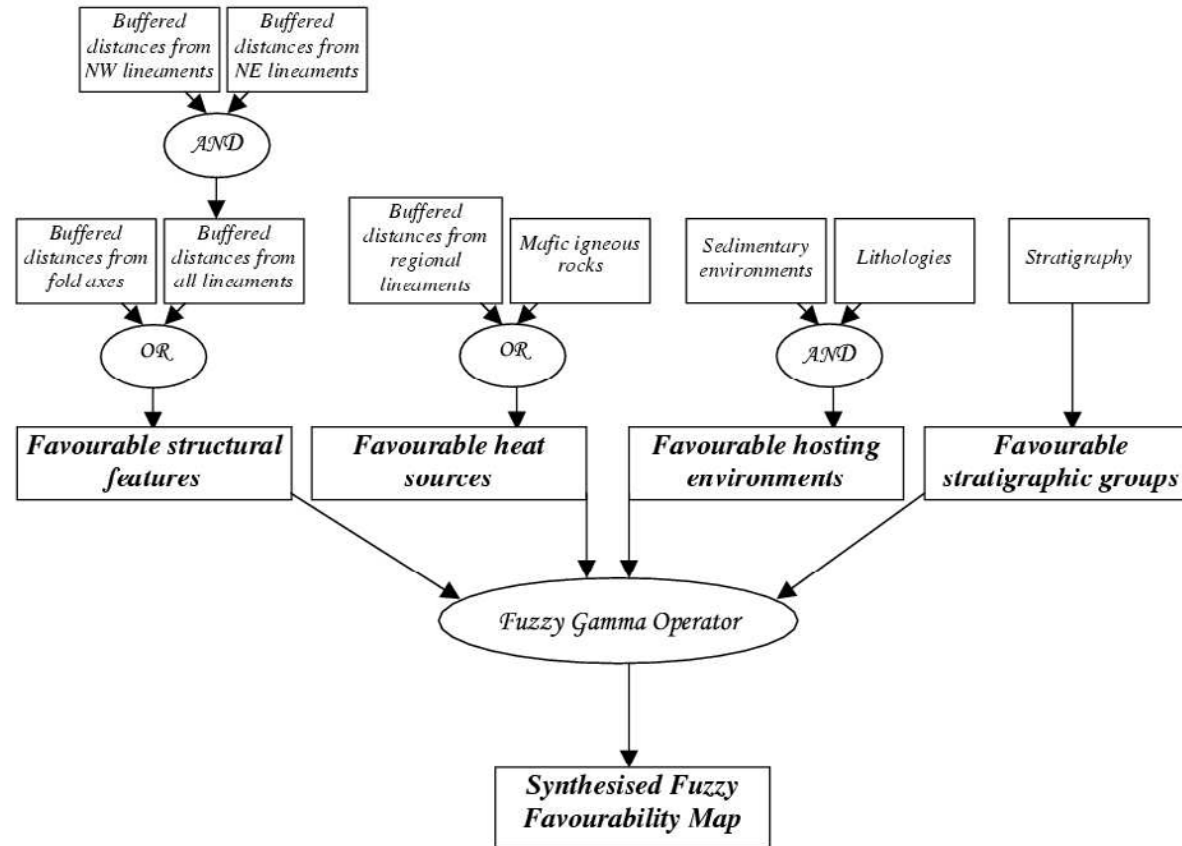
Figure 3.3: Two-stage inference engine used for generating synthesized fuzzy favorability maps in Fig. 3.4 and Fig. 3.7.

The maps more likely to be conditionally-dependent were combined in the first stage of the inference engine using the fuzzy AND and the fuzzy OR operators. The choice of the fuzzy AND operator or the fuzzy OR operator in the parallel networks described above depended upon whether the presence of only one of the two fuzzy predictor maps to be combined was sufficient or whether the presence of both fuzzy predictor maps was mandatory for the recognition of base-metal deposits in the province.

The intermediate fuzzy predictor maps were combined in the second stage of the inference engine using the fuzzy γ operator with $\gamma = 0.75, 0.79, 0.83$ and 0.87, to produce the four synthesized fuzzy favorability maps shown in Fig. 3.4.

Defuzzifier

Table 3.3 gives the combined fuzzy favorability values and their respective area coverage in the synthesized fuzzy favorability maps. The plots of the cumulative fuzzy favorability and the cumulative areas are shown in the Fig. 3.5. It can be seen from the plots and Table 3.3 that the threshold combined favorability value is less than 0.5 for the three maps obtained by using γ values of 0.75, 0.79 and 0.83, while it is 0.5 for the map obtained by using a γ value of 0.87. The former maps were therefore rejected and the latter was defuzzified using 0.5 as the threshold. The resulting binary favorability map is shown in Fig. 3.6.

Model validation

The knowledge-driven model was validated by overlaying the locations of known mineral deposits on the binary favorability map (Fig. 3.6). Table 3.4 shows that in the binary favorability map, high favorability areas, which occupy 8.9% of the study area, contain 87.0% of the known base-metal deposits.

3.4.3 Data-driven fuzzy modeling

In the data-driven model, the predictor maps were fuzzified using the piece-wise linear membership function defined in Equation 3.7. The studentized contrast values were calculated using the procedure and software described by Kemp *et al.* (1999). Table 3.2 gives the studentized contrast values and the data-driven fuzzy membership values for each predictor map.

The fuzzified predictor maps were combined using the same inference engine (Fig. 3.3) that was used in the knowledge-driven model. Fig. 3.7 shows
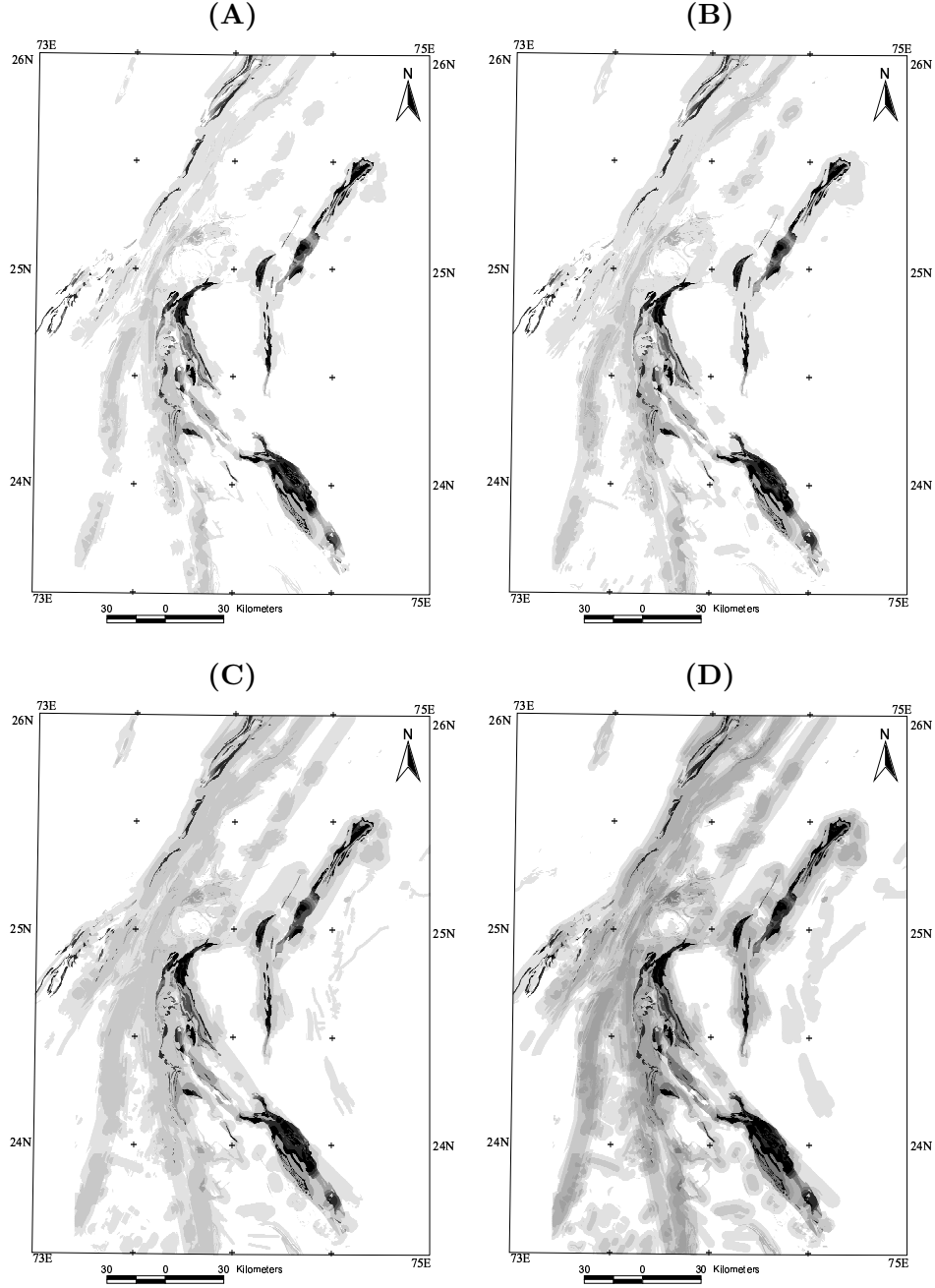
Figure 3.4: Continuous-scale knowledge-driven synthesized fuzzy favorability maps obtained by using a γ value of (A) 0.75, (B) 0.79, (C) 0.83 and (D) 0.87. Combined fuzzy favorability varies from 0 (white) to 1 (black).

(A)

(B)

(C)

(D)
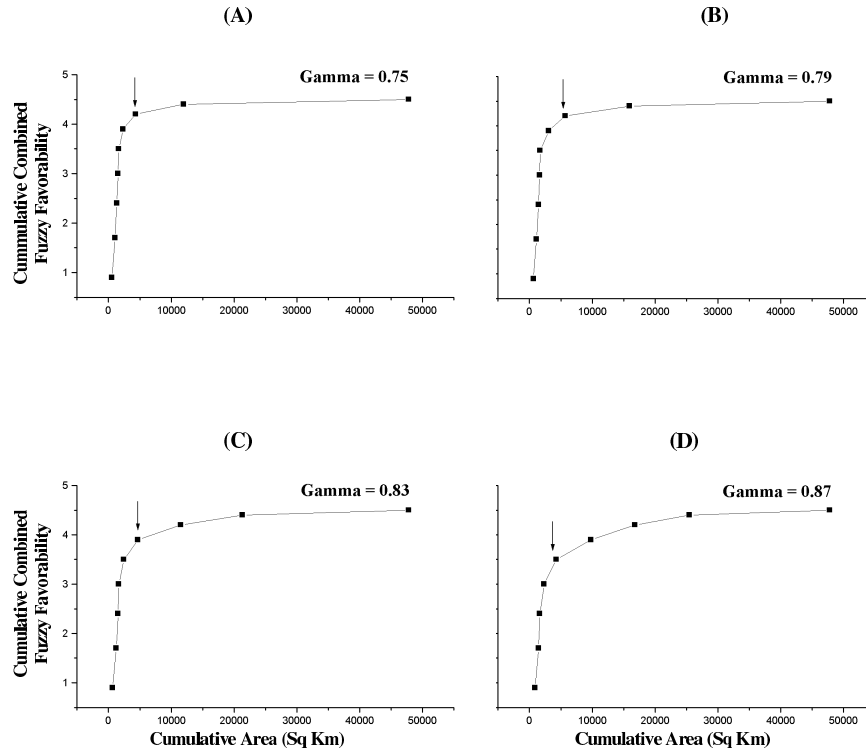
Figure 3.5: Variation of cumulative combined fuzzy favorability with cumulative area in knowledge-driven synthesized fuzzy favorability maps in (A) Fig. 3.4A, (B) Fig. 3.4B, (C) Fig. 3.4C and (D) Fig. 3.4D. Note sharp change in slope of curves (marked by arrows) at cumulative combined fuzzy favorability values of (A) 4.2 (B) 4.2 (C) 3.9 and (D) 3.5. These values, respectively, correspond to threshold combined fuzzy favorability values (Table 3.3) of (A) 0.3 (B) 0.3 (C) 0.4 and (D) 0.5.

Table 3.3: Defuzzification of Knowledge-driven synthesized fuzzy maps

Model	Combined Fuzzy Favorability Values (Class Marks)	Cumulative Combined Fuzzy Favorability Values	Area (Km^2)	Cumulative Area (Km^2)
γ=0.75	0.9	0.9	536	536
	0.8	1.7	499	1035
	0.7	2.4	298	1333
	0.6	3.0	196	1529
	0.5	3.5	132	1661
	0.4	3.9	670	2331
	<u>0.3</u>	<u>4.2</u>	<u>1997</u>	<u>4328</u>
	0.2	4.4	7681	12009
	0.1	4.5	35811	47820
γ=0.79	0.9	0.9	631	631
	0.8	1.7	499	1130
	0.7	2.4	320	1450
	0.6	3.0	166	1616
	0.5	3.5	96	1712
	0.4	3.9	1362	3074
	<u>0.3</u>	<u>4.2</u>	<u>2621</u>	<u>5695</u>
	0.2	4.4	10281	15976
	0.1	4.5	31844	47820
γ=0.83	0.9	0.9	674	674
	0.8	1.7	574	1248
	0.7	2.4	292	1540
	0.6	3.0	129	1669
	0.5	3.5	799	2468
	<u>0.4</u>	<u>3.9</u>	<u>2223</u>	<u>4691</u>
	0.3	4.2	6852	11543
	0.2	4.4	9784	21327
	0.1	4.5	26493	47820
γ=0.87 (Selected Model)	0.9	0.9	902	902
	0.8	1.7	544	1446
	0.7	2.4	209	1655
	0.6	3.0	682	2337
	<u>0.5</u>	<u>3.5</u>	<u>1942</u>	<u>4279</u>
	0.4	3.9	5533	9812
	0.3	4.2	7001	16813
	0.2	4.4	8662	25475
	0.1	4.5	22345	47820

Rows of underlined figures correspond to threshold combined favorability values for each model
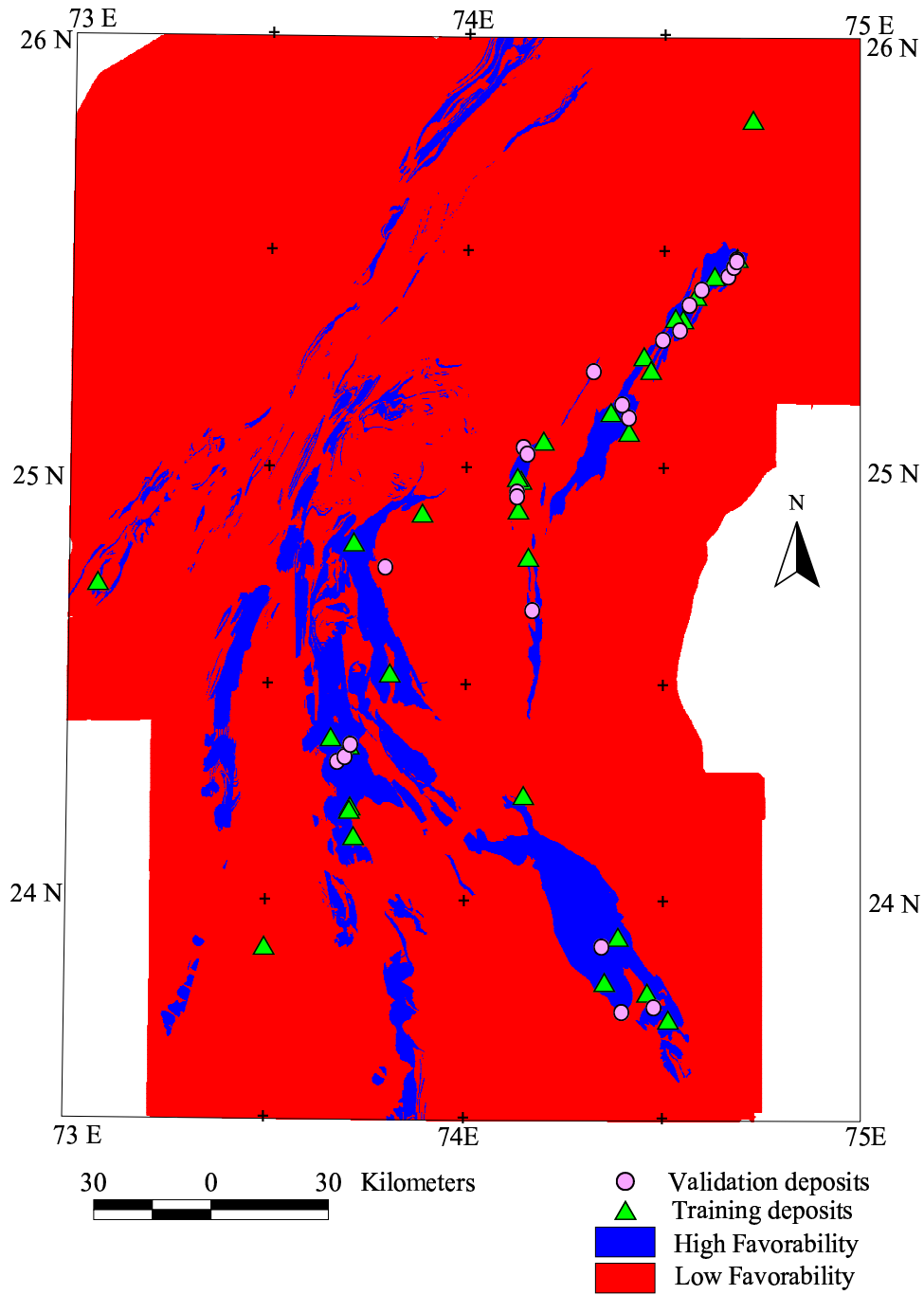
Figure 3.6: Knowledge-driven binary favorability map generated by defuzzification of synthesized fuzzy favorability map in Fig. 3.4D.
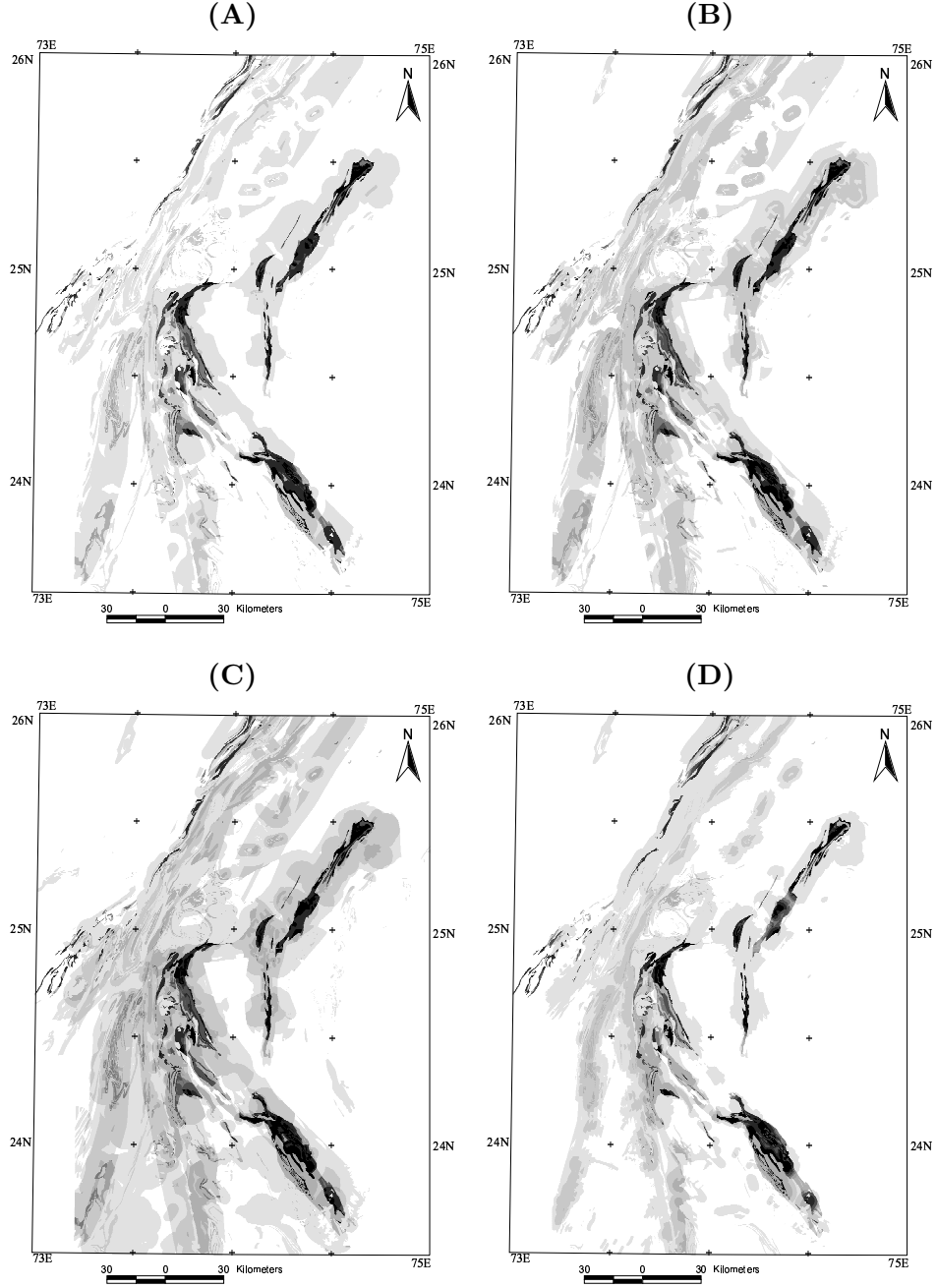
Figure 3.7: Continuous-scale data-driven synthesized fuzzy favorability maps obtained by using a γ value of (A) 0.75, (B) 0.79, (C) 0.83 and (D) 0.87. Combined fuzzy favorability varies from 0 (white) to 1 (black).

86
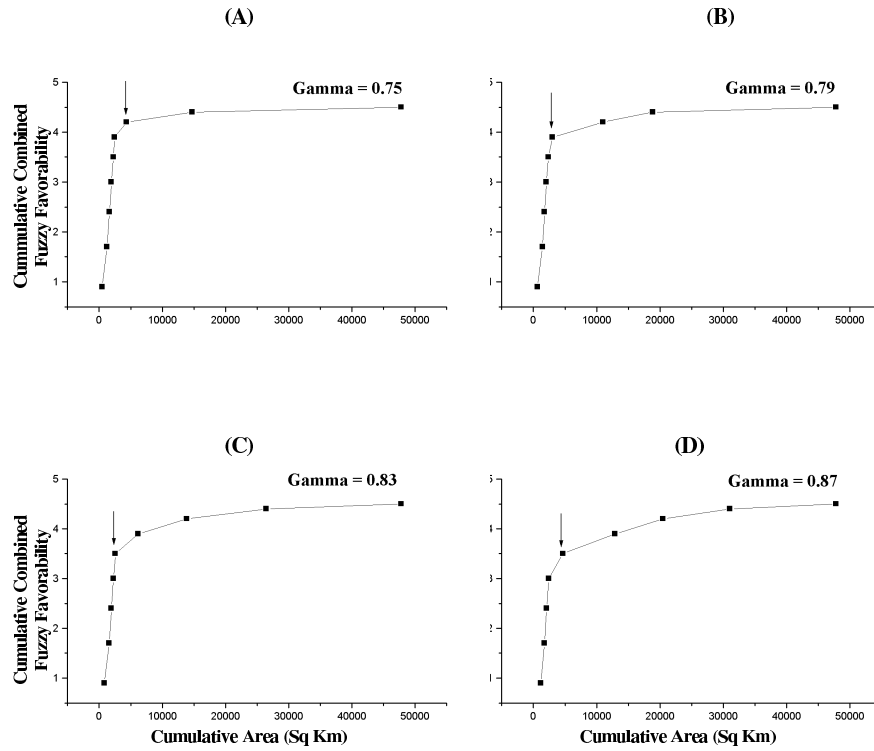
Figure 3.8: Variation of cumulative combined fuzzy favorability with cumulative area in data-driven synthesized fuzzy favorability maps in (A) Fig. 3.7A, (B) Fig. 3.7B, (C) Fig. 3.7C and (D) Fig. 3.7D. Note sharp change in slope of curves (marked by arrows) at cumulative combined fuzzy favorability values of (A) 4.2 (B) 3.9 (C) 3.5 and (D) 3.5. These values, respectively, correspond to threshold combined fuzzy favorability values (Table 3.5) of (A) 0.3 (B) 0.4 (C) 0.5 and (D) 0.5.
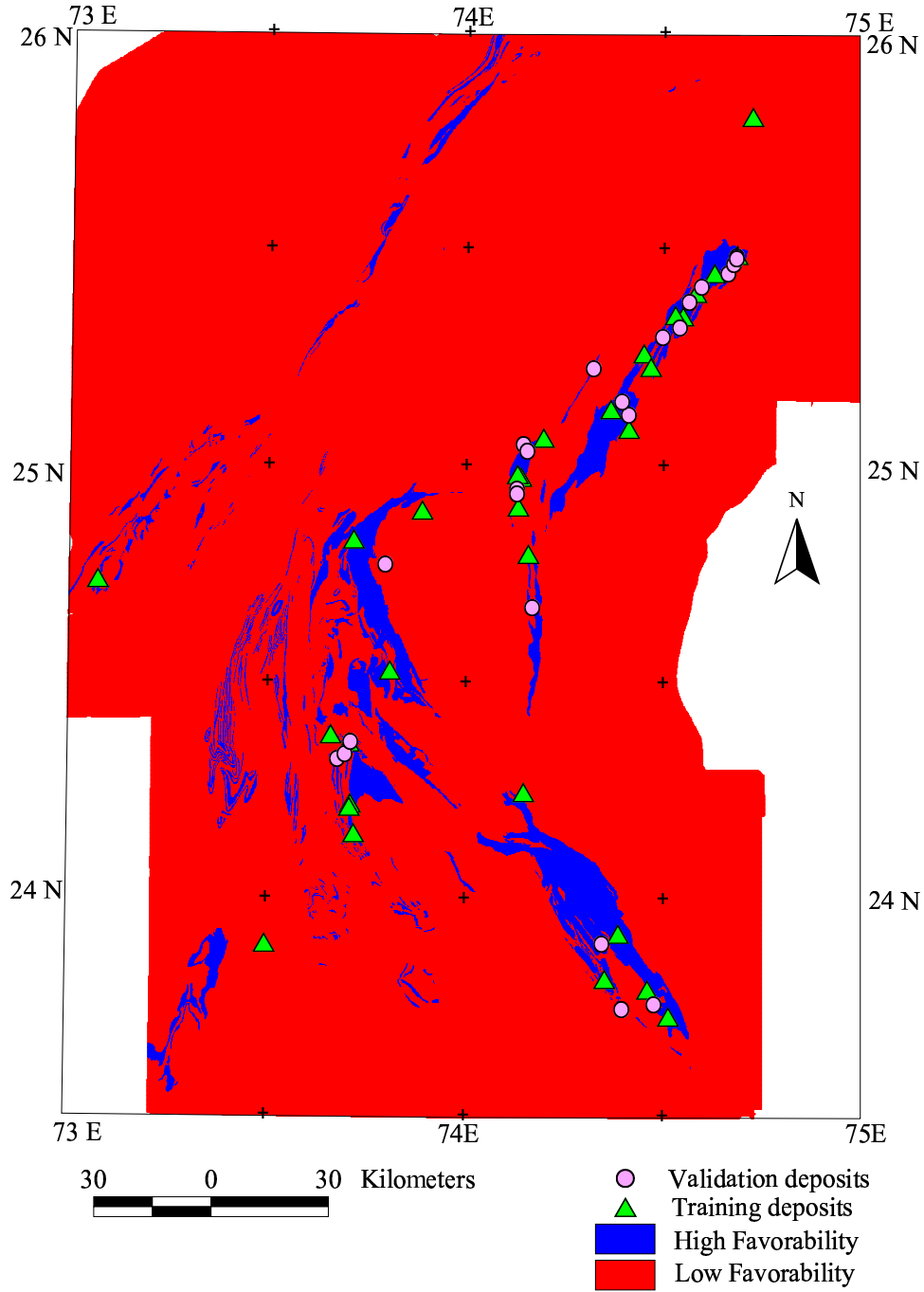
Figure 3.9: Data-driven binary favorability map generated by defuzzification of synthesized fuzzy favorability map in Fig. 3.7C.

Table 3.4: Validation of Favorability maps

Favorability Map	Favorability zone	Percent study area	Percent validation deposits	Percent training deposits
Based on knowledge-driven fuzzy model	High favorability	8.9	—-87.0—-	
	Low favorability	91.1	—-13.0—-	
Based on data-driven fuzzy model	High favorability	5.4	87.5	83.3
	Moderate favorability	94.6	12.5	16.7

the synthesized fuzzy favorability maps obtained using γ values of 0.75, 0.79, 0.83 and 0.87. The combined fuzzy favorability values and their respective area coverage in the four synthesized fuzzy favorability maps are given in Table 3.5. The plots of the cumulative fuzzy favorability and the cumulative areas are shown in Fig. 3.8. It can be seen from the plots and Table 3.5 that the threshold combined fuzzy favorability value is 0.3 and 0.4 for the synthesized fuzzy favorability maps obtained by using γ values of 0.75 and 0.79, respectively, while it is 0.5 for the synthesized fuzzy favorability maps obtained by using γ values of 0.83 and 0.87. The first two synthesized fuzzy favorability maps were rejected because the threshold combined favorability value is less than 0.5. For the last two synthesized fuzzy favorability maps, the threshold combined fuzzy favorability value corresponds to cumulative areas of 2582 km^2 and 4665 km^2 respectively. Of these maps, the synthesized fuzzy favorability map obtained by using a γ value of 0.83 was selected because the threshold combined fuzzy favorability value narrows down the search area more judiciously in this map. This map was therefore defuzzified by using 0.5 as the threshold combined favorability. The resulting binary favorability map is shown in Fig. 3.9.

Model validation

The model was validated by overlaying the validation base-metal deposits on the binary favorability map (Fig. 3.9). Table 3.4 shows that favorable areas, which occupy 5.4% of the study area, contain 87.5% of the validation deposits and 83.3% of the training deposits.

3.5 Discussion

As mentioned earlier, one of the most significant procedures in approaches to fuzzy modeling is the definition of fuzzy membership values. The logistic membership function (Equation 3.5) used as the fuzzifier in the knowledge-driven

Table 3.5: Defuzzification of Data-driven synthesized fuzzy maps

Model	Combined Fuzzy Favorability Values (Class Marks)	Cumulative Combined Fuzzy Favorability Values	Area (Km^2)	Cumulative Area (Km^2)
γ=0.75	0.9	0.9	481	481
	0.8	1.7	759	1240
	0.7	2.4	405	1645
	0.6	3.0	306	1951
	0.5	3.5	303	2254
	0.4	3.9	208	2462
	<u>0.3</u>	<u>4.2</u>	<u>1905</u>	<u>4367</u>
	0.2	4.4	10346	14713
	0.1	4.5	33107	47820
γ=0.79	0.9	0.9	648	648
	0.8	1.7	795	1443
	0.7	2.4	313	1756
	0.6	3.0	302	2058
	0.5	3.5	317	2375
	<u>0.4</u>	<u>3.9</u>	<u>650</u>	<u>3025</u>
	0.3	4.2	7977	11002
	0.2	4.4	7883	18885
	0.1	4.5	28935	47820
γ=0.83 (Selected Model)	0.9	0.9	810	810
	0.8	1.7	759	1569
	0.7	2.4	381	1950
	0.6	3.0	320	2270
	<u>0.5</u>	<u>3.5</u>	<u>311</u>	<u>2581</u>
	0.4	3.9	3623	6204
	0.3	4.2	7650	13854
	0.2	4.4	12606	26460
	0.1	4.5	21360	47820
γ=0.87	0.9	0.9	1152	1152
	0.8	1.7	582	1734
	0.7	2.4	365	2099
	0.6	3.0	340	2439
	<u>0.5</u>	<u>3.5</u>	<u>2226</u>	<u>4665</u>
	0.4	3.9	8249	12914
	0.3	4.2	7566	20480
	0.2	4.4	10569	31049
	0.1	4.5	16771	47820

Rows of underlined figures correspond to threshold combined favorability values for each model
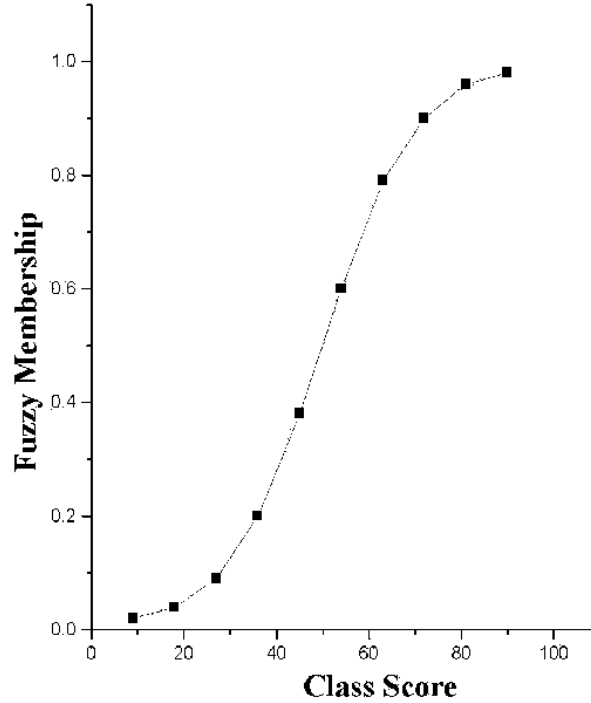
Figure 3.10: Variation of fuzzy membership values with class scores for predictor map of stratigraphy.

model is S-shaped, as demanded by several authors (Goguen, 1969; Zadeh, 1971), and returns membership values that lie between 0 and 1. The significance of this function lies in the fact that the relationship between physical units and perceptions is generally exponential (Helson, 1964; Zimmermann, 1991), and the function offers a mathematical way of expressing this relationship. Fig. 3.10 shows a plot of class scores and fuzzy membership values returned by this function for the predictor map of stratigraphy. It can be seen that the differences in the membership values are much larger in the central part of the curve than along its tails, which means that the function separates the unfavorable stratigraphic groups from the favorable stratigraphic groups quite clearly, although amongst the favorable (and unfavorable) stratigraphic groups the distinction is less well-defined. In a spatial domain, this implies that high favorability and low favorability areas are well-defined in the synthesized fuzzy favorability map and there are fewer areas in the low favorability and in the high favorability areas with transitional favorability. Defuzzification of the synthesized fuzzy favorability map is therefore more robust. This

91

is well-illustrated by the synthesized fuzzy favorability maps of the base-metal deposit potential in the study area predicted by the knowledge-driven model. For example, in the synthesized fuzzy favorability map obtained by using a γ value of 0.87 (Fig. 3.4D), 79% of the area has a combined fuzzy membership value of 0.3 or less (low favorability), 15% of the area has a combined fuzzy membership value between 0.4 and 0.5 (transitional favorability), while 6% of the area has the combined fuzzy membership value ≥ 0.6 (high favorability). This implies that 85% of the area has a well-defined favorability, whether high or low, whereas only 15% has a transitional favorability. The transitional favorability area can be further reduced by increasing the value of the parameter a and b (Equation 3.5), which control the shape of the logistic membership function. As demonstrated by Table 3.1 and Fig. 3.2, an increase in value of a increases the slope of the function, which in turn, results in a wider separation of the fuzzy membership values of the favorable predictor patterns from those of the unfavorable predictor patterns. However, the fuzzifier should be tuned very carefully, as very high values of the parameter a could convert a multi-class predictor map into a crisp map, rather than into a fuzzy map.

The concept of assignment of weight to a predictor map in order to calculate class scores in the knowledge-driven model is very similar to the concept of 'confidence value' proposed by Knox-Robinson (2000). A class score (product of the class and map weights; Equation 3.6) therefore reflects the relative importance of each map as well as that of each pattern on the map, as suggested by Bonham-Carter (1994).

The piece-wise linear membership function used for the fuzzification of predictor patterns maps in the data-driven model is similar to the one used by Cheng and Agterberg (1999) for calculating fuzzy membership values in their fuzzy weights-of-evidence model. However, the membership function (Equation 3.7) defined here differs in following aspects.

1. The function never returns a membership value of 0.

2. A piece-wise linear nature of the function ensures that it returns a membership value of 0.5 for a contrast value of 0. This is in keeping with the properties of the fuzzy membership function defined in Equation 3.3. A simple linear function, like the one used by Cheng and Agterberg (1999) would return a membership value of 0.5 if, and only if, the contrast values are symmetrically distributed about 0.

92

3. Instead of using map-wise maximum and minimum contrast values, the proposed function uses the maximum and minimum contrast values of the complete data set. As a result, the membership values have an element of map weight incorporated in them.

In the creation of a synthesized favorability map, one of the main functions of an inference engine is to filter out informational noise from the individual fuzzified predictor maps transmitted by the fuzzifier. The selection of appropriate fuzzy set operators at various stages in the inference networks is, therefore, very important. As pointed out by Knox-Robinson (2000), if there was an extremely low-value or high-value noise in any of the fuzzified predictor maps, the fuzzy AND or the fuzzy OR operators would propagate it to the synthesized fuzzy favorability map. The fuzzy algebraic sum and the fuzzy algebraic product operators, if used individually, could amplify the noise because of their respective increasive and decreasive tendencies. The fuzzy γ operator, which balances these tendencies of the fuzzy algebraic sum and fuzzy algebraic product operators by using appropriate values of γ, provides an effective way of controlling the propagation of extreme-value noise to the output. The synthesized fuzzy favorability maps produced by the fuzzy γ operator are therefore consistent and realistic.

The graphical method used here for defuzzification of synthesized fuzzy favorability maps allows further fine-tuning of the inference engine, if the threshold combined fuzzy favorability value is less than 0.5. However, this should be cautiously done, as an excessive use of increasive fuzzy operators or a very high γ value in the fuzzy γ operator can propagate extreme-value noise in the synthesized fuzzy favorability map and eventually in the binary favorability map.

The results of applying the knowledge-driven and data-driven fuzzy models to predictive mapping of base-metal deposit potential in the Aravalli province are remarkably similar, both in terms of their strengths and their weaknesses. In terms of strength, each model outlines potential zones occupying less than 10% of the study area, which predict over 85% of the known base-metal deposits. This is a significant result both in terms of reduction in search area and the number of deposits predicted. The data-driven model works better than the knowledge-driven model in that it narrows down the search area to less than 6% of the study area, while predicting roughly the same number of known deposits. However, in absolute terms, the search areas predicted by the knowledge-driven and data-driven models are still quite large (4279 km^2 and

93

2582 km^2, respectively). This is primarily because the focus in the present exercise was on demarcating favorable mineralized zones on a regional scale based on regional-scale (1:250,000) predictor maps. With larger-scale predictor maps, the same models can be further tested to demarcate specific prospects within the predicted favorable mineralized zones.

Both of the models are weak in that they fail to predict the Rampura-Agucha deposit, which is the only world-class base-metal deposit known in the province. The Rampura-Agucha deposit was discovered accidentally by the Rajasthan State Mines and Geology Department during one of its reconnaissance projects for non-metallic minerals in the area (although subsequent mining operations in the area revealed ancient workings dating back to Ca. 400 BC!). The deposit is located in a soil-covered local meta-sedimentary enclave, well within the basement complex, which shows no physical continuity with the main sedimentary basins of the Bhilwara belt and which is barely mappable on a regional scale. Since its discovery in late seventies, a number of Indian and multinational exploration agencies have been carrying out extensive exploration, including close-spaced airborne geophysical surveys, to locate a base-metal mineralized zone in the area, but not much success has been reported so far. The deposit, though having features of a typical SEDEX-deposit on a local scale, remains a spatial anomaly in its regional geological setting. Predicting such a deposit using regional-scale recognition criteria and data is rather difficult. A local-scale knowledge-driven model of the north-central part of the basement complex using large-scale predictor maps and local-scale recognition criteria could predict the Rampura-Agucha deposit and thus help in demarcating other favorable sedimentary enclaves within the basement complex. Alternatively, globally generated data-driven models could be used, as described by Singer and Kouda (1999).

A comparison of the binary favorability maps generated by the two models reveals some interesting features. As prognosticated by a high correlation coefficient of 0.85 between the data-driven and knowledge-driven fuzzy membership values, a majority of the favorable areas predicted by the data-driven fuzzy model are also predicted by the knowledge-driven fuzzy model. However, several narrow curvilinear zones of favorability in the Jharol belt are predicted only by the data-driven fuzzy model. These zones are occupied by thin bands of folded quartzite unit, which host a small base-metal deposit at Padar-Ki-Pal. As weights of evidence and contrast values depend on the number of training points contained by a feature and its area, the rock unit gets a high data-driven

fuzzy membership value. For the same reason, the corresponding stratigraphic group (Jharol group) and sedimentary environment (deep sea) also get high data-driven fuzzy membership values. The knowledge-driven fuzzy membership values are low because (1) quartzite is not a favorable host rock (2) deep sea is not a favorable sedimentary environment and (3) the Jharol group is far removed in temporal terms from major base-metal-hosting stratigraphic groups in the province. As a result, these zones are predicted favorable by the data-driven model and unfavorable by the knowledge-driven model. This implies that the knowledge-driven evaluation of the detailed geological setting of the Jharol belt requires a review, especially because the presence of quartzites indicate a local transgressive-shallow sedimentary environment. In the present application, the entire Jharol belt, which is dominated by carbonate-free pelitic sequences, was considered to be characterized by a deep sea sedimentary environment (Roy and Paliwal, 1981; Roy *et al.*, 1988, 1993).

3.6 Conclusions

The applications of knowledge-driven and data-driven fuzzy models to the study area result in demarcation of potential zones occupying less than 10% of the study area, which contain at least 83% of the known base-metal deposits. This is a significant result both in terms of reduction in search area and the number of deposits predicted, which validates the modeling procedures. The following conclusions can therefore be drawn from these applications.

- The application of fuzzy set theory to predictive mineral potential mapping provides a strong theoretical framework for dealing with the complexity of modeling multi-class predictor maps in a flexible and consistent way.

- The functionality of all the three basic modules, viz., the fuzzifier, the inference engine and the defuzzifier, is equally important for the successful implementation of a fuzzy model.

- The logistic membership function defined in Equation 3.5 provides an operational mathematical tool that simulates human cognition for the efficient fuzzification of multi-class predictor maps in a knowledge-driven fuzzy model.

- The use of the piece-wise linear membership function (Equation 3.7) as a fuzzifier successfully incorporates a data-driven approach in the fuzzy modeling for mineral potential mapping.

- Because an inference engine seeks to generate a synthesized fuzzy favorability map by combining individual fuzzified predictor maps though inference networks and fuzzy set operators, its design should reflect the subtle relationships among genetic processes, recognition criteria and predictor maps.

- The defuzzification procedure described in this chapter provides an objective method for interpreting synthesized fuzzy favorability maps and demarcating exploration target areas from them.

- A cross-validation of the result of one of the models by the result of the other model allows further scrutiny and accounting of the geological significance of each predicted model.

The favorability maps generated by both the knowledge-driven and data-driven fuzzy models reveal that large tract of areas in north-western and eastern parts of the study area have very low favorability (Fig. 3.11, *see also* Figs. 3.4 and 3.7). The tracts in the north-western part of the study area (marked as A in Figs. 3.11A and 3.11B) are occupied by Neoproterozoic magmatic rocks, which are Ca. 750 Ma in age and, hence, much younger than both the SEDEX and VMS phases of mineralizations in the Aravalli province (Chapter 2). The tracts in the eastern part (marked as B in Fig. 3.11A and 3.11B), on the other hand, are largely occupied by Archaean lithological assemblages comprising high-grade migmatites, gneisses and acidic and mafic intrusive rocks, which are more than 2500 Ma in age and, hence, much older than both the phases of base-metal mineralizations (Chapter 2). Based on both conceptual metallogenetic considerations and the results of the fuzzy models, it can be inferred that there is little possibility of base-metal mineralization in either of the two tracts. It was therefore decided to narrow down the study area by removing the low favorability tracts (Figs. 3.11A and 3.11B) from the original study area. The revised study area is shown in Fig. 3.11C.

In the data-driven fuzzy model described in this chapter, the theory of probability was used to calculate weights of evidence of various multi-class predictor maps for deriving fuzzy membership values. However, the fuzzy set theory was used for combining the predictor maps and generating favorability
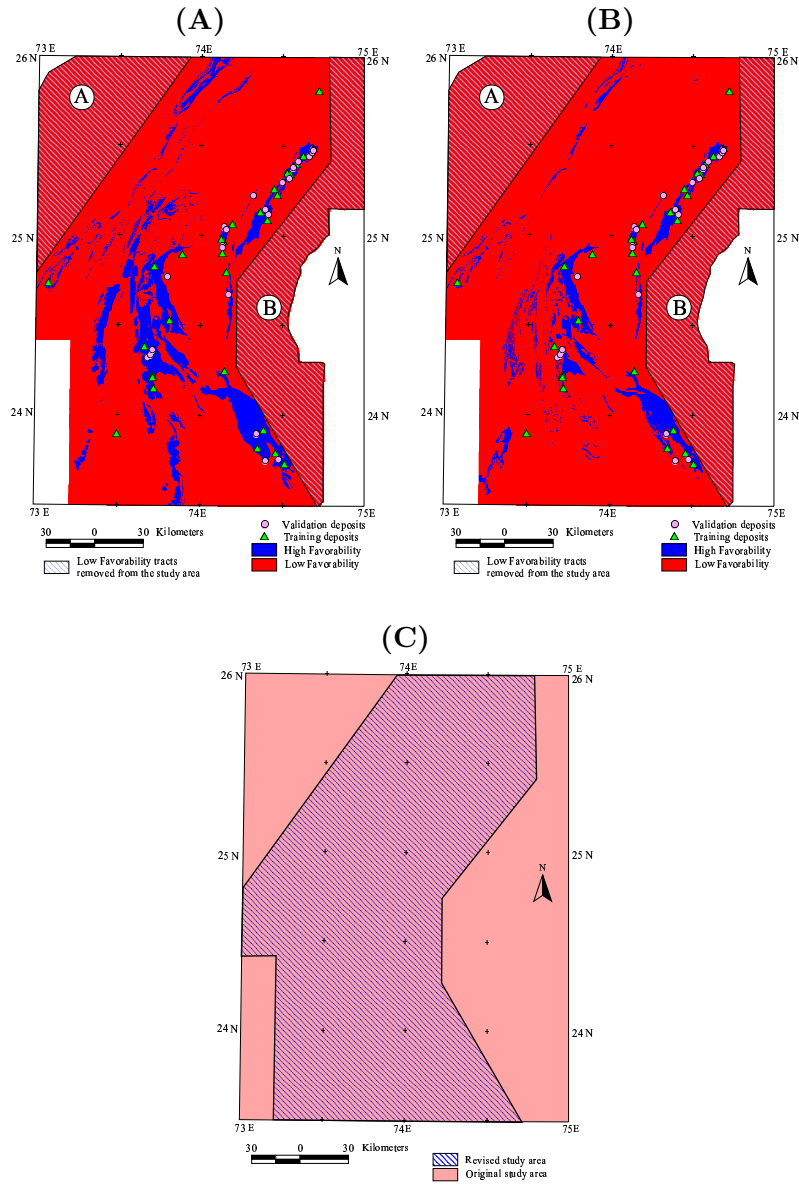
Figure 3.11: Low favorability tracts in binary favorability maps generated by (A) knowledge-driven fuzzy model and (B) data-driven fuzzy model. (C) Study area redefined on the basis of the fuzzy models.

maps. Therefore, the fuzzy values calculated here, which, like probability values, range from 0 to 1, do not represent probability of mineral occurrence but only indicate favorability in a relative sense. In the next chapter, a data-driven model is described that combines multi-class predictor maps and generate mineral potential maps based on a Bayesian probability framework.

Chapter 4

Extended Weights-of-Evidence Model

Approaches to mineral potential mapping based on weights-of-evidence modeling generally use binary maps, whereas, real-world geospatial data are mostly multi-class in nature. The consequent reclassification of multi-class maps into binary maps is a simplification that might result in a loss of information. This chapter thus describes "Extended Weights-of-Evidence Modeling for Predictive Mapping of base-metal Deposit Potential in Aravalli Province, Western India" (Porwal *et al.*, 2003b) to demonstrate optimization of mineral potential information by using multi-class predictor maps, as applied to the study area.

4.1   Introduction

The weights-of-evidence approach to mineral potential mapping uses the theory of conditional probability to quantify spatial association between a set of predictor maps and a set of known mineral deposits (Agterberg, 1989; Agterberg *et al.*, 1990; Bonham-Carter and Agterberg, 1990). The spatial association is expressed in terms of weights of evidence for each of the predictor maps. The weights of evidence are combined with the prior probability of occurrence of mineral deposits using Bayes' rule in a log-linear form under an assumption of conditional independence of the maps to derive posterior probability of occurrence of mineral deposits.

Approaches to weights-of-evidence modeling were originally developed for non-spatial applications, particularly in the field of quantitative medical diagnosis, where they are applied for weighing and combining evidences in the form

of clinical symptoms to predict occurrence of a disease in a patient (e.g., Lusted, 1968; Aspinall and Hill, 1983; Spiegelhalter and Knill-Jones, 1984; Reggia and Perricone, 1985; Spiegelhalter, 1986; Heckerman *et al.*, 1992). Bonham-Carter (1994) provides an in-depth exposition of the weights-of-evidence approach to mineral potential mapping.

4.1.1 Previous work

Weights-of-evidence models have been extensively applied to map potential of a variety of mineral deposits, for example, (a) vein-type gold deposits in Nova Scotia, Canada (Bonham-Carter *et al.*, 1988); (b) Carlin-type epithermal gold deposits in Nevada, USA (Mihalasky, 1999); (c) epithermal gold deposits in the Great Basin of the western USA (Raines, 1999), in northeast Washington State, USA (Boleneus *et al.*, 2001) and in the Baguio district, the Philippines (Carranza and Hale, 2000); (d) porphyry copper deposits in British Columbia, Canada (Singh *et al.*, 1993) and in the Benguet province, the Philippines (Carranza and Hale, 2002); (e) VHMS-type base-metal sulphide deposits in greenstone terrains of Manitoba, Canada (Wright and Bonham-Carter, 1996) and (f) SEDEX-type base-metal deposits in the Aravalli province, India (Porwal and Hale, 2000).

In most of the above-mentioned studies, the model is implemented using binary predictor maps. Although the computational effort required to implement the model is considerably reduced by the use of binary predictor maps, the generalization and reclassification involved in converting real-world geospatial data, which are commonly multi-class or continuous in nature, into binary maps may result in loss or distortion of valuable information. Moreover, with recent advances in computer technology, the advantage of using binary predictor maps in terms of computational effort is no longer such a significant determinant in deciding a modeling approach as it was when the weights-of-evidence model was first propounded for spatial applications. Given the easy availability of cost-effective and high-speed computer hardware, an extended weights-of-evidence model that uses multi-class predictor maps is preferable to a simple weights-of-evidence model that uses binary predictor maps, provided the statistical properties of the model are not degraded by the use of multi-class predictor maps.

Pan (1996) proposed an extended weights-of-evidence model that uses multi-class categorical predictor maps for obtaining 'pseudo-metal' estimates. Bonham-Carter and Agterberg (1999) provide a general introduction to the weights-of-

evidence approach in a multi-class framework. Goodacre *et al.* (1993) applied both 'grey-scale' weights-of-evidence model (based on multi-class predictor maps) and 'binary' weights-of-evidence model (based on binary predictor maps) to predictive mapping of seismic epicenters in western Quebec (Canada) and showed that the predictive maps generated using the two models are very similar. Porwal and Hale (2000) applied the weights-of-evidence analysis of multi-class predictor maps to generate a favorability map for SEDEX-type base-metal deposits in Aravalli province, India. Boleneus *et al.* (2001) used multi-class categorical and cumulative data in their weights-of-evidence model for assessment of epithermal gold deposit potential in northeast Washington State, USA.

4.2   Weights-of-Evidence Model

Bayes' theorem gives the rule for updating belief in a hypothesis H (i.e. the probability of H) given additional evidence E:

$$p(H|E) = p(H) \cdot p(E|H)/p(E), \tag{4.1}$$

where the left-hand term, $p(H|E)$, is called the posterior probability. The term $p(H)$ is the prior probability of H, i.e., the belief in H before the evidence E is considered. The term $p(E|H)$ is called the likelihood, and the last term, $1/p(E)$, which is independent of H, can be regarded as a normalizing or scaling constant.

Bayes' rule is derived by rearranging the terms in the product rule from probability. Using the product rule, Bayes' rule can be extended to n sequential updates using n additional evidences:

$$p(H|E) = \frac{p(H) \cdot p(E_1|H) \cdot p(E_2|E_1, H) \cdot ... \cdot p(E_n|E_{n-1}, ..., E_2, E_1)}{p(E_1) \cdot p(E_2|E_1) \cdot ... \cdot p(E_n|E_{n-1}, ..., E_2, E_1)}, \tag{4.2}$$

As each new piece of evidence is factored into the calculation, its effect is conditional on all previously-considered evidence. This difficulty is overcome by making an assumption of conditional independence. When multiple evidences E_i (for $i = 1$ to n) are conditionally-independent, the multiple update version of Bayes' rule reduces to:

$$p(H|E_1, E_2, ..., E_n) = p(H) \cdot \prod_{i=1}^{n} \frac{p(E_i|H)}{p(E_i)}. \tag{4.3}$$

For spatial application to mineral potential mapping, Agterberg (1989) and Agterberg *et al.* (1990) expressed the probability in terms of *odds*:

$$O(D|E_1, E_2, ..., E_n) = O(D) \cdot \prod_{i=1}^{n} \frac{p(E_i|D)}{p(E_i|\bar{D})}, \qquad (4.4)$$

where D and $\bar{D}$ indicate presence and absence, respectively, of target mineral deposit-type D. The above equation can be written in a log-linear form, as:

$$log_e[O(D|E_1, E_2, ..., E_n)] = log_e[O(D)] + \sum_{i=1}^{n} log_e \frac{p(E_i|D)}{p(E_i|\bar{D})}. \qquad (4.5)$$

Here, the hypothesis is that 'the given spatial unit contains a mineral deposit of the type D'. The expression on the left, $log_e[O(D|E_1, E_2, ..., E_n)]$, is the posterior *logit* (log of odds) of target mineral deposit-type, which is the prior logit of target mineral deposit-type, $log_e[O(D)]$, modified by the *presence* of n binary predictor map patterns E_i (i=1 to n).

Agterberg (1989) and Agterberg *et al.* (1990) constructed a similar expression for posterior logit of mineral deposits, given the *absence* of n binary predictor map patterns:

$$log_e[O(D|E_1, E_2, ..., E_n)] = log_e[O(D)] + \sum_{i=1}^{n} log_e \frac{p(\bar{E}_i|D)}{p(\bar{E}_i|\bar{D})}, \qquad (4.6)$$

where $\bar{E}_i$ indicates the absence of the predictor map E_i. The expressions $log_e \frac{p(E_i|D)}{p(E_i|\bar{D})}$ in Equation 4.5 and $log_e \frac{p(\bar{E}_i|D)}{p(\bar{E}_i|\bar{D})}$ in Equation 4.6 are called the positive and negative weights of evidence, W_i^+ and W_i^-, respectively, of the ith binary predictor map pattern ($i = 1$ to n). The strength of association between target mineral deposit-type and the binary predictor pattern E_i can be measured in terms of *contrast* (C_i), which is given by:

$$C_i = W_i^+ - W_i^-. \qquad (4.7)$$

A positive contrast value indicates a positive spatial association, while a negative contrast value indicates a negative spatial association.

The Bayesian model for mineral potential mapping based on several binary

predictor maps can therefore be represented as:

$$log_e[O(D|E_1, E_2, ..., E_n)] = log_e[O(D)] + \sum_{i=1}^{n} W_i^{+/-}. \quad (4.8)$$

The sign of W_i in the above equation depends upon whether the ith binary pattern is present $(+)$ or absent $(-)$. The updated posterior probability of mineral deposits can be calculated from posterior logit of mineral deposits:

$$p(D|E_1, E_2, ..., E_n) = \frac{e^{log_e[O(D|E_1, E_2, ..., E_n)]}}{1 + e^{log_e[O(D|E_1, E_2, ..., E_n)]}}. \quad (4.9)$$

The variances of weights of evidence of the ith binary pattern E_i (i=1 to n) are calculated from the following relations, which are based on the asymptotic maximum likelihood method (Bishop *et al.*, 1975), as discussed by Agterberg *et al.* (1990):

$$\sigma^2(W_i^+) = \frac{1}{p(D|E_i)} + \frac{1}{p(\bar{D}|E_i)} \quad (4.10)$$

and

$$\sigma^2(W_i^-) = \frac{1}{p(D|\bar{E}_i)} + \frac{1}{p(\bar{D}|\bar{E}_i)}. \quad (4.11)$$

The variance of posterior probability due to variances of weights of evidence is calculated using the following equation (Agterberg *et al.*, 1990; Bonham-Carter and Agterberg, 1990):

$$\sigma_1^2\{p(D|E_1, E_2, ..., E_n)\} = \{\frac{1}{nD} + \sum_{i=1}^{n} \sigma^2(W_i^{+/-})\} \cdot \{p^2(D|E_1, E_2, ..., E_n)\}, \quad (4.12)$$

where nD is the number of mineral deposits and the sign of W_i depends upon whether the ith binary pattern is present $(+)$ or absent $(-)$. The variance of posterior probability due to the missing j^{th} predictor pattern P_j is calculated using the following relation (Bonham-Carter and Agterberg, 1990):

$$\sigma_2^2\{p(D|E_1, E_2, ..., E_n)\} = \{p(D|E_j) - p(D)\}^2 \cdot p(E_j)$$
$$+ \{p(D|\bar{E}_j) - p(D)\}^2 \cdot p(\bar{E}_j), \quad (4.13)$$

where $p(D)$ is now the posterior probability calculated for a region where E_j is missing while $p(D|E_j)$ and $p(D|\bar{E}_j)$ are updated posterior probabilities calculated as if the missing pattern E_j is actually known (Bonham-Carter and

Agterberg, 1990). The total variance of posterior probability is the sum of variance due to weights of evidence and variance due to missing predictor patterns, as given below:

$$\sigma_{total}^2\{p(D|E_1,...,E_n)\} = \sigma_1^2\{p(D|E_1,...,E_n)\} + \sigma_2^2\{p(D|E_1,...,E_n)\}$$

(4.14)

The goodness of fit between expected frequencies of mineral deposits estimated from posterior probabilities and observed frequencies can be tested by using either a χ^2 test (Agterberg *et al.*, 1990) or a Kolmogorov-Smirnov test (Bonham-Carter and Agterberg, 1990). A statistically-significant difference between the observed and estimated frequencies may be due to conditional dependence amongst two or more of the predictor maps. In such a case, pairs of predictor maps should be tested for conditional independence using the standard χ^2 test (Bonham-Carter and Agterberg, 1990).

4.2.1 Extended relations

Consider that n multi-class predictor maps M_i (i=1 to n) are to be used for deriving posterior probability of mineral deposits of a type D in an area A using the theory of conditional probability and Bayes' rule. M_i (i=1 to n) can be represented as follows (Pan and Harris, 2000):

$$M_1 = (M_1^1, M_1^2, M_1^3, ..., M_1^k)$$
$$...\qquad\qquad ...\qquad\qquad ...$$
$$M_n = (M_n^1, M_n^2, M_n^3, ..., M_n^k),$$

(4.15)

where M_i^j is the jth pattern on the ith predictor map (for j=1 to k, i=1 to n).

Each predictor pattern M_i^j can be considered a binary, with present or absent status. Consequently, the same relations as in the simple weights-of-evidence model can be used for the extended version. Explicitly, the extended Bayesian model using multi-class predictor maps can be represented as follows:

$$log_e\{O(D|M_{i\ (i=1\ to\ n)}^{j\ (j=1\ to\ k)})\} = log_e[O(D)] + \sum_{i=1}^{n}\sum_{j=1}^{k} W_i^{j+/-},$$

(4.16)

where the sign of the weights of evidence W_i^j depends upon whether M_i^j is present (+) or absent (−). In the above equation, the positive and negative

weights of evidence for the jth pattern on the ith predictor map (for $j=1$ to k, $i=1$ to n) can be derived using the following relations, respectively:

$$W_i^{j+} = log_e \frac{p(M_i^j|D)}{p(M_i^j|\bar{D})} \tag{4.17}$$

and

$$W_i^{j-} = log_e \frac{p(\bar{M}_i^j|D)}{p(\bar{M}_i^j|\bar{D})}, \tag{4.18}$$

where $\bar{M}_i^j$ and $\bar{D}$ indicate, respectively, the absence of the predictor pattern M_i^j and target mineral deposit-type D. The updated posterior probability of target mineral deposit-type can be calculated from the posterior logit of the mineral deposit-type (Equation 4.16):

$$p(D|M_{i\ (i=1\ to\ n)}^{j\ (j=1\ to\ k)}) = \frac{e^{log_e\{O(D|M_{i\ (i=1\ to\ n)}^{j\ (j=1\ to\ k)})\}}}{1 + e^{log_e\{O(D|M_{i\ (i=1\ to\ n)}^{j\ (j=1\ to\ k)})\}}}. \tag{4.19}$$

The variances of weights of evidence are given by:

$$\sigma^2(W_i^j+) = \frac{1}{p(D|M_i^j)} + \frac{1}{p(\bar{D}|M_i^j)} \tag{4.20}$$

and

$$\sigma^2(W_i^j-) = \frac{1}{p(D|\bar{M}_i^j)} + \frac{1}{p(\bar{D}|\bar{M}_i^j)}. \tag{4.21}$$

The variance of posterior probability due to variances of weights of evidence is given by:

$$\sigma_1^2\{p(D|M_{i\ (i=1\ to\ n)}^{j\ (j=1\ to\ k)})\} =$$

$$\{\frac{1}{nD} + \sum_{i=1}^{n}\sum_{j=1}^{k}\sigma^2(W_i^{j+/-})\} \cdot \{p^2(D|M_{i\ (i=1\ to\ n)}^{j\ (j=1\ to\ k)})\}, \tag{4.22}$$

where nD is number of mineral deposits and the sign of W_i^j depends upon whether the jth pattern on the ith predictor map is present $(+)$ or absent $(-)$. The variance of posterior probability due to missing l^{th} pattern on the mth

105

predictor map is calculated using the following relation:

$$\sigma_2^2\{p(D|M_{i\ (i=1\ to\ n)}^{j\ (j=1\ to\ k)})\} = [p(D|M_m^l) - p(D)]^2 \cdot p(M_m^l)$$
$$+ [p(D|\bar{M}_m^l) - p(D)]^2 \cdot p(\bar{M}_m^l), \qquad (4.23)$$

where $p(D)$ is now the posterior probability calculated for a region where M_m^l is missing while $p(D|M_m^l)$ and $p(D|\bar{M}_m^l)$ are updated posterior probabilities calculated as if the missing pattern M_m^l is actually known. The total variance of posterior probability is the sum of variance due to weights of evidence and variance due to missing predictor patterns, as given below:

$$\sigma_{total}^2\{p(D|M_{i\ (i=1\ to\ n)}^{j\ (j=1\ to\ k)})\} =$$
$$\sigma_1^2\{p(D|M_{i\ (i=1\ to\ n)}^{j\ (j=1\ to\ k)})\} + \sigma_2^2\{p(D|M_{i\ (i=1\ to\ n)}^{j\ (j=1\ to\ k)})\}. \qquad (4.24)$$

The conditional independence of the input multi-class predictor maps can be verified by testing the goodness of fit between expected frequencies of mineral deposits estimated from posterior probabilities and observed frequencies using a χ^2 test (Agterberg *et al.*, 1990; Bonham-Carter and Agterberg, 1990), Kolmogorov-Smirnov test (Agterberg *et al.*, 1990; Bonham-Carter and Agterberg, 1990), omnibus test (OT; Bonham-Carter, 1994) and new omnibus test (NOT; Agterberg and Cheng, 2002). The performance of the model can also be tested using Brier score ($\bar{B}$), which has its root in predictive meteorology (Glahn and Lowry, 1972). It is given by the following relation:

$$\bar{B} = \left(\frac{\sum_{i=1}^n (P_i - O_i)^2}{n}\right) \qquad (4.25)$$

where P_i is the calculated posterior probability and the O_i is the observed probability (= 1, if a mineral deposit is present, and 0, if it is absent). Values of Brier score close to 0 indicate a good fit. However, Brier scores have to be interpreted with care, as they depend on the frequency of an event − the rarer the event, the better the Brier score. In probabilistic mineral potential mapping, where the frequency of mineral deposit occurrence is low or rare as compared to the occurrence of geological evidences, it can be used in a relative sense in comparing the performance of different models.

The wights-of-evidence models were implemented using the procedure and software described by Kemp *et al.* (2001).

4.3 Application to Base-Metal Potential Mapping in Aravalli Province

4.3.1 Data preprocesing

It was considered inappropriate to use the buffer corridors around the lineaments and the fold axes as multi-class categorical units in the weights-of-evidence analysis because the buffer distances were selected subjectively. Moreover, as pointed out by Pan and Harris (2000), the likelihood of violation of conditional independence increases with the number of predictor maps and number of patterns on each map. Therefore, the multi-class maps of buffered distances from regional lineaments, buffered distances from NW-trending lineaments, buffered distances from NE-trending lineaments and buffered distances from fold axes, were converted into binary predictor maps by determining threshold buffer distances in which spatial association between the linear features and the mineral deposits is maximized (Agterberg *et al.*, 1990). The spatial association is generally measured in terms of contrast (Agterberg *et al.*, 1990). In the present work, however, studentized contrast, which is a measure of certainty with which a contrast value is known (Bonham-Carter, 1994, p. 323) and therefore provides a more reliable measure of spatial association, was used for determining a threshold buffer distance.

The weights of evidence, contrasts and studentized contrasts (C/σ_C) were calculated for cumulative buffer distances. The maximum studentized contrasts for the regional lineaments, NW-trending lineaments, NE-trending lineaments and fold axes are obtained at distances of 5.5 km, 3 km, 5 km and 1.25 km, respectively (Fig. 4.1). These values were therefore respectively taken as threshold buffering distances for converting each of the multi-class buffer distance map into a binary map. The binary map of buffered regional lineaments (Fig. 4.2A), NW-trending lineaments (Fig. 4.2B), NE-trending lineaments (Fig. 4.2C) and fold axes (Fig. 4.2D), were used as predictor maps of favorable structures.

In the extended weights-of-evidence analysis, the remaining predictor maps, namely, the multi-class maps of lithologies, stratigraphic groups and sedimentary environments, and the binary map of mafic igneous rocks were used as such without any further processing.

For comparison, a simple weights-of-evidence analysis using all of the above predictor maps in binary form was also carried out. For this, each of the above-mentioned multi-class categorical maps was converted into a binary pre-

dictor map by merging patterns with contrast values having the same signs (Table 4.1). The binary maps are shown in Figs. 4.2 and 4.3.

Training and validation points. A subset of 41 deposits, regarded as 'discovered' and randomly extracted from the known base-metal deposits, was used to train the models. The remaining 13 deposits were regarded as 'undiscovered' and were subsequently used to validate the models. As compared to the fuzzy models, a larger training subset was used for training weights-of-evidence models in order to reduce uncertainty in the estimated posterior probabilities because of the use of multi-class predictor maps.

4.3.2 Weights-of-evidence modeling

Computation of weights of evidence

The weights of evidence of the multi-class predictor maps were calculated using Equations 4.17 and 4.18. Variance of the weights-of-evidence of the multi-class predictor maps were calculated using Equations 4.20 and 4.21. Similarly, the weights of evidence of the binary predictor maps were calculated using the relations given in Equations 4.5 and 4.6. Variance of the weights of evidence of the binary predictor maps were calculated using Equations 4.10 and 4.11. The computations were performed using gridded predictor maps taking 1 km^2 as the unit cell size for the analysis. The weights of evidence and contrast values along with the standard deviation of contrast and studentized contrast values for each of the predictor maps are given in Table 4.1.

It should be noted that, in Equation 4.17, if $p(M_i^j|D)$ is 0, then W_i^{j+} becomes indeterminable because $log_e(0)$ is mathematically invalid and hence indeterminable. In other words, the weights of evidence of a predictor pattern are indeterminable if the pattern does not contain any known deposit.

Combining predictor maps

Combining predictor maps in weights-of-evidence modeling involves generation of a unique conditions grid map (Bonham-Carter and Agterberg, 1990; Kemp *et al.*, 1999; *see* Chapter 1, p. 6). The attribute table associated with a unique conditions grid (unique conditions table) has one record per unique condition class, and additional fields containing calculated variables can be added for each record.
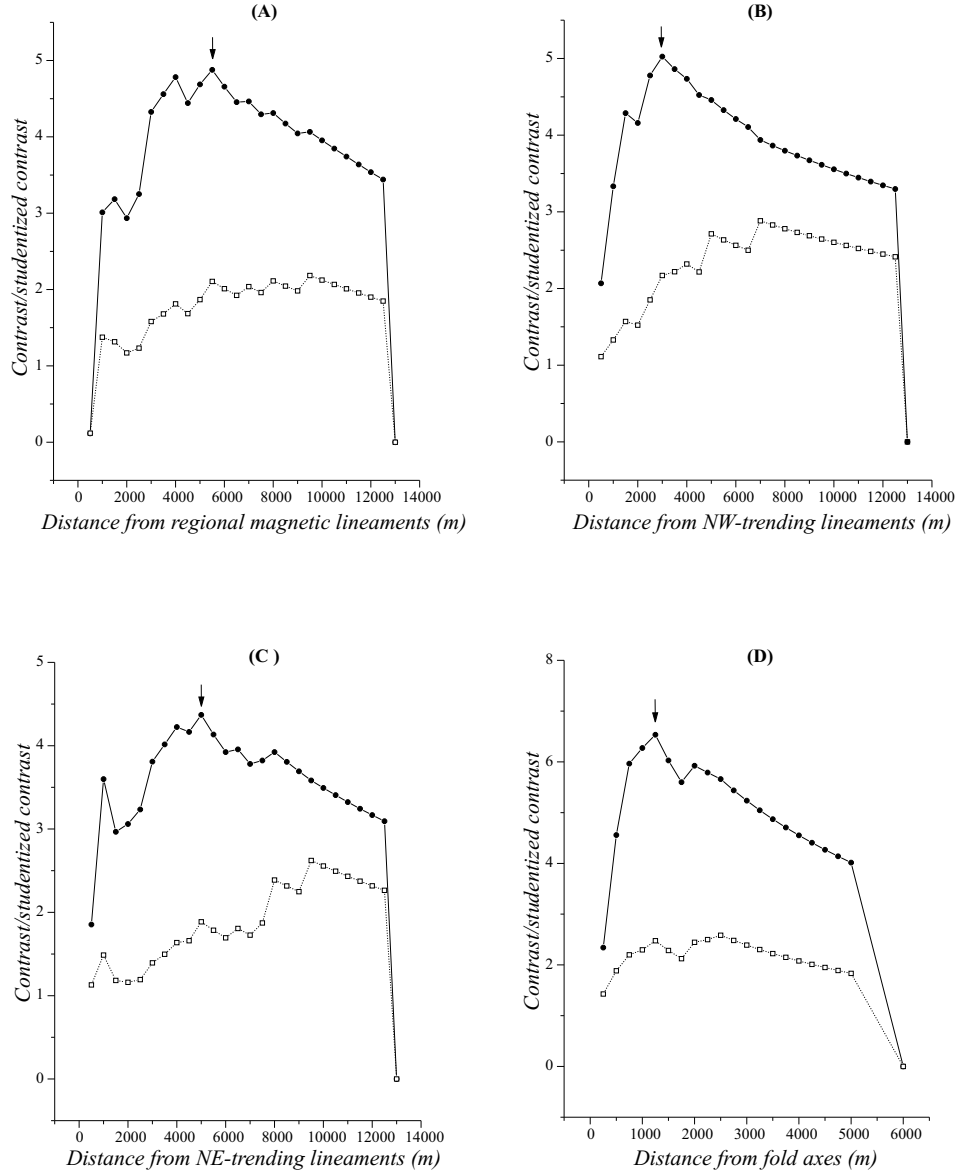
Figure 4.1: Variation of contrast (dashed line) and studentized contrast (solid line) with distance from (A) regional lineaments (B) NW-trending lineaments (C) NE-trending lineaments and (D) fold axes. Points of maximum studentized contrast are marked by arrows.
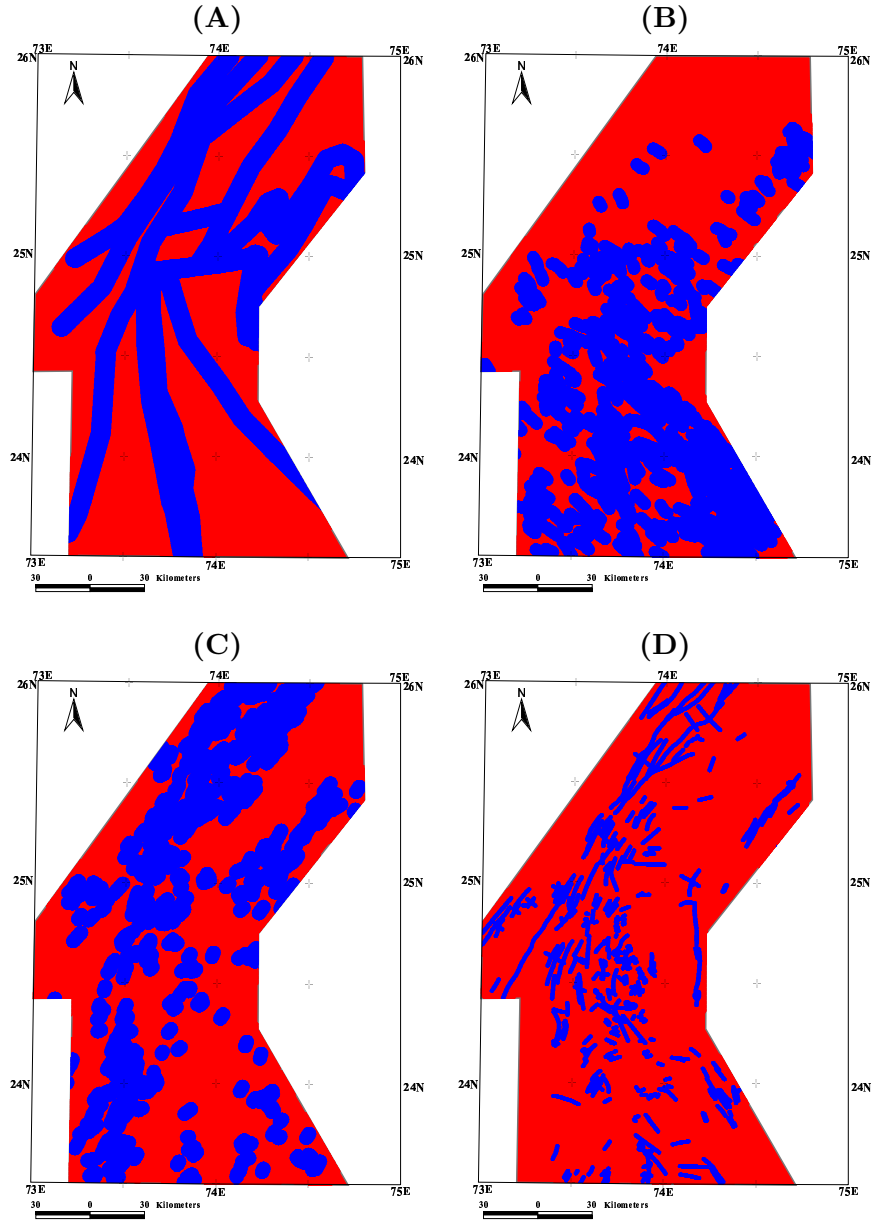
Figure 4.2: Binary predictor maps of (A) buffered distances from regional lineaments, (B) buffered distances from NW-trending lineaments, (C) buffered distances from NE-trending lineaments and (D) buffered distances from fold axes. Favorable areas based on each set of geological features are shown in blue and the unfavorable areas are shown in red.

110
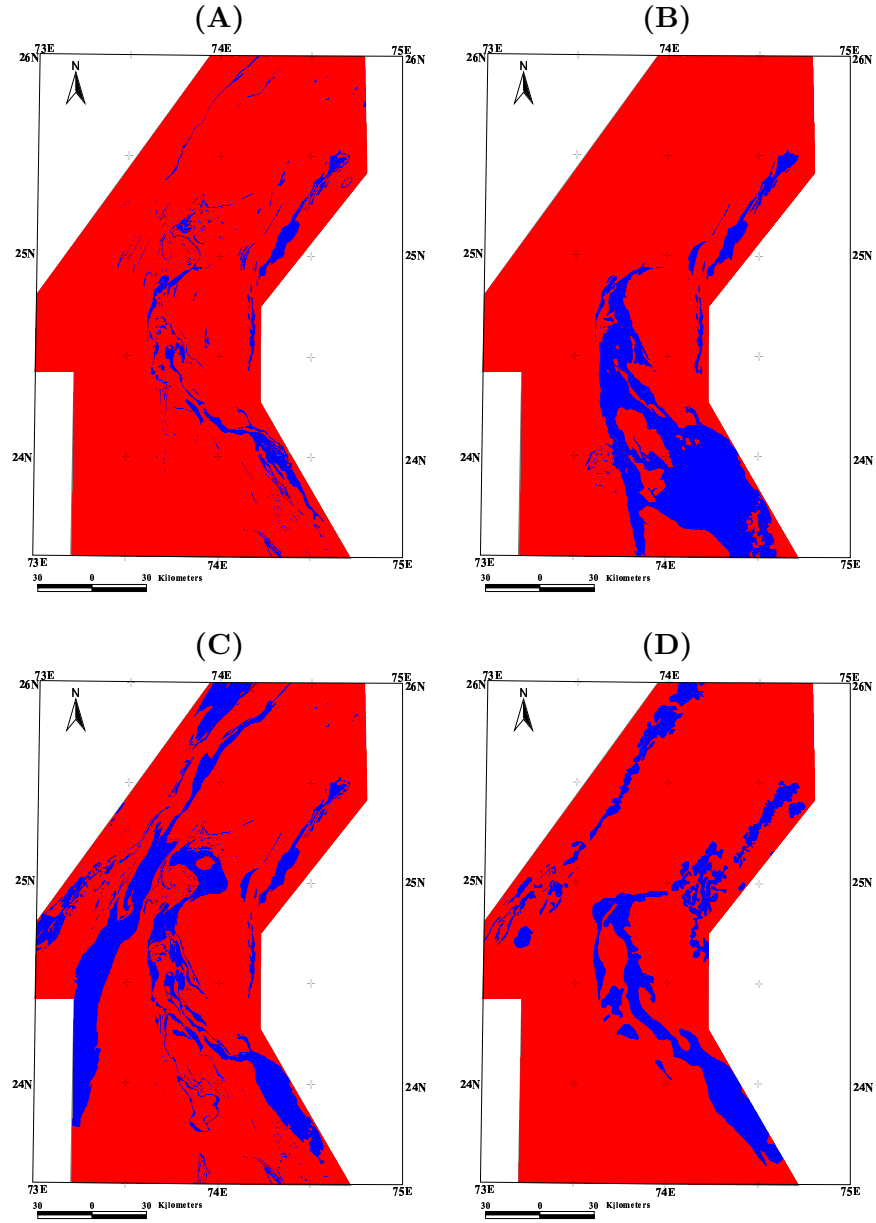
Figure 4.3: Binary predictor maps of (A) lithologies, (B) stratigraphic groups, (C) sedimentary environments and (D) mafic igneous rocks. Favorable areas based on each set of geological features are shown in blue and the unfavorable areas are shown in red.

Table 4.1: Weights of evidence, contrast and studentized contrast values for predictor maps

	Predictor map Pattern	W^+	$\sigma_{(W+)}$	W^-	$\sigma_{(W-)}$	Contrast (C)	$\sigma_{(C)}$	Student. Contrast
Predictor map of stratigraphy								
	Binary Map	1.7097	0.1628	-2.8071	0.7071	4.5168	0.7256	6.2248
1	Pur-Banera	3.4652	0.2631	-0.4582	0.2001	3.9234	0.3305	11.8702
2	Rajpura-Dariba	3.8084	0.3630	-0.2187	0.1769	4.0271	0.4038	9.9739
3	Debari	1.4099	0.3341	-0.1984	0.1797	1.6083	0.3794	4.2389
4	Nathdwara	1.9245	1.0041	-0.0217	0.1602	1.9462	1.0168	1.9141
5	Udaipur	0.2523	0.4476	-0.0314	0.1691	0.2836	0.4784	0.5928
6	Sandmata Complex	-1.4023	1.0001	0.0818	0.1602	-1.4842	1.0129	-1.4653
7	Jharol	-1.8215	1.0001	0.1425	0.1602	-1.9640	1.0129	-1.9391
8	Mangalwar Complex				—-not determinable—-			
9	Unrelated to base metals				—-not determinable—-			
Predictor map of lithologies								
	Binary Map	3.0894	0.1665	-3.5922	1.0000	6.6816	1.0138	6.5908
1	Magnetite quartzite	7.0037	0.6149	-0.1717	0.1769	7.1754	0.6398	11.2148
2	Dolomite	2.8047	0.2698	-0.4370	0.2042	3.2416	0.3384	9.5805
3	Calc-silicates	2.9783	0.3371	-0.2582	0.1858	3.2365	0.3849	8.4089
4	Graphitic meta-pelites	3.0631	0.3579	-0.2265	0.1827	3.2896	0.4018	8.1871
5	Quartzite-Arkose-Conglomerate	-1.1834	1.0002	0.0632	0.1645	-1.2466	1.0136	-1.2298
6	Calc-schist/gneiss				—-not determinable—-			
7	Migmatites and gneisses				—-not determinable—-			
8	Unrelated to base metals				—-not determinable—-			
Predictor map of sedimentary environments								
	Binary Map	1.6627	0.1586	-3.5090	1.0000	5.1717	1.0125	5.1078
1	Proximal shelf; partly anoxic	6.9492	0.6149	-0.1581	0.1691	7.1073	0.6377	11.1449
2	Proximal shelf; restricted; anoxic	2.8437	0.3368	-0.2350	0.1769	3.0786	0.3804	8.0929
3	Distal shelf; restricted; anoxic	3.7906	0.4591	-0.1273	0.1668	3.9179	0.4885	8.0211
4	Proximal shelf; anoxic	1.0581	0.2240	-0.4835	0.2183	1.5416	0.3128	4.9288
5	Deep sea	-2.2026	1.0001	0.2246	0.1582	-2.4272	1.0125	-2.3972
6	basement Complex				—-not determinable—-			
7	Unrelated to base metals				—-not determinable—-			

Table 4.1 Contd.

Predictor map Pattern	W^+	$\sigma_{(W+)}$	W^-	$\sigma_{(W-)}$	Contrast (C)	$\sigma_{(C)}$	Student. Contrast
Predictor map of mafic igneous rocks							
Binary map	1.7902	0.1803	-1.2761	0.3163	3.0663	0.3640	8.4230
Predictor map of buffered regional lineaments							
Binary map	0.3699	0.1770	-1.0915	0.4473	1.4613	0.4811	3.0377
Predictor map of buffered NW-trending lineaments							
Binary map	0.3354	0.1770	-0.8341	0.3781	1.1695	0.4174	2.8017
Predictor map of buffered NE-trending lineaments							
Binary map	0.3801	0.1859	-0.6508	0.3163	1.0310	0.3669	2.8099
Predictor map of buffered fold axes							
Binary map	0.9818	0.1929	-1.1348	0.3536	2.1166	0.4028	5.2544

Multi-class predictor maps. The three multi-class predictor maps of lithologies, stratigraphic groups and sedimentary environments, and the five binary predictor maps of mafic igneous rocks, buffered regional lineaments, buffered NW-trending lineaments, buffered NE-trending lineaments and buffered fold axes were combined using digital overlay, which resulted in a unique condition grid map containing 1936 unique conditions. The weights of evidence, uncertainty due to weights of evidence (standard deviation) and uncertainty due to missing patterns (standard deviation) were used to calculate the posterior probability and studentized posterior probability for each unique condition (Equations 4.16, 4.19, 4.22 and 4.23 and 4.24).

Binary predictor maps. The eight binary predictor maps of lithologies, stratigraphic groups, sedimentary environments, mafic igneous rocks, buffered regional lineaments, buffered NW-trending lineaments, buffered NE-trending lineaments and buffered fold axes were digitally superposed resulting in a unique conditions grid map with 724 unique conditions. The weights of evidence, uncertainty due to weights of evidence (standard deviation) and uncertainty due to missing patterns (standard deviation) were used to calculate the posterior probability and studentized posterior probability for each unique condition (Equations 4.8, 4.9, 4.12 and 4.13 and 4.14).

Table 4.2: χ^2 test for goodness of fit based on combining multi-class and binary predictor maps

Posterior Probability Class	Observed frequency of base-metal deposits (O_i)	Expected frequency of base-metal deposits (E_i)	$\dfrac{(O_i - E_i)^2}{E_i}$
0-0.1	6	1.12	21.177
0.1-0.2	1	1.70	0.290
0.2-0.3	1	0.90	0.012
0.3-0.4	1	2.01	0.510
0.4-0.5	2	3.56	0.686
0.5-0.6	0	1.38	1.378
0.6-0.7	1	3.83	2.091
0.7-0.8	4	6.86	1.191
0.8-0.9	2	3.32	0.524
0.9-1.0	23	16.31	2.740
			30.599

Goodness of fit

The goodness of fit between the observed distribution of base-metal deposits and the expected distribution based on the calculated posterior probabilities was tested using the χ^2 test (Agterberg *et al.*, 1990) and the Kolmogorov-Smirnov test (Bonham-Carter and Agterberg, 1990).

Table 4.2 gives the details of the χ^2 test. The calculated χ^2 value is 30.59, which is higher than the critical χ^2 value of 16.919 at 0.05 significance level and 9 degrees of freedom. The null hypothesis that the two distributions are the same would be rejected at 95% confidence level. The Kolmogorov-Smirnov goodness-of-fit test on the expected and observed cumulative distributions of base-metal deposits also indicates that the two distributions are statistically different (Fig. 4.4). The calculated value of Kolmogorov-Smirnov statistic is 0.2472, which is higher than the critical Kolmogorov-Smirnov statistic of 0.242 at 0.05 significance level and 30 degrees of freedom. The null hypothesis that the two distributions are the same would be rejected at 95% confidence level. A Brier score (Glahn and Lowry, 1972) of 0.054 for the estimated posterior probability distribution, however, indicates a relative good-fit (see below).

As the above tests indicated a problem of conditional dependence amongst one or more pairs of predictor maps, a pair-wise conditional independence test was carried out on the three multi-class and five binary predictor maps, using the method described by Bonham-Carter and Agterberg (1990). The results, given in Table 4.3 indicate that predictor map-pair of sedimentary environments-lithologies may be conditionally dependent. A test of condi-
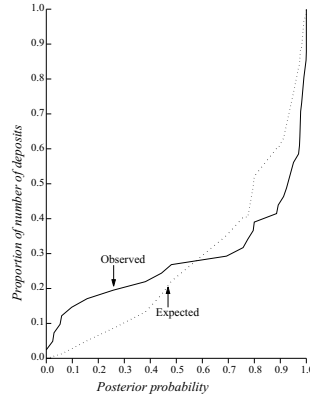
Figure 4.4: Variation of cumulative expected and observed frequencies of base-metal deposits with posterior probability based on 3 multi-class and 5 binary predictor maps.

tional independence on the eight binary maps (Table 4.4) also indicates a conditional dependence between the map-pairs of sedimentary environments-lithologies and sedimentary environments-stratigraphic groups.

The predictor map of sedimentary environment was therefore rejected, and the posterior probabilities along with the standard deviations were recalculated using the seven conditionally-independent maps only. This reduced the number of unique conditions to 1562 in the case using the multi-class and binary predictor maps and 504 in the case using only the binary predictor maps. The spatial distribution of the posterior probability and studentized posterior probability calculated using two multi-class (lithologies and stratigraphy) and five binary (same as before) predictor maps are shown in Fig. 4.5. Fig. 4.6 shows the spatial distribution of the posterior probability and studentized posterior probability calculated using seven binary maps (also the same as before, but excluding the binary predictor map of sedimentary environments).

The χ^2 test indicates a better fit between the observed and expected distribution based on the posterior probabilities calculated using the two multi-class and five binary maps (Table 4.5). The calculated χ^2 value in this case is 16.450, which is less than the critical χ^2 value of 16.919 at 0.05 significance level and 9 degrees of freedom. The hypothesis that the two distributions are the same cannot be rejected at 95% confidence level. The Kolmogorov-Smirnov goodness-of-fit test also indicates that the two distributions are similar (Fig. 4.7A). The calculated value of Kolmogorov-Smirnov statistic is 0.1629, which is less than the critical Kolmogorov-Smirnov statistic of 0.242 at 0.05 significance level and 30 degrees of freedom. The hypothesis that the two distributions are the same

cannot be rejected at 95% confidence level. The Brier Score estimated using combination of the two multi-class and five binary maps improves to 0.033 from 0.054 for the posterior probabilities estimated using the three multi-class and five binary maps, which indicates an improvement in goodness of fit after rejecting the map of sedimentary environments.

Table 4.6 shows the results of χ^2 test on the observed distribution and expected distribution of the base-metal deposits based on posterior probabilities calculated using the seven binary maps. The calculated χ^2 value in this case is 5.491, which is less than the critical χ^2 value of 15.507 at 0.05 significance level and 8 degrees of freedom. The hypothesis that the two distributions are the same cannot be rejected at 95% confidence level. The Kolmogorov-Smirnov test on the expected and observed cumulative distributions of base-metal deposits also gives a similar result (Fig. 4.7B). The Kolmogorov-Smirnov statistic obtained in this case is 0.1907, which is less than the critical Kolmogorov-Smirnov statistic of 0.264 at 0.05 significance level and 22 degrees of freedom. The Brier Score of the posterior probabilities estimated using the seven binary predictor maps is 0.034.

However, the omnibus test of conditional independence (Bonham-Carter, 1994) gives a value of 0.12 for the posterior probabilities estimated using the multi-class and the binary predictor maps and a value of 0.14 for the posterior probabilities calculated using only the binary maps, which still indicate conditional dependency amongst some of the input predictor maps. Similarly, the new omnibus test (NOT) for conditional independence (Agterberg and Cheng, 2002) gives a value of 14.32 for posterior probabilities calculated using the multi-class and binary predictor maps and 10.68 for posterior probabilities calculated using only the binary predictor maps. The results of NOT indicate that, in both the cases, the null hypothesis that the observed distribution and the estimated distribution of base-metal deposits are the same is rejected (p<0.0001) and, therefore, there may be conditional dependence amongst some of the input predictor maps.

Table 4.3: Pair-wise χ^2 test for conditional independence of multi-class and binary predictor maps

Predictor Maps	Lithologies	Sedimentary environments	Mafic igneous rocks	Buffered regional lineaments	Buffered NW lineaments	Buffered NE lineaments	Buffered fold axes
Stratigraphic groups	**49.02**(56) <u>74.468</u>	**57.66**(48) <u>65.171</u>	**6.36**(8) <u>15.507</u>	**0.74**(8) <u>15.507</u>	**0.96**(8) <u>15.507</u>	**8.89**(8) <u>15.507</u>	**1.91**(8) <u>15.507</u>
Lithologies		**68.42***(42) <u>58.124</u>	**3.01**(7) <u>14.067</u>	**0.85**(7) <u>14.067</u>	**6.44**(7) <u>14.067</u>	**7.28**(7) <u>14.067</u>	**1.19**(7) <u>14.067</u>
Sedimentary environments			**6.36**(6) <u>12.529</u>	**0.11**(6) <u>12.52</u>	**2.53**(6) <u>12.52</u>	**7.09**(6) <u>12.52</u>	**1.49**(6) <u>12.52</u>
Mafic igneous rocks				**00.46**(1) <u>3.84</u>	**0.01**(1) <u>3.84</u>	**0.07**(1) <u>3.84</u>	**0.03**(1) <u>3.84</u>
Buffered regional lineaments					**0.002**(1) <u>3.84</u>	**0.03**(1) <u>3.84</u>	**0.38**(1) <u>3.84</u>
Buffered NW lineaments						**1.53**(1) <u>3.84</u>	**3.83**(1) <u>3.84</u>
Buffered NE lineaments							**0.32**(1) <u>3.84</u>

Bold and underlined figures are calculated and tabulated χ^2 values (at 0.05% significance level), respectively. Figures in parentheses are degrees of freedom.
*Null hypothesis of conditional independence is rejected at 95% confidence level.

Table 4.4: Pair-wise χ^2 test for conditional independence of only binary predictor maps

Predictor Maps	Lithologies	Sedimentary environments	Mafic igneous rocks	Buffered regional lineaments	Buffered NW lineaments	Buffered NE lineaments	Buffered fold axes
Stratigraphic groups	4.12*	4.37*	2.81	0.005	0.22	0.35	0.31
Lithologies		8.99**	0.30	0.003	0.16	0.38	0.28
Sedimentary environments			0.36	0.005	0.22	0.35	0.31
Mafic igneous rocks				00.46	0.01	0.07	0.03
Buffered regional lineaments					0.002	0.03	0.38
Buffered NW lineaments						1.53	3.83
Buffered NE lineaments							0.32

Tabulated χ^2 values at 0.05% significance level for 1 degree of freedom is 3.84.

*Null hypothesis of conditional independence is rejected at 95% confidence level, but not at 98% at confidence level

**Null hypothesis of conditional independence is rejected at both 95% and 98% confidence levels

Table 4.5: χ^2 test for goodness of fit based on combining conditionally-independent multi-class and binary predictor maps

Posterior Probability Class	Observed frequency of base-metal deposits (O_i)	Expected frequency of base-metal deposits (E_i)	$\frac{(O_i - E_i)^2}{E_i}$
0-0.1	7	9.63	0.716
0.1-0.2	3	2.93	0.002
0.2-0.3	2	1.21	0.520
0.3-0.4	5	4.03	0.233
0.4-0.5	1	3.03	1.361
0.5-0.6	4	2.43	1.020
0.6-0.7	0	2.76	2.765
0.7-0.8	4	2.25	1.350
0.8-0.9	1	5.06	3.259
0.9-1.0	14	7.67	5.224
			16.450

Table 4.6: χ^2 test for goodness of fit based on combining conditionally-independent binary predictor maps

Posterior Probability Class	Observed frequency of base-metal deposits (O_i)	Expected frequency of base-metal deposits (E_i)	$\frac{(O_i - E_i)^2}{E_i}$
0-0.1	9	12.88	1.169
0.1-0.2	3	2.43	0.135
0.2-0.3	5	6.52	0.353
0.3-0.4	1	1.96	0.472
0.4-0.5	3	6.94	2.241
0.5-0.6	0	0.05	0.047
0.6-0.7	2	3.75	0.821
0.7-0.8	7	8.46	0.252
0.8-0.9	11	10.89	0.001
			5.491

4.3.3 Favorability maps

It is cumbersome to interpret the posterior probability maps shown in Figs. 4.5A and 4.6A in terms of delineating the areas favorable for base-metal mineralization, as they shows posterior probability of base-metal deposits in a continuous scale from the least probable (posterior probability=0) to the most probable (posterior probability≈1). Thresholding the posterior probabilities facilitates delineation of potential areas. To determine threshold posterior probabilities, cumulative posterior probability values (rearranged from highest to lowest) were plotted against corresponding percentage of cumulative area (Fig. 4.8). The percentage of cumulative area increases as the cumulative (of decreasing)

119

(A)　　　　　　　　　　**(B)**
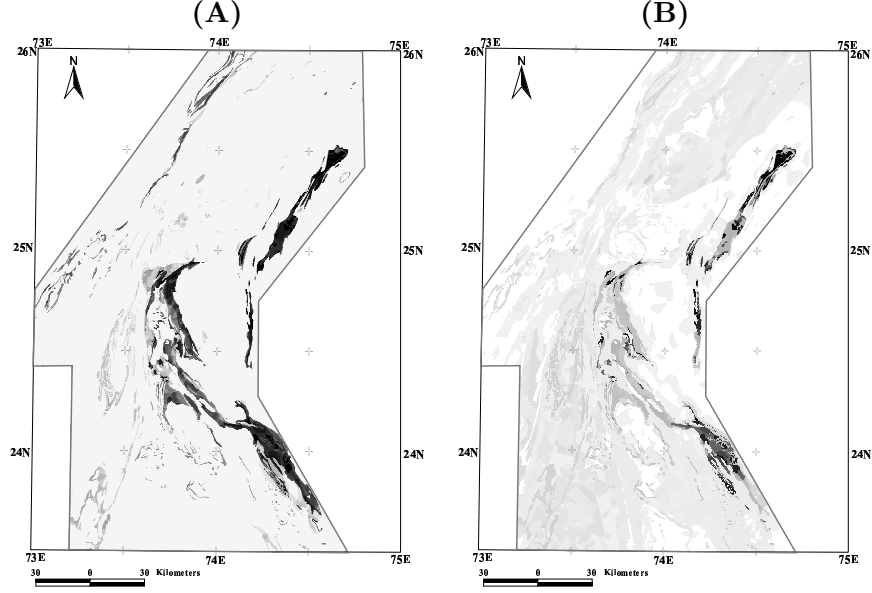
Figure 4.5: Continuous-scale maps derived by combining conditionally-independent multi-class and binary predictor maps: (A) posterior probability, which varies from 0.00 (white) to 0.99 (black) and (B) studentized posterior probability, which varies from 0.00 (white) to >5.84 (black).

posterior probability increases, but initially the increase in cumulative posterior probability is much higher than the corresponding increase in cumulative area, whereas later the cumulative area increases without any significant increase in the cumulative posterior probability. The curves for the posterior probability maps derived by using combination of the multi-class and binary maps (Fig. 4.5A) and by using only the binary maps (4.6A) are shown in Fig. 4.8.

Two inflection points can be identified in each curve at which the slope of the curve changes from steep to moderate and from moderate to flat. The part of curve below the lower inflection point represents (a) a much higher increase in cumulative posterior probability compared to increase in cumulative area and (b) high posterior probabilities in a few percentage of the study area. The part of curve between the lower and the upper inflection points represents (a) an almost equal increase in cumulative posterior probability and cumulative area and (b) moderate posterior probabilities in a few percentage of the study area. The part of the curve above the higher inflection point represents (a) a much lower (almost nil) increase in cumulative posterior probability compared

(A)   **(B)**
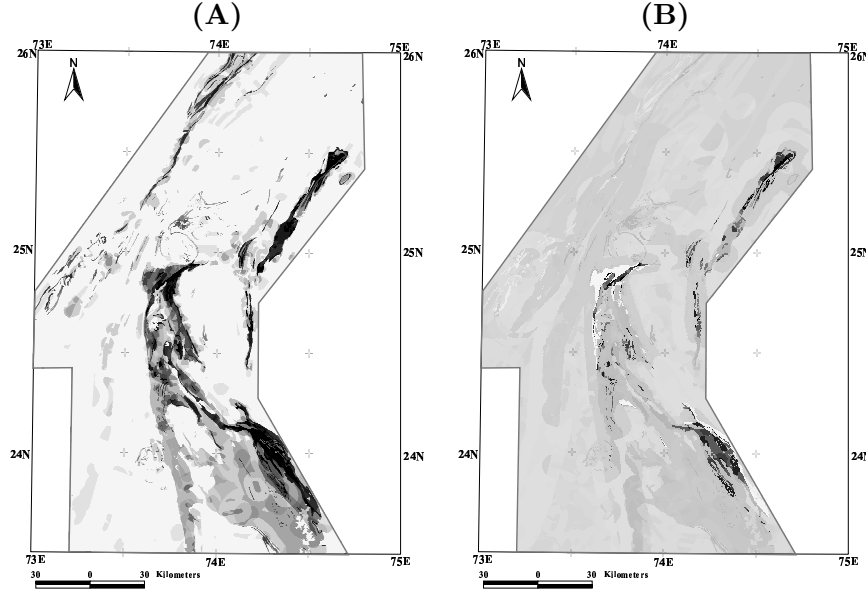
Figure 4.6: Continuous-scale maps derived by combining conditionally-independent binary predictor maps: (A) posterior probability, which varies from 0.00 (white) to 0.87 (black) and (B) studentized posterior probability, which varies from 0.21 (white) to >5.61 (black).

to increase in cumulative area and (b) low posterior probabilities in a very high percentage of the study area. The two inflection points on each curve were used as threshold values to reclassify the posterior probability maps into favorability maps showing high favorability, moderate favorability and low favorability zones. High favorability zones are those with posterior probability corresponding to the part of curve below the lower inflection point. Moderate favorability zones are those with posterior probability corresponding to the part of curve between the lower and the upper inflection points. Low favorability zones are those with posterior probability corresponding to the part of curve above the higher inflection point.

The threshold probabilities corresponding to the lower and upper inflection points on the curve in Fig. 8A are 0.0622 and 0.0001, respectively. The threshold probabilities corresponding to the lower and upper inflection points on the curve in Fig. 8B are 0.0175 and 0.0004, respectively. The resulting favorability maps are shown in Figs. 4.9 and 4.10. Fig. 4.11 shows the posterior probabilities as functions of percentage of cumulative area.

Fig. 4.11 indicates that the two favorability maps (Figs. 4.9 and 4.10) are

121
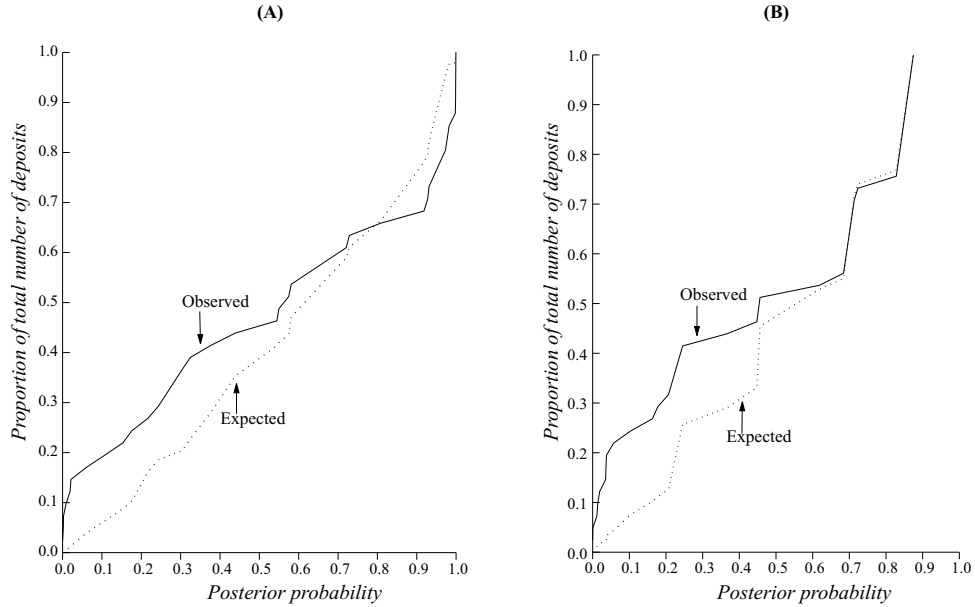
Figure 4.7: Variation of cumulative expected and observed frequencies of base-metal deposits with posterior probability based on using (A) multi-class and binary predictor maps and (B) only binary predictor maps.

very similar in respect of the distribution of the known base-metal deposits in the high favorability and moderate favorability zones. In the case of the curve shown in Fig. 4.11A, one deposit lies close to the threshold that defines boundary between the moderate favorability and low favorability zones, four in the middle portion of the part of the curve that corresponds to the moderate favorability zones, while the rest are either close to the threshold that defines the boundary between moderate favorability and high favorability zones or in the upper part of the curve that corresponds to the high favorability zones. In the case of the curve shown in Fig. 4.11B, two deposits lie at the threshold that defines boundary between the moderate favorability and low favorability zones, one in the middle portion of the part of the curve that corresponds to the moderate favorability zones, while the rest are either close to the threshold that defines boundary between the moderate favorability and high favorability zones or in the upper part of the curve that corresponds to the high favorability zones.

The two favorability maps (Fig. 4.9 and 4.10) are also very similar in terms of the areal extents of the high favorability zones, moderate favorability zones and low favorability zones. Based on combination of the multi-class and binary
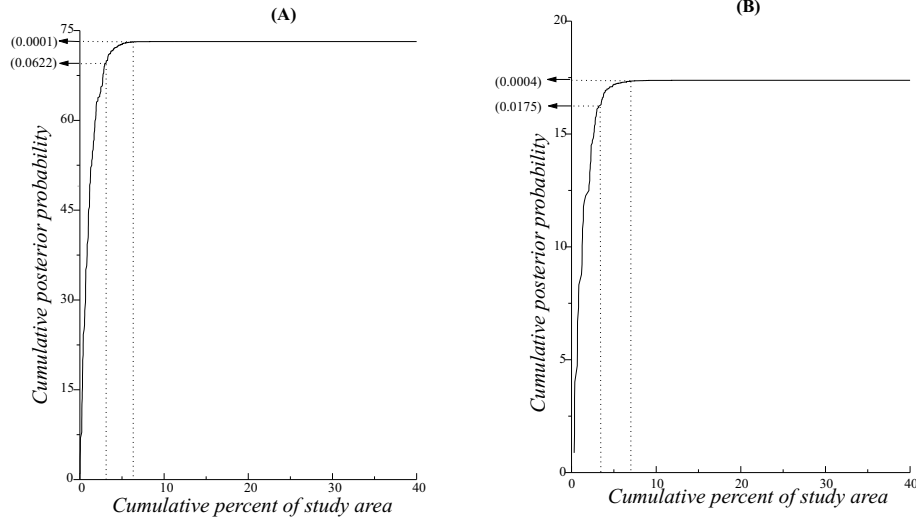
Figure 4.8: Variation of cumulative posterior probability with cumulative area in posterior probability maps shown in (A) Fig. 4.5A and (B) Fig. 4.6A. Inflection points (marked by arrows) correspond to threshold posterior probability values (figures in parenthesis) used in generating favorability maps.

predictor maps, the high favorability zones, the moderate favorability zones and the low favorability zones occupy 3.1%, 4.2% and 92.6% of the study area, respectively. Based on only the binary predictor maps, the high favorability, the moderate favorability and the low favorability zones occupy 4.0%, 3.6% and 92.4% of the study area, respectively.

The major difference between the two favorability maps is in the distribution of the known deposits in the low favorability zones. There are no deposits in the low favorability zones in the favorability map derived by combining multi-class and binary predictor maps (Figs. 4.9 and 4.11A), while there are two deposits in the low favorability zones in favorability map derived by using only the binary predictor maps (Figs. 4.10 and 4.11B).

Validation of favorability maps

The favorability maps were validated by overlaying the training subset and the validation subset of the known base-metal deposits on the favorability maps (Figs. 4.9 and 4.10) and by plotting on posterior probability curves the position of these deposits (Fig. 4.11). Table 4.7 shows that in the favorability map derived from combining the two multi-class and five binary predictor

123
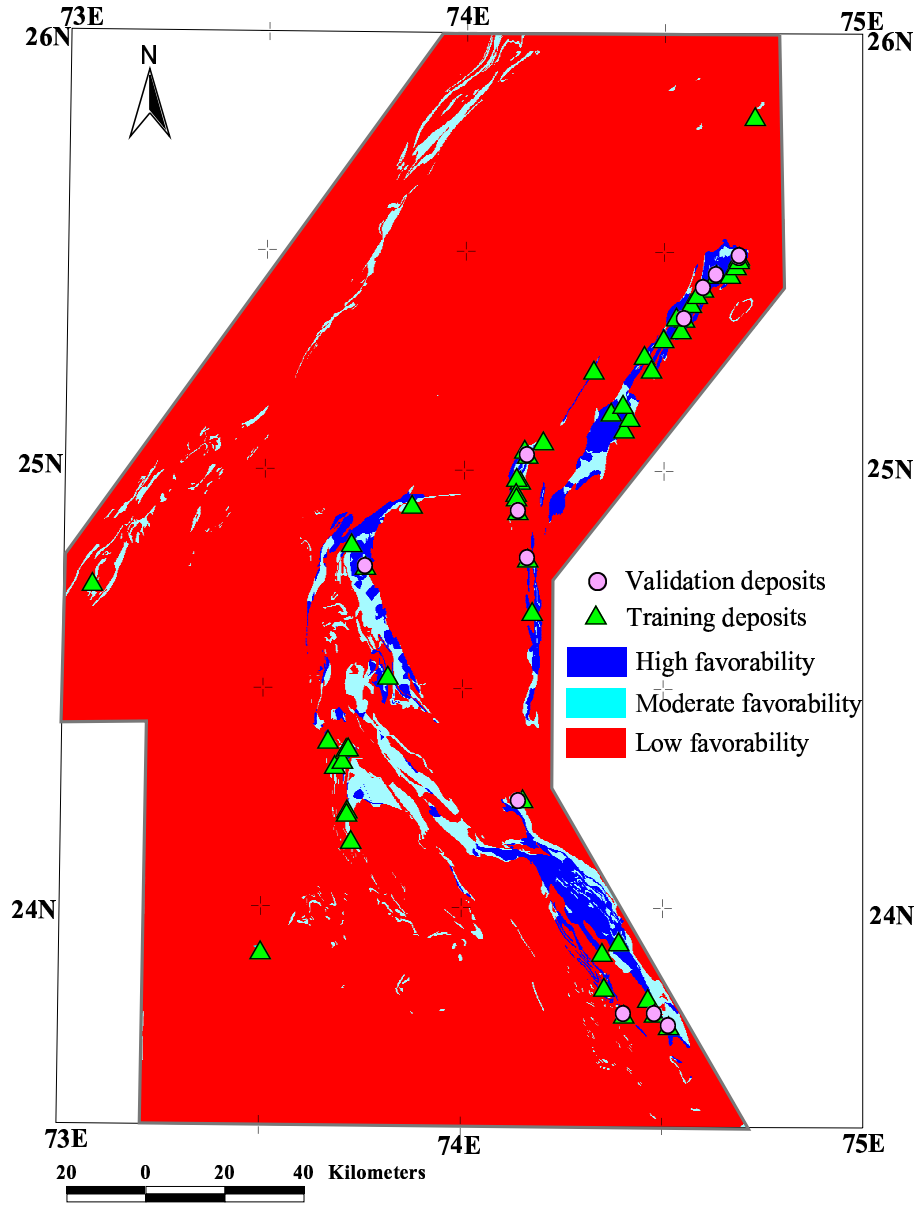
Figure 4.9: Favorability map generated by reclassification of posterior probability map shown in Fig. 4.5A.
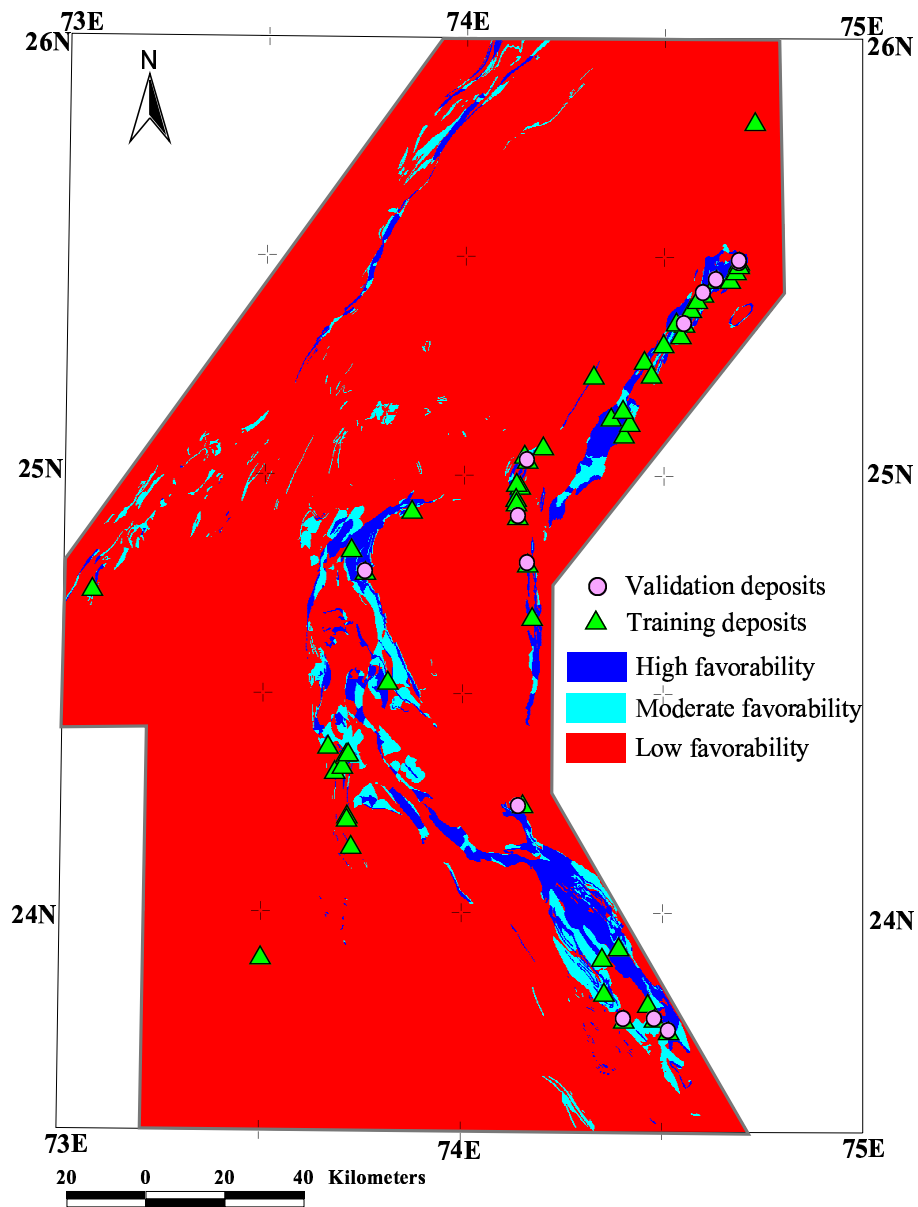
Figure 4.10: Favorability map generated by reclassification of posterior probability map shown in Fig. 4.6A.
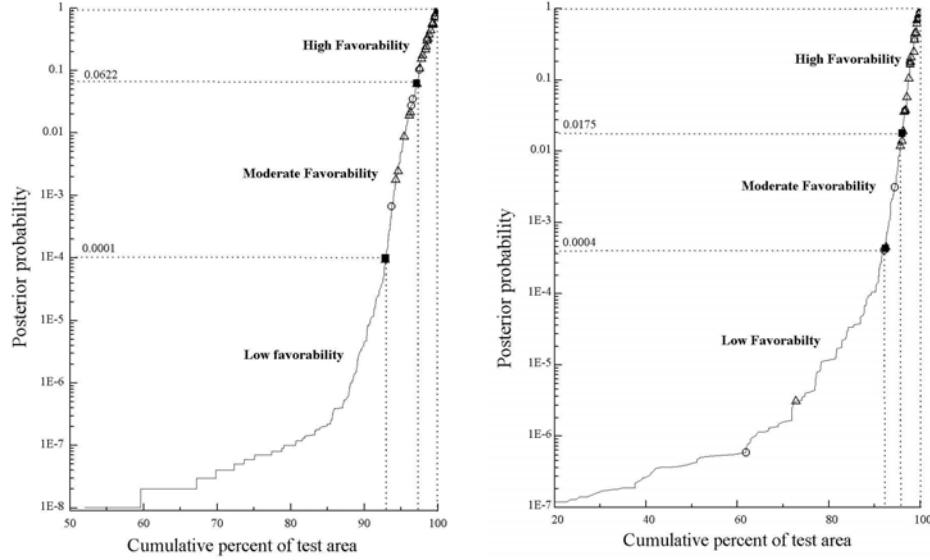
Figure 4.11: Variation of posterior probability with cumulative percent of study area based on (A) combining multi-class and binary predictor maps and (B) combining only binary predictor maps. Hollow triangles, filled circles and filled rectangles are posterior probabilities of training base-metal deposits, validation base-metal deposits and threshold points, respectively.

maps (Figs. 4.9; and 4.11A), the high favorability zones contain approximately 77% and 85% of the validation and training deposits, respectively, while the moderate favorability zone contains about 23% and 15% of the validation and training deposits, respectively. Furthermore, Table 4.7 shows that in the favorability map derived from using only the binary predictor maps (Figs. 4.10 and 4.11B), the high favorability zones contain approximately 77% and 88% of the validation and training deposits, respectively; the moderate favorability zones contain 15% and 10% of the validation and training deposits, respectively and the low favorability zones contain about 8% and 2% of the validation and training deposits.

4.4 Discussion

The graphical method adopted in the above applications for the classification of posterior probability maps into high favorability, moderate favorability and low favorability zones is based on the assumption that mineral-bearing areas occupy

126

Table 4.7: Validation of favorability maps

Favorability map	Favorability zone	Percent of study area	Percent of validation deposits	Percent of training deposits
Based on combination of multi-class and binary evidential maps	High favorability	3.12	76.9	85.4
	Moderate favorability	4.22	23.1	14.6
	Low favorability	92.66	nil	nil
Based on only binary evidential maps	High favorability	3.99	76.9	87.9
	Moderate favorability	3.58	15.4	9.7
	Low favorability	92.43	7.7	2.4

a very small proportion of the total area of a metallogenic province (Boleneus *et al.*, 2001). Consequently, in the favorability maps shown in Figs. 4.9 and 4.10, the high favorability zones are limited to a very small percentage of the study area (less than 4%), while the low favorability zones occupy a very large percentage (more than 90%). The transitional zones between the high favorability zones and the low favorability zones comprise the moderate favorability zones, which also occupy a very small part of the study area (less than 4%). Boleneus *et al.* (2001) obtained similar percentage values for high favorability, moderate favorability and low favorability regions for epithermal gold deposits in northeast Washington State, USA. The threshold posterior probability that defines the high favorability zones is approximately ten times higher than the prior probability of the training base-metal deposits in the study area, while the threshold posterior probability that defines the low favorability zones is approximately ten times lower than the prior probability.

In the plot of Fig. 4.11A, the Rampura-Agucha deposit lies in the middle part of the curve pertaining to the moderate favorability zones in the favorability map derived by combining multi-class and binary predictor maps. In the plot of Fig. 4.11B, the Rampura-Agucha deposit lies at the threshold that defines the moderate favorability and low favorability zones in the favorability map derived by using only the binary predictor maps. As discussed in Chapter 3, the deposit has several characteristics that make it a difficult deposit to predict. However, the use of multi-class predictor maps gives a higher posterior probability for the Rampura-Agucha deposit as compared to the posterior probability calculated using the same predictor maps, but reclassified into binary form.

An analysis of the studentized posterior probabilities indicates that the certainty of posterior probabilities increases exponentially with increasing posterior probabilities (Fig. 4.12). This trend is common to both the models

(Figs. 4.12A and Fig. 4.12B). The high favorability zones in both models comprise highly robust posterior probability values (posterior probability/$\sigma > 1.5$). Significantly, the studentized posterior probabilities in the high favorability zones are not adversely affected by the use of multi-class predictor maps. In the high favorability zones, the certainty of the posterior probabilities estimated by combining multi-class and binary predictor maps is higher than that of the posterior probabilities estimated by using only binary predictor maps (Fig. 4.13). The moderate favorability zones are characterized by studentized posterior probabilities ranging from 1.0 to 2.0, which indicate transitional certainty of the posterior probability values. The low favorability zones in both the models comprise highly uncertain posterior probability values (studentized posterior probabilities < 1.0). Occurrence of a negligible number of training points explains the high amount of uncertainty of posterior probabilities in the low favorability zones (Agterberg $et~al.$, 1990).

After the rejection of the conditionally-dependent map of sedimentary environments, the expected distribution of the base-metal deposits based on the estimated posterior probabilities shows a better fit with the observed distribution as indicated by the χ^2 and the Kolmogorov-Smirnov tests. The Brier score also indicates an improvement of goodness of fit after the rejection of the predictor map of sedimentary environment. However, the results of the omnibus and new omnibus tests for conditional independence on the estimated posterior probability values indicate that the possibility of conditional dependence amongst some of the input predictor maps cannot be ruled out in either case. Nevertheless, as the results of all the above-mentioned tests are similar for the posterior probabilities estimated using combination of the multi-class and binary predictor maps and only the binary predictor maps, it can be surmised that the conditional dependence is not significantly enhanced by the use of multi-class predictor maps in the present case.

In view of the suspected conditional dependence amongst the input predictor maps and the large amount of uncertainty in the estimated posterior probability values in a large part of the study area, the estimated posterior probabilities should not be interpreted in an absolute sense. The classification of the study area into the high favorability, moderate favorability and the low favorability zones, therefore, reflects only the relative favorability of various tracts in the study area, and should be interpreted as such. As pointed out by Pan and Harris (2000), the bias effect of the conditional dependence can be considerably mitigated by interpreting the posterior probabilities in rela-

tive terms. Alternatively, fuzzy operators like the fuzzy OR or the fuzzy AND can be used to combine the weights of evidence of suspected conditionally-dependent predictor maps, as suggested by Agterberg (1992).

4.5   Conclusions

The application of an extended weights-of-evidence model using multi-class predictor maps to the study area results in demarcation of high favorability zones occupying less than 4% of the study area, which predict at least 83% of the known base-metal deposits; moderate favorability zones, which occupy less than 4% of the study area and contain 17% of the known base-metal deposits; and low favorability zones that occupy 92% of the study area and do not contain any known base-metal deposit. The application of a simple weights-of-evidence model using only binary predictor maps to the study area results in demarcation of the high favorability, moderate favorability and low favorability zones that are similar in terms of areal extension to those demarcated by the extended weights-of-evidence model. However, in the case of the simple weights of evidence model, the low favorability zones contain approximately 4% of the known base-metal deposits. Based on a comparison of the two applications, the following conclusions can be drawn.

- The extended weights-of-evidence model derived using multi-class and binary predictor maps has a slightly better prediction rate than the simple weights-of-evidence derived using only binary predictor maps.

- The use of multi-class predictor maps in weights-of-evidence modeling results in enhanced and finely-differentiated posterior probabilities.

- The statistical properties of the weights of evidence, the contrasts and the posterior probabilities are not significantly degraded by the use of multi-class predictor maps in the weights-of-evidence modeling.

- In practice, it may not be always possible to rule out conditional dependence amongst two or more of the input predictor maps. As a result the estimated posterior probabilities may be artificially deflated or inflated. In such cases, these values can be used in relative terms to rank areas as highly favorable, moderately favorable or less favorable with respect to the target mineralization.
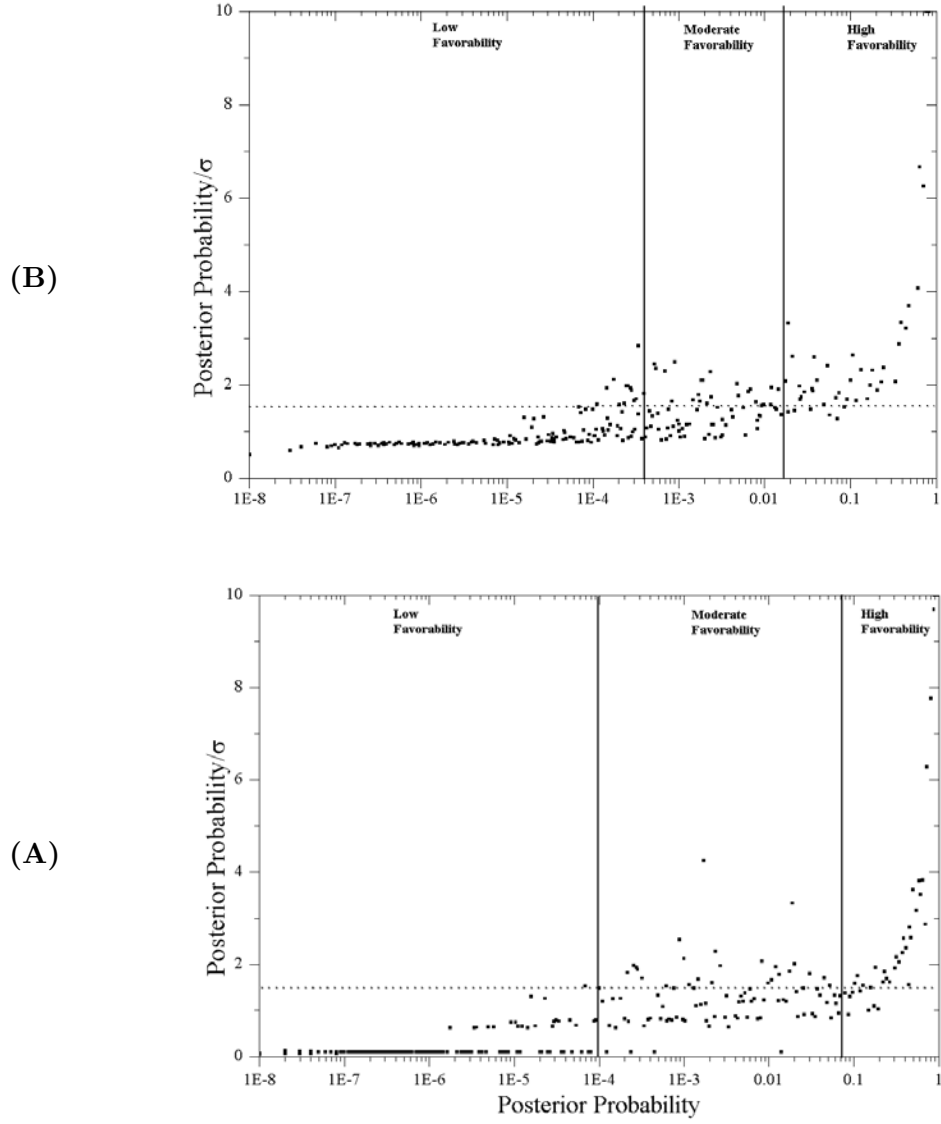
Figure 4.12: Variation of studentized posterior probability with posterior probability based on (A) combining multi-class and binary predictor maps and (B) combining only binary predictor maps.
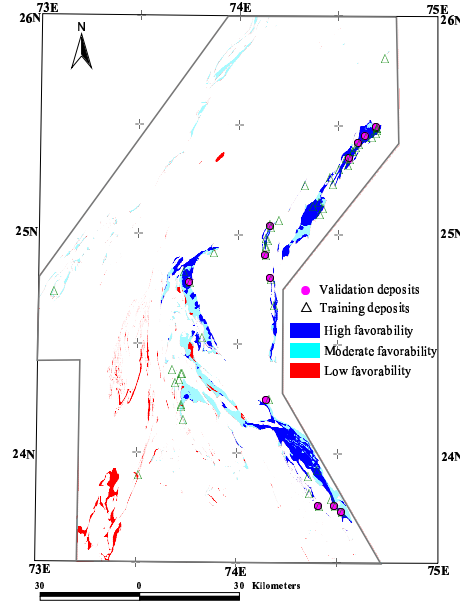
Figure 4.13: Favorability map (Fig. 4.9) showing high favorability, moderate favorability and low favorability zones in which posterior probabilities based on combining multi-class and binary predictor maps have higher certainty than posterior probabilities based only on binary predictor maps. Zones in which posterior probabilities based on combining multi-class and binary predictor maps have less certainty than posterior probabilities based only on binary predictor maps are masked out (in white).

The extended weight-of-evidence offers a simple and intuitive approach to mineral potential mapping based on multi-class predictor maps. However, the model may become less robust when applied to poorly-explored metallogenic provinces, which contain none or very few known mineral deposits. The problem can be addressed by extrapolating the weights of evidence for predictor maps that contain none or very few training deposits from weights-of-evidence models of geologically-similar, well-explored metallogenic provinces elsewhere in the world. It is also possible to assign 'expert weights of evidence' to such predictor maps based on available metallogenetic information. The next chapter describes a consistent method of using expert knowledge in a weights-of-evidence model by applying the theory of fuzzy sets.

Chapter 5

Hybrid Fuzzy Weights-of-Evidence Model

This chapter is based on a paper titled "A Hybrid Fuzzy Weights of Evidence Model for Mineral Potential Mapping"(Porwal *et al.*, 2006c). The model combines knowledge-based fuzzy membership values with data-based conditional probabilities for mineral potential mapping.

5.1 Introduction

Uncertainty in mineral potential mapping is generally attributed to insufficient data on predictor patterns or mineral deposits. This type of uncertainty (stochastic uncertainty, cf. Zimmerman, 1991), which arises from inadequate information, is dealt with appropriately by using the theory of probability under the assumption that model parameters and variables are well defined. Weights-of-evidence models (Agterberg, 1989; Agterberg *et al.*, 1990; Bonham-Carter and Agterberg, 1990), which are based on the Bayesian theory of conditional probability, offer methods of quantifying stochastic uncertainty in terms of variance of posterior probability. Owing to their intuitive approach and easy implementation, these models have been used to map potential of a variety of mineral deposit types (*see* Chapter 4 for references).

However, the spatial localization of a mineral deposit is seldom deterministic and therefore it is difficult to define all model variables that describe the phenomenon completely and adequately. Moreover, information on some of the variables may be derived from a subjective interpretation of primary data (for example, remote sensing or geophysical data), a process that is essen-

tially based on heuristics and expert-knowledge. This gives rise to systemic uncertainty, which is non-statistical and intrinsically associated with modeling procedures. Unlike stochastic uncertainty, it is not data-dependent and hence cannot be addressed using probabilistic approaches. Systemic uncertainty is best treated using the theory of fuzzy sets and fuzzy mathematics (Zadeh, 1965; Zimmerman, 1991). Fuzzy models have been widely used for dealing with systemic uncertainty in mineral potential mapping by applying appropriate fuzzy membership functions and inference engines (Porwal *et al.*, 2003a).

Cheng and Agterberg (1999) proposed a new fuzzy weights-of-evidence approach, which generalizes the classic weights-of-evidence approach by incorporating fuzzy mathematics in the modeling procedure. The method involves (a) creating a fuzzy set of 'favorable indicators of the target mineral deposit-type' for each predictor map, (b) defining a knowledge-based or data-based membership function to calculate a fuzzy membership value for each pattern on a predictor map in a corresponding fuzzy set, (c) calculating a fuzzy weight of evidence for each pattern on a predictor map, (d) combining the fuzzy weights of evidence to calculate, for each unique combination of predictor patterns, a fuzzy posterior probability and the variance of the fuzzy posterior probability due to missing patterns, mis-assigned patterns and fuzzy membership function, and (e) mapping the fuzzy posterior probabilities to generate a fuzzy posterior probability map. The fuzzy posterior probability map can be subsequently reclassified to generate a binary or ternary favorability map. The fuzzy weights-of-evidence approach is particularly suitable for provinces with meagre exploration data or very few known mineral deposits.

The fuzzy weights-of-evidence approach can be either (Cheng and Agterberg, 1999) (a) purely data-driven, when a data-based function is used for calculating fuzzy membership values or (b) hybrid knowledge-cum-data-driven, when a knowledge-based function is used for calculating fuzzy membership values. In both the forms, multi-class predictor maps can be used without generalization and reclassification into binary predictor maps. Cheng and Agterberg (1999) applied the fuzzy weights-of-evidence method in a purely data-driven form to map gold deposit potential in Meguma Terrane, Nova Scotia, Canada. Here, a hybrid knowledge-cum-data-driven weights-of-evidence approach is demonstrated.

5.2 Hybrid Fuzzy Weights-of-Evidence Model

If X is a superset of n multi-class conditionally independent predictor maps X_i (i=1 to n), each containing m patterns denoted generically by x_{ij} (j=1 to m), then the strength of x_{ij}, the jth pattern on the ith predictor map X_i, as an indicator of a target mineral deposit-type D can be estimated in terms of class score (cs_{ij}), which is defined as follows (Porwal et $al.$, 2003a):

$$cs_{ij} = w_i \times w_{ij} \quad (\forall \ x_{ij} \in X_i), \tag{5.1}$$

where w_i is the map weight of the ith predictor map and w_{ij} is the class weight of the jth pattern on the ith predictor map. The procedure for assigning class weights and map weights is described by Porwal et $al.$, (2003a) and given in Chapter 3 (p. 69).

Based on class scores, a set of n fuzzy sets $\tilde{A}_i$ (i=1 to n) in X, containing 'favorable indicators of target mineral deposit-type,' can be defined as follows (Porwal et $al.$, 2003a):

$$\tilde{A}_i = \left\{ \left(x_{ij}, \mu_{\tilde{A}_i}(x_{ij}) \right) \forall x_{ij} \in X_i \right\}, \tag{5.2}$$

where $\mu_{\tilde{A}_i}$ is the membership function for estimating the membership value of x_{ij} in the fuzzy set $\tilde{A}^1$. It is defined as follows (Porwal et $al.$, 2003a):

$$\mu_{\tilde{A}_i}(x_{ij}) = \frac{1}{1 + e^{-a(cs_{ij}-b)}}(\forall x_{ij} \in X_i), \tag{5.3}$$

where a and b are the parameters that, respectively, define the slope and the inflexion point of the Gaussian function.

Cheng and Agterberg (1999) proposed the following fuzzy weights-of-evidence model for deriving fuzzy posterior probability of the deposit type D, given n predictor maps X_i and n corresponding fuzzy sets as defined above in Equation 5.2:

$$log_e O[D|X_1, X_2...X_n] = log_e O[D] + \sum_{i=1}^{n} \sum_{j=1}^{m} W_{\mu_{\tilde{A}_i}(x_{ij})}, \tag{5.4}$$

where $W_{\mu_{\tilde{A}_i}(x_{ij})}$ is the fuzzy weight of evidence of the jth pattern on the ith predictor map, and is calculated using the following relation (Cheng and Agter-

berg, 1999):

$$W_{\mu_{\tilde{A}_i(x_{ij})}} = log_e \frac{\mu_{\tilde{A}_i}(x_{ij})P[A_{i1}|D] + \{1 - \mu_{\tilde{A}_i}(x_{ij})\}P[A_{i2}|D]}{\mu_{\tilde{A}_i}(x_{ij})P[A_{i1}|\bar{D}] + \{1 - \mu_{\tilde{A}_i}(x_{ij})\}P[A_{i2}|\bar{D}]}, \tag{5.5}$$

where $P[A_{i1}|D]$ and $P[A_{i2}|D]$ are the conditional probabilities of two crisp sets A_{i1} and A_{i2}, respectively, given the presence of a deposit, and $P[A_{i1}|\bar{D}]$ and $P[A_{i2}|\bar{D}]$ are the conditional probabilities of the two crisp sets A_{i1} and A_{i2}, respectively, given the absence of a deposit. The two crisp sets A_{i1} and A_{i2} (i=1 to n) in the fuzzy sets $\tilde{A}_i$ are defined as follows (Cheng and Agterberg, 1999):

$$A_{i1} = \{x_{ij}|\mu_{\tilde{A}_i}(x_{ij}) = MAX[\mu_{\tilde{A}_i}(x_{ij})]\forall x_{ij} \in X_i\},$$
$$A_{i2} = \{x_j|\mu_{\tilde{A}_i}(x_{ij}) = MIN[\mu_{\tilde{A}_i}(x_{ij})]\forall x_{ij} \in X_i\}. \tag{5.6}$$

Fuzzy posterior probability can then be calculated as (Cheng and Agterberg, 1999):

$$P[D|X_1, X_2...X_n] = \frac{e^{log_e O[D|X_1,X_2...X_n]}}{1 + e^{log_e O[D|X_1,X_2...X_n]}}. \tag{5.7}$$

The variance of fuzzy posterior probability due to the jth missing pattern x_{kj} on the kth predictor map X_k is estimated as follows (Cheng and Agterberg, 1999):

$$\sigma_{x_{kj}}^2(P[D|X_1, X_2...X_n]) =$$
$$\{P[D|x_{kj}] - P[D]\}^2 P[x_{kj}] + \{P[D|\bar{x}_{kj}] - P[D]\}^2 P[\bar{x}_{kj}], \tag{5.8}$$

where $\bar{x}_{kj}$ denotes the absence of the predictor pattern x_{kj}. For a predictor map X_l, the variance due to the mis-assigned pattern from x_{lj} to $\bar{x}_{lj}$ or vice versa is estimated as follows (Cheng and Agterberg, 1999):

$$\sigma_{x_{lj}}^2(P[D|X_1, X_2...X_n]) = \{P[D|\bar{x}_{lj}] - P[D|x_{lj}]\}^2 P[x_{lj}],$$
$$\sigma_{\bar{x}_{lj}}^2(P[D|X_1, X_2...X_n]) = \{P[D|x_{lj}] - P[D|\bar{x}_{lj}]\}^2 P[\bar{x}_{lj}], \tag{5.9}$$

where $\bar{x}_{lj}$ denotes the absence of the predictor pattern x_{lj}. The variance due to the fuzzy membership function, $\mu_{\tilde{A}_i}$, is expressed as (Cheng and Agterberg,

1999):

$$\sigma^2_{\mu_{\tilde{A}_i}}\left(P[D|X_1, X_2...X_n]\right) =$$

$$\frac{2\mu_{\tilde{A}_i}(1 - \mu_{\tilde{A}_i})}{P[\mu_{\tilde{A}_i}]} P[X_i]P[\bar{X}_i]\left\{\sigma^2_{X_i}(P[D|X_1, X_2...X_n]) + \sigma^2_{\bar{X}_i}(P[D|X_1, X_2...X_n])\right\}.$$

$$(5.10)$$

5.3 Application to Base-Metal Potential Mapping in Aravalli Province

5.3.1 Data preprocessing

Like the classic weights-of-evidence approach, the fuzzy weights-of-evidence approach also uses Bayes' rule under an assumption of conditional independence of input predictor maps for estimating fuzzy posterior probabilities. Because the results of various tests for goodness of fit between the observed and expected distribution of base-metal deposits in the study area and the map-pair wise χ^2 test for conditional independence, which have been described in Chapter 4 (pp. 114-118), indicate conditional dependence between the map pairs of (a) sedimentary environments and stratigraphic groups and (b) sedimentary environments and lithologies, it was decided not to include the map of sedimentary environments in the fuzzy weights-of-evidence analysis. However, because a fuzzy weights-of-evidence model uses both expert knowledge and exploration datasets for parameter estimation, it can be conveniently used with multi-class predictor maps, as discussed in Section 5.4 below. It was therefore decided to use all the remaining predictor maps, including the maps of buffer distances, in their original multi-class form.

Training and validation points. The fuzzy weights-of-evidence approach combines expert knowledge with empirical data and, hence, it can be effectively implemented in modeling situations where there are only a few training points available. Therefore, it was decided to use the same sets of training points and validation points that were used in fuzzy modeling (Chapter 3, p. 75).

5.3.2 Fuzzy weights-of-evidence modeling

Computation of fuzzy weights of evidence

For each pattern on a multi-class predictor map, the computation of a fuzzy weight of evidence requires (Equation 5.5) (a) a fuzzy membership value and (b) the conditional probabilities (given the presence and the absence of a base-metal deposit) of the patterns with the highest and lowest fuzzy membership values. Fuzzy membership values of the predictor maps were calculated using the membership function defined in Equation 5.3. The values of the parameters b and a of the function were taken as 50 and 0.1, respectively, which yield a curve that is symmetrical about the inflexion point. The class scores were calculated from class weights and map weights (Equation 5.1), which were assigned subjectively using the ranking procedure described by Porwal *et al.* (2003a) and given in Chapter 3 (p. 69). The detailed rationale for the ranking of the predictor maps and individual patterns has been elaborated by Porwal *et al.* (2003a) and can also be found in Chapter 3 (pp. 75-79).

The conditional probabilities of each individual pattern on a predictor map, given the presence and absence of a base-metal deposit, were also calculated. The class weights, map weights, class scores, knowledge-driven fuzzy membership values and conditional probabilities for the predictor maps are given in Table 5.1. Based on the fuzzy membership values and the conditional probabilities, fuzzy weights of evidence were calculated using Equations 5.5 and 5.6. The computations were performed using the gridded predictor maps taking 1 km^2 as the unit cell size. The fuzzy weights of evidence are also given in Table 5.1.

Combining predictor maps

The gridded multi-class predictor maps were combined using digital overlay, which resulted in a unique condition grid map containing 20258 unique conditions. The fuzzy posterior probability for each unique condition was estimated from the fuzzy weights of evidence and the prior probability of base-metal deposits (Equations 5.4 and 5.5). Similarly, the variance of fuzzy posterior probability due to missing patterns, mis-assigned patterns and fuzzy membership function were calculated using Equations 5.8, 5.9 and 5.10, respectively. The spatial distribution of fuzzy posterior probabilities is shown in Fig. 5.1. The spatial distributions of variance due to fuzzy membership function and vari-

Table 5.1: Class scores, fuzzy membership values and fuzzy weights of evidence

Predictor map Pattern (X_{ij})	Class weight (w_j)	Class score (x_{ij})	Fuzzy value $(\mu_{\tilde{A}_{ij}})$	Conditional probability $P[X_i|D]$	Conditional probability $P[X|\bar{D}]$	Fuzzy WofE
Predictor map of lithologies (Map weight - 10)						
1 Dolomite/dolomitic-marble	10	100	0.99	0.1739	0.022	1.8265
2 Calc-silicates	9	90	0.98	0.3043	0.0118	1.6288
3 Graphitic meta-pelites	8	80	0.95	0.3043	0.0096	1.1837
4 Magnetite quartzite	7	70	0.88	0.2174	0.0002	0.5244
5 Calc-schist/gneiss	5	50	0.5	0	0.0467	-1.264
6 Qzite-Arkose-Conglomerate	4	40	0.27	0	0.0839	-2.236
7 Migmatites; gneisses	2	20	0.05	0	0.2092	-4.174
8 Unrelated to base metals	1	10	0.02	0	0.5935	-5.12
Predictor map of stratigraphic groups (Map weight - 9)						
1 Rajpura-Dariba group	10	90	0.98	0.2609	0.0044	3.0684
2 Pur-Banera group	9	81	0.96	0.5217	0.0117	2.5593
3 Debari group	8	72	0.09	0.087	0.0545	1.7249
4 Nathdwara group	7	63	0.79	0	0.0036	0.9093
5 Udaipur group	5	45	0.38	0.087	0.0961	-0.87
6 Jharol group	4	36	0.20	0	0.1528	-1.762
7 Sandmata Complex	3	27	0.09	0.0435	0.1005	-2.688
8 Mangalwar Complex	2	18	0.04	0	0.1925	-3.551
9 Unrelated to base metals	1	9	0.02	0	0.3738	-4.265
Predictor map of mafic igneous rocks (Map weight - 8)						
1 Basic metavolcanic rocks	10	80	0.95	0.7391	0.1265	1.4737
2 Unrelated to base metals	1	8	0.01	0.2609	0.8731	-1.181
Predictor map of buffered distances from regional lineaments (Map weight - 8)						
1 0-2 Km	10	80	0.9526	0.2609	0.1897	0.2455
2 2-4 Km	8	64	0.8022	0.4348	0.1633	0.008
3 4-6 Km	6	48	0.4502	0.2174	0.1336	-0.622
4 6-8 Km	4	32	0.1419	0.0435	0.1066	-1.41
5 8-10 Km	2	16	0.0323	0	0.083	-1.843
6 >10 Km	1	8	0.0148	0.0435	0.3235	-1.929
Predictor map of buffered distances from NW-trending lineaments (Map weight - 6)						
1 0-1.5 Km	10	60	0.7311	0.4783	0.243	0.3142
2 1.5-3 Km	8	48	0.4502	0.2609	0.1822	-0.178
3 3-4.5 Km	6	36	0.1978	0.1739	0.1169	-0.858
4 4.5-6 km	4	24	0.0691	0	0.0793	-1.456
5 6-7.5 Km	2	12	0.0219	0.0435	0.0574	-1.795
6 >7.5 Km	1	6	0.0121	0.0435	0.3209	-1.881
Predictor map of buffered distances from NE-trending lineaments (Map weight - 6)						
1 0-1.5 Km	10	60	0.7311	0.3913	0.189	0.3257
2 1.5-3 Km	8	48	0.4502	0.2609	0.1678	-0.147
3 3-4.5 Km	6	36	0.1978	0.1304	0.136	-0.684
4 4.5-6 Km	4	24	0.0691	0.087	0.1056	-1.049
5 6-7.5 Km	2	12	0.0219	0.0435	0.0841	-1.211
6 >7.5 Km	1	6	0.0121	0.087	0.3171	-1.247

Table 5.1 contd.

	Predictor map Pattern (X_{ij})	Class weight (w_j)	Class score (x_{ij})	Fuzzy value $(\mu_{\tilde{A}_{ij}})$	Conditional probability $P[X_i|D]$	Conditional probability $P[X|\bar{D}]$	Fuzzy WofE
Predictor map of buffered distances from fold axes (Map weight - 7)						
1	0-0.5 Km	10	70	0.8808	0.6957	0.1128	1.7741
2	0.5-1 Km	9	63	0.7858	0.1739	0.1026	1.7303
3	1-1.5 Km	8	56	0.6457	0.0435	0.0908	1.6476
4	1.5-2 Km	7	49	0.475	0	0.0787	1.4992
5	2-2.5 Km	6	42	0.31	0	0.0699	1.2542
6	2.5-3 Km	5	35	0.1824	0	0.061	0.8911
7	3-3.5 Km	4	28	0.0998	0	0.0523	0.4135
8	3.5-4 Km	3	21	0.0522	0	0.0466	-0.154
9	4-4.5 Km	2	14	0.0266	0	0.0415	-0.783
10	4.5-5 Km	1	7	0.0134	0	0.0385	-1.444
11	>5 Km	1	7	0.0134	0.087	0.3051	-1.444

ance due to missing patterns and mis-assigned patterns are shown in Fig. 5.2. A comparison of Figs. 5.2A and Fig. 5.2B shows that, in all parts of the study area, the uncertainty in fuzzy posterior probabilities due to fuzzy membership function is much smaller than the uncertainty in fuzzy posterior probabilities due to missing patterns and mis-assigned patterns.

5.3.3 Favorability maps

It is cumbersome to interpret the fuzzy posterior probability map (Fig. 5.1) for selecting target areas for base-metal exploration, as it shows the fuzzy posterior probability of base-metal deposits in a continuous scale from the least probable (fuzzy posterior probability ~ 0) to the most probable (fuzzy posterior probability ~ 0.5). Moreover, a fuzzy posterior probability should not be interpreted in the absolute sense of probability *per se* (see below). The fuzzy posterior probability map (Fig. 5.1) was therefore reclassified into a ternary favorability map showing high favorability, moderate favorability and low favorability zones for base-metal deposits in the study area. The threshold fuzzy posterior probability values for the high favorability and low favorability zones were determined using the graphical method used by Porwal *et al.* (2003b) and described in Chapter 4 (pp. 119-**??**). The fuzzy posterior probabilities corresponding to the lower and the upper inflection points (0.0016 and 0.0002, respectively) in the plot of the cumulative fuzzy posterior probability values (rearranged in a descending order) against the percentage of cumulative area (Fig. 5.3) were taken as the threshold values for the reclassification of the fuzzy posterior probability map into a ternary favorability map (Fig. 5.4).
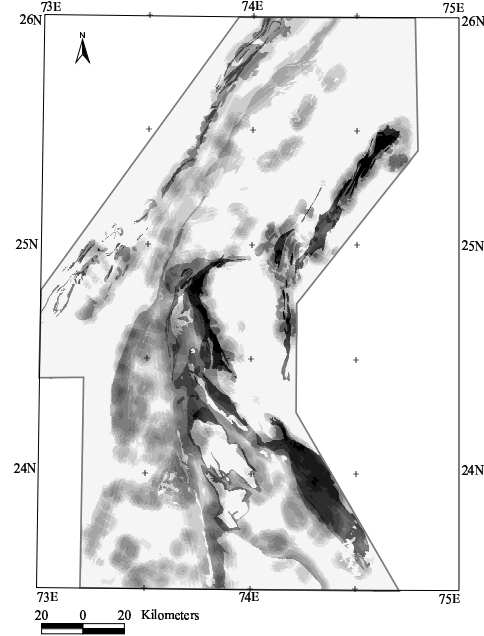
Figure 5.1: Continuous-scale map showing fuzzy posterior probability, which varies from 0.00 (white) to 0.48 (black).

Validation of favorability map

The favorability map (Fig. 5.4) was validated by overlaying the deposit training points and deposit validation points and by plotting the position of these deposits on a fuzzy posterior probability values versus percentage of cumulative area curve (Fig. 5.5). Table 5.2 shows that in the favorability map (a) the high favorability zones occupy 5.9% of the study area and contain 75% and 96.7% of the deposit validation points and deposit training points, respectively, (b) the moderate favorability zones occupy 4.3% of the study area and contain 12.5% of the deposit validation points and no deposit training points and (c) the low favorability zones occupy 89.7% of the study area and contain 12.5% and 3.3% of the deposit validation points and deposit training points, respectively.

Table 5.2: Validation of Favorability map

Favorability zone	Percent of study area	Percent of Validation deposits	Percent of Training deposits
High favorability	5.9	75.1	96.7
Moderate favorability	4.3	12.5	Nil
Low favorability	89.8	12.5	3.3
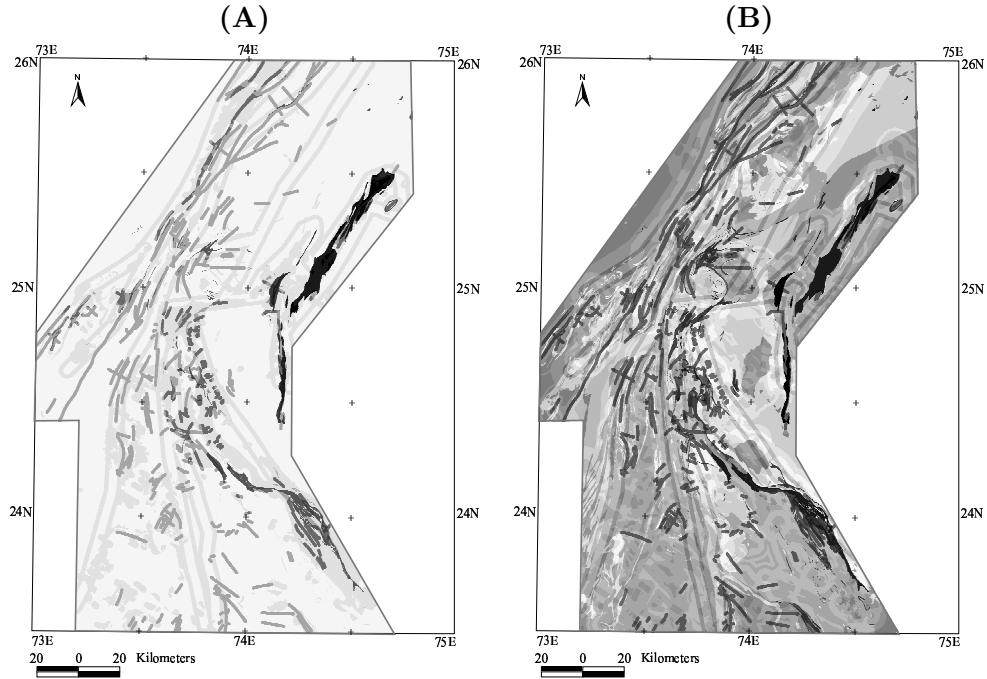
Figure 5.2: Continuous-scale maps showing (A) variance in fuzzy posterior probability due to fuzzy membership function, which varies from 0.0000 (white) to 0.0001 (black) and (B) variance in fuzzy posterior probability due to missing and mis-assigned patterns, which varies from 0.0000 (white) to 0.2148 (black).

5.4 Discussion

Systemic uncertainties in mathematical geological models for mineral potential mapping generally arise from (a) imprecision in mapping of predictor patterns, (b) involvement of heuristics in generation of one or more predictor patterns (for example, several predictor patterns the present application were based on interpretations of total magnetic field intensity data) and (c) unknown contribution of different genetic factors, and hence of predictor patterns which represent them, in spatial localization of mineral deposits. Unlike stochastic uncertainties, they are not data-dependent and hence cannot be addressed using probabilistic approaches. Systemic uncertainties are best treated using the theory of fuzzy sets and fuzzy mathematics (Zadeh, 1965; Zimmerman, 1991). The knowledge-based logistic function (Equation 5.3) used in the hybrid fuzzy weights-of-evidence model provides a framework for dealing with systemic uncertainties in a flexible and consistent way. The function uses map weights and

142
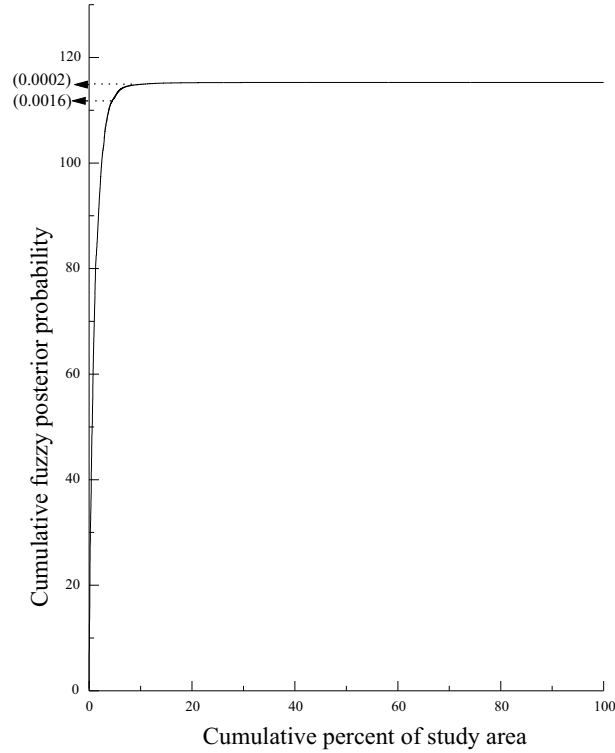
Figure 5.3: Variation of cumulative posterior probability with cumulative percent of study area.

class weights to derive fuzzy membership values of predictor patterns (Equations 5.2 and 5.3). Map weight, which is very similar in concept to 'confidence value' (Knox-Robinson, 2000), is assigned on the basis of (a) the fidelity and precision of a predictor map and (b) the relative importance of the recognition criteria represented by a predictor map.

The S-shaped logistic membership function transforms linearly-distributed class scores to logistically-distributed fuzzy membership values, so that the differences in fuzzy membership values are much larger in the central part of the curve than along its tails, as illustrated by Porwal *et al.* (2003a) and discussed in Chapter 3. The function therefore provides adequate quantitative differentiation between unfavorable patterns and favorable patterns, although amongst favorable (and unfavorable) patterns, the differentiation is not so well defined. In spatial domain, this results in a well-defined distinction between high favorability zones and low favorability zones.

Cheng and Agterberg (1999) used a linear fuzzy membership function based
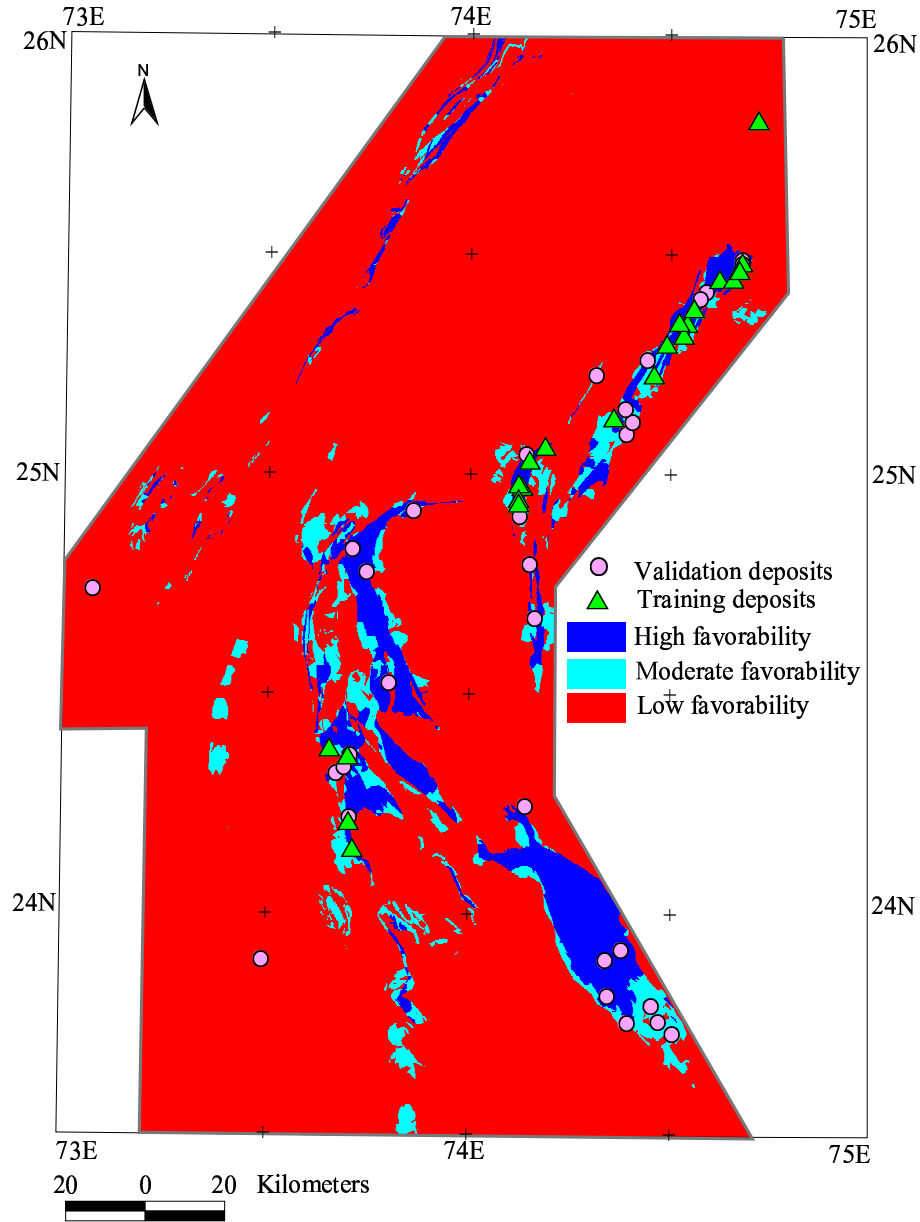
Figure 5.4: Favorability map generated by reclassification of fuzzy posterior probability map shown in Fig. 5.1.
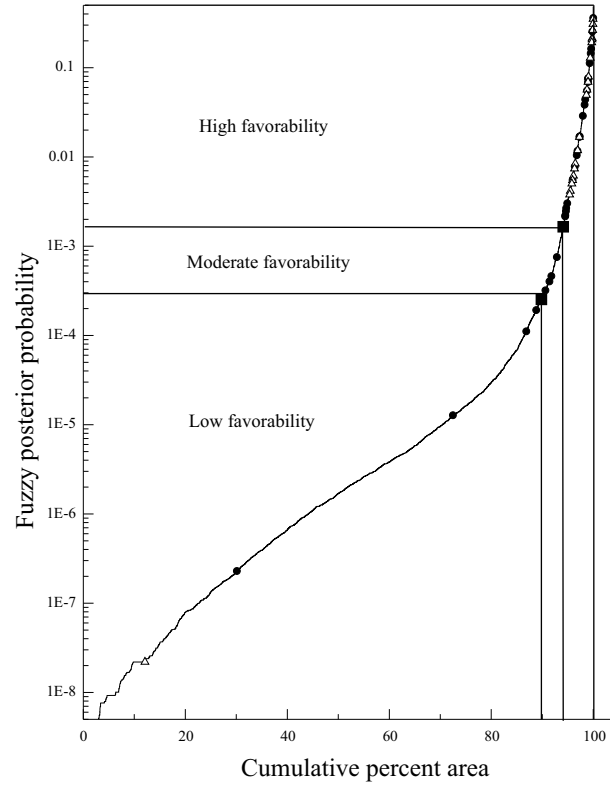
Figure 5.5: Variation of fuzzy posterior probability with cumulative percent of study area. Triangles are training base-metal deposits and circles are validation base-metal deposits.

on contrast (Bonham-Carter and Agterberg, 1990). The use of contrast for calculating fuzzy membership values incorporates a purely data-driven approach in the modeling procedure. However, it is suitable for multi-class predictor maps only if each pattern contains at least one known deposit, because contrast values $(W^+ - W^-)$ are calculated from weights of evidence and, if a pattern does not contain any training point, its weights of evidence and, therefore, contrast cannot be determined (see below). The knowledge-based logistic function (Equation 5.3), on the other hand, can be applied to derive fuzzy membership even if there are one or more patterns in a multi-class predictor map that do not contain any known deposits.

As discussed in Chapter 4, the weights of evidence for the predictor pattern x_i are calculated from the conditional probabilities of the pattern, given the absence and presence of a deposit, using the following equations (Agterberg,

145

1989; Agterberg *et al.*, 1990; Bonham-Carter and Agterberg, 1990):

$$W_j^+ = log\frac{p(x_i|D)}{p(x_i|\bar{D})},$$
$$W_j^- = log\frac{p(\bar{x}_i|D)}{p(\bar{x}_i|\bar{D})}. \qquad (5.11)$$

It follows from the above equations that a positive weights of evidence can be calculated for a predictor pattern, if, and only if, it contains at least one known deposit (as $log(0)$ is mathematically invalid and hence indeterminable). Classic weights-of-evidence models are therefore generally used with binary predictor maps. These models have been used with multi-class predictor maps also (Chapter 4 and references therein), but in such cases the weights of evidence are determinable only for the patterns that contain at least one known deposit (although it is possible to extrapolate the weights of evidence of the patterns that do not contain any known deposits from weights-of-evidence models of well-explored areas worldwide, as suggested by Singer and Kouda, 1999). On the other hand, the calculation of fuzzy weights of evidence (Equations 5.5 and 5.6) for all patterns in a predictor map requires the conditional probabilities of only the patterns with the highest and the lowest fuzzy membership values, given the presence and absence of a deposit. The fuzzy weights of evidence are therefore indeterminable if, and only if, neither the pattern with the highest fuzzy membership value nor the pattern with the lowest fuzzy membership value contains any known deposit, which can happen rarely. At the least, the pattern with the highest fuzzy membership value will always contain at least one known deposit. Consequently, fuzzy weights of evidence models are more conveniently used with multi-class predictor maps, even if there are very few known deposits available. For the same reason, the fuzzy weights-of-evidence can be effectively used for mineral potential mapping in poorly-explored provinces containing very few known mineral deposits.

The fuzzy weights-of-evidence model (Equation 5.4) uses a modified Bayes' rule (Cheng and Agterberg, 1999) under an assumption of conditional independence for combining fuzzy weights-of-evidence to derive fuzzy posterior probability. The linear nature of the model entails that fuzzy posterior probability is highly sensitive to the violation of the assumption of conditional independence amongst two or more predictor maps. As discussed by Singer and Kouda (1999), the assumption of conditional independence is often difficult to validate using a pair-wise χ^2 test. Even if Kolmogorov-Smirnov and χ^2

tests for goodness-of-fit return a statistically-significant goodness of fit between observed and expected frequencies of deposits, the omnibus (Bonham-Carter, 1994) and/or new omnibus (Agterberg and Cheng, 2002) tests for conditional independence may indicate conditional dependence between some of the input predictor patterns (Porwal *et al.*, 2003b; *see also* Chapter 4, pp. 114-119). In practice, it is often difficult to rule out the possibility of conditional dependence amongst two or more predictor patterns. In such cases, fuzzy posterior probabilities calculated using the modified Bayes' rule may be artificially inflated (in the case of favorable conditionally-dependent patterns) or deflated (in the case of unfavorable conditionally-dependent patterns) and hence cannot be interpreted in an absolute sense for decision-making. Moreover, a fuzzy posterior probability is an updated prior probability of a deposit-type, given the presence of a number of input predictor patterns, and can be accepted in an absolute sense, if, and only if, it is assumed that the input predictor patterns adequately represent all geologic processes that were responsible for the spatial localization of the deposit-type. Such an assumption may not justified in practice. In addition, there is always an uncertainty (due to missing patterns, mis-assigned patterns and fuzzy membership function) associated with fuzzy posterior probability values. However, the effect of overestimation and/or underestimation of fuzzy posterior probability can be considerably mitigated if the exploration targets are selected on the basis of relative favorability rather than absolute fuzzy posterior probabilities, as suggested by Pan and Harris (2000) for the ordinary weights-of-evidence approach. Therefore, the fuzzy posterior probabilities were interpreted to rank areas in terms of relative favorability with respect to base-metal deposits.

A comparison of uncertainty due to fuzzy membership function (Fig. 5.2A) and uncertainty due to missing and mis-assigned patterns (Fig. 5.2B) shows that the former is much lower in all parts of the study area, which indicates that if the 'missing pattern' areas are assigned appropriate fuzzy membership values then the total uncertainty in fuzzy posterior probabilities can be reduced, as suggested by Cheng and Agterberg (1999).

5.5 Conclusions

The fuzzy weights-of-evidence model predicts high favorability zones that occupy 6% of the study area, which contain 75% of the validation base-metal deposits. This result compares well with the result of the extended weights-of-

147

evidence model described in Chapter 4, although a smaller number of training points was used in the fuzzy weights-of-evidence model. The following conclusions are drawn from the application of the hybrid fuzzy weights-of-evidence procedure to the study area.

- The use of a knowledge-driven membership function in the fuzzy weights-of-evidence approach allows the treatment of systemic uncertainties in mineral potential mapping in a flexible and consistent way.

- The knowledge-based logistic membership function used in this application results in a well-defined distinction between favorable zones and unfavorable zones.

- Multi-class predictor maps can be more conveniently used in hybrid fuzzy weights-of-evidence models.

- A fuzzy weights-of-evidence model can be effectively implemented with fewer training points, which indicates its effectiveness in less-explored areas.

- In practice, it may not be always possible to rule out conditional dependence amongst two or more of the input predictor maps. As a result the estimated fuzzy posterior probabilities may be artificially deflated or inflated. In such cases, these values can be used in relative terms to rank areas in terms of favorability with respect to the target deposit-type.

The hybrid fuzzy weights-of-evidence and weights-of-evidence models described, respectively, in this and the previous chapter, assume a (log-)linear relationship between predictor maps and the target mineral deposit-type, and, therefore, use a simplified version of Bayesian equation under an assumption of conditional independence of predictor maps to approximate this relationship. The parameters of the function, namely, the prior probability and a conditional probability for each independent variable, are estimated from exploration data sets in weights-of-evidence models and from a combination of expert knowledge and exploration data sets in hybrid fuzzy weights-of-evidence models. However, given the complexity of earth systems that result in the formation of mineral deposits, linear functions may not adequately approximate the relation between predictor maps and the target mineral deposit-type. The fuzzy models described in Chapter 3 use non-linear fuzzy mathematics to approximate such a relationship. In these models, the parameters of various functions, namely,

the slope and inflexion of the gaussian function, the slope of the piece-wise linear function and the γ operator in the fuzzy aggregation operations, are estimated heuristically. Heuristic estimation of function parameters, however, may compound systemic uncertainty in a model. The next chapter describes an artificial neural network model that uses a series of non-linear radial basis functions to approximate the relationship between geological processes and mineral deposits. The parameters of the neural network are estimated algorithmically from the exploration data sets using a fullpropagation algorithm.

Chapter 6

Artificial Neural Network Model

This chapter describes a radial basis functional link net (RBFLN), which is an artificial neural network based on radial basis functions, and demonstrates its application to base-metal potential mapping in the study area.

The chapter has been published as "Artificial Neural Networks for Mineral Potential Mapping: A Case Study from Aravalli Province, Western India" (Porwal *et al.*, 2003c).

6.1 Introduction

Artificial neural networks (or neural networks) imitate human cognition in deriving knowledge inductively by learning on samples of training data and using it for generalization beyond the training data. Their architecture comprises a number of interconnected computational layers of neural units called neurons, which are essentially mathematical functions that map each sample of input feature vector in a training data set to its output target vector. The mapping is controlled by inter-neuron connection strengths known as *synaptic weights* (Haykin, 1994), which are dynamically modified until each input feature vector is mapped correctly to its known output target vector. Synaptic weights are therefore repositories of knowledge, which is used by a trained neural network for generalization beyond training data (Haykin, 1994).

Linear mathematical methods, despite of their well-known optimization techniques, can not be appropriately applied to model complex and vague patterns. On the other hand, neural networks, owing to their non-linear nature,

provide techniques for modeling complex real-world situations. Neural networks are good pattern recognition engines and robust classifiers, with the ability to generalize on the basis of imprecise input data. They offer ideal solutions to a variety of classification problems such as in speech, character, signal and pattern recognition (e.g., Waibel and Lee, 1990; LeCun *et al.*, 1990a; Guyon, 1991; Sackinger *et al.*, 1992; Zuqiang Zhao, 1992; Tsopanoglou and Mourjopoulos, 1994; Augusteijn and McCarthy, 1995; Bishop, 1995; Torkkola and Kohonen, 1995; Bennani, 1999; Kapusta and Gajer, 2000; Mitiche and Lebidoff, 2001). They can also be used for predictive modeling of complex natural phenomena due to physical processes that are not directly observable and therefore are ill-defined. For example, the formation and localization of mineral deposits are the end-result of a complex interplay of several earth processes that leave behind their signatures in form of geologic features associated with the mineral deposits. These geological features are characterized by their responses in one or more spatial geodata sets that are used as predictor maps in quantitative mineral potential mapping. The relationship between predictor maps and mineral deposits appears to be far too complex to be modeled adequately by using linear approximations. Probabilistic and regression approaches have been traditionally used to model this relationship for predictive mineral potential mapping (*see* Chapter 4 for references). However, the application of neural networks to predictive mineral potential mapping provides a robust non-linear alternative to these approaches.

6.1.1   Previous work

In a seminal work, Singer and Kouda (1996) used a three-layer feed-forward neural network with a single hidden layer of neurons to estimate distances to the nearest Kuroko-type base-metal deposit in the Hokuroku district, northern Japan. The input layer consisted of three variables derived from drill-hole data. The hidden layer comprised five neurons, each of which employed a hyperbolic tangent activation function. The output layer contained the distance to base-metal deposits. The neural network was trained on data from a subset of bore holes using the algorithm of annealing plus conjugate gradients described by Masters (1993). The synaptic weights were dynamically adjusted until the mean squared error of scaled distance to base-metal deposits was minimized. The trained neural network was validated by applying to data from all drill holes. It succeeded in identifying all of the known deposits in the study area.

Singer and Kouda (1997a) examined the capability of a probabilistic neural

network based on Parzen density estimation (Parzen, 1962) to classify mineral deposits into types based on the presence or absence of certain minerals. The probabilistic neural network was trained on a subset of deposits; the remaining deposits were used for validation only. The output, for each deposit, was one of several pre-defined deposit classes. The trained probabilistic neural network correctly classified 97% of the training deposits and 88% of the validation deposits.

Singer and Kouda (1997b) investigated the use of a similar probabilistic neural network for integrating information available in large mineral databases to classify sites by deposit-types. Using the algorithms developed by Masters (1995), they trained a probabilistic neural network on a number of reported ore and alteration minerals and generalized rock types from a large number of deposits. The output, for each deposit, was one of several well-typed deposit classes. The trained probabilistic neural network was validated by comparison of the probabilistic neural network's classification of a number of deposits from Nevada (USA) with that of experts. The authors report an overall 53% agreement between the probabilistic neural network and the experts, which is lower than the success rate reported by Singer and Kouda (1997a). These results reflect effects of sparse information available in mineral occurrence data compared to the well-studied deposit data use for training. However, based on a comparison of the spatial distribution of deposit classes estimated by probabilistic neural network and permissive tracts identified by experts, they concluded that the probabilistic neural network can be efficient in identifying terranes permissive for grouped deposit classes in over 95% of the cases.

Singer and Kouda (1999) demonstrated the superior performance of probabilistic neural networks as compared to the weights-of-evidence method in classification of locations as mineral deposits or non-deposits with data from Chisel Lake-Anderson Lake, Manitoba, Canada. On the basis of an analysis of the two approaches, they also concluded that the posterior probabilities produced by weights-of-evidence method are biased upwards and therefore probabilistic neural networks should be considered where unbiased estimates are required.

Harris and Pan (1999) demonstrated the application of a predictive probabilistic neural network for mapping gold potential in a well-explored control area and compared its performance with some traditional multivariate statistical techniques. They described each quadrat in the control area by the presence or absence of gold mineralization and measurements on eight geological variables, and trained a probabilistic neural network using the geological variables

153

of a small subset of the control quadrats. The output value, for each quadrat, was either 1 (mineralized) or 0 (barren). They used the trained probabilistic neural network to process all control quadrats and evaluated its performance by the extent to which all the quadrats were correctly classified as mineralized or barren with respect to gold. The trained probabilistic neural network correctly classified approximately 90% of all the quadrats in the control area. Significantly, the authors reported a higher percentage of correct classification of the control quadrats achieved by the probabilistic neural network than by traditional multivariate statistical techniques like logistic regression and discriminant analysis.

Brown *et al.* (2000) used a multilayer perceptron neural network to estimate the favorability for gold deposits in the Tenterfield area, New South Wales (Australia). They trained a series of multilayer perceptron neural networks with different sets of random initial weights using a gradient-descent back-propagation algorithm and selected the network that gave the best classification performance for an independent set of validation samples. Based on a comparison of several statistical measures of the prospectivity maps derived using the multilayer perceptron neural network, weights-of-evidence analysis and fuzzy logic, the authors concluded that the multilayer perceptron neural network out-performs, or at least matches the performance of the other two methods of mineral prospectivity mapping.

In order to address the problem of paucity of deposit samples in neural network applications to mineral potential mapping, Brown *et al.* (2003) experimented by training a multilayer perceptron neural network on a synthetic training dataset, which was generated by adding random noise to the original training dataset. Their experiments for gold potential mapping in the Kalgoorlie Terrane orogenic gold province show that the classification performance of a trained multilayer perceptron and the quality of the resultant favorability map increase significantly with increased numbers of deposit patterns.

Singer and Kouda (2003) tested the ability of a probabilistic neural network to classify deposits into types on the basis of deposit tonnage and average Cu, Mo, Ag, Au, Zn, and Pb grades in order to examine whether this type of system might serve as a basis for integrating geoscience information available in large mineral databases to classify sites by deposit type. Total tonnages and average grades of 1,137 well-explored deposits identified in published grade and tonnage models representing 13 deposit types were used to train and test the network. Tests were performed with a probabilistic neural network employ-

154

ing a Gaussian kernel and separate sigma weights for each class (type) and each variable (grade or tonnage). Deposit types were selected to challenge the neural network. The authors report an overall 75% agreement between the experts and the neural network, which is quite significant given the difficult test conditions. In a separate test, the probabilistic neural network correctly classed 93% of 336 deposits in eight deposit types when trained with presence or absence of 58 minerals and six generalized rock types. The authors conclude that the overall success rate of the probabilistic neural network when trained on tonnage and average grades would probably be more than 90% with additional information on the presence of a few rock types.

Bougrain *et al.* (2003) used artificial neural networks for continental-scale mineral potential mapping. They identified 25 attributes as known factors or potential factors controlling the formation of gold deposits in the Andes Cordillera and applied various multilayer perceptrons to discriminate possible mineralized sites from barren sites. They also used the optimal brain damage algorithm by LeCun *et al.* (1990b) to order the 25 attributes by their relevance to the classification. Their work demonstrates that neural networks can be used efficiently in continental-scale mineral potential mapping.

6.2 Radial Basis Functional Link Net

A radial basis function centered on an N-dimensional feature vector $\mathbf{v}$ with a spread parameter σ is defined on N-dimensional feature vectors $\mathbf{x}$ as follows:

$$\mathbf{y} = e^{[-\|\mathbf{x}-\mathbf{v}\|^2/2\sigma^2]}. \tag{6.1}$$

The response surface of a single radial unit is a Gaussian function, peaked at the center of the feature vector and descending outwards (Fig. 6.1). The name radial indicates that all points $\mathbf{x}$ equidistant from $\mathbf{v}$ return the same value of $\mathbf{y}$. A number M of these radial basis functions can be centered on M feature vectors so that their circular disks of radius σ cover a bounded region of interest in the feature space (Fig. 6.2). The values of a radial basis function satisfy the condition that $0 < \mathbf{y} \leq 1$.

A radial basis function network (Fig. 6.3) is a three-layer feed-forward network comprising the following layers:

1. an input layer of N(= number of variables or dimensions of feature vectors) neurons, each of which receives a component of input feature vector,

155
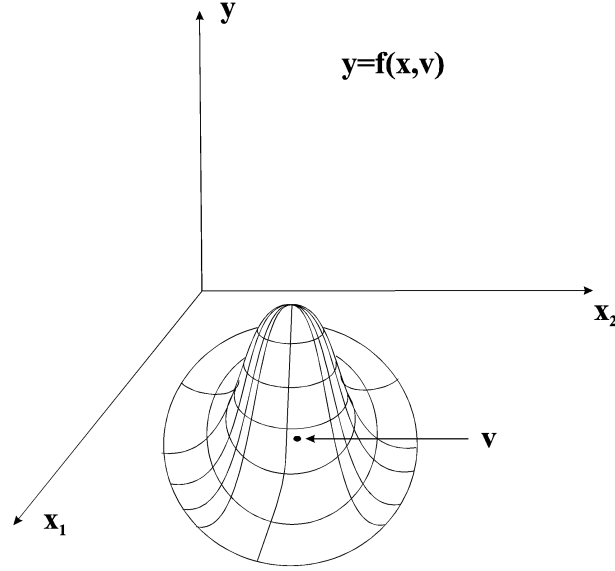
Figure 6.1: Perspective view of radial basis function in two-dimensional feature space.

2. a hidden layer of M neurons, each containing a radial basis function and

3. an output layer of $J(=$ number of target vectors) neurons, which return the output for each input feature vector.

It implements the following composite mapping:

$$\mathbf{x} \longrightarrow \mathbf{y} \longrightarrow \mathbf{z} \longleftarrow \mathbf{t}$$

where $\mathbf{z}$ and $\mathbf{t}$ are the output and target vectors, respectively.

Given a training data set containing Q vectors, an incoming vector $\mathbf{x}$ from the input layer activates a neuron (radial basis function) in the hidden layer, which returns a unique value of $\mathbf{y}$ (Looney and Yu, 2001):

$$\mathbf{y}_m^q = e^{[-\|\mathbf{x}^q - \mathbf{v}^m\|^2/2\sigma_m^2]}, \tag{6.3}$$

where v^m and σ_m (m=1 to M) are the centre vector and spread parameter of the mth radial basis function and x^q ($q = 1$ to Q) is the qth training vector.

The values of $\mathbf{y}$ are multiplied by synaptic weights along the lines connecting the neurons of the hidden layer to the neurons of the output layer and
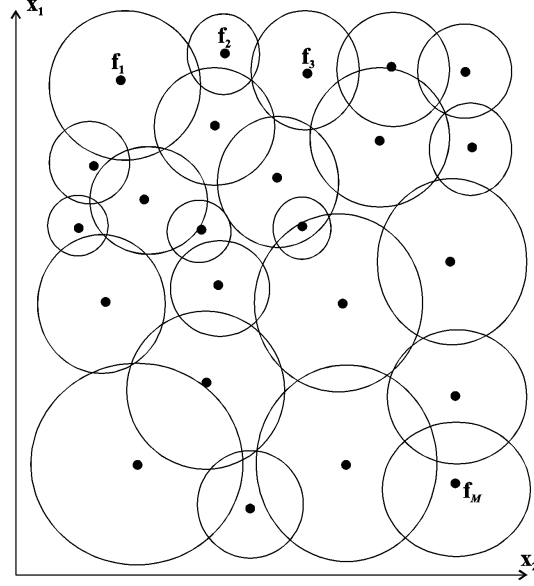
Figure 6.2: Plan view of two-dimensional feature space with M radial basis functions.

summed in the neurons of the output layer (Looney and Yu, 2001):

$$\mathbf{z}_j^q = (1/M)[\sum_{m=1}^{M} u_{mj} \times \mathbf{y}_m^q + b_j] \longleftarrow \mathbf{t}, \qquad (6.4)$$

where j=1 to J. The synaptic weights, u_{mj}, are dynamically modified to force the outputs $\mathbf{z}$ to match the targets $\mathbf{t}$ as closely as possible. The bias, b_j, is included at each neuron in the output layer.

Looney (2002) derived radial basis functional link nets (RBFLNs) by extending the radial basis function neural network architecture to random vector functional link nets described by Pao *et al.* (1994). An RBFLN is a near-replica of radial basis function neural network but differs in that it has additional lines of propagation that directly connect neurons in the input layer to neurons in the output layer (Fig. 6.3). An RBFLN therefore implements the following composite mapping:
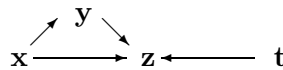
The lines connecting the N neurons in the input layer to the J neurons in the
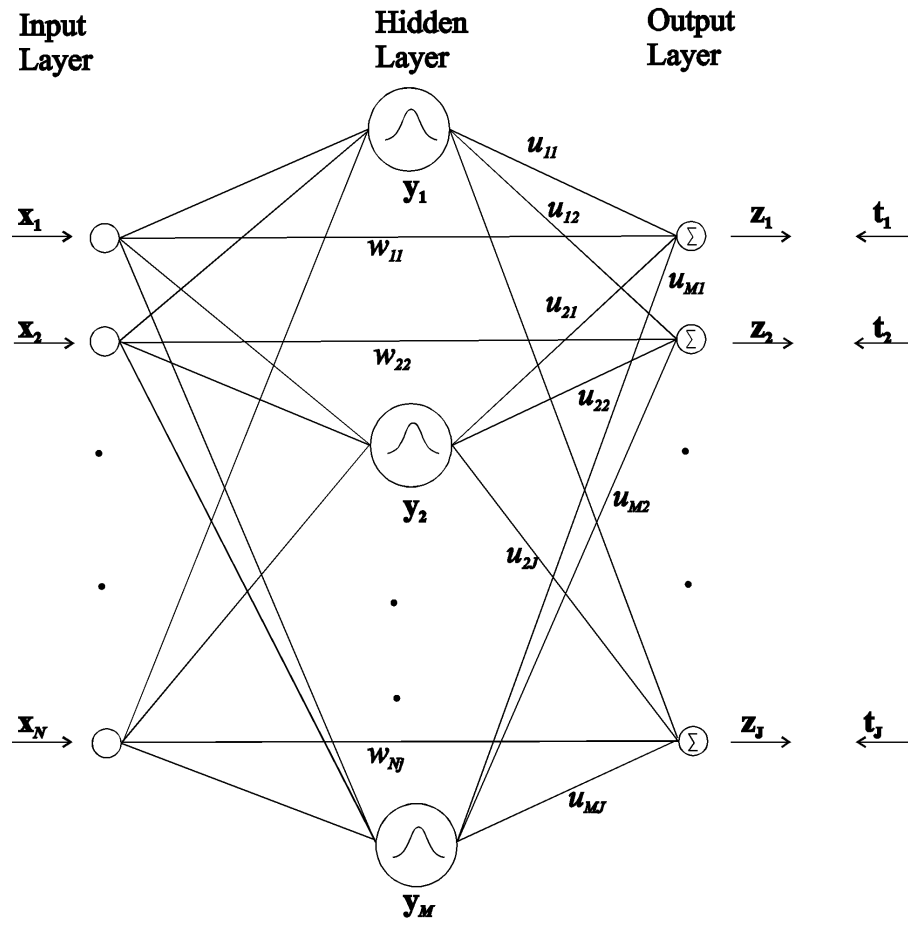
Figure 6.3: Radial basis functional link net (RBFLN).

output layer carry an extra set of synaptic weights, w_{nj} (Fig. 6.3). Clearly, RBFLNs are a generalization of radial basis function neural networks. The two are the same when the extra weights, w_{nj}, are set to zero. A radial basis function neural network represents a nonlinear model while an RBFLN includes that nonlinear model as well as a linear model (the direct lines from the input to the output nodes) so that the linear parts of a mapping do not need to be approximated by the nonlinear model. Thus the RBFLN is a more complete model of a general nonlinear mapping. The output components of RBFLNs differ from those of radial basis function neural network (Equation 6.4) and are given by (Looney and Yu, 2001):

$$\mathbf{z}_j^q = [1/(M+N)][\sum_{m=1}^{M} u_{mj} \times \mathbf{y}_m^q + \sum_{n=1}^{N} w_{nj} \times \mathbf{x}_n^q + b_j] \longleftarrow \mathbf{t}, \qquad (6.5)$$

where

$$\mathbf{y}_m^q = e^{[-\|\mathbf{x}^q - \mathbf{v}^m\|^2 / 2\sigma_m^2]}. \qquad (6.6)$$

6.2.1 Training of radial basis functional link nets

Given a training data set containing Q feature vectors and Q associated output target vectors

$$\{\mathbf{x}_q : q = 1, 2, ..., Q\} \qquad and \qquad \{\mathbf{t}_q : q = 1, 2, ..., Q\},$$

an RBFLN is trained in the following stages (Looney and Yu, 2001; Looney, 2002):

- initialization of centers, spread parameters and synaptic weights

- adjustment of synaptic weights and spread parameter to minimize the output total sum-squared error defined as the sum of partial sum-squared errors (Looney and Yu, 2001):

$$E = \sum_{q=1}^{Q} E^q = \sum_{q=1}^{Q} \sum_{j=1}^{J} (\mathbf{t}_j^q - \mathbf{z}_j^q)^2. \qquad (6.7)$$

Training on synaptic weights is via steepest descent iteration:

$$u_{mj} \leftarrow u_{mj} - \eta_1(\delta E/\delta u_{mj}) = u_{mj} + (\eta_1/(M+N)) \sum_{q=1}^{Q} (\mathbf{t}_j^q - \mathbf{z}_j^q)\mathbf{y}_m^q, \quad (6.8)$$

and

$$w_{mj} \leftarrow w_{mj} - \eta_2(\delta E/\delta w_{mj}) = w_{mj} + (\eta_2/(M+N)) \sum_{q=1}^{Q} (\mathbf{t}_j^q - \mathbf{z}_j^q)\mathbf{x}_m^q. \quad (6.9)$$

Each center and spread parameter is also updated with steepest descent iteration (Looney and Yu, 2001):

$$v_n^m \leftarrow v_n^m - \eta_3(\delta E/\delta \mathbf{v}_n^m) =$$
$$\mathbf{v}_n^m + [\eta_3/\sigma_m^2] \sum_{q=1}^{Q} \{ \sum_{j=1}^{J} (\mathbf{t}_j^q - \mathbf{z}_j^q)u_{mj} \}\mathbf{y}_m^q(\mathbf{x}_n^q - \mathbf{v}_n^m), \quad (6.10)$$

and

$$\sigma_m^2 \leftarrow \sigma_m^2 - \eta_4(\delta E/\delta \sigma_m^2) =$$
$$\sigma_m^2 + [\eta_4/\sigma_m^4] \sum_{q=1}^{Q} \{ \sum_{j=1}^{J} (\mathbf{t}_j^q - \mathbf{z}_j^q)u_{mj} \}[\mathbf{y}_m^q \|\mathbf{x}_n^q - \mathbf{v}_n^m\|^2]. \quad (6.11)$$

In Equations 6.8 to 6.11, η_i ($i=1$ to 4) are learning rates.

Using the fullpropagation method described by Looney (1997), the neural network is trained using the steepest descent iteration on the total sum-squared error, for all Q input feature vectors at a time, so that each adjustment of each synaptic weight is influenced by all Q input feature vectors.

Full learning algorithm for radial basis functional link nets

The high-level full training algorithm for RBFLNs, which adjusts the centers and spread parameters along with the synaptic weights, is given below (after Looney and Yu, 2001; Looney, 2002):

Full training initialization.

1. Given R randomly ordered sample vectors $\{\mathbf{x}^r : q = 1, ..., R\}$ of dimension N, select $Q(< R)$ vectors for training and save the remaining $(R - Q)$ for testing (validation of) the training.

2. For a very large Q, choose M such that M overlapping radial basis functions cover the entire feature space and take $\mathbf{v}^m = \mathbf{x}^m$ (for $m = 1, ..., M$). If $M > Q$, then take $\mathbf{v}^m = \mathbf{x}^m$ (for $m = 1, ..., M$) and draw the remaining $(M - Q)$ radial basis functions centered at random in the feature space.

3. Compute initial $\sigma = [1/(2M)]^{1/N}$ and take $\sigma_m = \sigma$ (for $m = 1, ..., M$).

4. Select all weights u_{mj} and w_{nj} randomly between 0.5 and 0.5 (for $j = 1, ..., J$; $m = 1, ..., M$ and $n = 1, ..., N$). Specify I iterations.

Full training iteration.

5. Compute $\mathbf{y}_m^q$ from Equation 6.6 (for each $m = 1, ..., M$ and $q = 1, ..., Q$).

6. Compute $\mathbf{z}_j^q$ from Equation 6.5 (for each $j = 1, ..., J$ and $q = 1, ..., Q$).

7. Update the synaptic weights from Equations 6.8 and 6.9.

8. Update the centers from Equation 6.10 and the spreads from Equation 6.11.

9. At every P^{th} iteration (e.g., $P = 20$ or $P = 50$), put the validation vectors through the network, record the *validation* total sum squared error value $(TSSE_{val})$ and stop when $TSSE_{val}$ increases for the first time and all training and test vectors are mapped into the correct targets.

10. If I iterations are done, then stop, else go to Step 5 above.

The algorithm was implemented using the procedure and software described by Looney and Yu (2001) and Kemp *et al.* (2001).

6.3 Implementation of Radial Basis Functional Link Nets

6.3.1 Data preprocessing

'Curse of dimensionality'

The term 'curse of dimensionality' was coined by Bellman (1961) to express problems caused by the growth of hypervolume as a function of dimensionality.

In neural network-based models, the curse of dimensionality is expressed in the following problem. Many neural networks are used for mapping an input feature space to an output feature space. In such cases, the neural network should be able to 'monitor' every part of its input feature space in order to know how that part of the feature space should be mapped. Covering the input feature space entirely takes resources (in terms of sample data) and, in most cases, the amount of resources needed is proportional to the hypervolume of the input space. The goodness of the representation in neural networks can be measured in terms of the average distance from a random point in the feature space to the nearest network unit: the shorter the distance, the better is the representation of the data. It is intuitively clear that the total number of units required to keep the average distance adequately small increases in direct proportion to the increase in dimensionality of the feature space. For example, in the case of an RBFLN, the number of radial basis functions required to keep the average distance between the centers of the radial basis functions adequately small increases in direct proportion to the increase in dimensionality of feature space. As the number of radial basis functions increases, the number of parameters of the RBFLN, namely, the spreads and centers of the radial basis functions and the synaptic weights, also increases. Because these parameters are, in effect, repositories of the knowledge, their robust estimation is vital for optimizing the generalization capability of the RBFLN, which requires a large number of training samples. This entails that the number of training samples required to train the RBFLN increases with the increase in the dimensionality of feature space. Because the dimensions of feature space are equal to the dimensions of input training samples, the higher the dimensionality of the training samples, the higher is the number of training samples required for an effective implementation of an RBFLN.

A priori information can help mitigate the curse of dimensionality. A careful selection and scaling of the input feature vectors can extenuate the severity of the problem. In an application to mineral potential mapping, this implies that, if an adequately large number of training samples (i.e., known mineral deposits) are not available, the available predictor maps should be carefully scrutinized, and on the basis of *a priori* conceptual-genetic information on the target mineral deposit-type, only the most relevant maps should be selected for modeling. Although multi-class predictor maps can be conveniently used in RBFLNs, the maps should be reclassified, if possible, in order to reduce the number of classes and the overall dimensionality of the data set.

162

Data encoding

An RBFLN, like all neural networks, can accept only numeric input data, and performs better if numeric input data are in a fairly-narrow range. This poses a problem when input data are non-numeric or missing or if they are in an unusual range. Real-world geospatial data are often non-numeric (categoric) and frequently missing in some parts.

Categorical predictor maps can be converted into numeric predictor maps using one-of-n encoding schemes (Masters, 1993), which involve transforming a multi-class predictor map containing n classes to n binary predictor maps. On each of the n binary maps, one and, only one, class is encoded 1; all of the remaining classes are encoded 0.

Feature vectors

In the context of an RBFLN, each unique combination of predictor patterns ('unique condition,' *see* Chapter 1, p. 6) can be considered a vector of predictor features (or a feature vector) and, therefore, a unique condition map can be termed a feature vector map. The components of feature vectors are defined by the attributes of unique conditions. In an N-dimensional feature space, the location of each feature vector is defined by the values of its N components.

Target, training and validation vectors. Target vectors define output vectors to which input feature vectors are mapped by a neural network. Input feature vectors with known target vectors constitute training samples for a neural network. Validation samples also have known target vectors, but are used exclusively for validating the training of the neural network.

In mineral potential mapping, there is only one single-dimensional binary target vector, encoded as 1 or 0, which represents presence or absence, respectively, of a mineral deposit. The feature vectors defined by presence or by absence of a mineral deposit constitute training and validation samples. The feature vectors that are defined by presence of a mineral deposit are referred to as deposit training/validation samples and those defined by absence of mineral deposits are referred to as non-deposit training/validation samples. It is simple to select the former because they constitute the feature vectors that are spatially-coincident with the locations of known mineral deposits. However, selecting without uncertainty non-deposit training samples is often difficult. Both data-driven and knowledge-driven approaches can be used for this

purpose. With the former approach, Kemp *et al.* (2001) suggested that non-deposit locations can be randomly extracted from the locations that have been previously-modeled as having very low probability of hosting a target mineral deposit type, and feature vectors spatially-coincident with these locations can be selected as non-deposit training/validation samples. Alternatively, based on an expert knowledge of genetic models of the target mineral deposit type, the feature vectors that are least-likely to be associated with the target mineral deposit type can be selected as non-deposit training/validation samples.

6.3.2 Training of radial basis functional link nets

Training an RBFLN involves determining (a) the number, centers and spread parameters of the radial basis functions (hidden neurons) and (b) the synaptic weights that induce a correct classification of all training samples with a minimum total sum squared error. However, the number of incorrectly classified training samples and the total sum squared error decreases indefinitely with increasing number of training iterations and hidden neurons.

With increasing number of training iterations, a specialized training on specific training samples sets in, which keeps decreasing the number of incorrectly-classified samples and the total sum squared error. Although the specialized training results in a correct classification of all training samples with a negligible sum squared error, it simultaneously reduces the capacity of the network to generalize and therefore generates an over-learned network that is highly efficient in classifying training samples, but is not so efficient in classifying other feature vectors.

For an optimal performance of an RBFLN, the number of radial basis functions in the hidden layer should be large enough to cover the entire feature space. This requires a large number of training samples, as each training sample forms the center of a radial basis function in the feature space. In practice, however, the number of training samples can never be considered sufficiently large to cover the entire feature space. Therefore, extra radial basis functions are drawn and centered randomly in the feature space, which provides higher resolution and more non-linearity and therefore improves the performance of an RBFLN. However, too many extra radial basis functions can induce an RBFLN to focus excessively on specific characters of individual training samples and thereby reduce its capability to generalize.

It is therefore necessary to tune the number of training iterations and hidden neurons in such a way that, on one hand, the generalized training is max-

imized and, on the other hand, the specialized training is avoided. A set of validation samples can be used to determine the onset of specialized training, which is indicated by (a) a reversal in the increasing trend of numbers of correctly-classified validation samples, (b) a reversal in the decreasing trend of total sum squared error for the validation samples or (c) a correct classification of all training samples.

Masters (1993) recommends that in feedforward neural networks as few hidden neurons should be used as possible, and it is preferable to start the training with too few hidden neurons. He also describes an effective training procedure to avoid over-learning, which involves using (a) a set of training samples to train a neural network, (b) a set of validation samples to validate the trained network and (c) a set of training test samples to check the generalization ability of the trained and validated network. However, if inadequate number of deposit samples are available, the set of validation samples can be used to both validate the training and infer the generalization capability of the trained RBFLN.

6.4 Application to Base-Metal Potential Mapping in Aravalli Province

6.4.1 Data preprocessing

As discussed above, in order to build a robust RBFLN-based model, sufficiently large number of training samples, in proportion to the dimensionality of training samples, should be available. Keeping in mind the inadequate number of training samples (see below), it was decided to reduce the dimensionality of input training feature vectors for a robust estimation of network parameters. The available predictor maps were scrutinized, and on the basis of *a priori* conceptual-genetic information and previous modeling experience, the map of sedimentary environments was excluded. This map, which shows strong dependence on the predictor maps of lithologies and stratigraphic groups (Chapter 4), was largely interpreted from lithological data (Chapter 2) and therefore some of the information contained in this map might be redundant. Similarly, the multi-class predictor maps of buffered distances, namely, the maps of buffered distances from regional lineaments, buffered distances from NW-trending lineaments, buffered distances from NE-trending lineaments and buffered distances from fold axes, were used in binary form, as explained in Chapter 4.

Therefore, the predictor maps used in the neural network model included the multi-class predictor maps of lithologies and stratigraphic groups, and the binary predictor maps of mafic igneous rocks, buffered distances from regional lineaments, buffered distances from NW-trending lineaments, buffered distances from NE-trending lineaments and buffered distances from fold axes.

Data encoding

The one-of-n encoding procedure was used for converting the multi-class categoric maps of lithologies and stratigraphic groups to binary maps. On each binary map, exactly one class was coded as 1 and the remaining classes were coded as 0. In this way 17 binary predictor maps were generated from the two multi-class predictor maps. Of these, 11 binary predictor maps were used for subsequent neural network processing. Three binary maps of lithologies, which have no known relationship with base-metal mineralization in the province, were not used. These maps included the binary maps of calc-schist, migmatites and other younger intrusive/extrusive rocks. Similarly, three binary maps of stratigraphic groups, which have no known relation with base-metal mineralization in the province, were not used. These maps are the binary maps of Sandmata Complex, Mangalwar Complex and younger stratigraphic groups.

Each of the two classes in the five binary predictor maps of mafic igneous rocks, buffered regional lineaments, buffered NW-trending lineaments, buffered NE-trending lineaments and buffered fold axes was coded as either 1 or 0, indicating, respectively, the presence or absence of the predictor pattern.

Feature vectors

The 16 binary predictor maps were digitally-superposed and unique combinations of the predictor maps in a unit area of 1 km^2 were mapped to generate a feature vector map constituting 519 feature vectors. As the operation was carried out in a GIS-environment, an associated database table was automatically generated, which held the components of the feature vectors. In the table, each feature vector is described by a unique identification number and 16 components, each representing a predictor pattern encoded as either 1 or 0.

Training and validation vectors The deposit training samples and deposit validation samples were selected on the basis of the same training and validation deposits that were used, respectively, for training and validating the

weights-of-evidence models (Chapter 4), with the exception of the VMS-type Basantgarh deposit, which was moved from the training set to the validation set. This was done in order to train the neural network exclusively on SEDEX-type deposits. The feature vectors spatially-coincident with the locations of the 40 training and 14 validation deposits were extracted to generate deposit training and deposit validation samples, respectively. As several feature vectors contained more than one deposit, a total of 24 deposit training samples and 12 deposit validation samples were generated.

For generating non-deposit training and non-deposit validation samples, 3 non-deposit locations, which were modeled by the extended weights-of-evidence analysis (Chapter 4) as having the lowest posterior probability of hosting base-metal deposits, were extracted from each of the 16 predictor maps. Of these, 2 locations were randomly extracted as non-deposit training points and 1 location was extracted as a non-deposit validation point. The feature vectors spatially-coincident with the non-deposit training and non-deposit validation points were extracted to generate 32 non-deposit training and 16 non-deposit validation samples, respectively.

The deposit and non-deposit training samples were combined to generate a set of 56 training samples, of which 24 contained a deposit. However, it was found during the training that the RBFLN learns to recognize the deposit validation samples more efficiently if the deposit and non-deposit samples are equally represented in the training set. Eight non-deposit training samples were therefore randomly selected and removed from the set of training samples (each predictor map was still represented by at least one non-deposit sample), giving a set of 48 training samples in which both deposit and non-deposit samples were equally represented. The deposit and non-deposit validation samples were combined to generate a set of 28 validation samples.

6.4.2 Training of radial basis functional link nets

Because of an inadequate number of training samples available in the study area, the set of validation samples was used to both validate the training and infer the generalization capability of the trained RBFLN. The two sets of training samples (see above) were used for training a series of RBFLNs having different numbers of hidden neurons. For both sets, an identical training procedure was followed and the same set of validation samples was used for validating the training.

The training was initiated with an RBFLN having 50 hidden neurons. The

167

network was trained for 100 iterations, using a set of randomly-initialized centers and weights, and the number of correctly-classified training samples and the total sum squared error ($TSSE_{trn}$) were recorded. Then the validation samples were processed using the same network and the number of correctly-classified validation samples and the total sum squared error ($TSSE_{val}$) were recorded. A threshold of 0.5 was applied to the output value for making a classification. This two-step process was repeated by stepping up the number of iterations in the increments of 20 until all training samples were correctly classified and ($TSSE_{trn}$) converged close to zero. The procedure was repeated five times, each time using a different set of randomly-initialized weights and centers, for selecting the set of initial weights and centers and that gave the best performance for the validation samples.

The same training procedure was repeated using 60, 70, 80, 100, 125 and 150 hidden neurons in the RBFLN. The results indicated that the generalized training of the RBFLN with 50, 60, 70, 80, 100, 125 and 150 hidden neurons was completed in 180, 180, 200, 200, 220, 240 and 260 iterations, respectively, using the first set of training samples (containing 24 deposit and 36 non-deposit samples) and in 220, 240, 240, 260, 260, 280 and 300 iterations, respectively, using the second set of training samples (containing 24 deposit and 24 non-deposit samples). Table 6.1 shows that, at the completion of the generalized training, the best performance in classification is achieved by the RBFLN having 70 neurons in the hidden layer and trained on the second set of training samples (containing equal number of deposit and non-deposit training samples). Any further increase in the number of hidden neurons does not improve the performance of the neural network. This network was therefore used for predictive classification of all the feature vectors.

6.4.3 Favorability maps

The output value for each feature vector predicts the extent to which the feature vector belongs to either the class that contains base-metal deposits or the class that does not contain a base-metal deposit. These values, which ranged from -0.1449 to 1.3388, were re-scaled between 0 and 1 and mapped to generate a predictive classification map (Fig. 6.4). Fig. 6.5 shows the plot of predictive classification values against the percentage of cumulative area.

It is cumbersome to interpret the predictive classification map shown in Fig. 6.4 in terms of delineating the areas favorable for base-metal mineralization, as it shows the predictive classification values in a continuous scale of

Table 6.1: Performance of RBFLNs at completion of generalized training

	Training Set 1			
No. of	(56 samples; 24 deposit & 32 non-deposit)			
hidden	No. of		% of correctly-classified	
neurons	iterations	$TSSE_{val}$	validation samples	
			deposit	non-deposit
50	180	1.7854	72.7	100
60	180	1.7853	72.7	100
70	200	1.7739	72.7	100
80	200	1.7783	72.7	100
100	220	1.7802	72.7	100
125	240	1.7844	72.7	100
150	260	1.7859	72.7	100

	Training Set 2			
No. of	(48 samples; 24 deposit & 24 non-deposit)			
hidden	No. of		% of correctly-classified	
neurons	iterations		validation samples	
			deposit	non-deposit
50	220	1.5716	72.7	100
60	230	1.5674	72.7	100
70	**240**	**1.5631**	**81.8**	**100**
80	260	1.5693	81.8	100
100	260	1.5690	81.8	100
125	280	1.5698	81.8	100
150	300	1.5699	81.8	100

0 to 1. Thresholding the predictive classification values facilitates the selection of exploration targets. Accordingly, the predictive classification map was reclassified into a binary favorability map (Fig. 6.6) and a ternary favorability map (Fig. 6.7). The binary favorability map (Fig. 6.6) was generated by applying a threshold of 0.5 on the predictive favorability map. The ternary favorability map (Fig. 6.7) was generated by applying two threshold predictive classification values, represented by the two inflexion points along the predictive classification values versus percentage of cumulative area curve (Fig. 6.5). The lower inflexion point (70.1, 0.182) represents a threshold for distinguishing zones with low favorability from zones with moderate favorability while the upper inflexion point (94.4, 0.495) represents a threshold value for distinguishing zones with moderate favorability from zones with high favorability.

Validation of favorability maps

The favorability maps were validated by overlaying the deposit training points and the deposit validation points and by plotting the position of these deposits on the predictive classification value versus percentage of cumulative area curve

Figure 6.4: Continuous-scale predictive classification map. Predictive classification values range from 0 (white) to 1 (black).

(Fig. 6.5). In the binary favorability map (Table 6.2 and Fig. 6.6), (a) the high favorability zones occupy 5.5% of the study area and contain 97.5% and 83% of the deposit training and validation points, respectively and (b) the low favorability zones occupy 94.5% of the study area and contain 2.5% and 17% of the deposit training and validation points, respectively. In the ternary favorability map (Table 6.2 and Fig. 6.7), (a) the high favorability zones occupy 6% of the study area and contain 97.5% and 83% of the deposit training and deposit validation points, respectively, (b) the moderate favorability zones occupy 24% of the study area and contain 2.5% and 17% of the deposit training and validation points, respectively and (c) the low favorability zones occupy 70% of the study area and do not contain any known deposits.

170
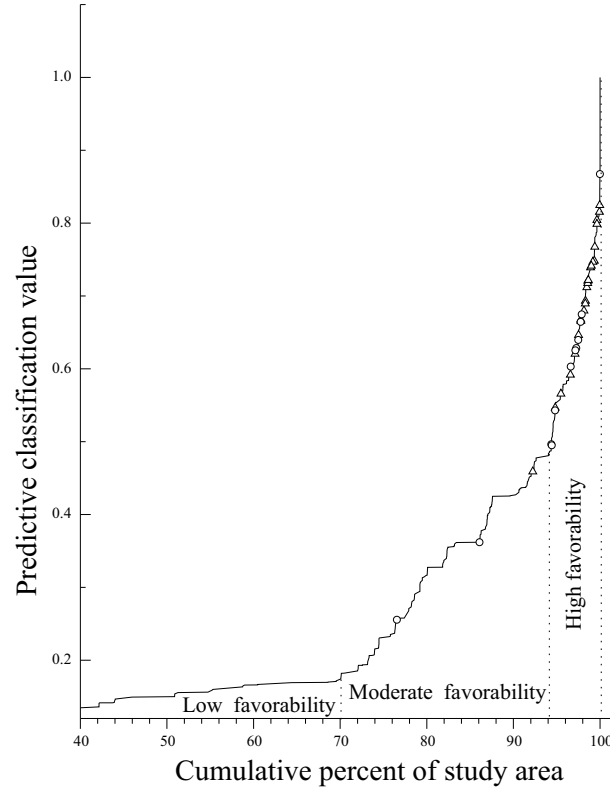
Figure 6.5: Variation of predictive classification values with cumulative percent of study area. Circles are validation deposits and triangles are training deposits.

6.5 Discussion

One of the most important procedures in the implementation of a neural network application is the selection of appropriate training samples that adequately represent all feature vectors to be classified. This implies that, in the case of an application to mineral potential mapping, the deposit samples and non-deposit samples should be represented in the same proportion in the set of training samples as they are expected to occur in the general population. However if deposit samples and non-deposit samples are represented in the training set in the same proportion as they are expected to occur in the general population, the performance of a neural network is optimized for recognizing non-deposit samples rather than deposit samples, as discussed by Brown *et al.* (2000). This may give rise to a large number of type II errors, which have serious consequences in mineral potential mapping. The problem can be addressed

171
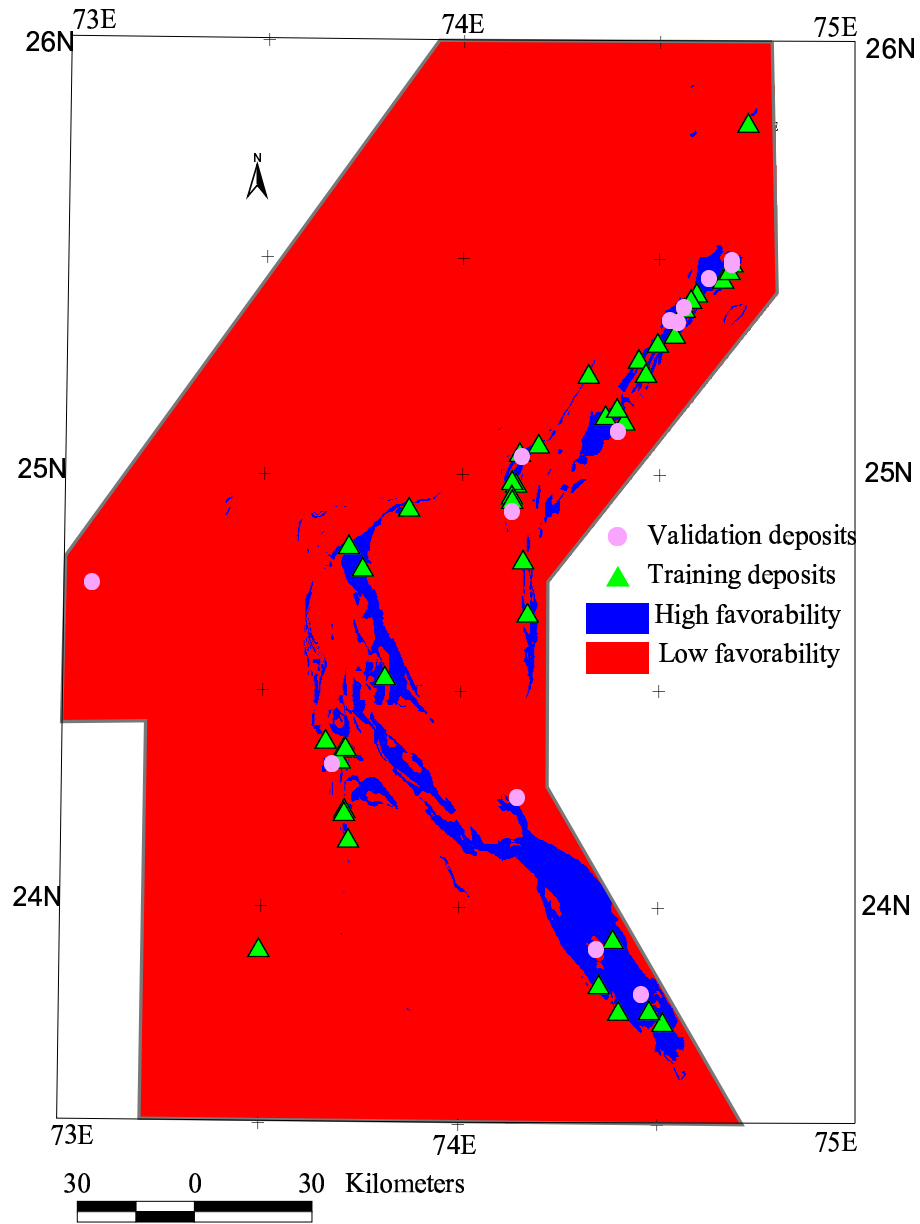
Figure 6.6: Binary favorability map generated by reclassification of predictive classification map shown in Fig. 6.4
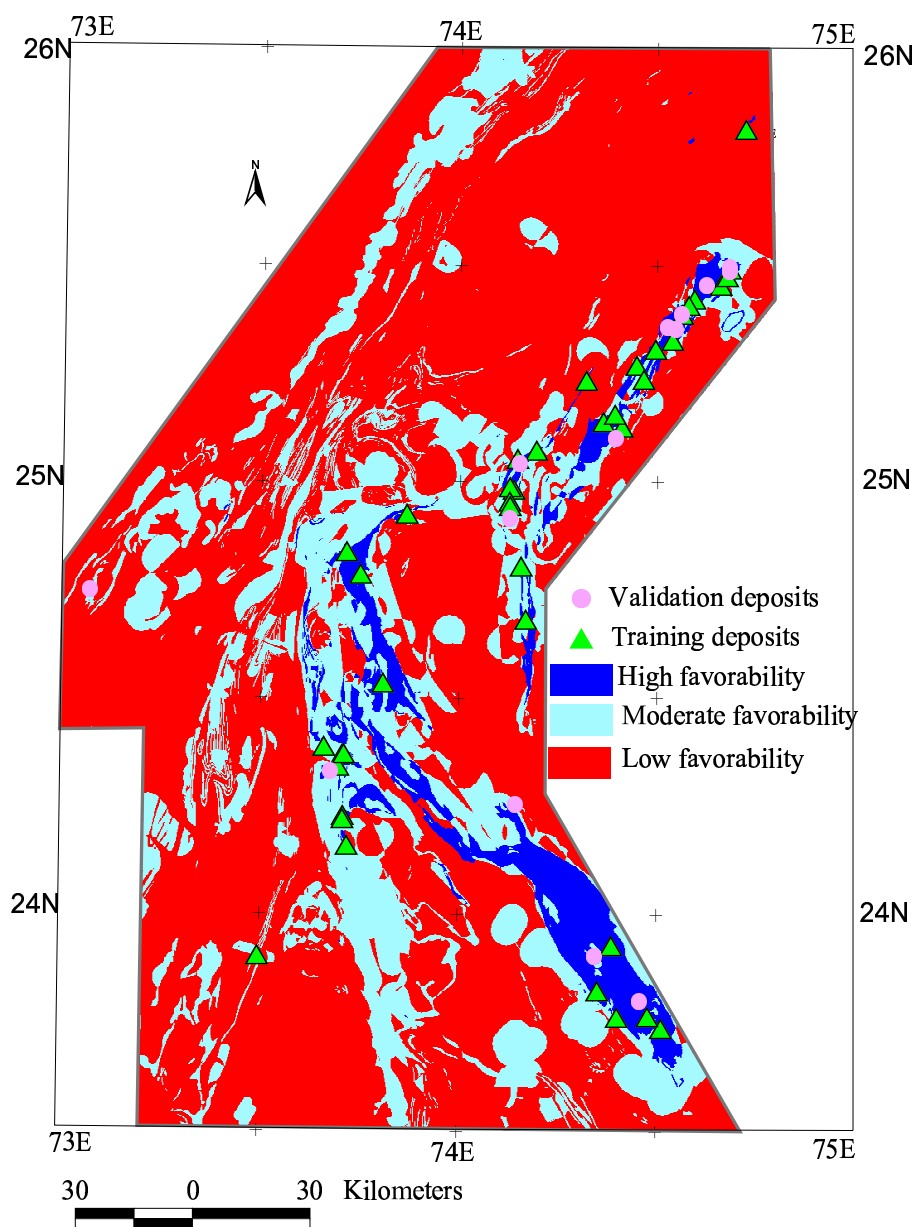
Figure 6.7: Ternary favorability map generated by reclassification of predictive classification map shown in Fig. 6.4

Table 6.2: Validation of Favorability maps

Favorability Map	Favorability zone	Percent of study area	Percent of Validation deposits	Percent of Training deposits
Binary	High favorability	5.5	83.0	97.5
	Low favorability	94.5	17.0	2.5
Ternary	High favorability	6.0	83.0	97.5
	Moderate favorability	24.0	17.0	2.5
	Low favorability	94.0	Nil	Nil

by using the one-sided selection procedure (Kubat and Matwin, 1997; Kubat *et al.*, 1998; Brown *et al.*, 2000) to balance the number of deposit samples and non-deposit samples in the training set. As Table 6.1 shows, the performance of an RBFLN is improved by using a set of training samples that contains an equal number of deposit and non-deposit training samples, irrespective of their expected probability of occurrence in the total population.

As compared to the weights-of-evidence approach, multi-class evidential maps can be more conveniently used in the neural network approach. One-of-n encoding schemes provide a consistent method of using multi-class categorical maps in a neural network application. Moreover, in the weights of evidence approach, the output posterior probability values are highly sensitive to the violation of the assumption of conditional independence because of the linear nature of Bayes' equation used for combining evidential maps. As discussed by Singer and Kouda (1999) and Porwal *et al.* (2003b), the assumption of conditional independence is often difficult to validate. The non-linear nature of neural networks, on the other hand, ensures that the output is not likely to be affected by the conditional dependence amongst two or more input evidential maps.

Nevertheless, RBFLNs are sensitive to the curse of dimensionality. Consequently, unless a large number of training samples are available, it is preferable to preprocess predictor maps in order to reduce the dimensionality of input feature vectors. Alternatively, statistical tools like factor analysis or principal component analysis can be used to reduce the dimensionality of input feature vectors (Porwal *et al.*, 2004a).

In the favorability maps (Figs. 6.6 and 6.7), the high favorability zones are confined to specific lithologies in the stratigraphic groups of Palaeoproterozoic age, which suggests a strong lithostratigraphic control over base-metal mineralization in the province. This is consistent with the conceptual model of base-metal metallogeny in the Aravalli province proposed by Deb and Thorpe

(2001), which envisages (a) a Palaeoproterozoic metallogenic epoch at ca. 1800 Ma and (b) a Mesoproterozoic metallogenic epoch at ca. 1000 Ma. The former resulted in the formation of the SEDEX type deposits of the Bhilwara and the Aravalli belts, while the latter resulted in the formation of the smaller VMS-type deposits of the South Delhi belt. Because the two types of mineralizations have different characteristics, it was not considered appropriate to use the same RBFLN to map the potential of both types of base-metal deposits and therefore the VMS-type Basantgarh deposit was removed from the set of training deposits. As a result, the trained RBFLN did not learn to recognize the specific characteristics of VMS-type deposits and hence the Mesoproterozoic metallogenic epoch is not represented in the high favorability zones.

The high favorability zones contain all major SEDEX-type base-metal deposits of the study area, including the world class deposit of Rampura-Agucha and other large deposits of the Bhilwara and Aravalli belts. As discussed in Chapter 3, the Rampura-Agucha has several characteristics that makes it a particularly difficult deposit to predict using mathematical geological tools. The deposit is classified in low favorability zones in the favorability maps derived using the fuzzy, weights-of-evidence and hybrid fuzzy weights-of-evidence approaches (Chapters 3, 4 and 5). The correct classification of the Rampura-Agucha deposit (predictive classification value: 0.566) by the RBFLN therefore demonstrates the ability of an RBFLN to recognize the critical component(s) (in this case, the host lithology of graphitic schist) in a feature vector and respond in a highly non-linear way to maximize the contribution of such component(s) to the output. The neural network also classifies three more similar small metasedimentary enclaves in the basement complex (in vicinity of the Rampura-Agucha deposit) in the high favorability zones.

The moderate favorability zones (Fig. 6.7) contain one training deposit and two validation deposits. The training deposit (Padar-Ki-Pal) has a predictive classification values of 0.459, which is close to the threshold of high favorability (Fig. 6.7). It is a small, low grade Cu-(Zn-Pb) deposit hosted by quartzites in the Jharol belt. So far, this is the only reported occurrence of base-metal mineralization from the Jharol belt. However, the ternary favorability map (Fig. 6.7) shows that there are several areas of moderate favorability in the Jharol belt that can be potential targets for base-metal exploration in the Jharol belt. One of the two validation deposits contained in the moderate favorability zones is the VMS-type Basantgarh deposit of the South Delhi belt, which is genetically different from the deposits of the Bhilwara and Aravalli

175

belts that were used for training the neural network. Although the deposit shares two common characteristics with the deposits of Bhilwara and Aravalli belt, viz., association of mafic volcanic rocks and proximity to crustal-scale faults, the neural network returns a much lower predictive classification value (0.256) for the deposit as compared to the deposits of the Bhilwara and Aravalli belt. This demonstrates the ability of the neural network to recognize overall difference between the feature vector representing the Basantgarh deposit and the feature vectors used for training the neural network, especially the lack of critical components (favorable host lithology and stratigraphy) in the former, and respond by returning a low predictive classification value. The other validation deposit classified in the moderate favorability zones is a minor low grade Cu deposit hosted by quartzites in the basal sequences of the Aravalli belt.

6.6 Conclusions

The application of an RBFLN to base-metal deposit potential mapping in the Aravalli province results in a regional-scale demarcation of (a) high favorability zones occupying 6% of the study area, which predict 92% of the known base-metal deposits, (b) moderate favorability zones, which represent an additional 24% area and contain 8% of the known deposits and (c) low favorability areas that occupy 70% of the study area and do not contain any known deposits. Significantly, the neural network identifies the Rampura-Agucha deposit in high favorability zones.

The following conclusions can be drawn from the application of the RBFLN to map the potential of base-metals in the study area.

- One-sided selection of the training data, i.e., selecting an approximately equal number of deposit and non-deposit samples in the training data, can effectively enhance the performance of an RBFLN for mineral potential mapping.

- Because of the non-linear nature of RBFLNs, their output is not likely to be affected by conditional dependence amongst predictor maps. However, high dimensionality of input feature vectors may adversely affect the performance of an RBFLN, particularly if adequately large number of training samples are not available. Consequently, input predictor maps should be scrutinized for possible redundancy and suitably preprocessed

to reduce dimensionality.

- RBFLNs have the capability of recognizing the critical features in a data set that are required to make a correct classification and of responding in a highly non-linear fashion, so that the contribution of such features is maximized in the output.

- RBFLNs can be effectively used for selecting target areas for exploration. However, in this application, regional-scale predictor maps were used for demarcating favorability zones in the study area. Radial-basis-functional-link-net-based models require further testing for modeling larger-scale predictor maps to demarcate specific prospects within the predicted high favorability zones.

- The spatial distribution of the high favorability zones is consistent with the conceptual models of base-metal metallogeny in the province, which emphasize a strong litho-stratigraphic control over base-metal mineralization (Chapter 2. However, in the present application, the RBFLN was trained on only SEDEX-type deposits and therefore areas favorable for VMS-type deposits are not represented in the high favorability zones. Similar RBFLNs can be trained on VMS-type deposits to demarcate zones favorable for VMS-type base-metal deposits in the province.

The high performance level of the RBFLN can be attributed to the flexibility of the neural network and its ability to take into account the input variables as well as the relationships between them. Furthermore, the neural network is able to detect patterns and trends in the noisy exploration data sets and to condition its response so as to maximize the contribution of the patterns that are critical for making correct classifications.

However, it is purely a data-driven model and therefore the output of the neural network is entirely dependent on the fidelity of training samples in representing the target mineralization. It is not possible to incorporate expert knowledge in the modeling procedure to compensate for possible deficiencies in the training data. On the other hand, the knowledge-based fuzzy model described in Chapter 3 provides efficient system for using expert knowledge but offers no mechanism for incorporating exploration data in the modeling procedure. In the next chapter, a hybrid neuro-fuzzy model is described, which consistently utilizes both expert knowledge and exploration data by implementing a fuzzy inference system in the framework of artificial neural networks.

Chapter 7

Hybrid Neuro-fuzzy Model

This chapter describes "A Hybrid Neuro-Fuzzy Model for Mineral Potential Mapping"(Porwal *et al.*, 2004a). The model implements a Takagi-Sugeno type fuzzy inference system in a four-layered feed-forward adaptive neural network, which is demonstrated for application to base-metal potential mapping in the study area.

7.1   Introduction

Earth science information that is used in mineral potential mapping has an empirical component comprising an exploration data-base and a conceptual component comprising an expert knowledge-base. Data-driven approaches to mineral potential mapping are based on the empirical component whereas knowledge-driven approaches are based on the conceptual component. However, the two approaches are generally considered dichotomous and therefore implemented in mutual exclusion. On the one hand, data-driven approaches do not support a direct use of conceptual information in modeling procedures, although it is used for identification of recognition criteria and preprocessing of input evidential maps. On the other hand, knowledge-driven approaches do not support a direct use of empirical information in modeling procedures, although it is used in an inductive way to strengthen knowledge-base. Consequently, a significant proportion of available earth science information remains under-utilized in both types of approaches to mineral potential mapping.

Optimal utilization of earth science information requires a supplementary as well as a complementary utilization of the conceptual and empirical compo-

nents. There are several methods available, which allow a supplementary use of conceptual information in a data-driven approach. For example, Porwal *et al.* (2003a) proposed a data-driven fuzzy approach, which uses a knowledge-based inference engine for combining fuzzified evidential maps (Chapter 3). Similarly, in the data-driven weights-of-evidence approach, a mineral deposit expert can use his knowledge to assign 'expert weights of evidence' to patterns that contain few or no training points.

Cheng and Agterberg (1999) proposed a fuzzy weights-of-evidence approach that, in a hybrid form, allows a complementary utilization of both empirical and conceptual information. In the hybrid fuzzy weights-of-evidence approach, knowledge-based fuzzy membership values are combined with data-based conditional probabilities to derive fuzzy weights of evidence and fuzzy posterior probabilities (Chapter 5).

The hybrid neuro-fuzzy model described in this chapter effectively combines the conceptual and empirical components of available earth science information for predictive mineral potential mapping. The model, which can be viewed as a knowledge-based artificial neural network, develops and implements a fuzzy inference system in the framework of adaptive neural networks.

Mineral potential mapping of an area involves predictive classification of each spatial unit having a unique combination of spatially-coincident predictor patterns (unique conditions) as mineralized or barren with respect to the target mineral deposit type. In the hybrid neuro-fuzzy approach, each unique condition is considered an input feature vector, whose components are derived by expert-knowledge-based ordinal encoding of the constituent predictor patterns. A subset of feature vectors with known targets (i.e., unique conditions known to be associated with either a mineralized or a barren location) is extracted from the set of all feature vectors and is used as a set of training samples. Components of training feature vectors are fuzzified using appropriate fuzzy membership functions and combined using fuzzy if-then rules in a fuzzy inference system. The parameters of the fuzzy inference system are iteratively modified to map each training sample to its target. The fuzzy inference system that produces the best mapping is used to fuzzify and combine the components of all feature vectors. The output predictive classification value, for each feature vector, indicates the extent to which the feature vector belongs to either the mineralized class or the barren class. These values can be mapped to generate a favorability map for the target mineral deposit type.

7.2 Hybrid Neuro-Fuzzy Model

A fuzzy inference system simulates human cognition in modeling the conceptual component of information by employing fuzzy membership functions and fuzzy if-then rules. Several fuzzy inference systems have been described by different workers (Zadeh, 1973; Mamdani, 1974; Mamdani and Assilian, 1975; Tsukamoto, 1979; Takagi and Sugeno, 1985; Sugeno and Kang, 1988; Sugeno and Tanaka, 1991) but the most commonly-used are Mamdani type (Mamdani, 1974; Mamdani and Assilian, 1975) and Takagi-Sugeno type, which is also known as Takagi-Sugeno-Kang type (Takagi and Sugeno, 1985; Sugeno and Kang, 1988; Sugeno and Tanaka, 1991). In the case of a Mamdani type fuzzy inference system, both premise (if) and consequent (then) parts of a fuzzy if-then rule are fuzzy propositions. In the case of a Takagi-Sugeno type fuzzy inference system, where the premise part of a fuzzy rule is a fuzzy proposition, the consequent part is a mathematical function, usually a zero or first degree polynomial function.

The hybrid neuro-fuzzy model for mineral potential mapping described here is a Takagi-Sugeno type fuzzy inference system, which is implemented in the framework of adaptive neural networks. It is an adaptation of "adaptive-network-based fuzzy inference system" (ANFIS; Jang, 1993) for mineral potential mapping.

7.2.1 Theoretical background

If X is a superset of n multi-class predictor maps X_i (i=1 to n), each containing m patterns, then the strength of x_{ij}, the jth (j=1 to m) pattern on the ith predictor map X_i, as an indicator of a target mineral deposit-type can be estimated in terms of class score (cs_{ij}), which is defined as (Porwal *et al.*, 2003a):

$$cs_{ij} = w_i \times w_{ij} \quad (\forall \ x_{ij} \in X_i), \tag{7.1}$$

where w_i is the map weight of the ith predictor map and w_{ij} is the class weight of the jth pattern on the ith predictor map. The procedure for assigning class weights and map weights is described by Porwal *et al.* (2003a) and given in Chapter 3 (p. 69).

Based on the class scores of predictor patterns, n fuzzy sets $\tilde{A}_i^1$ (i=1 to n) in X, containing 'favorable indicators of target mineral deposit-type,' can be

defined as:

$$\tilde{A}_i^1 = \left\{ \left(x_{ij}, \mu_{\tilde{A}_i^1}(x_{ij}) \right) \forall x_{ij} \in X_i \right\}, \tag{7.2}$$

where the fuzzy membership function $\mu_{\tilde{A}_i^1}$ for estimating the fuzzy membership value of x_{ij} in $\tilde{A}_i^1$ is defined as:

$$\mu_{\tilde{A}_i^1}(x_{ij}) = e^{\frac{-(cs_{ij} - c_{i1})^2}{2\sigma_{i1}^2}} \quad (\forall x_{ij} \in X_i), \tag{7.3}$$

where c_{i1} (i=1 to n) and σ_{i1} (i=1 to n) are the parameters that, respectively, define the center and the spread of the Gaussian function and cs_{ij} is the class score of x_{ij} (Equation 7.1).

Similarly, n fuzzy sets $\tilde{A}_i^2$ (i=1 to n) in X, containing 'unfavorable indicators of target mineral deposit-type,' can be defined as follows:

$$\tilde{A}_i^2 = \left\{ \left(x_{ij}, \mu_{\tilde{A}_i^2}(x_{ij}) \right) \forall x_{ij} \in X_i \right\}, \tag{7.4}$$

where the fuzzy membership function $\mu_{\tilde{A}_i^2}$ for estimating the fuzzy membership value of x_{ij} in $\tilde{A}_i^2$ is defined as:

$$\mu_{\tilde{A}_i^2}(x_{ij}) = e^{\frac{-(cs_{ij} - c_{i2})^2}{2\sigma_{i2}^2}} \quad (\forall x_{ij} \in X_i), \tag{7.5}$$

where c_{i2} (i=1 to n) and σ_{i2} (i=1 to n) are the parameters that, respectively, define the center and the spread of the Gaussian function and cs_{ij} is the class score of x_{ij} (Equation 7.1).

In the context of a hybrid neuro-fuzzy model, each unique combination of spatially-coincident predictor patterns ('unique conditions,' *see* Chapter 1, p. 6) is considered a vector of predictor features (or a feature vector). Because each predictor map is represented by one, and only one, pattern in a feature vector, the number of components (or dimensions) of the feature vector is equal to the number of predictor maps. The favorability of a feature vector with respect to target mineral deposit-type is estimated as follows.

Consider, for simplicity, a two-dimensional feature vector $T = [x_{1j}, x_{2j}]$, where x_{1j} and x_{2j} are the patterns representing, respectively, the predictor maps X_1 and X_2 in the feature vector. The membership values of x_{1j} in the fuzzy sets $\tilde{A}_1^1$ and $\tilde{A}_1^2$ are estimated using the fuzzy membership functions $\mu_{\tilde{A}_1^1}$ (Equation 7.3) and $\mu_{\tilde{A}_1^2}$ (Equation 7.5), respectively. Similarly, the membership values of x_{2j} in the fuzzy sets $\tilde{A}_2^1$ and $\tilde{A}_2^2$ are estimated using the fuzzy

membership functions $\mu_{\tilde{A}_2^1}$ (Equation 7.3) and $\mu_{\tilde{A}_2^2}$ (Equation 7.5), respectively. The favorability of T with respect to target mineral deposit-type is derived by combining the fuzzy membership values of x_{1j} in $\tilde{A}_1^1$ and $\tilde{A}_1^2$ and those of x_{2j} in $\tilde{A}_2^1$ and $\tilde{A}_2^2$ using a Takagi-Sugeno type fuzzy inference system based on fuzzy if-then rules (Jang and Sun, 1995; Jang, 1993).

A typical fuzzy if-then rule in a generalized Takagi-Sugeno type fuzzy inference system has the following form (Jang and Sun, 1995):

$$\text{IF } x \text{ is } a \text{ AND } y \text{ is } b \text{ THEN } z = f(x,y)$$

where x and y are input variables, a and b are fuzzy membership values of x and y, respectively, in the antecedent part of the fuzzy if-then rule and $z = f(x,y)$ is a crisp function in the consequent part of the rule. Usually, $f(x,y)$ is a polynomial in the input variables x and y, but it can be any function as long as it can appropriately describe the output of the system (Jang and Sun, 1995). When $f(x,y)$ is a first-order polynomial, the resulting fuzzy inference system in called a first-order Takagi-Sugeno type fuzzy inference system (Jang and Sun, 1995), which was originally proposed by Takagi and Sugeno (1985). When $f(x,y)$ is a constant, the resulting fuzzy inference system in called a zero-order Takagi-Sugeno type fuzzy inference system (Jang and Sun, 1995). The higher the order of the polynomial function in a fuzzy inference system, the larger is the number of the function parameters and, consequently, the larger is the number of training samples required for a robust estimation of these parameters. Therefore, the order of a fuzzy inference system used in an application is largely determined by the number of available training samples.

In the case of the feature vector T, there are two input predictor patterns, x_{1j} and x_{2j}, and four membership functions, $\mu_{\tilde{A}_1^1}$, $\mu_{\tilde{A}_1^2}$, $\mu_{\tilde{A}_2^1}$ and $\mu_{\tilde{A}_2^2}$, which can be combined using a first-order Takagi-Sugeno type fuzzy inference system based on the following fuzzy if-then rules:

1. IF x_{1j} is $\mu_{\tilde{A}_1^1}(x_{1j})$ AND x_{2j} is $\mu_{\tilde{A}_2^1}(x_{2j})$ THEN $F_1 = P_{10} + P_{11}x_{1j} + P_{12}x_{2j}$,

2. IF x_{1j} is $\mu_{\tilde{A}_1^1}(x_{1j})$ AND x_{2j} is $\mu_{\tilde{A}_2^2}(x_{2j})$ THEN $F_2 = P_{20} + P_{21}x_{1j} + P_{22}x_{2j}$,

3. IF x_{1j} is $\mu_{\tilde{A}_1^2}(x_{1j})$ AND x_{2j} is $\mu_{\tilde{A}_2^1}(x_{2j})$ THEN $F_3 = P_{30} + P_{31}x_{1j} + P_{32}x_{2j}$,

4. IF x_{1j} is $\mu_{\tilde{A}_1^2}(x_{1j})$ AND x_{2j} is $\mu_{\tilde{A}_2^2}(x_{2j})$ THEN $F_4 = P_{40} + P_{41}x_{1j} + P_{42}x_{2j}$,

where P_{ki} ($k = 1$ to 4, $i = 0$ to 2) is the parameter of the polynomial function in the consequent part of the kth fuzzy if-then rule.

The above fuzzy inference system is characterized by four fuzzy if-then rules, each of which contains, in the consequent part, a first-order polynomial function characterized by three parameters. Therefore, a first-order Takagi-Sugeno type fuzzy inference system with two input predictor maps and two fuzzy membership functions for each map results in $2^2(=4)$ fuzzy if-then rules and $2^2(2+1)(=12)$ function parameters. In general, a first-order Takagi-Sugeno type fuzzy inference system with n predictor maps and $2n$ fuzzy membership functions contains 2^n fuzzy if-then rules and $2^n(n+1)$ function parameters. Even for a moderately-large n, robust estimation of the function parameters would require a large number of training samples of known mineral deposits, which may not always be available. In such cases, it is preferable to use a zero-order Takagi-Sugeno type fuzzy inference system, which, in the case of the feature vector T, comprises the following fuzzy if-then rules:

1. IF x_{1j} is $\mu_{\tilde{A}_1^1}(x_{1j})$ AND x_{2j} is $\mu_{\tilde{A}_2^1}(x_{2j})$ THEN $F_1 = P_1$,

2. IF x_{1j} is $\mu_{\tilde{A}_1^1}(x_{1j})$ AND x_{2j} is $\mu_{\tilde{A}_2^2}(x_{2j})$ THEN $F_2 = P_2$,

3. IF x_{1j} is $\mu_{\tilde{A}_1^2}(x_{1j})$ AND x_{2j} is $\mu_{\tilde{A}_2^1}(x_{2j})$ THEN $F_3 = P_3$,

4. IF x_{1j} is $\mu_{\tilde{A}_1^2}(x_{1j})$ AND x_{2j} is $\mu_{\tilde{A}_2^2}(x_{2j})$ THEN $F_4 = P_4$,

where P_k ($k = 1$ to 4) is the parameter of the constant function in the consequent part of the kth fuzzy if-the rule. The number of function parameters is reduced to $2^2(=4)$ for the zero-order Takagi-Sugeno fuzzy inference system from $2^2(2+1)(=12)$ for the first-order Takagi-Sugeno fuzzy inference system. In general, a zero-order Takagi-Sugeno type fuzzy inference system with n predictor maps and $2n$ fuzzy membership functions contains 2^n fuzzy if-then rules and 2^n function parameters.

The firing strengths s_i ($i = 1$ to 4) of the above fuzzy if-then rules are calculated using *prod* t-norm operator as follows (Jang, 1993):

$$
\begin{aligned}
s_1 &= \mu_{\tilde{A}_1^1(x_{1j})} \times \mu_{\tilde{A}_2^1(x_{2j})}, \\
s_2 &= \mu_{\tilde{A}_1^1(x_{1j})} \times \mu_{\tilde{A}_2^2(x_{2j})}, \\
s_3 &= \mu_{\tilde{A}_1^2(x_{1j})} \times \mu_{\tilde{A}_2^1(x_{2j})}, \\
s_4 &= \mu_{\tilde{A}_1^2(x_{1j})} \times \mu_{\tilde{A}_2^2(x_{2j})}.
\end{aligned}
\tag{7.6}
$$

As a matter of fact, other t-norm operators that perform generalized AND can also be used for combining the fuzzy membership values in order to determine

the firing strengths of the fuzzy if-then rules (Jang, 1993). The output, O_k, of the kth ($k = 1$ to 4) fuzzy if-then rule is:

$$O_k = s_k \cdot F_k, \tag{7.7}$$

where F_k ($k = 1$ to 4) is the value of the function in the consequent part of the kth fuzzy if-then rule. The overall output of the fuzzy inference system is the weighted average of the output of all the four fuzzy if-then rules:

$$Overall\ Output = \frac{\sum_{k=1}^{4} O_k}{\sum_{k=1}^{4} s_k}. \tag{7.8}$$

The overall output is a measure of combined favorability of the feature vector T with respect to a target mineral deposit-type.

The above procedure can be easily extended for estimating the favorability of a feature vector comprising more than two predictor maps.

In a simple Takagi-Sugeno type fuzzy inference system, the parameters of fuzzy membership functions and consequent polynomial functions are estimated heuristically. However, in a hybrid neuro-fuzzy model, an ANFIS is used for estimating these parameters (Jang, 1993; Jang and Sun, 1995).

7.2.2 Architecture of adaptive neuro-fuzzy inference system

The basic architecture of an ANFIS comprises a Takagi-Sugeno type fuzzy inference system in a five-layer feed-forward network (Jang, 1993). Fig. 7.1 shows the simplified four-layer ANFIS architecture used in a hybrid neuro-fuzzy model for mineral potential mapping. The basic functionality of each layer is summarized in the following paragraphs.

Layer 1. There are $2n$ (=the number of fuzzy sets defined in the superset X) nodes in this layer. One half of the nodes ($= n$) contain the adaptive Gaussian fuzzy membership function defined in Equation 7.3, each of which receives one component (a predictor pattern x_{ij} encoded as a class score cs_{ij}) of an incoming n-dimensional feature vector and returns its membership value in the fuzzy set $\tilde{A}_i^1$ ($i = 1$ to n) containing 'favorable indicators of target mineral deposit-type'. The other half of the nodes ($= n$) contain the adaptive Gaussian fuzzy membership function defined in Equation 7.5, each of which also receives one component of the incoming feature vector and returns its membership value in the fuzzy set $\tilde{A}_i^2$ ($i = 1$ to n) containing 'unfavorable indicators of target

185
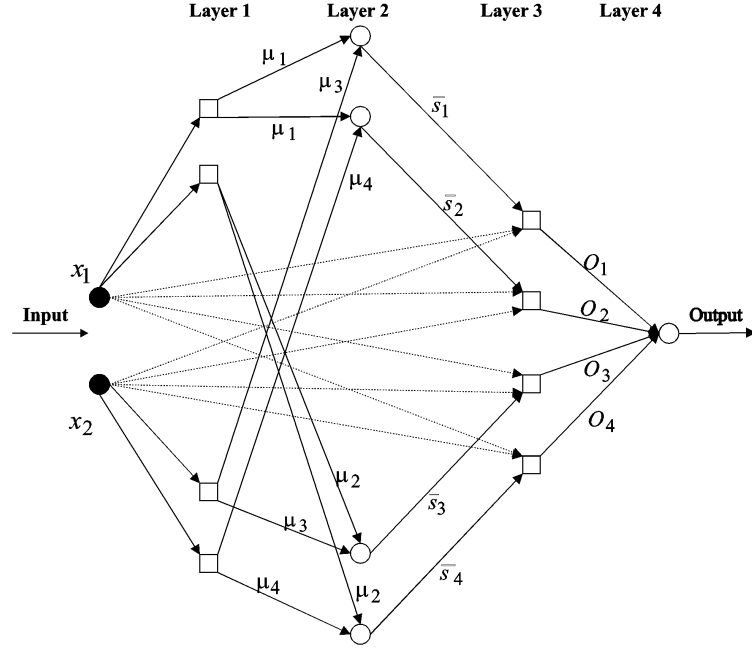
Figure 7.1: Simplified ANFIS for mineral potential mapping. Square and circular nodes contain, respectively, adaptive and fixed functions.

mineral deposit-type'. The parameters c and σ, which control the shape of a node function, and therefore output fuzzy membership values, are referred to as *premise parameters* (Jang, 1993).

Layer 2 Each of the 2^n (=the number of fuzzy if-then rules) nodes in this layer contains a *prod* t-norm operator as a node function, which synthesizes information transmitted by Layer 1 and returns a firing strength for each of the fuzzy if-then rules (cf. Equation 7.6):

$$s_k = \mu_{\tilde{A}_1^q}(x_{1j}) \times \mu_{\tilde{A}_2^q}(x_{2j}) \times ... \times \mu_{\tilde{A}_n^q}(x_{nj}), \qquad (7.9)$$

where $q = 1$ or 2, depending on whether $\mu_{\tilde{A}_i^q}$ defines fuzzy membership value of x_{ij} in the fuzzy set $\tilde{A}_i^1$ or in the fuzzy set $\tilde{A}_i^2$ ($i = 1$ to n). The output of each node is the normalized firing strength $\bar{s}_k$ ($k = 1$ to 2^n) of the kth fuzzy if-then rule given by:

$$\bar{s}_k = \frac{s_k}{\sum_{k=1}^{2^n} s_k}. \qquad (7.10)$$

186

Layer 3 Each of the 2^n (=the number of fuzzy if-then rules) nodes in this layer contains the following adaptive function:

$$O_k = \bar{s}_k \cdot F_k = \bar{s}_k(P_{k0} + P_{k1}x_{1j} + P_{k2}x_{2j} + ... + P_{kn}x_{nj}), \qquad (7.11)$$

where O_k is the output of the kth fuzzy if-then rule. The parameters P_{ki} ($k = 1$ to 2^n, $i=0$ to n) are referred to as *consequent parameters* (Jang, 1993). In the case of a zero-order Takagi-Sugeno type fuzzy inference system, $F_k = P_{k0}$.

Layer 4 The single node in this layer synthesizes information transmitted by Layer 3 and returns the overall output using the following fixed function:

$$Overall\ Output = \sum_{k=1}^{2^n} O_k \qquad (7.12)$$

7.2.3 Hybrid learning algorithm

Assuming that an ANFIS has two input variables, x_1 and x_2, the overall output is (Equations 7.11 and 7.12):

$$\begin{aligned}
O_1 + O_2 &= \bar{s}_1(P_{10} + P_{11}x_1 + P_{12}x_2) + \bar{s}_2(P_{20} + P_{21}x_1 + P_{22}x_2) \\
&= (\bar{s}_1)P_{10} + (\bar{s}_1x_1)P_{11} + (\bar{s}_1x_2)P_{12} + (\bar{s}_2)P_{20} + (\bar{s}_2x_2)P_{21} + (\bar{s}_2x_2)P_{22},
\end{aligned}$$
$$(7.13)$$

which is linear in the consequent parameters P_{ki}, if the premise parameters and, therefore, the firing strengths s_k of the fuzzy if-then rules are fixed. ANFIS uses a hybrid learning procedure (Jang and Sun, 1995) for estimation of the premise and consequent parameters. The hybrid learning procedure estimates the consequent parameters (keeping the premise parameters fixed) in a forward pass and the premise parameters (keeping the consequent parameters fixed) in a backward pass. In the forward pass, the information propagates forward until Layer 3 where the consequent parameters are estimated by the least square estimator method. In the backward pass, the error signals propagate backwards and the premise parameters are updated by a gradient descent method. The following description of the hybrid learning procedure is drawn from Jang (1993) and Jang and Sun (1995).

Forward pass: Least square estimator method.

For 2^n fuzzy if-then rules and Q n-dimensional training vectors (where n is the number of input predictor maps), Equation 7.13 can be expressed as:

$$B = AX \tag{7.14}$$

where B is a column vector containing output values of training vectors, A is a matrix containing one row for each training vector and X is an unknown vector whose elements are the consequent parameters P_{ki}. As the number of consequent parameters is $2^n(n+1)(= M$, say), the dimensions of A, X and B are $Q \times M$, $M \times 1$ and $Q \times 1$, respectively.

A least square estimate of X, denoted by X^*, can be used to minimize squared error $\|AX\text{-}B\|^2$. It can be computed as below:

$$X^* = (A^T A)^{-1} A^T B, \tag{7.15}$$

where A^T is the transpose of A and $(A^T A)^{-1}$ A^T is the pseudo-inverse of A, if $A^T A$ is non-singular. The above equation is expensive in computation when dealing with matrix inversion and, more over, becomes ill-defined if $A^T A$ is singular. ANFIS uses a recursive least-square method for estimating X as follows.

If a_q^T is the qth row vector of A and b_q^T is the qth element of B, then X can be calculated iteratively as follows:

$$X_{q+1} = X_q + \sum\nolimits_{q+1} a_{q+1}(b_{q+1}^T - a_{q+1}^T X_q) \tag{7.16}$$

$$\sum\nolimits_{q+1} = \sum_q - \frac{\sum_q a_{q+1} a_{q+1}^T \sum_q}{1 + a_{q+1}^T \sum_q a_{q+1}} \quad (for \ q = 0, 1, ..., Q-1), \tag{7.17}$$

where $\sum$ is called covariance matrix and the least square estimate X^* is equal to X_q. The initial conditions are $X_0 = 0$ and $\sum_0 = \gamma I$, where γ is a large positive number and I is an identity matrix of $M \times M$ dimensions.

Backward pass: Back-propagation method

Premise parameters of ANFIS are estimated iteratively by using a modified back-propagation learning rule (Rumelhart *et al.*, 1986) along with the chain rule as follows. In Equation 7.14, if the estimated output of the qth row vector, a_q, of the matrix A is o_q and the actual output is b_q, the qth element of B, then

an error margin for the qth training vector a_q can be defined as:

$$E_q = (b_q - o_q)^2. \tag{7.18}$$

If E_q is zero, then the actual output exactly matches the estimated output. Thus, the objective is to minimize an overall error measure, which is defined as $\sum_{q=1}^{Q} E_q$, where Q is the total number of training vectors.

In order to use the gradient descent method to minimize the error measure, a gradient vector is required to be calculated. It should be noted that a small change in the premise parameters (c or σ) will affect the output of the node containing the parameters, which, in turn, will affect the output of the single node in Layer 4 and, hence, the error measure will also change. Therefore in order to calculate the gradient vector of the parameters, a form of derivative information has to be passed, starting from Layer 4 and travelling back to Layer 1.

An error signal, $\epsilon_{(l,i)}$, can be defined as the ordered derivative (Werbos, 1974) of the error measure E_q with respect to the output of node i in Layer l ($l = 1$ to 4) as follows:

$$\epsilon_{l,i} = \frac{\partial^+ E_q}{\partial o_{(l,i)}}, \tag{7.19}$$

where $o_{(l,i)}$ is the output of the ith node of Layer l.

The error signal for the single output node of Layer 4 can be calculated as:

$$\epsilon_4 = \frac{\partial^+ E_p}{\partial o_{(4,1)}} = \frac{\partial E_p}{\partial o_{(4,1)}}, = -2(b_q - o_q).$$

For the ith node of the (non-output) Layer l ($l = 1$ to 3), the error signal can be derived using the chain rule:

$$\epsilon_{(l,i)} = \frac{\partial^+ E}{\partial o_{(l,i)}} = \sum_{m=1}^{N_{(l+1)}} \frac{\partial^+ E}{\partial o_{(l+1,m)}} \frac{\partial f_{(l+1,m)}}{\partial o_{(l,i)}} \tag{7.21}$$

$$= \sum_{m=1}^{N_{(l+1)}} \epsilon_{(l+1,m)} \frac{\partial f_{(l+1,m)}}{\partial o_{(l,i)}},$$

where $N_{(l+1)}$ is the number of nodes in Layer $(l+1)$, $o_{(l+1,m)}$ is the output of the mth node in Layer $(l+1)$, $f_{(l+1,m)}$ is the nodal function of the mth node in Layer $(l+1)$, $o_{(l,i)}$ is the output of the ith node in Layer l and $\epsilon_{(l+1,m)}$ is the

189

error signal at the mth node of Layer $(l + 1)$. In other words, the error signal of an internal node at Layer l can be expressed as a linear combination of the error signal of the nodes at Layer (l+1). Therefore, for the ith node of Layer 1, the error signal, $\epsilon_{(1,i)}$, can be obtained by first applying Equation 7.20 once to get error signals at the Layer 4 and then applying Equation 7.21 iteratively until Layer 1 is reached.

Because the consequent parameters are fixed in the backward pass, the gradient vector is defined as the derivative of the error measure with respect to each of the two premise parameters, c and σ, which reside in the nodes of Layer 1. The chain rule is applied to determine the gradient vectors as follows:

$$\frac{\partial^+ E_p}{\partial c_i} = \frac{\partial^+ E_p}{\partial o_{(1,i)}} \frac{\partial \mu_{1,i}}{\partial c_i} = \epsilon_{(1,i)} \frac{\partial \mu_{(1,i)}}{\partial c_i} \tag{7.22}$$

and

$$\frac{\partial^+ E_p}{\partial \sigma_i} = \frac{\partial^+ E_p}{\partial o_{(1,i)}} \frac{\partial \mu_{1,i}}{\partial \sigma_i} = \epsilon_{(1,i)} \frac{\partial \mu_{(1,i)}}{\partial \sigma_i}. \tag{7.23}$$

In the above equations, c_i and σ_i are, respectively, center and spread of the gaussian membership function $\mu_{(1,i)}$ in the ith node of layer 1.

The derivative of the overall error measure E with respect to c_i is:

$$\frac{\partial^+ E}{\partial c_i} = \sum_{q=1}^{Q} \frac{\partial^+ E_q}{\partial c_i} = \sum_{q=1}^{Q} \epsilon_{(1,i)} \frac{\partial \mu_{(}1,i)}{\partial c_i}, \tag{7.24}$$

where Q is the total number of training vectors. The update expression for the parameter c_i is given by:

$$\triangle c_i = -\eta \frac{\partial^+ E}{\partial c_i}, \tag{7.25}$$

where η is the learning rate, which can be expressed as follows:

$$\eta = \frac{\kappa}{\sqrt{\sum_{i=1}^{N(1)} (\frac{\partial E}{\partial c})^2}}, \tag{7.26}$$

where $N(1)$ is the total number of nodes in Layer 1 and κ is the step size or the length of each transition along the gradient direction in parameter space.

Similarly, the derivative of the overall error measure E with respect to σ_i is:

$$\frac{\partial^+ E}{\partial \sigma_i} = \sum_{q=1}^{Q} \frac{\partial^+ E_q}{\partial \sigma_i} = \sum_{q=1}^{Q} \epsilon_{(1,i)} \frac{\partial \mu_{(}1,i)}{\partial \sigma_i}, \tag{7.27}$$

where Q is the total number of training vectors. The update expression for the parameter σ_i is given by:

$$\triangle \sigma_i = -\eta \frac{\partial^+ E}{\partial \sigma_i}, \tag{7.28}$$

where η is the learning rate, which can be expressed as follows:

$$\eta = \frac{\kappa}{\sqrt{\sum_{i=1}^{N(1)}(\frac{\partial E}{\partial \sigma})^2}}, \tag{7.29}$$

where $N(1)$ is the total number of nodes in Layer 1 and κ is the step size or the length of each transition along the gradient direction in parameter space.

The above learning procedures were implemented using the software and procedure described by Jang and Gulley (1995).

7.3 Implementation of Hybrid Neuro-fuzzy Model

7.3.1 Data preprocessing

Curse of dimensionality

For a robust estimation of model parameters of an ANFIS, the number of training samples should be several times larger than the number of model parameters. However, as the dimensionality of feature space rises, the number of fuzzy if-then rules and, hence, the number of model parameters rises exponentially. For an n-dimensional feature space, 2^n fuzzy if-then rules are required for the construction of an adequate fuzzy inference system and therefore $2^n \times (n+1)$ consequent parameters are required to be estimated. For example, if the dimensionality of feature space is 1, the number of consequent parameters in the fuzzy inference system are 4; however, if the dimensionality of the feature space rises to 2, the number of consequent parameters in the fuzzy inference system rises six times to 12. Consequently, the number of training samples required for a robust estimation of model parameters also rises exponentially with an increase in the dimensionality of feature space. Training an ANFIS on insufficient number of training samples can lead to poor estimations of model parameters and hence lower the generalization capabilities of the ANFIS.

The problem can be addressed by (a) by reducing the dimensions of input data or (b) by using a zero-order Takagi-Sugeno type fuzzy inference system, which reduces the number of consequent parameters from $2^n(n+1)$ to 2^n (see Section 7.2.1) or (c) by using a combination of (a) and (b).

In an application of ANFIS to mineral potential mapping, if an adequately large number of training samples (i.e., known mineral deposits) are not available, the available predictor maps should be carefully scrutinized, and on the basis of *a priori* conceptual-genetic information on the target mineral deposit-type, only the most relevant maps should be selected for modeling. It is also possible to use statistical tools like principal component analysis and factor analysis to reduce the dimensionality of input data.

Data encoding

For adaptive neurofuzzy processing in an ANFIS, each input predictor pattern is encoded as a class score, which is calculated using Equation 7.1 and the knowledge-based ranking procedure described by Porwal *et al.* (2003a) and given in Chapter 3 (p. 69). This type of encoding is intuitive, simple, objective and, at the same time, easily interpretable.

Feature vectors

In the context of ANFIS, each unique condition is considered a feature vector and a unique condition map is considered a feature vector map (Chapter 6, p. 163). However, each component of a feature vector is defined by an ordinal class score. In an N-dimensional feature space, the location of each feature vector is defined by the class-score values of its N components.

Target, training and validation Vectors. Target vectors define output vectors to which input feature vectors are mapped by an ANFIS. Input feature vectors with known target vectors constitute training samples for an ANFIS. Validation samples also have known target vectors, but are used exclusively for validating the training of an ANFIS.

In mineral potential mapping, there is only one single-dimensional binary target vector, encoded as 1 or 0, which represents presence or absence, respectively, of a mineral deposit. The feature vectors defined by presence or by absence of a mineral deposit constitute training and validation samples. The feature vectors that are defined by presence of a mineral deposit are referred to as deposit training/validation samples and those defined by absence of mineral deposits are referred to as non-deposit training/validation samples. The procedures for selecting training and validation samples are described in Chapter 6 (p. 163).

192

7.3.2 Training of adaptive neuro-fuzzy inference system

The training of an ANFIS involves estimating the values of the premise and the consequent parameters, which map input training samples to their targets with a minimum total sum of squared error. However, the total sum of squared error may decrease indefinitely as a result of the onset of a specialized training on noisy training samples with increasing number of training epochs. The specialized training generates a fuzzy inference system that is overlearnt on training samples and therefore has poor generalization capabilities. In order to avoid specialized training, an early stopping procedure (Wang *et al.*, 1994) is used, which involves monitoring the total sum of squared error for an independent set of validation samples at the end of each training epoch and halting the training when it converges to a minimum.

7.4 Application to Base-Metal Potential Mapping in Aravalli Province

7.4.1 Data preprocessing

The predictor maps used in the application of the hybrid neuro-fuzzy model to base-metal potential mapping in the study area included the multi-class predictor maps of lithologies and stratigraphic groups, and the binary predictor maps of mafic igneous rocks, buffered distances from regional lineaments, buffered distances from NW-trending lineaments, buffered distances from NE-trending lineaments and buffered distances from fold axes. These are the same maps that were used in the weights-of-evidence and neural network applications described in Chapter 4 and Chapter 6, respectively.

Data encoding: Computation of class Scores

The class scores of the predictor patterns were calculated from class weights and map weights (Equation 7.1), which were assigned subjectively using the knowledge-based ranking procedure described by Porwal *et al.* (2003a). The detailed rationale for the ranking of the predictor maps and individual patterns is given in Chapter 3 (pp. 75-79). For each predictor map, the class scores of 'missing patterns' were derived by taking an area-weighted average of class scores of all patterns. The class weights, map weights and class scores for the input predictor maps are given in Table 7.1. Each predictor pattern was

193

encoded as a class score for the subsequent adaptive neuro-fuzzy processing.

Feature vectors

The seven predictor maps encoded as class scores were digitally-superposed and unique combinations of the predictor patterns in a unit area of 1 km^2 were mapped to generate a map constituting 1562 feature vectors. As the operation was carried out in a GIS-environment, an associated database was automatically generated, which held the components of the feature vectors. In the table, each 7-dimensional feature vector is described by a unique identification number and seven numeric components, each representing a predictor map encoded as a class score.

Training and validation vectors. The deposit training samples and deposit validation samples were selected on the basis of the same training and validation deposits that were used, respectively, for training and validating the neural network model (Chapter 6). The feature vectors spatially-coincident with the locations of the 40 training and 14 validation deposits were extracted to generate deposit training and deposit validation samples, respectively. As some feature vectors contained more than one deposit, a total of 36 deposit training samples and 12 deposit validation samples were generated.

For generating non-deposit training and non-deposit validation samples, the procedure described in Chapter 6 (p. 163) was used. At least 2 non-deposit locations, which were modeled by the weights-of-evidence analysis as having the lowest posterior probability of hosting base-metal deposits, were extracted from each of the 35 predictor patterns. Of these, 1 location was randomly extracted as non-deposit training points and the remaining locations were used as non-deposit validation points. The feature vectors spatially-coincident with the non-deposit training and non-deposit validation points were extracted to generate non-deposit training and non-deposit validation samples, respectively. To balance the number of deposit and non-deposit vectors in the training set, one non-deposit validation vector was randomly selected and shifted from the validation set to the training set.

The deposit and non-deposit training vectors were combined to generate a set of 72 training samples and the deposit and non-deposit validation vectors were combined to generate a set of 57 validation samples. Because there are 1562 feature vectors in this case as compared to 519 in the case of the RBFLN application, fewer feature vectors contain more than one deposit or

Table 7.1: Map weights, class weights and class scores

	Predictor map/Pattern	Map weight	Class weight	Class score
Predictor map of lithology				
1	Dolomite/dolomitic Marble	10	10	100
2	Calc-silicates	10	9	90
3	Graphic meta-pelites	10	8	80
4	Magnetite quartzite	10	7	70
5	Calc-schist/calc-gneiss	10	5	50
6	Quartzite/Arkose/Conglomerate	10	4	40
7	Migmatite/Gneisses	10	2	20
8	Not related to base metals	10	1	10
9	Missing Patterns	10	2.000	20
Predictor map of stratigraphy				
1	Rajpura-Dariba group	9	10	90
2	Pur-Banera group	9	9	81
3	Debari groups	9	8	72
4	Nathdwara group	9	7	63
6	Udaipur group	9	5	45
7	Jharol group	9	4	36
8	Sandmata Complex	9	3	27
9	Mangalwar Complex	9	2	18
10	Not related to base metals	9	1	9
11	Missing Patterns	9	2.778	25
Predictor map of mafic igneous rocks				
1	Mafic volcanic rocks	8	10	80
2	Not related to base metals	8	1	8
3	Missing Patterns	8	2.125	17
Predictor map of buffered distances from regional lineaments				
1	0-5.5 km	8	10	80
2	>5.5 km	8	1	8
3	Missing Patterns	8	4.875	39
Predictor Map of Buffered Distances from NW-trending Lineaments				
1	0-3 km	6	10	60
2	>3 km	6	1	6
3	Missing Patterns	6	5.000	30
Predictor map of buffered distances from NE-trending lineaments				
1	0-5 km	6	10	60
2	>5 km	6	1	6
3	Missing Patterns	6	5.000	30
Predictor map of buffered distances from fold axes				
1	0-1.25 km	7	10	70
2	>1.25 km	7	1	7
3	Missing Patterns	7	2.286	16

non-deposit, and therefore there are more training and validation samples in this application.

Reduction of dimensionality of input data: Factor analysis

A first-order Takagi-Sugeno-type ANFIS, which is capable of processing 7-dimensional input feature vectors, will contain 1024 consequent parameters and 28 premise parameters (see further above). A prohibitively-large number of training samples will be required for a robust estimation of such a large number of parameters. As discussed above, the number of parameters can be significantly reduced by using a zero-order Takagi-Sugeno-type fuzzy inference system. However, a zero-order Takagi-Sugeno-type ANFIS that is capable of processing 7-dimensional input feature vectors, will still contain 128 consequent parameters and 28 premise parameters. The number of parameters will still be too high to be robustly estimated using the 72 available training samples. It was therefore decided to use statistical tools for reducing the dimensionality of input feature vectors.

A principal components approach (Davis, 1986) was used for the factor analysis of the original set of 1562 seven-dimensional feature vectors. This involved (a) creation of a correlation matrix for the set of all feature vectors, (b) an eigenanalysis of the correlation matrix for extraction of seven eigenvectors (or factors) and eigenvalues, (c) retention of the first three factors, whose eigenvalues are more than 1 (i.e., the factors that contain more variance than the seven original standardized variables) and (d) rotation of the three factors using the varimax method with Kaiser normalization (Davis, 1986).

The contribution made by each of the seven predictor maps to each rotated factor can be estimated from the rotated factor matrix (Table 7.2). The major contributors to the first factor are the predictor maps of lithology and stratigraphy, which represent the primary controls of base-metal mineralization in the Aravalli province (recognition criteria 1 and 2; Chapter 2, p. 47). The major contributors to the second rotated factor are the predictor maps of mafic igneous rocks and buffered NE-trending lineaments, which represent, respectively, the heat sources for circulation of exhalative brines (recognition criterion 4, Chapter 2; p. 47) and favorable structures (recognition criterion 5, Chapter 2; p. 47). The major contributors to the third rotated factor are the predictor maps of buffered regional lineaments (representing favorable structural conduits for heat sources and hydrothermal discharge; recognition criterion 5, Chapter 2; p. 47) and buffered NW-trending lineaments and fold

196

Table 7.2: Rotated factor matrix showing loadings of Predictor maps

	Factor(eigenvalue)		
Predictor map	**1**(1.537)	**2**(1.034)	**3** (1.010)
Lithologies	0.824	-0.00781	-0.128
Stratigraphic groups	0.742	0.147	0.178
Mafic igneous rocks	0.121	0.678	0.166
Buffered regional lineaments	0.286	0.322	-0.555
Buffered NW-lineaments	0.192	0.176	0.792
Buffered NE-lineaments	-0.00612	0.72	-0.132
Buffered fold axes	0.0037	0.00085	0.503

axes (representing favorable structures- recognition criterion 5; Chapter 2, p. 47). The rotated factors are therefore interpreted to represent all the five significant recognition criteria for base-metal deposits in the Aravalli province.

Subsequently, the original seven components (predictor maps encoded as class scores) of each of the 1562 feature vectors were replaced by three components (*rotated factors*) to generate a transformed set of 1562 three-dimensional feature vectors.

7.4.2   Construction of adaptive neuro-fuzzy inference system

Based on the prototypical ANFIS for mineral potential mapping described above, an ANFIS was constructed with a network topology of 6-8-8-1 (Fig. 7.2).

Layer 1

As a result of factor analysis and rotation, the two fuzzy sets $\tilde{A}^1$ and $\tilde{A}^2$ (Equations 7.2 and 7.4) are now defined in terms of rotated factor scores and not class scores. Accordingly, the adaptive node functions given in Equations 7.3 and 7.5 are, respectively, modified as follows:

$$\mu_{\tilde{A}^1_{v_i}} = e^{\frac{-(f_j - c_{i1})^2}{2\sigma_{i1}^2}} \quad (\forall v_i \in V_j), \tag{7.30}$$

and

$$\mu_{\tilde{A}^2_{v_i}} = e^{\frac{-(f_j - c_{i2})^2}{2\sigma_{i2}^2}} \quad (\forall v_i \in V_j), \tag{7.31}$$

where f_j is the rotated factor score of the ith component v_i (i=1 to 3) of the jth feature vector V_j.

Layer 1 contains six nodes, of which three nodes return a fuzzy membership

197
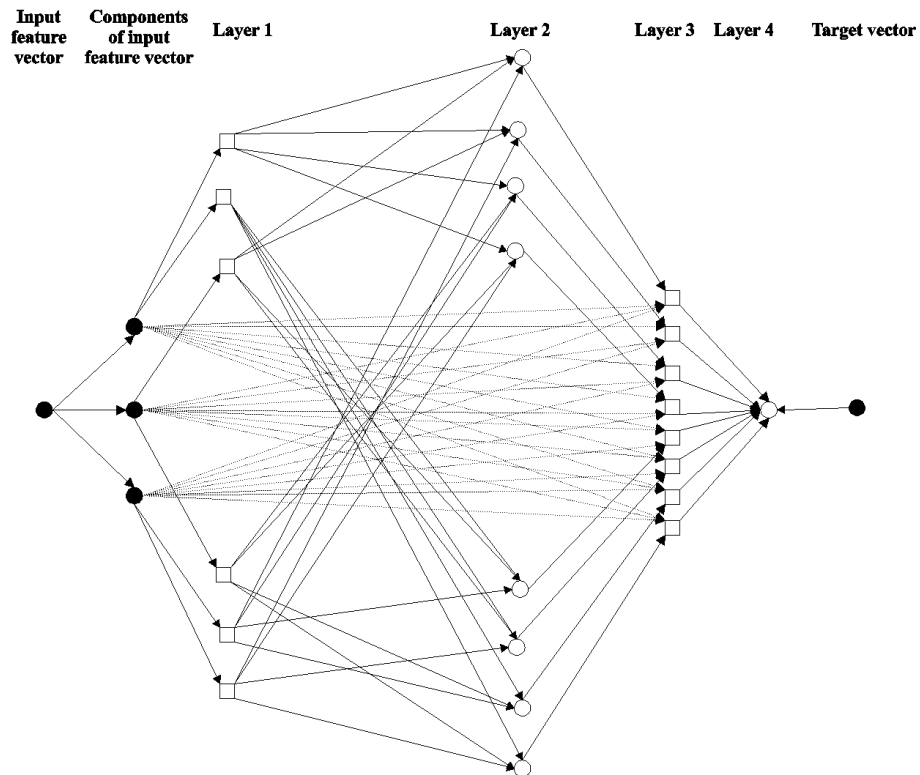
Figure 7.2: ANFIS with network topology of 6-8-8-1 for mapping base-metal potential in study area. Hollow square and hollow circles are, respectively, adaptive and fixed nodes.

value for each component of an input feature vector in $\tilde{A}^1$ and three nodes return a fuzzy membership value of each component of an input feature vector in $\tilde{A}^2$. Because each node contains a Gaussian function characterized by two parameters, there are in all 12 premise parameters to be estimated in this layer.

Layer 2

The ANFIS is based on the following eight zero-order Takagi-Sugeno type fuzzy if-then rules:

1. IF v_1 is unfavorable AND v_2 is unfavorable AND v_3 is unfavorable THEN output is P_{10}

2. IF v_1 is unfavorable AND v_2 is unfavorable AND v_3 is favorable THEN output is P_{20}

3. IF v_1 is unfavorable AND v_2 is favorable AND v_3 is unfavorable THEN output is P_{30}

4. IF v_1 is unfavorable AND v_2 is favorable AND v_3 is favorable THEN output is P_{40}

5. IF v_1 is favorable AND v_2 is unfavorable AND v_3 is unfavorable THEN output is P_{50}

6. IF v_1 is favorable AND v_2 is unfavorable AND v_3 is favorable THEN output is P_{60}

7. IF v_1 is favorable AND v_2 is favorable AND v_3 is unfavorable THEN output is P_{70}

8. IF v_1 is favorable AND v_2 is favorable AND v_3 is favorable THEN output is P_{80}

The firing strengths of the above fuzzy if-then rules are computed in Layer 2. The layer contains eight fixed nodes, one for each fuzzy if-then rule. Every node contains a *prod* t-norm operator, which computes and returns a *normalized* firing strength (Equations 7.9 and 7.10) for a corresponding fuzzy if-then rule.

199

Layer 3

This layer contains eight adaptive nodes, one for each fuzzy if-then rule. Each node computes the output of a fuzzy if-then rule using the following function:

$$O_k = \bar{s}_k \times P_{k0} \quad (k = 1 \ to \ 8), \tag{7.32}$$

The total number of consequent parameters to be estimated in this layer is 8.

Layer 4

The single fixed node in this layer sums the output of Layer 3 and returns an overall output for an input feature vector as follows:

$$Overall \ Output = \sum_{k=1}^{8} O_k \tag{7.33}$$

7.4.3 Training of adaptive neuro-fuzzy inference system

The ANFIS on the training data for 100 epochs using the hybrid learning algorithm, and monitored the total sum of squared error for the validation samples at the end of each epoch. The total sum of squared error for validation samples converged to a minimum of 0.194 at the end of 70 training epochs (Fig. 7.3). Therefore the adaptive neuro-fuzzy inference system was trained for 70 epochs to estimate the values of the premise parameters and consequent parameters.

The trained Takagi-Sugeno type fuzzy inference system was used for a predictive classification all 1562 feature vectors.

7.4.4 Favorability maps

The output predictive classification value for each feature vector predicts the extent to which the feature vector belongs to either the class that contains base-metal deposits or the class that does not contain a base-metal deposit and therefore can be interpreted as a measure favorability of the feature vector with respect to base-metal mineralization in the study area. The predictive classification values, which ranged from -0.1133 to 1.0248, were rescaled between 0 and 1 and mapped to generate a continuous-scale predictive classification map (Fig. 7.4). Fig. 7.5 shows the plot of predictive classification values against cumulative percent area.

200
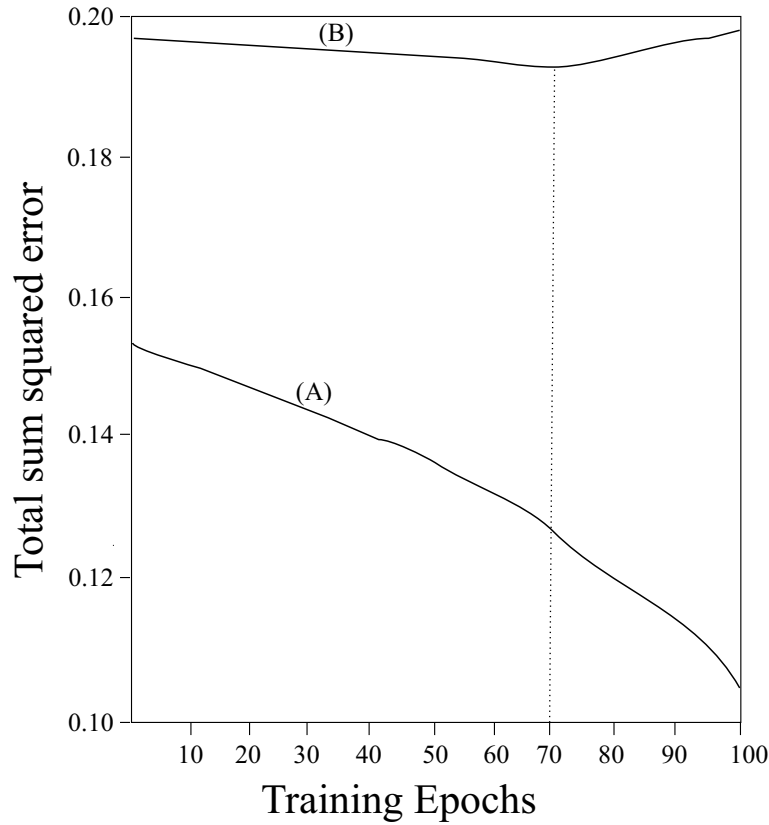
Figure 7.3: Number of training epochs versus total sum of squared error for training vectors (curve A) and validation vectors (curve B).

It is difficult to interpret the continuous-scale predictive classification map for demarcating target areas for base-metal exploration. The continuous-scale predictive classification map was therefore reclassified into a binary favorability map (Fig. 7.6) showing zones with high favorability and low favorability for base-metal deposits based on a threshold predictive classification value represented by the inflexion point (90.25, 0.388) along the curve in Fig. 7.5.

Validation of favorability map

The binary favorability map was validated by overlaying the deposit training and deposit validation points on the map (Fig. 7.6) and by plotting the position of these deposits on the predictive classification value versus percent cumulative percent area curve (Fig. 7.5). Table 7.3 shows that the high favorability zones
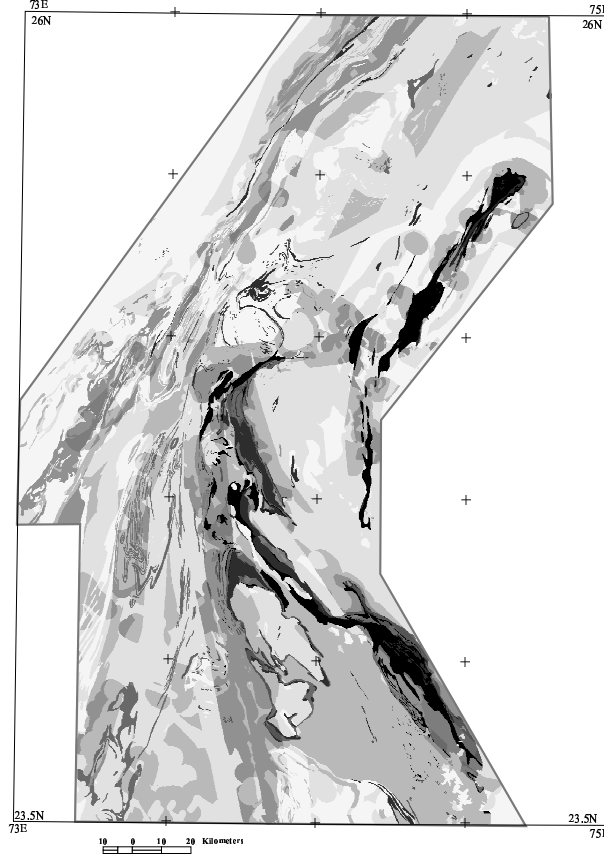
Figure 7.4: Continuous-scale predictive classification map. Predictive classification value varies from 0 (white) to 1 (black).

occupy 9.75% of the study area and contain all training deposits and 83.3% of the validation deposits and the low favorability zones occupy 90.25% of the study area and contain 16.7% of the validation deposits.

All major base-metal deposits of the province, including the world class deposit of Rampura-Agucha and other large deposits of the Rajpura-Dariba and Zawar belts, are contained in the high favorability zones. One of the two validation deposits contained in the low favorability zones is the VMS-type Basantgarh deposit of the South Delhi belt, which is genetically different from the SEDEX-type deposits used for training the ANFIS. The other deposit contained in the low favorability zones is a minor deposit hosted by the basal sequences of the Aravalli belt.
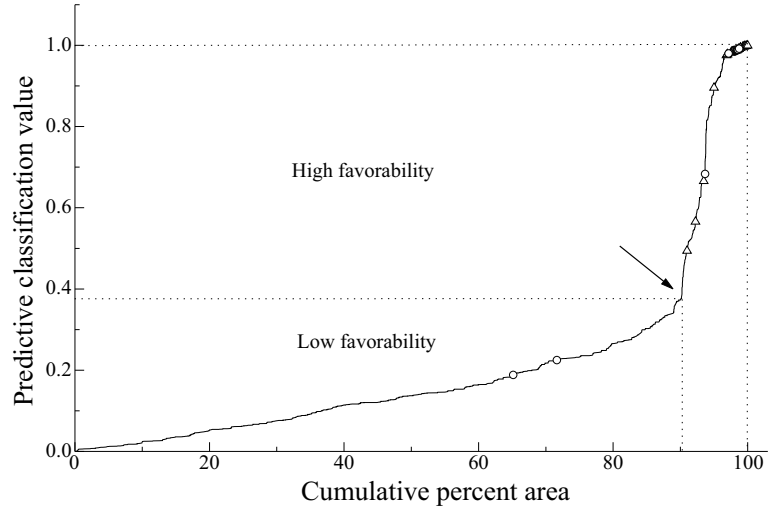
Figure 7.5: Variation of predictive classification values with cumulative percent area. Inflection point (marked by arrow) correspond to threshold value used for generating binary favorability map. Triangles are training base-metal deposits and circles are validation base-metal deposits.

Table 7.3: Validation of favorability map

Favorability zone	Percent of study area	Percent of validation deposits	Percent of training deposits
High favorability	9.75	83.3	100
Low favorability	90.25	16.7	Nil

7.5 Discussion

One of the most significant procedures in hybrid neuro-fuzzy modeling is the definition of fuzzy membership values. The Gaussian fuzzy membership functions (Equations 7.3 and 7.5) used in the present model are S-shaped, as advocated by several authors (Goguen, 1969; Zadeh, 1971; Zimmermann, 1991), and return membership values that lie between 0 and 1. However, fuzzy membership values returned by these functions are determined by the values of the parameters c and σ, which, respectively, define the center and the spread of the functions. Because the fuzzy membership values propagate through a model and control the final output, it is important to estimate the values of these parameters precisely. Porwal *et al.* (2003a) used a similar Gaussian function for calculating fuzzy membership values in the knowledge-driven fuzzy model

203
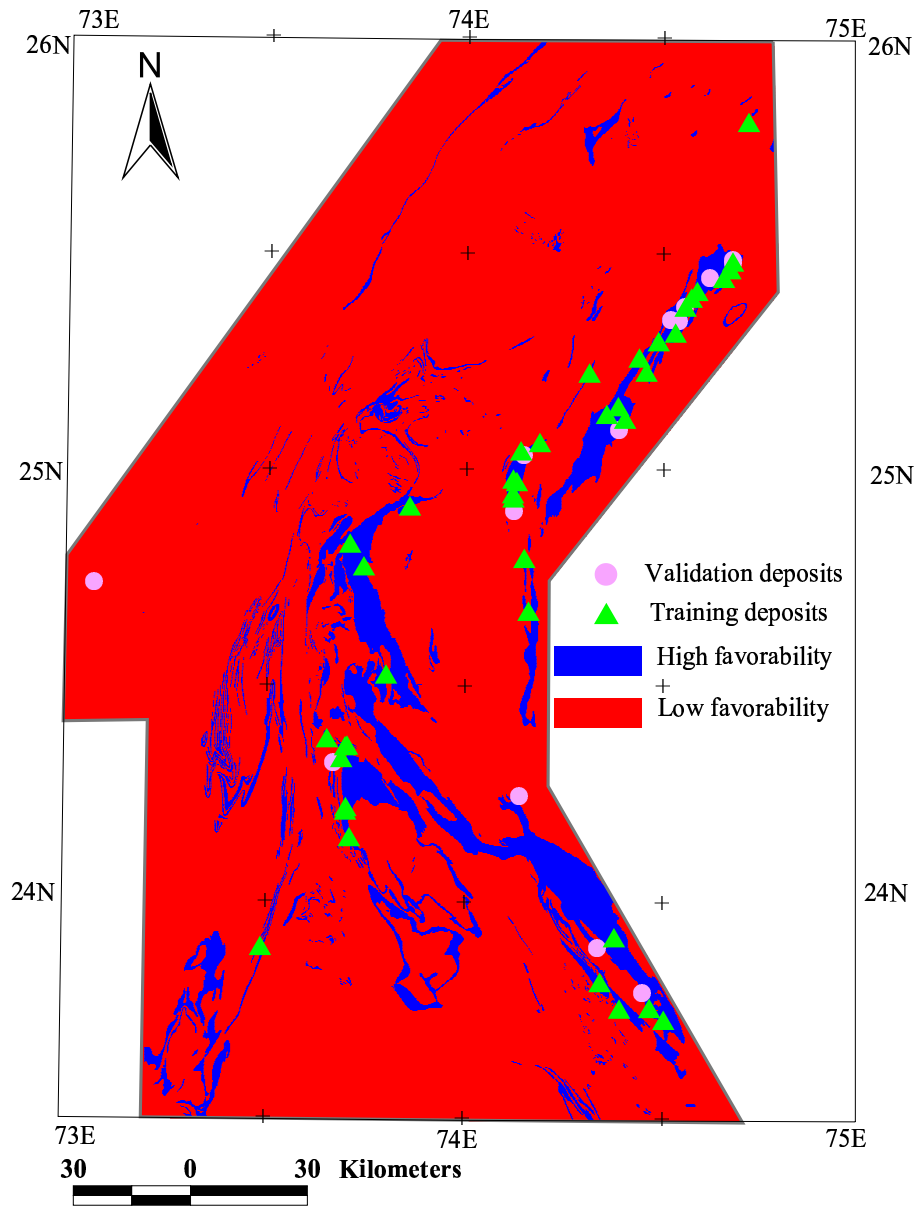
Figure 7.6: Binary favorability map.

for mineral potential mapping (*see also* Chapter 3, p. 69). However, a fuzzy model does not possess a learning capability and therefore the values of parameters of the function were estimated heuristically. Neural networks, on the other hand, possess an excellent capability of learning from empirical data and therefore the implementation of fuzzy model in the framework of adaptive neural networks provides a more efficient method for parameter estimation.

The use of neural networks in hybrid neuro-fuzzy models also provides a way of compensating for the possible errors in the estimations of class scores, which are based on a subjective assessment of relative favorability of input predictor patterns. By adjusting the parameters of the fuzzy inference system, the neural network in a hybrid neuro-fuzzy model minimizes the contribution of class scores that are inconsistent with known output.

Because the adaptive neuro-fuzzy inference system in the present application was required to classify an input feature vector as favorable or unfavorable with respect to base-metal deposits, only one single-dimensional binary target vector that represented presence or absence of a base-metal deposit was defined. Moreover, only two fuzzy sets were defined, one containing favorable indicators of base-metal deposits and the other containing unfavorable indicators of base-metal deposits. Theoretically it is possible to create several sets of fuzzy sets. For example, a third set of fuzzy sets containing 'moderately favorable indicators of target mineral deposit-type' can be created using a bell-shaped Gaussian function. However, a large number of fuzzy sets results in an undesirably large number of model parameters and therefore should be used only if a sufficiently large number of training samples are available.

The output of a hybrid neuro-fuzzy model is not likely to be affected by conditional dependence amongst two or more input predictor maps because (a) t-norm operators, which implement generalized intersection operations, are used for calculating firing strengths of fuzzy if-then rules and therefore the contributions of conditionally dependent component is filtered out and (b) values of the parameters of the consequent linear functions are estimated by a neural network and are therefore so adjusted that the contributions of conditionally dependent components are minimized.

In weights-of-evidence models, the weights of evidence for an evidential pattern can be calculated, if, and only if, it contains at least one known deposit of the target deposit-type. Weights-of-evidence models are therefore generally implemented using binary evidential maps, as discusses in Chapter 5 (p. 146). These models, however, have also been used with multi-class evidential maps

(*see* Chapter 4 for references) but in such cases the weights of evidence are determinable only for the patterns that contain at least one known deposit of the target deposit-type (although it is possible to extrapolate the weights of evidence of the patterns that do not contain any known deposits from weights-of-evidence models of well-explored areas worldwide, as suggested by Singer and Kouda, 1999). In contrast, hybrid neuro-fuzzy models can be conveniently implemented using multi-class evidential maps, because class scores of evidential patterns are estimated on the basis of expert knowledge only, irrespective of whether or not they contain known deposits.

However, a large number of input evidential maps poses a problem in the application of the hybrid neuro-fuzzy approach to mineral potential mapping, if the number of available training vectors is small (curse of dimensionality; Bellman, 1961). This is because as the number of input evidential maps increases, there is an of an exponential increase in the number of fuzzy if-then rules and, therefore, in the number of consequent parameters. The problem can be addressed, however, by using a zero-order Takagi-Sugeno type neuro-fuzzy inference system, which reduces the number of consequent parameters significantly. In extreme modeling situations, where there are a large number of evidential maps and very few training vectors available, the values of consequent parameters of a zero-order Takagi-Sugeno type fuzzy inference system can be fixed as 1. This reduces a Takagi-Sugeno type neuro-fuzzy inference system to the simple knowledge-driven fuzzy model described by Porwal *et al.* (2003a) with the difference that, in this case, the parameters of fuzzy membership functions are estimated by a neural network. Alternatively, the dimensions of input feature vectors can be reduced by using statistical methods like principal component analysis or factor analysis (Davis, 1986), as demonstrated in the present application. The modeling results indicate that factor analysis provides an efficient way of reducing the dimensionality of input feature vectors and thus contributes to a robust estimation of model parameters.

The results also demonstrate the ability of an adaptive neuro-fuzzy inference system to recognize the patterns that are critical indicators of the target mineral deposit-type and estimate the values of model parameters in such a way that the contribution of such patterns is maximized. For example, the world class deposit of Rampura-Agucha is located in a peneplained and soil-covered local meta-sedimentary enclave, well-within the basement complex, which shows no physical continuity with the main sedimentary basins of the Bhilwara belt. Moreover public-domain structural data are meagre from the

area and the deposit is not covered in the regional aeromagnetic data used in this research. However, the hybrid neuro-fuzzy model returned a high predictive classification value of 0.895 for the deposit.

7.6 Conclusions

The application of adaptive neuro-fuzzy inference system to base-metal potential mapping in the study area results in demarcation of high favorability zones occupying 9.75% of the study area, which predict 96% of the known base-metal deposits. This is a significant result both in terms of reduction in search area and the number of deposits predicted. From this application, therefore, the following conclusions are drawn.

- The hybrid neuro-fuzzy approach provides a strong modeling framework for a consistent utilization of both conceptual and empirical components of earth science information for mineral potential mapping.

- The class score-based Gaussian membership functions provide operational mathematical tools for an efficient utilization of knowledge-base in the modeling procedure.

- By implementing a fuzzy inference system in the framework of an adaptive neural network, the hybrid neuro-fuzzy approach provides a robust data-based method for estimating the parameters of the fuzzy inference system.

- The output of a hybrid neuro-fuzzy model is not likely to be affected by the conditional dependence amongst two or more predictor maps. Moreover, multi-class predictor maps can be conveniently used in a hybrid neuro-fuzzy model.

- In the hybrid neuro-fuzzy approach, the problems related to dimensionality of input feature vectors can be addressed by using zero-order Takagi-Sugeno type fuzzy inference systems and/or statistical methods like factor analysis.

- Similar hybrid neuro-fuzzy inference system can be constructed and implemented for modeling larger-scale evidential maps to demarcate specific prospects within the predicted potentially-mineralized zones.

The high performance levels of the hybrid neuro-fuzzy and neural network models, described, respectively, in this and the previous chapters, indicate that machine learning algorithms can efficiently recognize and account for possible conditional dependencies amongst input predictor patterns. Considering that the most serious theoretical objection to Bayesian probabilistic models for mineral potential mapping is posed by the violation of the assumption of conditional independence, suitable parameter learning algorithms can be used to induce Bayesian models to recognize and account for possible conditional dependencies amongst input predictor patterns. In the next chapter, a Bayesian network classifier is described that uses probabilistic machine learning algorithms for dealing with conditional dependencies amongst input predictor patterns. The tolerance of Bayesian classifiers for the violation of the conditional independence assumption is also examined in the next chapter.

Chapter 8

Bayesian Network Classifier Models

In this chapter, three Bayesian network classifiers for mineral potential mapping are described: (a) a naive Bayesian classifier that assumes complete conditional independence of input predictor patterns, (b) an augmented naive Bayesian classifier that recognizes and accounts for conditional dependencies amongst input predictor patterns and (c) a selective naive classifier that uses only conditionally-independent predictor patterns. The three classifiers are applied to base-metal potential mapping in the study area.

The chapter has been published as "Bayesian Network Classifiers for Mineral Potential Mapping" (Porwal *et al.*, 2006a).

8.1   Introduction

A Bayesian network is an annotated directed acyclic graph (DAG) that models uncertain relationships amongst variables in a complex system (Fig. 8.1). Fundamental to Bayesian networks is the idea of modularity, i.e., a complex system can be decomposed into several consistent modules, which are represented by Markov blankets of the variables. The Markov blanket of a variable comprises its parent variables, its child variables and parents of its child variables (Pearl, 1988). Parent and child variables are identified on the basis of mutual dependencies - a child variable is conditionally dependent on a set of parent variables. The Markov blankets of all variables can be connected to obtain a comprehensive representation of the whole complex system.

A Bayesian network is completely described by two components: (a) a

Variable 3	Variable 4	Variable 5	
		Absent	Present
Absent	Absent	0.995	0.005
Absent	Present	0.790	0.210
Present	Absent	0.125	0.875
Present	Present	0.400	0.600
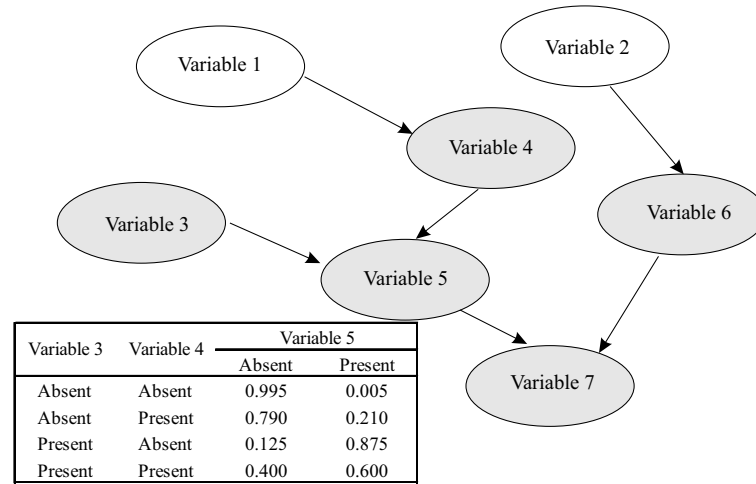
Figure 8.1: Simple Bayesian network on seven binary variables. Nodes and directed arcs represent variables and conditional dependencies, respectively. Shaded nodes constitute Markov blanket of Variable 5. Contingency table illustrates parameters (conditional dependencies) associated with Variable 5.

DAG and (b) numeric parameters. The DAG specifies the topological configuration of nodes, which represent variables, and directed arcs, which represent causal relationships or dependencies amongst the variables. The numeric parameters quantify the inter-variable dependencies in terms of conditional probabilities. The use of formal probabilistic semantics makes a Bayesian network amenable to statistical manipulation (Pearl, 1988; Heckerman, 1995).

In their original conception, Bayesian networks were based on a concept-driven (or *Bayesian*; Heckerman, 1995) interpretation of probability and therefore were mainly used for encoding and propagating uncertain expert knowledge in expert systems (for example, Duda *et al.*, 1978). However, statistical roots of Bayesian networks and advancement in machine learning led to the development of intelligent Bayesian networks that are capable of inductive learning and generalization (for example, Cooper and Herskovits, 1992; Badsberg, 1992; Aliferis and Cooper, 1994; Buntine, 1994; Heckerman *et al.*, 1995; Ramoni and Sebastiani, 1999; Cheng *et al.*, 2002). As in the case of neural networks, input data for Bayesian networks are formatted as matrices of feature vectors.

A Bayesian classifier is a special Bayesian network in which one, and only one, variable represents a *class variable* and all other variables are considered as *attributes* characterizing the class variable. The class variable is at the root

of the network, i.e., it has no parent variables, while each attribute has *at least* the class variable as a parent (depending upon the structure of a Bayesian classifier, it is possible for an attribute to have other attributes as parents; see further below). A class variable can have two or more states, with each state representing a discrete class label. Similarly, attributes can also be binary or multi-state. The task of a Bayesian classifier is to map an input feature vector comprising particular instances of attributes to a specific class label. For this, the classifier is trained on a set of pre-classified feature vectors, which results in the induction of conditional probabilities of all attributes given the class variable. The trained classifier applies Bayes' rule to compute the posterior probabilities of all states of the class variable given the particular instances of attributes in the feature vector and predicts the class label that gets the highest posterior probability.

Mineral potential mapping of an area can be interpreted in terms of predictive classification of each spatial unit having a unique combination of spatially-coincident predictor patterns (or unique conditions) as mineralized or barren with respect to a target mineral deposit-type. If (a) the target mineral deposit-type is considered a binary class variable (with the labels 'mineralized' and 'barren'), (b) predictor patterns are considered attributes that characterize the class variable and (c) each unique condition is considered a feature vector containing instances of attributes, then a Bayesian classifier can be constructed and trained on a subset of pre-classified feature vectors (i.e., the unique conditions that are associated with either a known mineralized or a known barren location). The trained classifier can be used for processing all feature vectors. The output determines the extent to which a feature vector belongs to either the mineralized class or the barren class and can be mapped to generate a favorability map.

One simple Bayesian classifier that can be used in mineral potential mapping is *naive Bayesian classifier* described by Duda and Hart (1973) and Langley *et al.* (1992). However, this classifier assumes complete conditional independence amongst attributes, which is unrealistic for many predictor patterns used in mineral potential mapping. Although a naive Bayesian classifier performs well in several domains (Domingos and Pazzani, 1996; Friedman, 1997), Friedman *et al.* (1997) show that its performance can be improved by relaxing the assumption of conditional independence. Several Bayesian

classifiers unrestricted* by the conditional independence assumption are described in literature, for example, *semi-naive Bayesian classifier* (Kononenko, 1991); *Bayesian multinet classifier* (Heckerman, 1990; Geiger and Heckerman, 1996), *tree-augmented naive Bayesian classifier* (Friedman *et al.*, 1997); *augmented naive Bayesian classifier* (Friedman *et al.*, 1997) etc. Langley and Sage (1994) proposed a *selective naive Bayesian classifier*, which is essentially a naive Bayesian classifier that makes classification based on only conditionally-independent variables.

8.2 Bayesian Classifiers

Given a finite set $\mathbf{U} = \{X_1, ... X_n\}$ of discrete random variables, a Bayesian network on $\mathbf{U}$ is defined as the following pair (Friedman *et al.*, 1997):

$$B = \langle G, \Theta \rangle, \tag{8.1}$$

where G is a DAG and Θ is a set of parameters that quantifies the network. The DAG G encodes the following assumption: each variable X_i is independent of its non-descendants, given its parents in G. The set Θ contains a parameter $\theta_{x_i | \Pi_{x_i}}$ for each possible value x_i of X_i and Π_{x_i} of Π_{X_i}, where Π_{X_i} denotes the set of parents of X_i in G. The Bayesian network B defines a unique joint probability distribution over $\mathbf{U}$:

$$Prb_B(X_1, ..., X_n) = \prod_{i=1}^{n} Prb_B(\Pi_{X_i}) = \prod_{i=1}^{n} \theta_{X_i | \Pi_{X_i}}.$$

Consider the special case of a set $\mathbf{U}^* = \{P_1, ..., P_I, D\}$, where the variables $P_1, ..., P_I$ represent predictor patterns (or, in short, predictors) and D represents the class variable 'target mineral deposit-type'. It is assumed that (a) P_i and D are random discrete variables, (b) P_i can have J (≥ 2) states such that $P_i = \{p_{i1}, ..., p_{iJ}\}$ and (c) D is binary such that $D = \{d_0$ (barren), d_1 (mineralized)$\}$. Let $\Pi_i = \{\pi_{i1}, ..., \pi_{iK}\}$ be the set of K ($K \geq 1$) parents of P_i and $\Pi_{i\bar{D}} = \{\Pi_i - D\}$. Let Π_D be the set of parents of D. Consider a Bayesian network $B = \langle G, \Theta \rangle$ in which D is at the root, i.e., $\Pi_D = \emptyset$ and every predictor

---

*In this thesis, the terms *augmented naive Bayesian classifier* (shortened to *augmented naive classifier*) and *naive Bayesian classifier* (shortened to *naive classifier*) are used, respectively, for naive Bayesian classifiers unrestricted by the assumption of conditional independence and naive Bayesian classifiers *sensu stricto* (*see also* Friedman *et al.*, 1997).

has D as its one, and only one, parent, i.e., $\Pi_i = D$ and $\Pi_{i\bar{D}} = \emptyset$. The joint probability distribution of such a network is given by:

$$Prb_B(P_1, ..., P_I, D) = \alpha \cdot Prb(D) \cdot \prod_{i=1}^{I} Prb(P_I|D),$$

where α is a normalizing constant. This is a naive Bayesian classifier as defined by Langley *et al.*, 1992). Let $\mathbf{f_m} = [p_{1j}, p_{2j}, ..., p_{Ij}]$ be an I-dimensional input feature vector, which is required to be classified as either d_0 (barren) or d_1 (mineralized). The posterior probabilities of d_0 and d_1 for $\mathbf{f_m}$ are calculated using the following sequential updating over every predictor:

$$Prb(d_1|p_{1j}) = \frac{Prb(d_1) \cdot Prb(p_{1j}|d_1)}{Prb(d_1) \cdot Prb(p_{1j}|d_1) + Prb(d_0) \cdot Prb(p_{1j}|d_0)},$$

$$Prb(d_0|p_{1j}) = 1 - Prb(d_1|p_{1j});$$

$$Prb(d_1|p_{1j}, p_{2j}) = \frac{Prb(d_1|p_{1j}) \cdot Prb(p_{2j}|d_1)}{Prb(d_1|p_{1j}) \cdot Prb(p_{2j}|d_1) + Prb(d_0|p_1) \cdot Prb(p_{2j}|d_0)},$$

$$Prb(d_0|p_{1j}, p_{2j}) = 1 - Prb(d_1|p_{1j}, p_{2j});$$

$$...$$

$$\quad (8.4)$$

$$Prb(d_1|p_{1j}, p_{2j}..p_{Ij}) =$$

$$\frac{Prb(d_1|p_{1j}, p_{2j}, ..p_{(I-1)j}) \cdot Prb(p_{Ij}|d_1)}{Prb(d_1|p_{1j}, p_{2j}, ..p_{(I-1)j}) \cdot Prb(p_{Ij}|d_1) + Prb(d_0|p_{1j}, p_{2j}, ..p_{(I-1)j}) \cdot Prb(p_{Ij}|d_0)},$$

$$Prb(d_0|p_{1j}, p_{2j}..p_{Ij}) = 1 - Prb(d_1|p_{1j}, p_{2j}..p_{Ij}).$$

If $Prb(d_1|p_{1j}, p_{2j}..p_{Ij}) > Prb(d_0|p_{1j}, p_{2j}..p_{Ij})$, $\mathbf{f_m}$ is classified as d_1, otherwise as d_0.

Augmented naive Bayesian classifiers are obtained from naive Bayesian classifiers by relaxing the restriction that every predictor can have the target mineral deposit-type as the one, and only one, parent, i.e., $\Pi_{i\bar{D}}$ need not necessarily be a null set. An augmented naive classifier estimates the posterior probabilities of d_0 and d_1 for $\mathbf{f_m}$ using a sequential updating procedure similar to the one used by a naive classifier. However, while updating the probability over a predictor P_i, an augmented naive classifier also takes $\Pi_{i\bar{D}}$ into account:

$$Prb(d_1|p_{1j}, p_{2j}..p_{Ij}) =$$

$$\frac{Prb(d_1|p_{1j}, ..p_{(I-1)j}) \cdot Prb(p_{Ij}|\Pi_{i\bar{D}}, d_1)}{Prb(d_1|p_{1j}, ..p_{(I-1)j}) \cdot Prb(p_{Ij}|\Pi_{i\bar{D}}, d_1) + Prb(d_0|p_{1j}, ..p_{(I-1)j}) \cdot Prb(p_{Ij}|\Pi_{i\bar{D}}, d_0)}$$

$$Prb(d_0|p_{1j}, p_{2j}..p_{Ij}) = 1 - Prb(d_1|p_{1j}, p_{2j}..p_{Ij}). \quad (8.5)$$

The relations in Equations 8.4 and 8.5 can be easily expanded for multi-state class variables. Bayesian classifiers can therefore be applied to any generalized classification problem in earth sciences.

8.2.1 Training of Bayesian classifiers

The training of B involves estimating (a) the parameters Θ and (b) the DAG G that provides the best approximation of conditional dependencies in $\mathbf{U}^*$. Obviously, a naive classifier is a special case of an augmented naive classifier when G is predefined and only Θ is required to be estimated.

Estimation of parameters

Consider the augmented Bayesian classifier B on $\mathbf{U}^*$ defined above. Assuming that G is given, the standard Bayesian method to estimate Θ is based on conjugate analysis (Ramoni and Sebastiani, 1999). Θ is estimated as $\{\Theta_i\}$, where $\Theta_i = \{\Theta_{i1}, .., \Theta_{iK}\}$ is the set of parameters containing the conditional probability distribution of $P_i | \Pi_i$. Because $\Pi_i = \{D\}$ in the case of a naive classifier and $\Pi_i = \{D, \Pi_{i\bar{D}}\}$ in the case of an augmented naive classifier, these conditional probabilities can be directly used in Equations 8.4 and 8.5 , respectively, to estimate the posterior probabilities of d_0 and d_1.

Let $\mathbf{T} = \{\mathbf{t_1}, ..., \mathbf{t_M}\}$ be a set of M $(I+1)$-dimensional training vectors. Let $\Theta_{ik} = [\theta_{i1k}, .., \theta_{iJk}]$ be the parameter vector containing conditional probability distribution of $P_i | \pi_{ik}$ and $\theta_{ijk} = Prb(p_{ij} | \pi_{ik})$ be the conditional probability of $p_{ij} | \pi_{ik}$. Let $n(p_{ij} | \pi_{ik})$ be the frequency of pairs $(p_{ij} | \pi_{ik})$ and $n(\pi_{ik}) = \sum_{j=1}^{J} n(p_{ij} | \pi_{ik})$ be the frequency of (π_{ik}) in $\mathbf{T}$. Assuming that Θ_{ik} and $\Theta_{i'k}$ are independent $\forall i \neq i'$ (*global independence*) and Θ_{ik} and $\Theta_{ik'}$ are independent $\forall k \neq k'$ (*local independence*), the joint prior density factorizes into:

$$Prb(\Theta | \mathbf{T_0}) = \prod_{i=1}^{I} \prod_{k=1}^{K} Prb(\Theta_{ik} | \mathbf{T_0}),$$

where $\mathbf{T_0}$ symbolizes 'prior to seeing the training set $\mathbf{T}$', and the joint posterior density of Θ factorizes into the products of local likelihoods $\prod_{j=1}^{J} \theta_{ijk}^{n(p_{ij} | \pi_{ik})}$ as follows:

$$Prb(\Theta | \mathbf{T}) \propto \prod_{i=1}^{I} \prod_{k=1}^{K} \{Prb(\Theta_{ik} | \mathbf{T_0}) \prod_{j=1}^{J} \theta_{ijk}^{n(p_{ij} | \pi_{ik})}\},$$

thus allowing an independent local update of Θ_{ik} (Spielgelhalter and Lauritzen, 1990; Ramoni and Sebastiani, 1999). Further, if a Dirichlet distribution with hyper-parameters $\{\alpha_{i1k}, \alpha_{i2k}, ..., \alpha_{iJk}\}$ ($\alpha_{ijk} > 0$) is used to model the prior distribution of Θ_{ik}, i.e., $\Theta_{ik}|\mathbf{T_0} \sim D(\alpha_{i1k}, \alpha_{i2k}, ..., \alpha_{iJk})$, then the prior density of Θ_{ik} can be estimated (Ramoni and Sebastiani, 1999) as:

$$\Theta_{ik} \propto \prod_{j=1}^{J} \theta_{ijk}^{(\alpha_{ijk}-1)},$$

which is conjugate to the local likelihood. Because $(\alpha_{ijk} - 1)$ in the prior density plays the role of $n(p_{ij}|\pi_{ik})$ in the local likelihood, the prior hyper-parameters α_{ijk}, which encode the modeler's prior belief, can be interpreted as frequencies of real or imaginary instances of $p_{ij}|\pi_{ik}$ the modeler has seen prior to the training set $\mathbf{T}$ (Friedman *et al.*, 1997; Ramoni and Sebastiani, 1999). The frequency of real or imaginary instances of p_{ij} in the parent configuration of π_{ik} ($= \sum_{j=1}^{J}(\alpha_{ijk} - 1)$) is called *local prior precision* and the frequency of real or imaginary instances of α_i ($=\sum_{j=1}^{J} \alpha_{ij}$) is called *global prior precision* (Ramoni and Sebastiani, 1999). For consistency and in order to enforce local and global independence of parameters, it is necessary to assume $\alpha_1 = \alpha_2 = ... = \alpha_I$ (Geiger and Heckerman, 1997). Because the variance of θ_{ijk} is a decreasing function of α_{ik} (Ramoni and Sebastiani, 1999), a smaller value of global prior precision denotes a greater uncertainty in the prior belief. Friedman *et al.* (1997) describe criteria for selecting the value of global prior precision. In order to avoid bias due to the prior precision, a value much smaller than the number of training samples should be used (a global prior precision of 1 is a reasonable starting point).

Given a global prior precision of $\alpha(= \alpha_1 = \alpha_2 = ... = \alpha_I)$, α_{ijk} can be calculated as:

$$\alpha_{ijk} = \frac{\alpha}{J \cdot K}, \tag{8.9}$$

where J is the total number of states of the predictor P_i and K is the total number of parents in Π_i, and α_{ik} can be calculated as:

$$\alpha_{ik} = \sum_{j=1}^{J} \alpha_{ijk}. \tag{8.10}$$

Table 8.1: Contingency table

Π_i	P_i					Marginal row total
	p_{i1}	...	p_{ij}	...	p_{iJ}	
π_{i1}	$n(p_{i1}|\pi_{i1})$	...	$n(p_{ij}|\pi_{i1})$	...	$n(p_{iJ}|\pi_{i1})$	$n(\pi_{i1})$
$\vdots$			$\vdots$		$\vdots$	$\vdots$
π_{ik}	$n(p_{i1}|\pi_{ik})$	...	$n(p_{ij}|\pi_{ik})$	...	$n(p_{iJ}|\pi_{ik})$	$n(\pi_{ik})$
$\vdots$			$\vdots$		$\vdots$	$\vdots$
π_{iK}	$n(p_{i1}|\pi_{iK})$	...	$n(p_{ij}|\pi_{iK})$	...	$n(p_{iJ}|\pi_{iK})$	$n(\pi_{iK})$

The prior probability of $p_{ij}|\pi_{ik}$ can be estimated as prior expectation of $\theta_{ijk}|\mathbf{T_0}$:

$$E(\theta_{ijk}|\mathbf{T_0}) = Prb(p_{ij}|\pi_{ik}) = \frac{\alpha_{ijk}}{\alpha_{ik}},$$

and the posterior probability of $(p_{ij}|\pi_{ik})$ can be estimated as posterior expectation of $\theta_{ijk}|\mathbf{T}$ (Ramoni and Sebastiani, 1999):

$$E(\theta_{ijk}|\mathbf{T}) = Prb(p_{ij}|\pi_{ik}) = \frac{\alpha_{ijk} + n(p_{ij}|\pi_{ik})}{\alpha_{ik} + n(\pi_{ik})} \tag{8.12}$$

Thus the information conveyed by $\mathbf{T}$ is captured by a simple update of the prior hyper-parameters α_{ijk} by adding the frequency of the pairs (p_{ijk}, π_{ik}) in $\mathbf{T}$. Consequently, $Prb(p_{ij}|\pi_{ik})$ can be directly estimated from a contingency table of frequencies of child-parent dependencies (for example, Table 8.1) using Algorithm-1.

Estimation of directed acyclic graph

The DAG G can be estimated from training data using score-based or dependency-based approaches. The score-based approaches view the estimation as a search for the structure that best fits the training data. In a score-based approach, the algorithm initializes a structure with no dependencies amongst any nodes and iteratively adds a directed arc to a particular node and, based on some score, compares the structure with the previous structure after every new addition. The process continues until there is no further improvement in the score for that particular node. The procedure is repeated for every node. Several scoring functions are reported in literature, for example, Bayesian scoring function (Cooper and Herskovits, 1992; Heckerman *et al.*, 1995; Ramoni and Sebastiani, 1999), entropy-based function (Herskovits, 1991), minimum description length function (Suzuki, 1996; Lam and Bacchus, 1994) etc. Many of these

---

Algorithm-1

1   Based on the confidence in the prior belief, select a value of the global prior precision (α).

2   Given G and $\mathbf{T}$, construct a contingency table for P_1 by collecting the frequency distribution of the child-parent dependencies.

3   Calculate prior hyper-parameters (α_{1jk}) using Equation 8.9.

4   Substitute every $[n(p_{1j}|\pi_{1k})]$ by $[\alpha_{1jk} + n(p_{1j}|\pi_{1k})]$ and re-calculate marginal row totals.

5   Divide every $[\alpha_{1jk} + n(p_{1j}|\pi_{1k})]$ by the corresponding marginal row total. Substitute every $[\alpha_{1jk} + n(p_{1j}|\pi_{1k})]$ by the result to obtain Θ_i.

6   Repeat Steps 2 to 5 for every predictor P_i ($i = 2$ to I) to obtain Θ.

---

algorithms require a partial or complete search order (Chickering *et al.*, 1994). The dependency-based approaches, on the other hand, apply certain conditional independence tests to identify dependencies in the training data and use these dependencies to develop the structure of G (for example, Wermuth and Lauritzen, 1983; Srinivas *et al.*, 1990; Sprites *et al.*, 1997; Cheng *et al.*, 2002). Cheng *et al.* (2002) provide a recent review of published score-based and dependency-based algorithms. Heckerman *et al.* (1995) show that score-based functions are generally more efficient than dependency-based methods. In the present work, a score-based function is employed to estimate G.

In the case of a naive classifier, G is completely predefined, i.e., it is assumed that (a) $\Pi_D = \emptyset$ and (b) $\Pi_i = \{D\}$. In the case of an augmented naive classifier, G is only partially predefined, i.e., it is assumed that (a) $\Pi_D = \emptyset$ and (b) $\{D\} \in \Pi_i$, but the members of $\Pi_{i\bar{D}}$ are not known.

A marginal likelihood-based score (Cooper and Herskovits, 1992; Ramoni and Sebastiani, 1999) can be used to estimate Π_i in an augmented naive classifier as follows. Let $\mathcal{G} = \{G_0, G_1, ..., G_G\}$ be a set of DAGs that model all possible dependencies in an augmented naive classifier. Let $Prb(G_g|\mathbf{T_0})$ be the prior probability of the gth model G_g. Let $\Theta^{(g)}$ be the set of parameters which contains the conditional probability distribution of $P_i|\Pi_i^{(g)}$ ($\forall i = 1$ to I), where $\Pi_i^{(g)}$ is specified by the gth DAG G_g. Given $\mathbf{T}$, Bayes equation can be used to

write the following expression:

$$Prb(G_g|\mathbf{T}) \propto Prb(G_g|\mathbf{T_0})Prb(\mathbf{T}|G_g),$$

where $Prb(\mathbf{T}|G_g)$ is the marginal likelihood of G_g with respect to $\Theta^{(g)}$. If $Prb(G_g|\mathbf{T_0}) = Prb(G_{g'}|\mathbf{T_0}) \ \forall g \neq g'$, then

$$Prb(G_g|\mathbf{T}) \propto Prb(\mathbf{T}|G_g),$$

and, therefore, in order to select the most probable DAG, it is sufficient to estimate and compare the marginal likelihood $Prb(\mathbf{T}|G_g)$ of all DAGs in $\mathcal{G}$. The marginal likelihood of G_g is given by:

$$Prb(\mathbf{T}|G_g) = \int Prb(\Theta^{(g)}|\mathbf{T})Prb(\mathbf{T}|\Theta^{(g)})d\Theta^{(g)},$$

which has a closed form provided (Cooper and Herskovits, 1992) (a) the set of training samples is complete, i.e., there are no missing data, (b) given $\Theta^{(g)}$, the training samples are independent and (c) the prior distribution of parameters is conjugate to $Prb(\mathbf{T}|\Theta^{(g)})$, or in other words, $\Theta_{ik}^{(g)}|\mathbf{T_0} \sim D(\alpha_{i1k}, \alpha_{i2k}, ..., \alpha_{iJk})$ and the parameters are locally and globally independent. Under the above assumptions, the marginal likelihood of G_g can be estimated (Cooper and Herskovits, 1992; Ramoni and Sebastiani, 1999) as:

$$Prb(\mathbf{T}|G_g) = \prod_{i=1}^{I}\prod_{k=1}^{K} \frac{\Gamma(\alpha_{ik})}{\Gamma(\alpha_{ik} + n(\pi_{ik}))} \prod_{j=1}^{J} \frac{\Gamma(\alpha_{ijk} + n(p_{ij}|\pi_{ik}))}{\Gamma(\alpha_{ijk})},$$

where $\Gamma(\cdot)$ is the Gamma function (Wilks, 1962). The marginal likelihood of G_g can be decomposed into local marginal likelihood ($\mathbf{g}(P_i, \Pi_i)$) of the predictor P_i given Π_i in G_g:

$$\mathbf{g}(P_i, \Pi_i) = \prod_{k=1}^{K} \frac{\Gamma(\alpha_{ik})}{\Gamma(\alpha_{ik} + n(\pi_{ik}))} \prod_{j=1}^{J} \frac{\Gamma(\alpha_{ijk} + n(p_{ij}|\pi_{ik}))}{\Gamma(\alpha_{ijk})}. \tag{8.17}$$

Because the value of $\mathbf{g}(P_i, \Pi_i)$ is very small, its natural logarithm can be used:

$$\ln[\mathbf{g}(P_i, \Pi_i)] = \{\sum_{k=1}^{K} \ln[\Gamma(\alpha_{ik})] + \sum_{j=1}^{J} \ln[\Gamma(\alpha_{ijk} + n(p_{ij}|\pi_{ik}))]\} -$$
$$\{\sum_{k=1}^{K} \ln[\Gamma(\alpha_{ik} + n(\pi_{ik}))] + \sum_{j=1}^{J} \ln[\Gamma(\alpha_{ijk})]\}. \qquad (8.18)$$

Local marginal log likelihood of a predictor given a set of parents can be calculated by substituting values for various frequencies in Equation 8.18. The values can be directly read from a contingency table of frequencies of various parent-child dependencies (for example, Table 8.1).

Equation 8.17 decomposes the global search for the best DAG into the computationally more tractable local searches for the best set of parents for individual predictors. However, for a large number of predictors, even the local search for parents can become intractable (Chickering *et al.*, 1994) and therefore conceptual genetic models are used to limit the search space (a) by specifying a search order on the predictors, so that the search space for the parents of a predictor is limited to its predecessors in the search order and (b) by forbidding certain dependencies. Additionally, an upper limit to the number of parents can be defined.

Let $P = \{P_1, P_2, ...P_I\}$ be the set of I predictors and let $SO_P = \{P_1 \succ P_2 \succ P_3 \succ ... \succ P_I\}$, where $\Pi_i \subseteq \{P_1, P_2, ..., P_{i-1}\}$, be the search order on P. Let $F_{P_i}(\subset P)$ be a set of predictors that are forbidden to be parents of P_i. Let MAX be the maximum number of parents allowed for any predictor. Given SO_P and F_{P_i}, the best set of parents for P_i is estimated by adapting the K2 algorithm (Cooper and Herskovits, 1992) as follows: (a) initialize a naive classifier, so that $\Pi_D = \emptyset$ and $\Pi_i = D$ (b) move top down in SO_P to iteratively add a predecessor ($\notin F_{P_i}$) of P_i to Π_i and compute marginal log likelihood after each addition, (c) expand Π_i by including predictors that maximize the marginal log likelihood and (d) stop when there is no further increase in the log marginal likelihood or $n(\Pi_i) = MAX$.

Validation of classifiers: n-Fold cross validation

Most published studies on quantitative mineral potential mapping use hold-back validation, which involves using a part (for example, about three quarters) of training samples for training the model and holding back the rest for vali-

219

Algorithm-2 (Pseudocode).

Input: global prior precision (α); set of training samples ($\mathbf{T}$), target deposit-type (D), number of predictors (I); search order (SO_P); forbidden parents ($F_{P_i}, i = 1$ to I) and maximum number of parents (MAX).
Output: $\Pi_i (i = 1$ to I)

START

set $\Pi_D = \emptyset$ *set D at the root of DAG*

FOR ($i = 1; i = I; i++$) *starting with P_1, iterate for every predictor in SO_P*

  $\Pi_i = D$ *add directed arc from D to P_i*

  calculate α_{ijk} *use Eq. 8.9 to calculate prior hyper-parameters*

  calculate α_{ik} *use Eq. 8.10 to calculate local prior precision*

  calculate $\ln[\mathbf{g}(P_i, \Pi_i)]$ *use Eq. 8.18 to calculate likelihood of $\Pi_i = \{D\}$*

  $max\{\ln[\mathbf{g}(P_i, \Pi_i)]\} = \ln[\mathbf{g}(P_i, \Pi_i)]$ *set current likelihood as maximum likelihood*

    FOR ($i' = 1; i' < i; i'++$) *starting with P_1, iterate for every predecessor of P_i*

      WHILE ($n(\Pi_i) \leq MAX$) *verify that current number of parents is less than*
               maximum allowed

        IF ($P_{i'} \notin F_{P_i}$) *if $P_{i'}$ is not forbidden parent of P_i*

          $\Pi_i = \Pi_i + P_{i'}$ *add directed arc from $P_{i'}$ to P_i*

          calculate $\ln[\mathbf{g}(P_i, \Pi_i)]$ *use Eq. 8.18 to calculate likelihood of current Π_i*

          IF ($\ln[\mathbf{g}(P_i, \Pi_i)] > max\{\ln[\mathbf{g}(P_i, \Pi_i)]\}$) *if current likelihood is more than*
                  current maximum likelihood

            $max\{\ln[\mathbf{g}(P_i, \Pi_i)]\} = \ln[\mathbf{g}(P_i, \Pi_i)]$ *set current likelihood as maximum*
                  likelihood and save the directed arc

          ELSE $\Pi_i = \Pi_i - P_{i'}$ *else remove the directed arc*

          END IF

        ELSE $\Pi_i = \Pi_i$ *if $P_{i'}$ is forbidden parent, do not add the directed arc*

        END IF

      END WHILE *if current number of parents is already equal to maximum*
               allowed, abort nested FOR loop

    END FOR *end of nested FOR loop*

END FOR *end of main FOR loop*

END

Algorithm-3

1. Partition $\mathbf{T}$ into n subsets $\mathbf{T^i}$ ($i = 1$ to n), each having (M/n) samples.

2. Leave $\mathbf{T^1}$ out and pool remaining $(n-1)$ subsets to generate a new set $\mathbf{T^{\bar{1}}}$ for training a classifier.

3. Train the classifier on $\mathbf{T^{\bar{1}}}$.

4. Validate the classifier on $\mathbf{T^1}$ and record the number of correct classifications.

5. Report percent correct classifications for all subsets.

---

dating the model. The method, although computationally efficient, has several limitations, for example, (a) it requires a large number of training samples for minimizing uncertainty and avoiding over-fitting, (b) the validation is biased by the selection of training and validation samples and (c) it does not make an optimal use of available data. These limitations are addressed by leave-one-out validation, which involves leaving exactly one sample out, training a model on the rest of the samples and validating the model on the left-out sample. The process is implemented iteratively for all training samples. This method is extremely accurate but computationally expensive and, in some situations, impracticable. In the present application, n-fold cross-validation is used, which retains the advantages of leave-one-out validation and, at the same time, is computationally more tractable. Given the set of training samples ($\mathbf{T}$) containing M samples, Algorithm-3 can be used to implement n-fold cross validation.

Clearly, the higher the value of n, the higher the accuracy of validation (at $n = M$, the method becomes leave-one-out validation) and the higher the computational expense.

The above algorithms were implemented using the software described by Ramoni and Sebastiani (2000).

8.3 Implementation of Bayesian classifiers

8.3.1 Data preprocessing

In the case of mineral potential mapping, the class variable is generally binary with the labels 'mineralized' and 'barren'. The feature vectors associated with known mineralized or with known barren locations constitute training samples, which are referred to as deposit or non-deposit training samples, respectively.

Appropriate preprocessing of the exploration database and selection of training samples is important for a successful implementation of Bayesian classifiers. The following factors require especial consideration.

Firstly, conditional dependencies are generally state specific and seldom map specific. Consider, for example, multi-state maps of lithologies and stratigraphic groups. In the absence of ubiquitous geochronological data, stratigraphic classifications are generally made on the basis of lithological associations, which results in significant correlations between stratigraphic groups and lithologies. These correlations, however, are state specific, i.e., a particular stratigraphic group is correlated with specific lithologies. If each map is used as a single multi-state predictor in an augmented naive classifier and Algorithm-2 estimates a significant likelihood of the map of lithologies being a parent of the map of stratigraphic groups, then every state (lithology) of the map of lithologies is indiscriminately included in the set of parents of every state (stratigraphic group) of the map of stratigraphic groups. This may result in a large number of erroneous dependencies. More importantly, it results in manifold increase in the number of parameters, which may lead to over-fitting because of dimensionality problems (see below). It is therefore preferable to use 1-of-n encoding (Masters, 1993) for transforming an n-state map into n binary maps, as described in Chapter 6 (p. 163). This forces the algorithm to search for dependencies amongst individual states and hence only true dependencies are identified.

Secondly, exploration data sets are highly imbalanced and biased towards the barren class. If deposit and non-deposit samples are represented in the training set in the same proportion as they are expected to occur in the general population, the performance of a Bayesian classifier is optimized for recognizing non-deposit samples. This may give rise to a large number of type II errors, which have severe consequences in mineral potential mapping. The problem can be addressed by one-sided selection (Kubat and Matwin, 1997; Kubat *et al.*, 1998; *see also* Chapter 6) to balance the training set.

Curse of dimensionality

For a robust estimation of the parameters of a Bayesian classifier, the number of training samples should be several times larger than the number of model parameters. However, as the dimensionality of input feature vectors rises, the number of parameters of a Bayesian classifier, i.e., the number of conditional probabilities to be estimated also increases. The increase is multiplicative in the case of a naive classifier ($= 2n$, where n is the number of dimensions of input feature vectors), but may become exponential in the case of an augmented naive classifier, depending on the number of parent-child dependencies. This may lead to poor estimations of the parameters, especially if adequately large number of training samples are not available.

As discussed in Chapter 6, *a priori* information can help mitigate the curse of dimensionality. A careful selection and scaling of the input feature vectors can extenuate the severity of the problem. In an application to mineral potential mapping, this implies that, if an adequately large number of training samples (i.e., known mineral deposits) are not available, the available predictor maps should be carefully scrutinized, and on the basis of *a priori* conceptual-genetic information on the target mineral deposit-type, only the most relevant maps should be selected for modeling.

Class variables and feature vectors

In the context of Bayesian classifiers, the target mineral deposit-type is considered a binary class variable (with the labels 'mineralized' and 'barren'). Predictor patterns are considered attributes that characterize the class variable and each unique condition is considered a feature vector containing instances of attributes (Chapter 6, p. 163).

A set of pre-classified feature vectors (i.e., the unique conditions that are associated with either a known mineralized or a known barren location) is used for training a Bayesian classifier. However, the use of n-fold validation procedures obviates the need of a separate set of pre-classified feature vectors for validating the performance of the Bayesian classifier. The procedure described in Chapter 6 (p. 163) can be used for selecting training feature vectors.

8.3.2 Training of Bayesian classifiers

The training of a Bayesian classifier involves estimating (a) the DAG that provides the best approximation of conditional dependencies amongst the input

predictor patterns and (b) the parameters (conditional probabilities) that are associated with each node (predictor pattern).

After selecting a suitable global prior precision value and specifying the search order and forbidden dependencies, a Bayesian classifier is first trained using Algorithm-2 for estimating the DAG that best simulates the dependencies amongst the predictor patterns. The Bayesian classifier is then trained using Algorithm-1 for estimating the parameters associated with each node of the DAG. The performance of the Bayesian classifier is validated using n-fold cross validation procedures (Algorithm-3).

8.4 Application to Base-Metal Potential Mapping in Aravalli Province

8.4.1 Data preprocessing

As discussed above, in order to build robust Bayesian classifiers, sufficiently large number of training samples, in proportion to the dimensionality of training samples, should be available. Keeping in mind the inadequate number of the available training samples (see below), it was decided to reduce the dimensionality of input training feature vectors. The available predictor maps were scrutinized, and on the basis of *a priori* conceptual-genetic information (Chapter 2) and the experience of modeling using machine learning algorithms (Chapters 6 and 7), the following predictor maps were used in the Bayesian classifiers: the multi-class predictor maps of lithologies and stratigraphic groups and the binary predictor maps of mafic igneous rocks, buffered distances from regional lineaments and buffered distances from fold axes.

Data encoding

Using the one-of-n encoding procedure described in Chapter 6 (p. 166), the multi-class categoric maps of lithologies and stratigraphic groups were transformed into to a series of binary maps. On each binary map, exactly one class was coded as 1 and the remaining classes were coded as 0. In this way 17 binary predictor maps were generated from the two multi-class predictor maps. Of these, 11 binary predictor maps were used for subsequent processing. Three binary maps of lithologies, which have no known relationship with base-metal mineralization in the province, were not used. These maps included the binary maps of calc-schist, migmatites and other younger intrusive/extrusive rocks.

224

Similarly, three binary maps of stratigraphic groups, which have no known relationship with base-metal mineralization in the province, were not used. These maps included the binary maps of Sandmata Complex, Managalwar Complex and other younger stratigraphic groups.

Each of the two classes in the three binary predictor maps of mafic igneous rocks, buffered regional lineaments and buffered fold axes was coded as either 1 or 0, indicating, respectively, the presence or absence of the predictor pattern.

The resulting 14 binary maps were superposed and unique combinations of the maps in unit areas of 1 km^2 were mapped to generate a feature vector map constituting 472 feature vectors. As the operation was carried out in a GIS-environment, an associated database table was automatically generated, which held the components of the feature vectors. In the table, each feature vector is described by a unique identification number and 14 components representing each evidential map encoded as either present or absent.

The feature vectors associated with known base-metal deposits were extracted to create a subset of 36 deposit samples. An equal number of feature vectors, which were considered, on the basis of expert knowledge, least-likely to be associated with base-metal deposits were extracted to create a subset of 36 non-deposit samples. The two subsets were merged to generate a set containing 72 samples. No separate set of validation vectors was required because n-fold cross validation procedure was used for validating the performance of the classifiers.

8.4.2   Training of Bayesian classifiers

Algorithm-2 was used with a global prior precision of 1 to train an augmented naive classifier on the training set to determine the DAG that best simulates the dependencies in the data. To limit the search space, (a) dependencies amongst the binary maps of lithologies and amongst the binary maps of stratigraphic groups were forbidden, (b) the maximum number of parents for each predictor was set to 3 and (c) the following search order was specified:
Buffered regional lineaments ≻ Lithologies ≻ Buffered fold axes ≻ Mafic igneous rocks ≻ Stratigraphic groups.
The above search order is based on the following considerations.

- The regional lineaments represent fundamental tectonic features (crustal-scale faults) that mark the boundaries of major intracratonic rift sequences in the province (Porwal *et al.*, 2003a; *see also* Chapter 2). There-

fore there is little possibility of the map of buffered regional lineaments being dependent on any other predictor.

- A (meta)-sedimentary rock is a product of its (palaeo)-environment, which, in turn, is tectonically controlled (Pettijohn, 1975). Therefore there exists a possibility of dependence of the maps of lithologies on the map of buffered regional lineaments. However, there is little possibility of the maps of lithologies being dependent on any of the other predictors.

- Folding obviously postdates rifting and sedimentation and therefore there can be no possibility of the map of buffered fold axes being a parent of either the map of buffered regional lineaments or the maps of lithologies.

- The regional lineaments mark the crustal-scale faults that could be possible conduits for the mafic rocks in the province (Porwal *et al.*, 2003a; *see also* Chapter 2). Therefore there exists a possibility of the map of buffered regional lineaments being a parent of the map of mafic igneous rocks.

- Stratigraphic classification of the province in various groups is largely based on regional tectonic boundaries, lithological associations and deformation patterns (Gupta *et al.*, 1997). Therefore there exists a strong possibility of the binary maps of stratigraphic groups being dependent on several of the other predictors.

After determining the DAG of the augmented naive classifier, a selective naive classifier was constructed by removing the conditionally-dependent predictors. The DAGs of the trained naive, augmented naive and selective naive classifiers are shown in Fig. 8.2. Finally, Algorithm-1 was used for estimating the parameters (conditional probabilities) associated with every node in each classifier.

Cross validation. A 25-fold cross validation was implemented using Algorithm-3 to validate each classifier. The results (Table 8.2) show that the augmented naive classifier gives the best performance, followed by the naive classifier and then the selective naive classifier.

(A)

Dolomite · Graphitic schist · Magnetite quartzite · Regional lineaments · Calc-silicates · Fold axes · **Base metal Deposits** · Quartzite · Mafic Igneous rocks · Udaipur group · Debari group · Nathdawara group · Jharol group · Rajpura-Dariba group · Pur-Banera group

Deposit	Rajpura-Dariba group	
	Absent	Present
Absent	0.995	0.005
Present	0.790	0.210

(B)

Jharol group · Quartzite · Regional lineaments · Udaipur group · Fold axes · Dolomite · Magnetite quartzite · **Base metal Deposits** · Nathdwara group · Debari group · Calc-silicates · Graphitic schist · Pur-Banera group · Rajpura-Dariba group · Mafic igneous rocks

Graphitic schist	Deposit	Rajpura-Dariba group	
		Absent	Present
Absent	Absent	1.000	0.000
Absent	Present	0.907	0.093
Present	Absent	1.000	0.000
Present	Present	0.300	0.700

(C)

Dolomite · Magnetite quartzite · Regional lineaments · Calc-silicates · Mafic Igneous rocks · **Base metal Deposits** · Debari group · Quartzite · Graphitic schist

Figure 8.2: Trained Bayesian classifiers for base-metal potential mapping in study area: (A) naive classifier, (B) augmented naive classifier and (C) selective naive classifier. Nodes and directed arcs represent binary predictors and conditional dependencies, respectively. Parameters associated with Rajpura-Dariba group are shown for illustration.

Table 8.2: 25-fold cross validation

Classifier	Correct classifications %
Naive	86.8
Augmented naive	88.7
Selective naive	83.0

8.4.3 Favorability maps

The trained classifiers were used for processing all feature vectors. The output posterior probability of d_1 (mineralized class) for each feature vector is interpreted as a measure of favorability of the feature vector with respect to base-metal mineralization in the province. Figs. 8.3A, 8.3B and 8.3C show the continuous-scale posterior probability maps derived by mapping the output of the naive classifier, augmented naive classifier and selective naive classifier, respectively. Figs. 8.4, 8.5 and 8.6 show the binary favorability maps generated by the reclassification of the continuous-scale posterior probability maps given in Figs. 8.3A, 8.3B and 8.3C, respectively, using 0.5 as the threshold.

Validation of favorability maps

The binary favorability maps (Figs. 8.4, 8.5 and 8.6) were validated by overlaying the known base-metal deposits on the maps and by plotting the position of these deposits on the predictive classification value versus percent cumulative percent area curves (Fig. 8.3D). Table 8.3 shows that (a) the naive classifier demarcates favorable zones that occupy 7% of the study area and contain 89% of the known deposits, (b) the augmented naive classifier demarcates favorable zones that occupy 11% of the study area and contain 93% of the known deposits and (c) the selective naive classifier demarcates favorable zones that occupy 11% of the study area and contain 83% of the known deposits.

8.5 Discussion

The formation and localization of mineral deposits are the end-results of a complex interplay of several metallogenetic processes that exhibit signatures in the form of geologic features associated with the mineral deposits. These geological features (or recognition criteria) are characterized by their responses in one or more geodata sets that are used as predictors in mineral potential
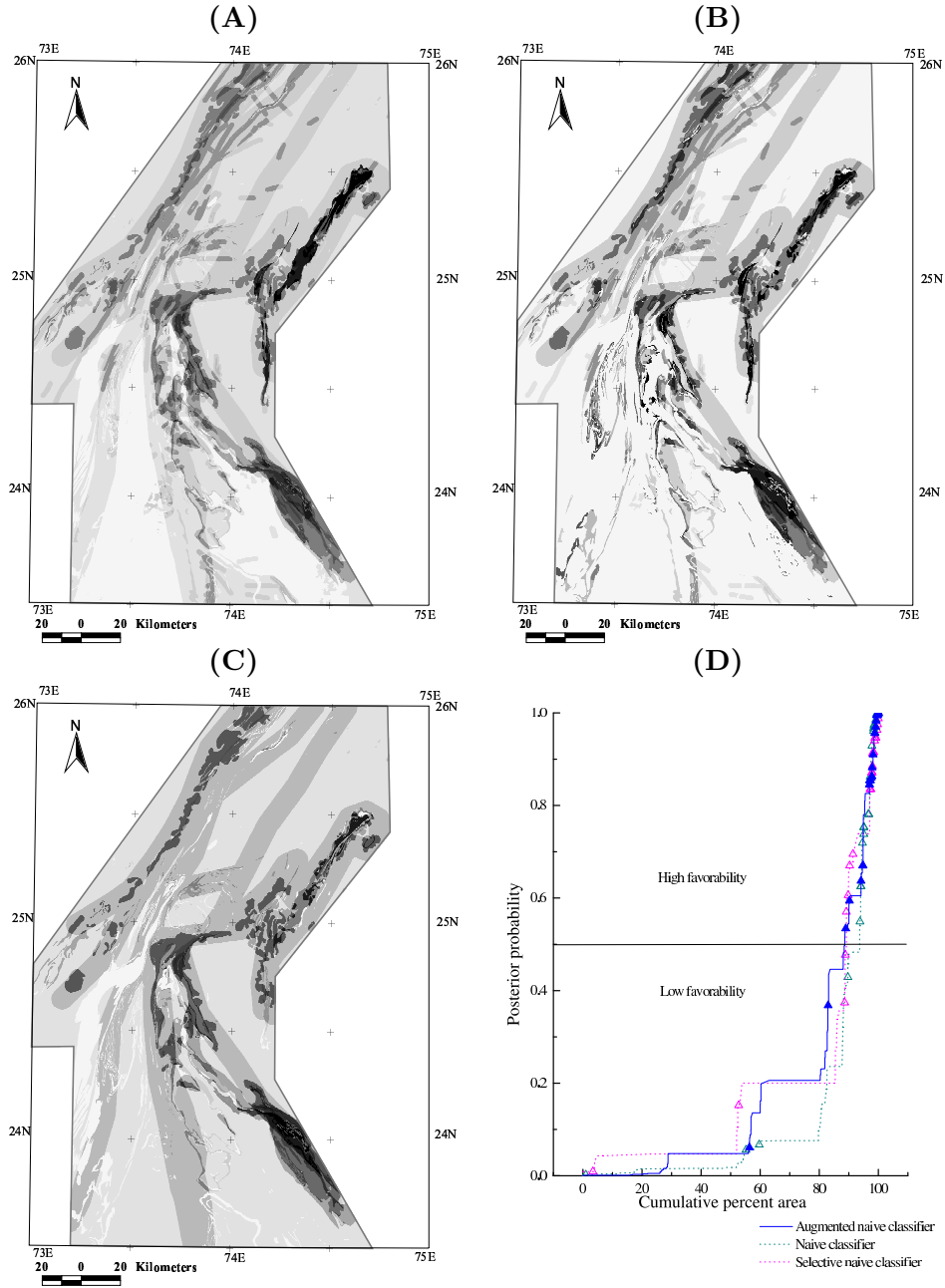
Figure 8.3: Continuous-scale posterior probability maps [posterior probability varies from 0 (white) to 1 (black)] generated using (A) naive classifier, (B) augmented naive classifier and (C) selective naive classifier. (D) Variation of posterior probability with cumulative percent area.

229
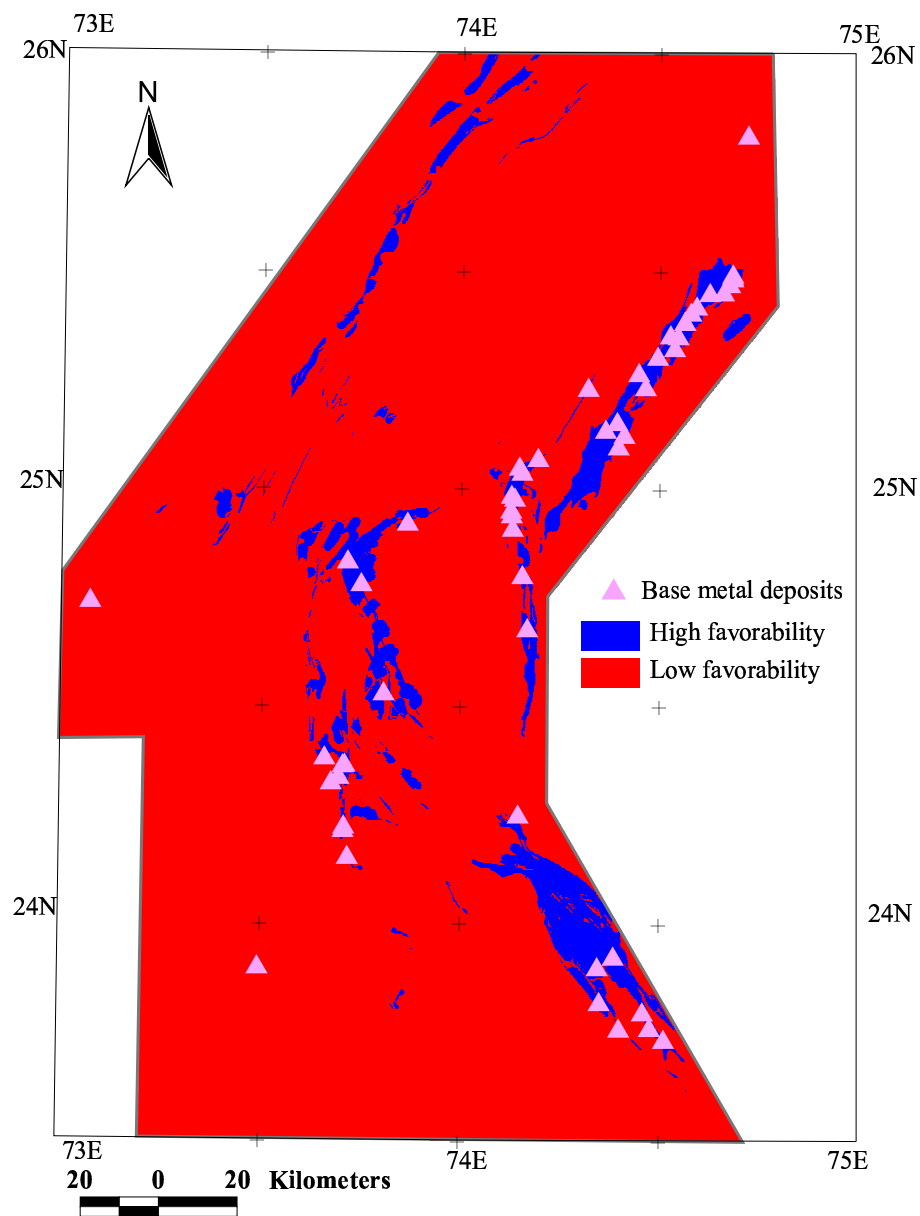
Figure 8.4: Binary favorability map generated using naive classifier.
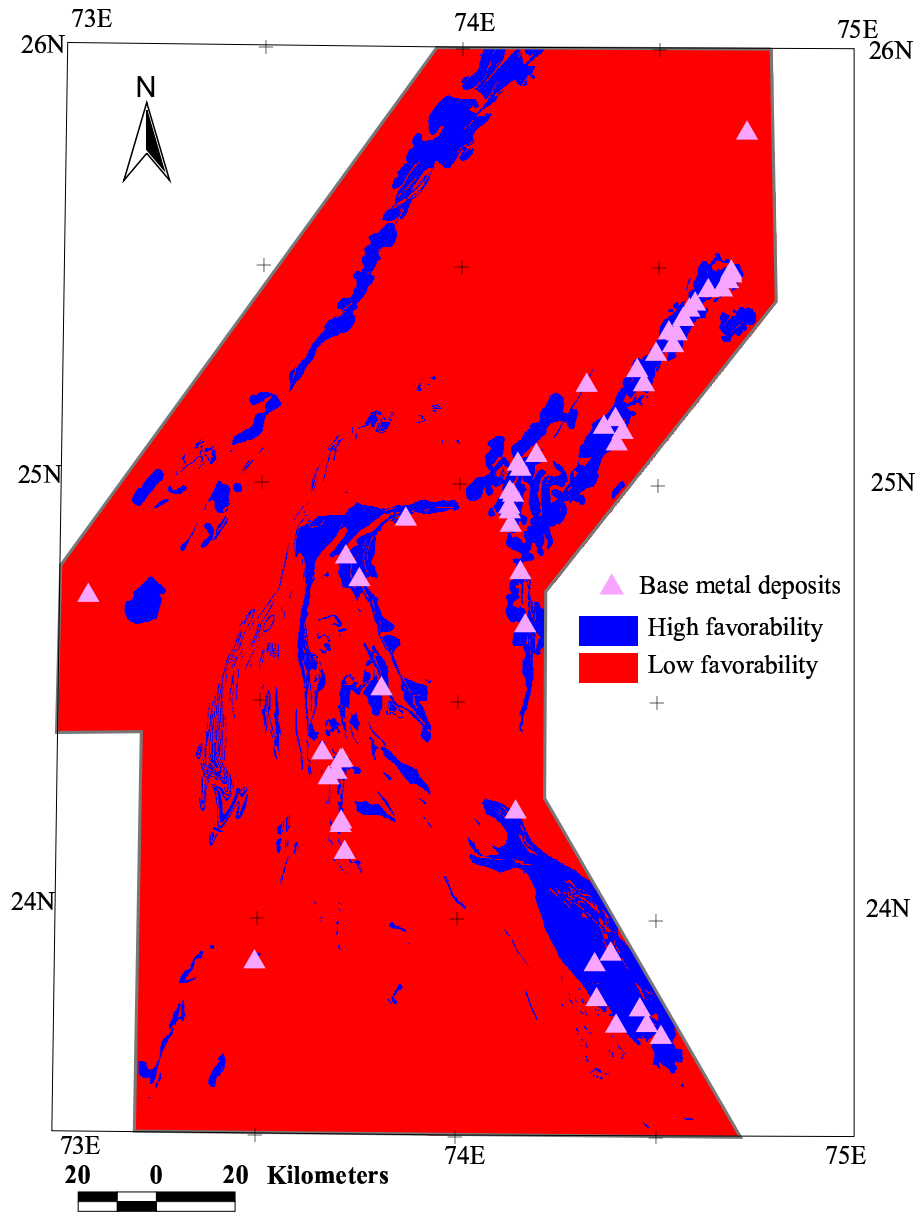
Figure 8.5: Binary favorability map generated using augmented naive classifier.
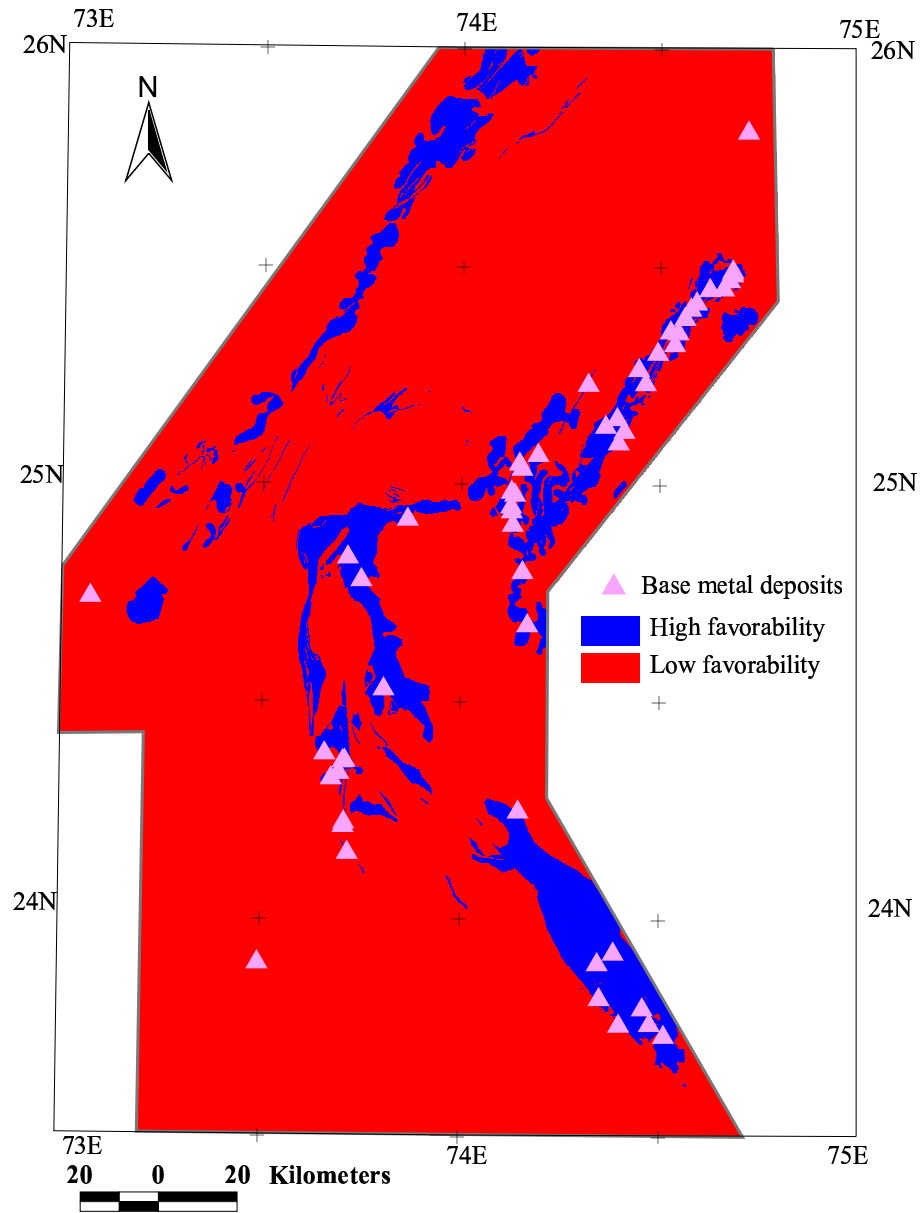
Figure 8.6: Binary favorability map generated using selective naive classifier.

mapping. It is unrealistic to assume independence of the predictors because (a) a particular geologic feature can partially respond in two or more geodata sets, (b) a particular metallogenetic process can be partially responsible for two or more geologic features or (c) two or more metallogenetic processes can be genetically related. In addition, the response of a geologic feature in one geodata set may be conditioned by the response of another geologic feature in a different geodata set.

Considering that the violation of the conditional independence assumption is generally unavoidable in mineral potential mapping, the results of the applications described above are examined in the following paragraphs in order to understand the implications of this violation for Bayesian approaches to mineral potential mapping.

In general, the naive classifier performs well in the predictive mapping of base-metal potential in the study area (Tables 8.2 and 8.3), which suggests that a naive classifier can tolerate significant violations of the conditional independence assumption (*see also* Domingos and Pazzani, 1996; 1997). This also implies that a weights-of-evidence model, which can be considered a logarithmic naive classifier (although with some significant differences*), may not be seriously hampered by the violation of the conditional independence assumption provided that its output is interpreted as a measure of relative favorability rather than absolute posterior probability (see below). This also explains the wide spread and generally successful application of weights-of-evidence models to mineral potential mapping.

However, the results (Tables 8.3 and 8.4) indicate that the performance of the naive classifier is improved if the conditional independence assumption is relaxed by recognizing and accounting for some of the dependencies in the training data. The augmented naive classifier identifies several zones of high favorability in the Jharol belt that are missed by the naive classifier (Figs. 8.4 and 8.5). Moreover, the high favorability zones tend to cluster around known deposits in Fig. 8.4, while they show a wider spatial distribution in Fig. 8.5, which suggests that the augmented naive classifier has better generalization capability compared to the naive classifier. This is further evidenced by comparing the outputs of the three classifiers for the misclassified deposits (Table 8.4), which shows that the augmented naive classifier returns a higher value for all

---

*In a weights-of-evidence model, all feature vectors that are associated with the unit areas that do not contain a known mineral deposit are indiscriminately used as non-deposit samples. In a naive classifier, on the other hand, only the feature vectors that are associated with the unit areas that are reasonably well known to be barren are used as non-deposit samples.

233

Table 8.3: Favorability maps

Classifier	Zone	Percent of study area	Percent of Deposits
Naive	High favorability	7.1	88.9
	Low favorability	92.9	11.1
Augmented naive	High favorability	11.3	92.6
	Low favorability	88.7	7.4
Selective naive	High favorability	11.2	83.3
	Low favorability	88.8	16.7

Table 8.4: Outputs for misclassified* deposits

Deposit	Domain	Naive	Augmented naive	Selective naive
Padar-Ki-Pal	Jharol	0.002	0.534	0.009
Rampura-Agucha	-	0.056	0.091	0.102
Baroi	Aravalli	0.067	0.910	0.374
Anjani	Aravalli	0.076	0.206	0.196
Basantgarh	South Delhi	0.406	0.482	0.352
Bara	Aravalli	0.429	0.637	0.615
Wari Lunera	Bhilwara	0.946	0.931	0.200
Dariba	Bhilwara	0.985	0.973	0.470
Dariba Extn.	Bhilwara	0.985	0.973	0.470
Rajpura A	Bhilwara	0.985	0.973	0.470

*Threshold of 0.500 is applied to make a classification

deposits misclassified by the naive classifier. Because the geological settings of the misclassified deposits are different in many respects from the geological settings of majority of deposits in the study area, it indicates that the generalization capability of a naive classifier is improved by recognizing and accounting for dependencies amongst predictors.

On the other hand, the naive classifier returns higher values for the deposits of the Bhilwara belt (where there are strong dependencies amongst favorable predictors), which suggests a significant influence of dependencies amongst predictors on the output of a naive classifier. Given the functional similarity between naive classifiers and weights-of-evidence models, it implies that the output of a weights of evidence model may be similarly biased by dependencies amongst predictors (Singer and Kouda, 1999), and therefore it is preferable to interpret the output of a weights of evidence model as a measure of relative favorability rather than an absolute probability, as suggested by Pan and Harris (2000).

The selective naive classifier misclassifies all but one deposit that are misclassified by the naive classifier (Table 8.4; Fig. 8.6). In addition, it also misclassifies several deposits of the Bhilwara belt, which is clearly a result of the

rejection of conditionally-dependent maps of stratigraphic groups. Evidently, dependent predictors make a significant independent contribution to the information content of a naive classifier (except when there is a perfect correlation) and therefore the rejection of a dependent predictor affects its performance adversely, as discussed by Friedman *et al.* (1997). It is also possible that a dependent predictor makes only a minor independent contribution to the information content, yet that contribution is crucial for making a correct classification. Therefore, in order to minimize the bias due to dependencies amongst predictors, it is preferable to augment a naive classifier by relaxing the independence assumption and accounting for the dependencies than to abridge it by rejecting dependent predictors. Similarly, in the case of a weights of evidence model, it is preferable to preserve dependent predictors by making logical combinations of correlated predictors rather than to eliminate them by applying Boolean operators.

8.6 Conclusions

In the study area, the augmented naive classifier successfully demarcates favorable zones that occupy 11% of the area and contain 93% of the known base-metal deposits; the naive classifier demarcates favorable zones that occupy 7 % of the area and contain 89% of the known base-metal deposits; and the selective naive demarcates favorable zones that occupy 11 % of the area and contain 83% of the known base-metal deposits. From the three application studies described in this chapter, the following conclusions can be drawn.

- A naive classifier provides an efficient tool for mineral potential mapping. It is easy to construct, train and implement. Although it is based on the strong assumption of conditional independence of input predictor patterns, it shows significant tolerance for the violations of the assumption.

- The performance of a naive classifier is significantly improved if the conditional dependence assumption is relaxed by recognizing and accounting for dependencies amongst the predictor patterns in an augmented naive classifier.

- Rejection of conditionally-dependent predictor patterns in a selective naive classifier degrades the performance of a naive classifier.

Chapter 9

Conclusions

9.1 Introduction

This research sought to identify mathematical function(s) that can be effectively used in the framework of mathematical geological models to approximate the relationship between a set of recognition criteria and the target mineral deposits for mineral potential mapping. Because there is no *a priori* definition of the nature of this relationship, it was alternatively hypothesized to be either linear or non-linear and, accordingly, several linear and non-linear models were investigated in this research by applying them to base-metal potential mapping of a study area in the Aravalli metallogenic province of India. The performance of these models is analytically compared in this chapter in order to draw conclusions regarding their (a) efficacy in approximating the relationship between recognition criteria and mineral deposits and (b) strengths and limitations as tools for mineral potential mapping. The chapter also evaluates the base-metal potential of the study area and outlines some recommendations for future research.

9.2 Recognition Criteria for Base-Metal Deposits

Conjunctive interpretations of geological and geophysical datasets and a comprehensive review of published tectono-stratigraphic studies of the study area were used to define a conceptual model of base-metal metallogenesis in the framework of overall tectono-stratigraphic evolution of the study area. Using the conceptual model and the generalized geological setting of SEDEX deposits, a number of regional-scale recognition criteria for base-metal deposits

in the study area were identified. Empirical modeling of spatial associations between known base-metal deposits and the recognition criteria (represented as predictor maps) was performed to validate the identified recognition criteria.

The following conclusions are drawn from this phase of the research.

- Host rock lithology, stratigraphic position, (palaeo-)sedimentary environment, association of mafic volcanic rocks and proximity to favorable structures are the most important recognition criteria for base-metal deposits in the study area.

- Empirical models of positive spatial associations between known base-metal deposits and identified recognition criteria validate the latter.

- Important recognition criteria can be identified effectively through conceptual modeling of mineralogenesis.

The identified recognition criteria (represented as predictor maps) were used as independent predictor variables in applications of various mathematical geological models to base-metal potential mapping in the study area.

9.3   Performance of mathematical geological Models

An evaluation of the linear models and the non-linear models based only on their performance in classifying training and validation deposits in high favorability zones is not appropriate for three reasons. First, the knowledge-driven fuzzy model did not require separate sets of validation and training deposits and, hence, all deposits were used to validate it. Second, a different set of validation and training deposits was used in the data-driven fuzzy model and the fuzzy weights-of-evidence model in order to test the ability of these hybrid models to function with smaller numbers of training points. Third, an n-fold cross validation method was used for validating the augmented Bayesian classifier model, while all other models were validated using a hold-back validation method.

The models are evaluated based on a number of criteria, which include percentage of correctly-classified known deposits, theoretical requirement of conditional independence, interpretability of model parameters, ease of implementation, susceptibility to the curse of dimensionality and ability to quantify uncertainties (Table 9.1). The ability of a model to conjunctively use both conceptual and empirical components of available geoscientific information of an

area is also used as an evaluation criterion, because it allows the model to compensate the deficiencies of one component with the other component. A correct classification of the Rampura-Agucha deposit is also included as an evaluation criterion. Rampura-Agucha, the only world-class Zn-Pb deposit of India, is a difficult deposit to predict, not least because of its unusual regional geological setting (see Chapter 3, p. 94). The correct classification of the deposit can therefore be interpreted as an indication of the ability of a mathematical geological model to predict mineral deposits in unusual geological settings. Table 9.1 summarizes the performance of the linear and the non-linear mathematical geological models with respect to the above evaluation criteria.

Table 9.1 indicates that both linear and non-linear models demarcate high favorability zones that occupy less than 10% of the search area and predict more than 80% of the known base-metal deposits. This indicates that both categories of models can efficiently narrow down search areas for mineral exploration. However, the non-linear models generally perform better in predicting the known base-metal deposits (Table 9.1). This suggests that, given the complexity of earth systems that result in the formation of mineral deposits, non-linear functions more adequately approximate the relation between predictor patterns and target mineral deposits and therefore fit the data more efficiently. This interpretation is reinforced by a comparison of the predictive classification results of the linear and the non-linear models with respect to the Rampura-Agucha deposit. The deposit is incorrectly classified in low favorability zones by all linear models, whereas two of the non-linear models, namely, the neural network model and the hybrid neuro-fuzzy model, correctly classify the deposit. The correct classification of the Rampura-Agucha deposit by two of the non-linear models may be attributed to the ability of the non-linear functions used in the two models to recognize the critical predictor pattern(s) and respond in a highly non-linear way to maximize the contribution of such component(s) to the output.

The linear models, which are based on simplified and modified Bayesian equations, require conditional independence of input predictor maps (Table 9.1) and by assuming it, they ignore the effects of possible interactions amongst input predictor patterns. The assumption is often difficult to validate, although several statistical tests have been proposed by different workers to test conditional independence (Singer and Kouda, 1999; Porwal *et al.*, 2003b). Given the peculiar nature and interdependency of geological processes that result in

Table 9.1: Performance of mathematical geological models with respect to some evaluation criteria

Evaluation criterion	Linear models			Non-linear models				
	Weight-of-evidence	Hybrid fuzzy weights-of-evidence	Knowledge-driven fuzzy	Data-driven fuzzy	Neural network	Hybrid neuro-fuzzy	Augmented naive Bayesian classifier
% of known deposits classified in high favorability zones	83.3	87.0	87.0	85.2	94.4	96.3	88.9
% of study area classified in high favorability zones	3.1	5.9	8.9	5.4	6.0	9.5	11.3
Whether Rampura-Agucha deposit classified in high favorability zones	No	No	No	No	Yes	Yes	No
Assumption of conditional independence	Required	Required	Not required	Not required	Not required	Not required	Not required
Whether parameters easily interpretable	Yes	Yes	No	No	No	No	Yes

Table 9.1 contd.

Evaluation criterion	Linear models		Non-linear models				
	Weight-of-evidence	Hybrid fuzzy weights-of-evidence	Knowledge-driven fuzzy	Data-driven fuzzy	Neural network	Hybrid neuro-fuzzy	Augmented naive Bayesian classifier
Whether parameter learning easily implemented in GIS	Yes	Yes	Yes	Yes	No	No	No
Whether affected by the curse of dimensionality	Not significantly	No	No	Not significantly	Yes	Yes	Yes
Whether uncertainty quantified	Stochastic uncertainties quantified	Yes	No	No	No	No	No
Basis of parameter estimation	Data	Both data and knowledge	Knowledge	Both data and knowledge	Data	Both data and knowledge	Data

mineral deposits, the possibility of conditional dependencies amongst predictor patterns is often hard to rule out. The moot question, however is: how seriously is the performance of these Bayesian models affected by conditional dependencies in input data? The question was explored in this research (see Chapter 8, pp. 228-235) and there appears to be some evidence that their performance is not seriously degraded, especially if the output posterior probabilities are interpreted as relative favorability values. Nevertheless, as shown in Chapter 8, the performance of a Bayesian model improves if it is implemented in a non-linear mode without assuming conditional independence of input predictor patterns. The better performance of the non-linear models as compared to the linear models may therefore be partially attributed to their ability to recognize and compensate for conditional dependencies amongst input predictor patterns.

However, although the simplified and modified Bayesian equations used in the linear models may not fit the data perfectly, they allow significant insights into the data. The parameters of the linear models can be interpreted easily (Table 9.1) to gain insights into the relative contributions of various predictor patterns (or recognition criteria) and, hence, into genetic processes that formed target mineral deposits (Bonham-Carter, 1994). The non-linear functions, on the other hand, may fit the data more efficiently, but their parameters are generally not amenable to direct geoscientific interpretations.

The linear models also have an advantage over the non-linear models in that they are easily implemented in a GIS environment (Table 9.1). The non-linear models, on the other hand, require specialized computer programs for parameter estimations and, therefore, are generally implemented outside the GIS[*] and the output values are imported back into the GIS in order to generate favorability maps.

The linear models are, in general, not seriously affected by high dimensionality of input data (Table 9.1). On the other hand, the non-linear models (again, with the exceptions of the fuzzy models) are more susceptible to the curse of dimensionality and, if implemented without caution, may over-fit the training data. Although over-fitting can be controlled by following efficient training procedures (Chapter 6, p. 165), it is often necessary to reduce dimensionality of the input data in order to avoid it.

Quantification of uncertainty in the output of a model is important because it facilitates effective decision making. The linear models used in this research

---

[*]The fuzzy models are exceptions in this respect, but that is because their parameters are estimated heuristically from knowledge and, therefore, do not require algorithmic estimations.

quantify uncertainties in their outputs (Table 9.1). The non-linear models, on the other hand, do not quantify the uncertainties in their outputs.

Most mathematical geological models, both linear and non-linear, are implemented either in a data-driven mode or in a knowledge-driven mode, which entails that a significant proportion of the geoscientific information remains under-utilized. Moreover, these models cannot 'cross-compensate' possible deficiencies in either the knowledge-base or in the database. This research attempted to address this problem by applying 'hybrid' models that can conjunctively use both data and knowledge for parameter estimation. Table 9.1 shows that, in both linear and non-linear categories, the hybrid models perform better than the purely knowledge-driven or purely data-driven models.

Based on the above discussions, the following conclusions can be drawn about various mathematical geological models described in this thesis.

- Both linear and non-linear models can be effectively used for narrowing down search areas for mineral exploration.

- The non-linear models perform better, as compared to the linear models, in predicting base-metal deposits in the study area, which indicates that, as compared to the linear functions, the non-linear functions more adequately approximate the relationship between predictor patterns and target mineral deposits.

- The non-linear models, especially the neural network and the hybrid neuro-fuzzy models, can perform better than the linear models in predicting deposits in unusual geological settings.

- The non-linear functions have the ability to take into account the possible conditional dependencies amongst predictor pattern and therefore the response of the non-linear models is conditioned in such a way that the contribution of conditionally-dependent patterns is minimized.

- The parameters of the linear models are amenable to direct geoscientific interpretations. On the other hand, the parameters of the non-linear models can not always be interpreted to gain insights into the data and genetic processes.

- The linear models are conveniently implemented in a GIS-environment, where as the non-linear models require specialized computer software for implementation.

- A susceptibility to the curse of dimensionality and an inability to quantify uncertainties in the outputs are major limitations of the non-linear models.

- Hybrid mathematical geological models perform better than purely knowledge-driven and purely data-driven models.

Amongst the mathematical geological models described in this thesis, there is no 'best' model that can be effectively used for mineral potential mapping in all situations. The selection of the best model depends mainly on (a) geoscientific information available for the modeling, (b) computer hardware and software resources available for the modeling and (c) whether gaining insights into the data is also an objective of the modeling. The above conclusions provide rough guidelines for selecting the best model in a given modeling situation.

9.4 Base-Metal Potential of the Study Area

Table 9.1 shows that, on an average, about 10% of the study area has potential for base-metal deposits. The predicted high-favorability zones show a broadly similar spatial distribution pattern on the favorability maps generated by various spatial models (compare Figs. 3.6, 3.9, **??**, 5.4, **??**, 7.6 and 8.4).

The high-favorability zones are generally confined to specific lithologies and stratigraphic groups of the Bhilwara, Aravalli and Sendra-Ambaji domains, which reflect a strong lithostratigraphic control on base-metal mineralization in the province. The predicted high-favorability zones are also closely associated with regional magnetic lineaments (Fig.2.5B), which indicate that crustal-scale faults played an important role in the spatial localization of base-metal mineralizations in the study area.

However, the predicted high-favorability zones do not show strong affinity with the NE-trending lineaments (Fig. 2.18B), NW-trending lineaments (Fig. 2.19A) and regional fold axes (Fig. 2.19B). This suggests that, although seemingly important controls on a deposit-scale (see Chapter 2), these structures played less important roles in localizing mineralization on a regional-scale as compared to crustal scale faults.

The spatial distributions of predicted high favorability zones are, in general, consistent with conceptual models of metallogenesis in the study area. The three episodes of base-metal mineralizations in the study area at ca. 2000 Ma, ca. 1800 Ma and ca. 1000 Ma, which were identified on the basis of

conceptual-genetic studies, are generally well-represented by high-favorability zones in the Aravalli, Bhilwara and Sendra-Ambaji domains, respectively. In addition, several zones of high favorability are demarcated in the Jharol domain, in which only one small deposit has been located so far. These zones are potential target areas for base-metal exploration in the Jharol domain.

9.5   Recommendations for Future Research

- In this research mathematical geological models were applied to demarcate potentially-mineralized zones based on regional-scale (1:250,000) predictor maps. The same models need further testing by modeling larger-scale predictor maps to demarcate specific prospects within the predicted potentially-mineralized zones.

- This research indicates that neural network, hybrid neuro-fuzzy and augmented Bayesian network classifier models have high performance levels, but, at the same time, they are sensitive to the curse of dimensionality if there is a paucity of known mineral deposits. In such cases, predictor maps may require significant preprocessing before they can be used in these models, which may result in loss of information. Future research aimed at finding methods to address this problem can help in further improving the performance levels of these models. In this context, the work of Brown *et al.* (2003), who introduced random noise to augment the training data, can be a useful starting point.

- Further research aimed at developing mathematical methods for quantifying both systemic and stochastic uncertainties in the outputs of the non-linear mathematical geological models described here can increase the utility of their output favorability maps for decision-making.

- The mathematical geological models in this research were tested by regional-scale mapping of SEDEX-type base-metal deposits. The models require further testing on other deposit types; if found unsatisfactory, problems should be identified and techniques to solve them should be developed.

References

Agterberg, F.P., 1974. Automated contouring of geological maps to detect target areas for mineral exploration. Mathematical Geology, v. 6(4), p. 373-395.

Agterberg, F.P., 1989. Systematic approach to dealing with uncertainty of geoscience information in mineral exploration. Proceedings of the 21st APCOM Symposium, Las Vegas, USA, Chapter 18, p. 165-178.

Agterberg, F.P., 1992. Combining indicator patterns in weights of evidence modeling for resource estimation. Nonrenewable Resources, v.1, p. 39-50.

Agterberg, F.P., and Bonham-Carter, G.F., 1990. Deriving weights-of-evidence from geoscience contour maps for prediction of discrete events. Proceedings of the 22nd APCOM Symposium, Berlin, Germany, v.2, p. 381-395.

Agterberg, F.P., and Cheng, Q., 2002. Conditional independence test for weights-of-evidence modeling. Natural Resources Research, v. 11(4), p. 249-255.

Agterberg, F.P., Bonham-Carter, G.F. and Wright, D.F., 1990. Statistical pattern integration for mineral exploration. In: Gaál, G. and Merriam, D.F.(Eds.), Computer Applications in Resource Estimation Prediction and Assessment for Metals and Petroleum. Pergamon Press, Oxford-New York, p. 1-21.

Alberti, P.M., and Uhlmann, A., 1982. Stochasticity and Partial Order: Double Stochastic Map and Unitary Mixing. Series: Mathematics and Its Applications, Hazewinkel, M. (Series Ed.) Vol. 9, Springer, Boston, 132 pp.

Aliferis, C., and Cooper, G., 1994. An evaluation of an algorithm for inductive learning of Bayesian belief networks using simulated data sets. Proceedings of Tenth Conference on Uncertainty in Artificial Intelligence, Morgan Kaufmann, Seattle, WA, p. 8-14.

An, P., Moon, W.M., and Rencz, A., 1991. Application of fuzzy set theory for integration of geological, geophysical and remote sensing data. Canadian Journal of Exploration Geophysics, v. 27, 1-11.

Aspinall, P.J., and Hill, A.R., 1983. Clinical inferences and decisions-I: Diagnosis and Bayes' theorem. Ophthalmic and Physiologic Optics, v. 3, p.295-304.

Augusteijn, M. F. and McCarthy, K. K., 1995. Image indexing applied to character font recognition by means of a Kohonen neural network hierarchy. Intelligent Engineering Systems Through Artificial Neural Networks, Vol. 5, Fuzzy Logic and Evolutionary Programming - Proceedings of the Artificial Neural Networks in Engineering (ANNIE'95), ASME Press, p. 431-436.

Badsberg, J., 1992. Model search in continegency tables by CoCo. In: Dodge, Y., and Wittaker, J. (Eds.), Computational Statistics, Physica Verlag, Heidelberg, p. 251-256.

Bateman, A.M., 1951a. Economic Mineral Deposits. Wiley and Sons, New York, 916 pp.

Bateman, A.M., 1951b. The Formation of Mineral Deposits. Wiley and Sons, New York, 371 pp.

Bellman, R., 1961, Adaptive Control Processes: A Guided Tour. Princeton University Press, NJ, 255 pp.

Bennani, Y., 1999. Adaptive weighting of pattern features during learning IJCNN'99. International Joint Conference on Neural Networks Proceedings, IEEE Service Center, v. 5, p. 3008-3013.

Beeson, R., 1990. Broken Hill-type lead-zinc deposits - an overview of their occurrence and geological setting. Institute of Mining and Metullurgical Transections, v. 99, p. B163-B175.

Bishop, C.M., 1995. Neural Networks for Pattern Recognition, Oxford University Press, New York, 482 pp.

248

Bishop, Y. M. M., Fienberg, S. E., and Holland, P. W., 1975. Discrete Multivariate Analysis: Theory and Practice, MIT Press, Cambridge, MA, 587 pp.

Boleneus, D.E., Raines, G.L., Causey, J.D., Bookstrom, A.A., Frost, T.P., and Hyndman, P.C., 2001. Assessment method for epithermal gold deposits in northeast Washington State using weights-of-evidence GIS modeling. USGS Open-File Report 01-501, 52 pp.

Bonham-Carter, G.F., 1994. Geographic Information Systems for Geoscientists: Modeling with GIS. Pergamon Press, Ontario, Canada, 398 pp.

Bonham-Carter, G.F., and Agterberg, F.P., 1990. Application of a microcomputer based geographic information system to mineral-potential mapping. In: Hanley, J.T., and Merriam, D.F., (Eds.), Microcomputer-based Applications in Geology, II, Petroleum, Pergamon Press, New York, p. 49-74.

Bonham-Carter, G.F., and Agterberg, F.P., 1999. Arc-WofE: a GIS tool for statistical integration of mineral exploration datasets. Proceedings of International Statistical Institute, Helsinki, August 11-16, p. 497-500.

Bonham-Carter, G.F., Agterberg, F.P. and Wright, D.F., 1988. Integration of geological datasets for gold exploration in Nova Scotia. Photogrammetry and Remote Sensing, v. 54(11), p. 1585-1592.

Bonissone, P.P., and Decker, K.S., 1986. Selecting uncertainty calculi and granularity: An experiment in trading-off precision and complexity. In: Kanal, L.N., and Lemmer, J.F., (Eds.), Uncertainty in Artificial Intelligence, Elsevier Science Publishers B.V., North-Holland, p. 217-247.

Bose, U., 2000. The nature, origin and evolution of the banded gneissic complex basement rocks of Rajasthan. In: Deb, M. (Ed.), Crustal Evolution and Metallogeny in the Northwestern Indian Shield, Narosa Publication House, New Delhi, p. 73-86.

Bott, M.H.P., and Hinze, W.J., 1995. Potential field methods. In: Olsen, K.H. (Ed.), Continental rifts: Evolution, Structure,

Tectonics: Development in Geotectonics, v. 5, Elsevier, Amsterdam, p. 93-98.

Bougrain, L., Gonzalez, M., Bouchot, V., Cassard, D., and Lips, A. L. W., 2003. Knowledge Recovery for Continental-Scale Mineral Exploration by Neural Networks. Natural Resources Research, v. 12(3), p. 173-182.

Boyce, J.I., and Morris, W.A., 2002. Basement-controlled faulting of Paleozoic strata in southern Ontario, Canada: new evidence from geophysical lineament mapping. Tectonophysics, v. 353, p. 151-171.

Briggs, I.C., 1974. Machine contouring using minimum curvature. Geophysics, v. 39(1), p. 39-48.

Brown, W.M., Gedeon, T.D., Groves, D.I., and Barnes, R.G., 2000. Artificial neural networks: a new method for mineral prospectivity mapping: Australian Journal of Earth Sciences, v. 47, p. 757-770.

Brown, W.M., Gedeon, T.D., and Groves, D.I., 2003. Use of noise to augment training data: a neural network method of mineral potential mapping in regions of limited known deposit examples. Natural Resources Research, v. 12(3), p. 141-152.

Buntine, W., 1994. Operations for learning with graphical models. Journal of Artificial Intelligence Research, v. 2, p. 159-225.

Carranza, E.J.M., and Hale, M., 2000. Geologically constrained probabilistic mapping of gold potential, Baguio district, Philippines. Natural Resources Research, v. 9(3), p. 237-253.

Carranza, E.J.M., and Hale, M., 2001. Geologically constrained fuzzy mapping of gold mineralization potential, Baguio district, Philippines. Natural Resources Research, v. 10(2), p. 125-136.

Carranza, E.J.M., and Hale, M., 2002. Where are porphyry copper deposits spatially localized? a case study in Benguet province, Philippines. Natural Resources Research, v. 11(1), p. 45-59.

Chauhan, D.S., 1977. Dariba main lode of Rajpura-Dariba zinc-lead-copper belt, Udaipur district, Rajasthan. Journal of the Geological Society of India, v. 18, p. 611-616.

250

Cheng, J., Greiner, R., Kelly, J., Bell, D., and Liu, W., 2002. Learning Bayesian network from data: an information-theory based approach. Artificial Intelligence, v. 137, p. 43-90.

Cheng, Q., and Agterberg, F.P., 1999. Fuzzy weights of evidence and its application in mineral potential mapping. Natural Resources Research, v. 8(1), p. 27-35.

Chickering, D.M., Geiger, D., and Heckerman, D, 1994. Learning Bayesian networks is NP-hard. Technical Report MSR-TR-94-l7, Microsoft Research, Microsoft Corporation, 22 pp.

Chodhary, A.K., Gopalan, K., and Sastry, A., 1984. Present status of the geochronology of the Precambrian rocks of Rajasthan. Tectonophysics, v. 105, p. 131-140.

Cooper, G.F., and Herskovits, E., 1992. A Bayesian method for the induction of probabilistic networks from data. Machine Learning, v. 9, p. 309-347.

Crawford, A.R., 1970. The Precambrian geochronology of Rajasthan and Bundelkhand, northern India. Canadian Journal of Earth Sciences, v. 7(91), p. 91-110.

Davis, J.C., 1986. Statistics and Data Analysis in Geology, John Wiley and Sons, New York, 646 pp.

Deb, M., 1986. Sulfur and carbon isotope compositions in the stratiform Zn-Pb-Cu sulfide deposits of the Rajpura-Dariba belt, Rajasthan: a model of ore genesis. Mineralium Deposita, v. 21, p. 313-321.

Deb, M., 1990. Isotope constitution of sulphur in the conformable base-metal sulphide deposits in the Proterozoic Aravalli-Delhi orogenic belt, NM India. In: Naqvi, S.M. (Ed.), Precambrian Continental Crust and Its Mineral Resources, Development in Precambrian Geology, vol. 8, Elsevier, Amsterdam, p. 631-651.

Deb, M., 1999. Metallic mineral deposits of Rajasthan. In: Kataria, P., (Ed.), Proceedings of Seminar on Geology of Rajasthan - Status and Perspective, M.L. Sukhadia University, Udaipur, India, p. 213-237.

Deb, M., 2000a. Crustal Evolution and Metallogeny in the Northwestern Indian Shield, Narosa Publishing House, New Delhi,

527 pp.

Deb, M., 2000b. VMS deposits: geological characteristics, genetic models and a review of their metallogenesis in the Aravalli range, NW India. In: Deb, M. (Ed.), Crustal Evolution and Metallogeny in the Northwestern Indian Shield, Narosa Publishing House, New Delhi, p. 217-239.

Deb M., and Bhattacharya, A.K., 1980. Geological settings and conditions of metamorphism of Rajpura-Dariba polymetallic ore deposit, Rajasthan, India. Proceedings of 5th Quad. IAGOD Symposium, Schweiz-Verlag, Stuttgart, pp. 679-697.

Deb, M., and Kumar, R., 1982. The volcano-sedimentary environment of Rajpura-Dariba polymetallic ore deposit, Udaipur district. Proceedings of symposium on Metallogeny of the Precambrian, Geological Survey of India, New Delhi, p. 1-17.

Deb, M., and Sarkar, S.C., 1990. Proterozoic tectonic evolution and metallogenesis in the Aravalli-Delhi orogenic complex, NW India. Precambrian Research, v. 46, p. 115-137.

Deb, M., and Thorpe, R.I., 2001. Geochronological constraints in the Precambrian geology of northwestern India and their metallogenic implications. Proceedings of International Workshop on Sediment-hosted Lead-Zinc Deposits in the Northwestern Indian Shield, New Delhi and Udaipur, India, p. 137-152.

Deb, M., Thorpe, R. I., Cumming, G. L., and Wagner, P. A., 1989. Age, source and stratigraphic implications of Pb isotope data for conformable, sediment-hosted base-metal deposits in the Proterozoic Aravalli-Delhi orogenic belt, NW India. Precambrian Research, v. 43, p. 1-22.

Deb, M., Thorpe, R.I., Krstic, D., Corfu, F., and Davis, D.W., 2001. Zircon U-Pb and galena Pb isotope evidence for an approximate 1.0 Ga terrane constituting the western margin of the Aravalli-Delhi orogenic belt, Northwestern India. Precambrian Research, v. 108, 195-213.

DMGR, 1990. Mineral Wealth of Rajasthan, Department of Mines and Geology (Rajasthan) publication, Udaipur, 109 pp.

Domingos, P., and Pazzani, M., 1996. Beyond Independence: Conditions for optimality of the simple Bayesian classifier. In: Saitta (Ed.), Proceedings of the Thirteenth International Conference on Machine Learning, Morgan Kaufmann, San Francisco, CA, p. 105-112.

Domingos, P., and Pazzani, M., 1997. On the optimality of the simple Bayesian classifier under zero-one loss. Machine Learning, v. 29, p. 103-130.

Duda, R.O., and Hart, P.E., 1973. Pattern Classification and Scene Analysis. John Wiley and Sons, New York, 482 pp.

Duda, R.O., Hart, P.E., Nilsson, N.J., and Sutherland, G.L., 1978. Semantic network representations in rule-based interference systems. In: Waterman, D.A., and Hayes-Roth, F. (Eds.), Pattern-Directed Inference Systems, Academic Press, p. 203-221.

Fareeduddun and Kroner, A., 1998. Single zircon age constraints on the evolution of Rajasthan granulite. In: Paliwal, B.S., (Ed.), The Indian Precambrian, Scientific Publishers, Jodhpur, p. 547-556.

Friedman, J. H., 1997. On bias, variance, 0/1 - loss and the curse-of-dimensionality. Data Mining and Knowledge Discovery, v. 1, p. 55-77.

Friedman, N., Geiger, D., and Goldszmidt, M., 1997. Bayesian network classifiers. Machine Learning, v. 29, p. 131-161.

Fry, N., 1979. Random point distribution and strain measurement in rocks. Tectonophysics, v. 60, p. 806-807.

Gandhi, S.M., 2001. The geology and mineralization of Rampura-Agucha zinc-lead deposit, India. Proceedings of International Workshop on Sediment-hosted Lead-Zinc Deposits in the Northwestern Indian Shield, New Delhi and Udaipur, India, p. 227-249.

Gandhi, S.M., Paliwal, H.V., and Bhatnagar, S.N., 1984. Geology and ore reserve estimation of Rampura-Agucha lead-zinc deposit, Bhilwara, Rajasthan. Journal of the Geological Society of India, v. 25, p. 689-705.

Geiger, D., and Heckerman, D., 1996. Knowledge representation and inference in similarity networks and Bayesian multinets. Artificial Intelligence, v. 82, p. 45-74.

Geiger, D., and Heckerman, D., 1997. A characterization of Dirichlet distributions through local and global independence. Annals of Statistics, v. 25, p. 1344-1368.

Gettings, M.E., and Bultman, M.W., 1993. Quantifying favorableness for occurrence of a mineral deposit type - an example from Arizona. USGS Open-File Report 93-392, 23 pp.

Glahn, H.R., and Lowry, D.A., 1972. The Use of Model Output Statistics (MOS) in Objective Weather Forecasting. Journal of Applied Meteorology, v. 11(8), p. 1203-1211.

Goguen, J.A., 1969. The logic of inexact concepts. Synthese, v. 19, p. 325-373.

Goodacre, A., Bonham-Carter, G.F., Agterberg, F.P., and Wright, D.F., 1993. A statistical analysis of the spatial association of seismicity with drainage patterns and magnetic anomalies in western Quebec. Tectonophysics, v. 217, p. 205-305.

Goodfellow, W.D., 1987. Anoxic stratified oceans as a source of sulphur in sediment-hosted stratiform Zn-Pb deposits (Selwyn Basin, Yukon, Canada). Chemical Geology, v. 65, 359-382.

Goodfellow, W.D., 2001. Attributes of modern and ancient sediment-hosted, sea-floor hydrothermal deposits.Proceedings of International Workshop on Sediment-hosted Lead-Zinc Deposits in the Northwestern Indian Shield, New Delhi and Udaipur, India, p. 1-31.

Gopalan, K., MacDougall, J.D., Roy, A.B., and Murali, A.V., 1990. Sm-Nd evidence for 3.3 Ga old rocks in Rajasthan, northwestern India. Precambrian Research, v. 48, p. 287-197.

GSI, 1981. Total intensity aeromagnetic map and map showing the magnetic zones of the Aravalli region, southern Rajasthan and northwestern Gujarat, India (1:250,000). Geological Survey of India press, Hyderabad, India, 4 sheets.

Gupta, S.N., Arora, Y.K., Mathur, R.K., Iqballuddin, Prasad, B., Sahai, T.N., and Sharma, S.B., 1997. The Precambrian geology

254

of the Aravalli Region, Memoirs of Geological Survey of India, v. 123, Geological Survey of India press, Hyderabad, India, 262 pp.

Gupta, S.N., Arora, Y.K., Mathur, R.K., Iqballuddin, Prasad, B., Sahai, T.N., and Sharma, S.B., 1995a. Lithostratigraphic map of Aravalli region, 2nd edition (1:250,000). Geological Survey of India Press, Calcutta, India, 4 sheets.

Gupta, S.N., Arora, Y.K., Mathur, R.K., Iqballuddin, Prasad, B., Sahai, T.N., and Sharma, S.B., 1995b. Structural map of the Precambrian of Aravalli region, 2nd edition (1:250,000). Geological Survey of India Press, Calcutta, India, 4 sheets.

Gupta, S.N., Arora, Y.K., Mathur, R.K., Iqballuddin, Prasad, B., Sahai, T.N., and Sharma, S.B., 1980. Lithostratigraphic map of Aravalli region, southern Rajasthan and northeastern Gujarat (1:1,000,000). Geological Survey of India, Hyderabad, India, 1 sheet.

Guyon, I., Albrecht, P., LeCun, Y., Denker, J.S., and Hubbard W., 1991. Design of a neural network character recognizer for a touch terminal. Pattern Recognition, v. 24(2), p. 105-119.

Haldar, S.K., 2001. Grade-tonnage model for lead-zinc deposits of Rajasthan, India. Proceedings of an International Workshop on Sediment-hosted Lead-Zinc Deposits in the Northwestern Indian Shield, New Delhi and Udaipur, India, p. 153-160.

Haldar, S.K., and Deb, M., 2001. Geology and mineralization of Rajpura-Dariba lead-zinc belt, Rajasthan. Proceedings of International Workshop on Sediment-hosted Lead-Zinc Deposits in the Northwestern Indian Shield, New Delhi and Udaipur, India, p. 177-187.

Harris, D.P., and Pan, G.C., 1999. Mineral favorability mapping: a comparison of artificial neural networks, logistic regression and discriminate analysis. Natural Resources Research, v. 8(2), p. 93-109.

Haykin, S., 1994, Neural networks: A comprehensive foundation 2nd edition, Prentice Hall, Upper Saddle River, NJ, 842 pp.

Heckerman, D.E., Horvitz, E.J., and Nathwani, B.N., 1992. Towards normative expert systems: Part I the Pathfinder project. Methods of Information in Medicine, v. 31, p. 90-105.

Heckerman, D., 1990. Probabilistic similarity networks. Networks, v. 20, p. 607-636.

Heckerman, D., 1995. A Tutorial on Learning with Bayesian Networks. Technical Report MSR-TR-95-06, Microsoft Research, 40 pp.

Heckerman, D., Geiger, D., and Chickering, D., 1995. Learning Bayesian networks: The combination of knowledge and statistical data. Machine Learning, v. 20, p. 197-243.

Hellendoorn, H., and Thomas, C., 1993. Defuzzification in fuzzy controllers. Journal of Intelligent & Fuzzy Systems, v.1, p. 109-123.

Helson, H., 1964. Adaption-level theory, Harper and Row, New York, 732 pp.

Heron, A.M., 1917. The geology of northeastern Rajputana and adjacent districts. Memoirs of Geological Survey of India, v. 14, Geological Survey of India Press, Calcutta, India, 128 pp.

Heron, A.M., 1939. The geology of southeastern Rajputana. Memoirs of Geological Survey of India, v. 68, Geological Survey of India Press, Calcutta, India, 120 pp.

Heron, A.M., 1953. The geology of central Rajputana. Memoirs of Geological Survey of India, v. 79(1), Geological Survey of India Press, Calcutta, India, 389 pp.

Herskovits, E., 1991. Computer-based probabilistic network construction. Doctoral Dissertation, Medical Information Science, Stanford University, Stanford, CA, 225 p.

Hodgson, C.J., and Troop, D. G., 1988. A new computer-aided methodology for area selection in gold exploration: A case study from the Abitibi greenstone belt. Economic Geology, v. 83(5), p. 952-977.

Jang, J.S.R., 1993. ANFIS: Adaptive-network-based fuzzy inference system. IEEE Transactions on Systems, Man and Cybernetics, v. 23, p. 665-685.

Jang, J.S.R., and Sun, C. T., 1995, Neuro-fuzzy modeling and control. Proceedings of IEEE, v. 83, p. 378-406.

Jang, J.S.R., and Gulley, N., 1995. The Fuzzy Logic Toolbox for use with MATLAB. The MathWorks, Inc., Natick, MA.

Kala, P.P., 2001. Economic aspects of exploration planning. HINDZ-INC TECH, January 2001, Hindustan Zinc Ltd. publication, p. 2-15

Kapusta, M., and Gajer, M. , 2000. The usage of the Kohonen neural networks for the pathological speech recognition. Pomiary-Automatyka-Kontrola, no.7, July 2000, p.10-15.

Kemp, L.D., Bonham-Carter, G.F., and Raines, G.L., 1999. Arc-WofE: ArcView extension for weights of evidence mapping. http://gis.nrcan.gc.ca/software/arcview/wofe.

Kemp, L.D., Bonham-Carter, G.F., Raines, G.L., and Looney, C.G., 2001. Arc-SDM: ArcView extension for spatial data modeling using weights of evidence, logistic regression, fuzzy logic and neural network analysis. http://ntserv.gis.nrcan.gc.ca/sdm/.

Knox-Robinson, C.M., 2000. Vectorial fuzzy logic: a novel technique for enhanced mineral prospectivity mapping with reference to the orogenic gold mineralization potential of the Kalgoorlie Terrane, Western Australia. Australian Journal of Earth Sciences, v. 47(5), p. 929-942.

Kochar, 2000. Attributes and significance of the A-type Malani magmatism, northwestern Peninsular India. In: Deb, M., (Ed.), Crustal Evolution and Metallogeny in the Northwestern Indian Shield, Narosa Publishing House, New Delhi, India, pp. 158-188.

Kononenko, I., 1991. Semi-naive Bayesian classifier. In: Kodratoff, Y., (Ed.), Proceedings of the Sixth European Working Session on Learning, Springer-Verlag, Berlin, p. 206-219.

Kubat, M., and Matwin, S., 1997. Addressing the curse of imbalanced training sets: One-sided selection. Proceedings of the Fourteenth International Conference on Machine Learning, ICML'97, Nashville, TN, p. 179-186.

Kubat, M., Holte, R., and Matwin, S., 1998. Detection of oil spills in radar images of sea surface. Machine Learning, v. 30, p. 195-215.

Lam, W., and Bacchus, F., 1994. Learning Bayesian belief networks: An approach based on the MDL principle, Computational Intelligence, v. 10(4), p. 269-293.

Langley, P., and Sage, S., 1994. Induction of selective Bayesian classifiers. In: Lpez de Mantars and Poole, D. (Eds.), Proceedings of the Tenth Conference on Uncertainty in Artificial Intelligence (UAI '94), Morgan Kaufmann, San Francisco, CA, p. 399-406.

Langley, P., Iba, W., and Thompson, K., 1992. An analysis of Bayesian classifier. Proceedings of the National Conference on Artificial Intelligence (AAAI '92), AAAI Press, Menlo Park, CA, p. 223-228.

Large, R.R., Boden, S., Davidson, G.J., and Cooke, D.R., 1996. The chemistry of BHT ore formation - one of the keys to understanding the difference between SEDEX and BHT deposits. In: Pongratz, J., and Davidson, G.J., (Eds.), New Developments in Broken Hill Type Deposits, Codes Special Publication No. 1, University of Tasmania, Hobart, p. 105-111.

LeCun, Y., Matan, O., Boser, B., Denker, J.S., Henderson, D., Howard, R.E., Hubbard, W., Jackel, L.D., and Baird, H.S., 1990a. Handwritten Zip Code Recognition with Multilayer Networks. Proceedings of the International Conference on Pattern Recognition, (IAPR), Atlantic City, pp. 35-40.

LeCun, Y., Denker, J. S., Solla, S., Howard, R. E., and Jackel, L. D., 1990. Optimal Brain Damage. In: Touretzky, D., (Ed.), Advances in Neural Information Processing Systems 2 (NIPS*89), Denver, CO, p. 172-180.

Looney, C.G., 1997. Pattern recognition using neural networks: theory and algorithms for engineers and scientists, Oxford University Press, New York, 458 pp.

Looney, C.G., 2002. Radial basis functional link nets and fuzzy reasoning: Neurocomputing, v. 48(1-4), p. 489-509.

Looney, C.G., and Yu, H., 2001. Special software development for neural network and fuzzy clustering analysis in geological information system.
http://ntserv.gis.nrcan.gc.ca/sdm/.

Lusted, L.B., 1968. Introduction to Medical Decision Making. Charles Thomas, Springfield, 271 pp.

Lydon, J.W, 1996. Sedimentary exhalative sulphides (SEDEX). In: Eckstrand, O.R., Sinclair, W.D., and Thorpe, R.I., Geology of Canadian Mineral Deposit Types, Geological Survey of Canada, no. 8, p. 130-152.

Lydon, J.W., 2001. Exploration criteria and genetic models for SEDEX deposits: the Belt-Purcell Basin and the Sullivan deposit. Proceedings of an International Workshop on Sediment-hosted Lead-Zinc Deposits in the Northwestern Indian Shield, New Delhi and Udaipur, India, p. 197-223.

MacDougall, J.D., Gopalan, K., Lugmair, G.W., and Roy, A.B., 1983. The Banded Gneissic Complex of Rajasthan, India: early crust from a depleted mantle at $\sim$3.5 AE? EOS Transactions of American Geophysical Union, v. 64(18), p. 351.

MacDougall, J.D., Willis, R., Lugmair, G.W., Roy, A.B., and Gopalan, K., 1984. The Aravalli sequence of Rajasthan, India: A Precambrian continental margin. Workshop on the Early Earth: the Interval from Accretion to the Older Archaean. Lunar Planetary Institute, Houston, Texas, p. 55-56.

MacLeod, I.N., Jones, K., and Dai, T.F., 1993. 3D analytic signal in the interpretation of total magnetic field data at low magnetic latitudes. Exploration Geophysics v. 24, p. 679-687.

Mamdani, E.H., 1974. Applications of fuzzy algorithm for control of a simple dynamic plant. Proceedings of IEEE, v. 121(12), p. 1585-1588.

Mamdani E.H., and Assilian S., 1975. An Experiment in Linguistic Synthesis with a Fuzzy Logic Controller. International Journal of Man-Machine Studies, v. 7(1), p. 1-13.

Masters, T., 1993. Practical neural network recipes in C++, Academic Press, New York, 493 pp.

Masters, T., 1995, Advanced Algorithms for Neural Networks: A C++ Source book, Academic Press, New York, 431 pp.

Menzie, W.D., and Mosier, D.L., 1986. Grade and tonnage model of sedimentary exhalative Zn-Pb. In: Cox, D.P., and Singer, D.A. (Eds.), Mineral deposit models, U.S. Geological Survey Bulletin 1693, p. 212-215.

Mihalasky, M.J., 1999. Mineral potential modeling of gold and silver mineralization in the Nevada Great Basin. Ph.D. Dissertation (Unpublished), University of Ottawa, 354 pp.

Minty, B.R.S., 1991. Simple microlevelling for Aeromagnetic data. Exploration Geophysics, v. 22, p. 591-592.

Mishra, D.C., Singh, B., Tiwari, V.M., Gupta, S.B., and Rao, M.B.S.V., 2000. Two cases of continental collisions and related tectonics during the Proterozoic period in India: insights from gravity modelling constrained by seismic and magnetotelluric studies. Precambrian Research, v. 99, p. 149-169.

Mishra, D.C., Singh, B., Tiwari, V.M., Gupta, S.B., Rao, N.K., and Rao, M.B.S.V., 1998. An integrated crustal model along Nagaur-Jhalawar geotransect. Journal of Geophysics, v. 19(2), p. 125-131.

Mitiche, A. and Lebidoff, M., 2001. Pattern classification by a condensed neural network Neural Networks, v. 14(4-5), p. 575-580.

Mizumoto, M., 1989. Pictorial representations of fuzzy connectives, Part I: cases of T-norms, T-conorms and averaging operators: Fuzzy Sets and Systems, v. 31, p. 217-242.

Mookherjee, A., 1964a. Thermal metamorphism of sulphide minerals at Zawar, Rajasthan, India. Economic Geology, v. 59, p. 498-501.

Mookherjee, A., 1964b. The geology of the Zawar lead-zinc mine, Rajasthan, India. Economic Geology, v. 59, p. 656-677.

Mookherjee, A., 1965. Regional structural framework of the lead-zinc deposit at Zawar, Rajasthan, India. Journal of the Geological Society of India, v. 6, p. 67-80.

Nelson, R., 1995. Probability, Stochastic Processes, and Queueing Theory : The Mathematics of Computer Performance Modeling. Springer-Verlag, New York, 583 pp.

Paliwal, H.V., Bhatnagar, S.N., and Haldar, S.K., 1986. Lead-zinc resource prediction in India: An application of Zipf Law. Mathematical Geology, v. 18(6), p. 539-549.

Pan, G.C., 1996. Extended weights of evidence modeling for the pseudo-estimation of metal grades. Nonrenewable Resources, v. 5, p. 53-76.

Pan, G.C., and Harris, D.P., 2000. Information Synthesis for Mineral Exploration. Oxford University Press, New York, 461 pp.

Pao, Y.H., Park, G. H., and Sobajic, D. J., 1994. Learning and generalization characteristics of the random vector functional link net. Neurocomputing, v. 6, 163-180.

Parzen, E., 1962. On estimation of a probability density function and mode. Annals of Mathematical Statistics, v. 33, p. 1065-1076.

Pearl, J., 1988. Probabilistic Reasoning in Intelligent Systems: Networks of Plausible Inference, Morgan Kaufmann, Palo Alto, CA, 383 pp.

Pettijohn, F.J., 1975. Sedimentary Rocks. Harper and Row, New York, pp. 628.

Plimer, I.R., 1986. Sediment-hosted exhalation Pb-Zn deposits - products of contrasting ensiallic rifting. Geological Society of South Africa, Transactions, v. 89, p. 57-73

Poddar, B.C., 1965, Lead-zinc mineralization in the Zawar belt, India. Economic Geology, v. 60, p. 636-638.

Poddar, B.C., 1974. Evolution of sedimentary sulphide rhythmites into metamorphic tectonites in the base metal deposits of Rajpura-Dariba, Raajsthan, Golden Jubilee Volume, Quarterly Journal of Geological, Mining and Metallurgical Society of India, v. 46, p. 207-221.

Pongratz, J., and Davidson, G.J., 1996. New Developments in Broken Hill Type Deposits, Codes Special Publication No. 1, University of Tasmania, Hobart, 164 pp.

Porwal, A., and Hale, M., 2000. GIS-based weights-of-evidence analysis of multi-class spatial data for predictive mineral mapping: a case study from Aravalli province, western India. Proceedings of XIV International Conference on Applied Geologic Remote Sensing, Las Vegas, Nevada, p. 377-384.

Porwal, A., and Sides, E.J., 2000. A predictive model for basemetal exploration in a GIS environment. International Archives of Photogrammetry and Remote Sensing, v. XXXIII, part B7, Amsterdam, 1178-1184.

Porwal, A., Carranza, E.J.M., and Hale, M., 2003a. Knowledge-driven and data-driven fuzzy models for predictive mineral potential mapping. Natural Resources Research, v. 12(1), p. 1-25.

Porwal, A., Carranza, E.J.M., and Hale, M. 2003b. Extended weights-of-evidence modelling for predictive mapping of base-metal deposit potential in Aravalli province, western India. Exploration and Mining Geology, v. 10(4), p. 155-163.

Porwal, A., Carranza, E.J.M., and Hale, M., 2003c. Artificial neural networks for mineral potential mapping: A case study from Aravalli province, western India. Natural Resources Research, v. 12(3), p. 155-177.

Porwal, A., Carranza, E.J.M., and Hale, M., 2004. A hybrid neuro-fuzzy model for mineral potential mapping. Mathematical Geology, v. 36(7), p. 803-826.

Porwal, A., Carranza, E.J.M., and Hale, M., 2006a. Bayesian network classifiers for mineral potential mapping. Computers and Geosciences, v. 32(1), p. 1-16.

Porwal, A., Carranza, E.J.M., and Hale, M., 2006b. Tectonostratigraphy and base-metal mineralization controls, Aravalli province (western India): new interpretations from geophysical data. Ore Geology Reviews (in press).

Porwal, A., Carranza, E.J.M., and Hale, M., 2006c. A Hybrid fuzzy weights-of-evidence model for mineral potential mapping. Natural Resources Research, v. 15(1).

Raghunandan, K. R., Dhruba Rao, B.K., and Singhal, M.L., 1981. Exploration for copper, lead and zinc ores in India. Bulletin of

Geological Survey of India, Series A, no. 47, 222 pp.

Raines, G.L., 1999. Evaluation of weights of evidence to predict ep-ithermal gold deposits in the Great Basin of the western United States. Natural Resources Research, v. 8(4), p. 257-276.

Raja Rao, C.S., Poddar, B.C., And Basu, K.K., and Dutta, A.K., 1971. Precambrian stratigraphy of Rajasthan: a review. Records Geological Survey of India, v. 101(2), p. 60-79.

Rajendra Prasad, B., Tewari, H.C., Vijaya Rao, V., Dixit, M.M., and Reddy, P.R., 1999. Seismic and magnetotelluric studies over a crustal scale fault zone for imaging a metallogenic province of Aravalli Delhi fold belt region. Current Science, v. 76, p. 1027-1031.

Rajendra Prasad, B., Tiwari, H.C., Vijaya Rao, V., Dixit, M.M., and Reddy, P.R., 1998. Structure and tectonics of Aravalli-Delhi fold belt in northwestern India from deep seismic reflec-tion studies. Tectonophysics, v. 288, p. 31-41.

Ramakrishna, T.S., and Bhaskar Rao, K.V.S., 1981. A geophysical study of the environment of base-metal belts and related deep geological features to guide future exploration in Rajasthan: Part II. Geological Survey of India (Unpublished Report), 17 pp.

Ramoni, M., and Sebastiani, P., 1999. Bayesian methods. In: Berthold, M., and Hand, D.J. (Eds.), Intelligent Data Analysis: An Introduction, Springer, New York, p. 129-166.

Ramoni, M., and Sebastiani, P., 2000. Bayesian knowledge discov-erer system. Knowledge Media Institute, The Open University, UK.
http://kmi.open.ac.uk/projects/bkd/.

Ranawat, P.S., and Sharma, N.K., 1990. Petrology and Geochem-istry of the Precambrian Lead-Zinc Deposits of Rampura-Agucha, India. In: Spry, P.G., (Ed.), Metamorphism of Massive Sulfide, VSP, Utrecht, the Netherlands, p. 197-227.

Ranawat, P.S., Bhatnagar, S.N., and Sharma, N.K., 1988. Meta-morphic characteristics of Rampura-Agucha lead-zinc deposit, Rajasthan. In: Roy, A.B. (Ed.), Precambrian of the Aravalli

Mountain Rajasthan, India. Memoir Geological Society of India, v. 7, pp. 397-409.

Reddi, A.G.B., and Ramakrishna T.S., 1988a. Bouguer gravity atlas of western India (Rajasthan-Gujarat), Geological Survey of India Press, Calcutta, India, 45 pp.

Reddi, A.G.P., and Ramakrishna T.S., 1988b. Subsurface structure of the shield area of Rajasthan-Gujarat as inferred from gravity. In: Roy, A.B. (Ed.), Precambrian of the Aravalli Mountain, Rajasthan, India. Memoir Geological Society of India, v. 7, p. 279-184.

Reggia, J.A., and Perricone, B.T., 1985. Answer justification in medical decision support systems based on Bayesian classification. Computers in Biology and Medicine, v. 15(4), p. 161-167.

Robinson, V.B., 2003. A perspective on the fundamentals of fuzzy sets and their use in geographic information systems. Transactions in GIS, v. 7(1), p. 3-10.

Roest, W.E., Verhoef, J., and Pilkington, M., 1992. Magnetic interpretation using 3D analytic signal. Geophysics, v. 57, p. 116-125.

Roy, A. B., 1988a. Precambrian of the Aravalli Mountain Rajasthan. Memoir Geological Society India, v. 7, 289 pp.

Roy, A.B., 1988b. Stratigraphic and tectonic frame work of the Aravalli Mountain Range. In: Roy, A.B., (Ed.), Precambrian of the Aravalli Mountain Rajasthan, India, Memoir Geological Society of India, v. 7, p. 3-31.

Roy, A.B., 1990. Evolution of the Precambrian crust of the Aravalli Mountain Range. In: Naqvi, S.M. (Ed.), Precambrian Continental Crust and its Economic Resources, Developments in Precambrian Geology, v. 8, Elsevier, Amsterdam, pp. 327-348.

Roy, A.B., 2001. Tectono-stratigraphy of Pb-Zn sulphide deposits in the Palaeoproterozoic Aravalli supergroup: examples from Zawar and Rampura-Agucha ore deposits. Proceedings of International Workshop on Sediment-hosted Lead-Zinc Deposits

in the Northwestern Indian Shield, New Delhi and Udaipur, India, pp. 161-176.

Roy, A.B., and Paliwal, B.S., 1981. Evolution of lower Proterozoic epicontinental deposits: stromatolite bearing Aravalli rocks of Udaipur, Rajasthan, India. Precambrian Research, v. 14, pp. 49-74.

Roy, A.B., and Das, A.R., 1985. A study of time relations between movements, metamorphism and granite emplacement in the middle Proterozoic Delhi Supergroup of Rajasthan. Journal of the Geological Society of India, v. 26, p. 726-733.

Roy, A.B., and Kroner, A., 1996. Single zircon evaporation ages constraining the growth of the Archaean Aravalli craton, northwestern Indian Shield. Geological Magazine, v. 133 (3), p. 333-342.

Roy, A.B., and Kataria, P., 1999. Precambrian geology of the Aravalli mountains and neighbourhood: Analytical update of recent studies. In: Kataria, P. (Ed.), Geology of Rajasthan: Status and Perspective, M.L. Sukhadia University, Udaipur, India, p. 1-56.

Roy, A. B., Paliwal, B. S., Shekhawat, S. S., Nagori, D. K., Golani, P. R., and Bejarniya, B. R., 1988. Stratigraphy of the Aravalli Supergroup in type area. In: Roy, A. B., (Ed.), Precambrian of the Aravalli Mountain Rajasthan, Memoir Geological Society India, v. 7, p. 121-131.

Roy, A.B., Sharma, B.L., Paliwal, B.S., Chauhan, N.K., Nagori, D.K., Golani, P.R., Bejarniya, B.R., Bhu, H., and Ali Sabah, M., 1993. Lithostratigraphic and tectonic evolution of the Aravalli Supergroup: a protogeosynclinal sequence. In: Cassyap, A.M., (Ed.), Rift Basins and Aulacogens, Gyanodaya Prakashan, Nainital, p. 73-90.

Rumelhart, D.E., Hinton, G.E., and Williams, R.J., 1986. Learning internal representations by error propagation. In: Rumelhart, D.E., and McClelland, J.L., (Eds.), Parallel Distributed Processing: Explorations in the Microstructure of Cognition, volume 1, Foundations, MIT Press, Cambridge, p. 318-362.

Sackinger, E., Boser, B., Bromley, J., LeCun, Y., and Jackel, L.D., 1992. application of the ANNA neural network chip to high-speed character recognition. IEEE Transaction on Neural Networks, v. 3(2), p. 498-505.

Sahu, K.C., and Mathur, A.K., 1991. On the occurrence of Sargur-type banded iron formation in the Banded Gneissic Complex of South Rajasthan. Journal of the Geological Society of India, v. 38, p. 299-302.

Sarkar, S.C., 2000. Geological setting, characteristics, origin and evolution of sediment-hosted sulphide ore deposits of Rajasthan: a critique with comments in their implications for future exploration. In: Deb, M., (Ed.), Crustal Evolution and Metallogeny in the Northwestern Indian Shield, Narosa Publishing House, New Delhi, p. 240-292.

Sarkar, G., Bishui, P.K., Chattopadhyay, B., Chowdhary, I., Saha, K.C., and Kumar, A., 1992. Geochronology of granites and felsic volcanic rocks of Delhi old belt. Records of Geological Survey of India, v. 125(2), p. 21-23.

Satyavani, N., Dixit and M.M., and Reddy, P.R., 2001. Crustal velocity structure along the Nagaur-Rian sector of the Aravalli fold belt, India, using reflection data. Journal of Geodynamics, v. 31, p. 429-443.

Sharma, R.S., 1988. Patterns of metamorphism in the Precambrian rocks of the Aravalli Mountain Belt. In: Roy, A.B., (Ed.), Precambrian of the Aravalli Mountain Rajasthan, India, Memoir Geological Society of India, v. 7, p. 33-75.

Singer, D.A., and Kouda, R., 1996. Application of a feedforward neural network in the search for Kuroko Deposits in the Hokuroku district, Japan. Mathematical Geology, v. 28(8), p. 1017-1023.

Singer, D.A., and Kouda, R., 1997a. Classification of mineral deposits into types using mineralogy with a probabilistic neural network. Nonrenewable Resources, v. 6(1), p. 69-81.

Singer, D.A., and Kouda, R., 1997b. Use of a neural network to integrate geoscience information in the classification of mineral deposits and occurrences. In: Gubins, A.G. (Ed.), Proceedings

of Exploration 97: Fourth Decennial International Conference on Mineral Exploration, p. 127-134.

Singer, D.A., and Kouda, R., 1999. A comparison of the weights of evidence method and probabilistic neural networks. Natural Resources Research, v. 8(4), p. 287-298.

Singer, D.A., and Kouda, R., 2003. Typing Mineral Deposits Using Their Grades and Tonnages in an Artificial Neural Network. Natural Resources Research, v. 12(3), p. 201-208

Singh. N.N., 1988. Tectonic and stratigraphic framework of the lead-zinc sukfide mineralization at Zawarmala, district Udaipur, Rajasthan. Journal Geological Society of India, v. 31, p. 546-564.

Singh, P.K., Grunsky, E.C., Keller, E.V., and Keller, C.P., 1993. Porphyry copper potential mapping using probabilistic methods and geographic information systems in British Columbia. In Eyes on the future: Proceedings of the 1993 International Symposium on GIS, p. 381-394.

Sinha-Roy, S., 1984. Precambrian crustal interactions in Rajasthan, NW India. Proceedings of Indian Journal of Earth Science Seminar on Crustal Evolution of the Indian Shield and its Bearing on Metallogeny, p. 84-91.

Sinha-Roy, S., 1985. Granite-greenstone sequence and geotectonic development of SE Rajasthan. Bulletin of the Geological, Mining and Metallurgical Society of India, v. 34, p. 233-244.

Sinha-Roy, S., 1988. Proterozoic Wilson cycles in Rajasthan. In: Roy, A.B. (Ed.), Precambrian of the Aravalli Mountain Rajasthan, India. Memoir Geological Society of India, v. 7, p. 95-107.

Sinha-Roy, S., 1989. Strike-slip faults and pull-apart basins in Proterozoic fold development in Rajasthan. Industrial Minerals, v. 43, p. 226-240.

Sinha-Roy, S., 2000. Precambrian metallotects and mineralisation types in Rajasthan: their relation to crustal evolution. In: Deb, M. (Ed.), Crustal Evolution and Metallogeny in the Northwest-

ern Indian Shield, Narosa Publishing House, New Delhi, p. 217-239.

Sinha-Roy, S., 2001. Precambrian terranes of Rajasthan and their linkages with metallogeny. Proceedings of International Workshop on Sediment-hosted Lead-Zinc Deposits in the Northwestern Indian Shield, New Delhi and Udaipur, India, p. 123-135.

Sinha-Roy, S., and Chore, S.A., 1991. Relation of basement and cover rocks and Proterozoic pull apart basin development of SE Rajasthan. Industrial Minerals, v. 45, p. 149-162.

Sinha-Roy, S., Mohanty, M., and Guha, D.B., 1993. Banas dislocation zone in Nathdwara-Khamnor area, Udaipur district, Rajasthan and its significance on the basement-cover relations in Aravalli fold belt. Current Science, v. 65, p. 68-72.

Sinha-Roy, S., Malhotra, G., and Guha, D.B., 1995. A transect across Rajasthan Precambrian terrane in relation to geology, tectonics and crustal evolution of south-central Rajasthan. In: S. Sinha-Roy and K.R. Gupta (Eds.), Continental Crust of NW and Central India, Memoir Geological Society of India, v. 31, p. 63-90.

Sinha-Roy, S., Malhotra, G., and Mohanty, M., 1998. Geology of Rajasthan, Geological Society of India, Bangalore, India, 278 pp.

Sivaraman, T.V., and Odom, A.L., 1982. Zircon geodhronology of Berach granite of Chittaurgarh, Rajasthan. Journal Geological Society of India. v. 23, p. 575-577.

Spiegelhalter, D.J., 1986. Uncertainty in expert system. In: Gale, W.A. (Ed.), Artificial Intelligence and Statistics, Addison-Wesley, Reading, MA, p. 17-55.

Spiegelhalter, D.J., and Knill-Jones, R.P., 1984. Statistical and knowledge-based approaches clinical decision support systems, with an application in gastroenterology. Journal of the Royal Statistical Society, A, Part 1, p. 35-77.

Spielgelhalter, D.J., and Lauritzen, 1990. Sequential updating of conditional probabilities on directed graphical structures. Networks, v. 20, p. 157-224.

Spirtes, P., Richardson, T., and Meek, C., 1997. Heuristic greedy search algorithms for latent variable models. Proceedings of Al & STAT'97, Ft. Lauderdale, FL, p. 481-488.

Srinivas, S., Russell, S., and Agogino, A., 1990. Automated construction of sparse Bayesian networks from unstructured probabilistic models and domain information. In: Henrion, M., Shachter, R.D., Kanal, L.N. and Lemmer, J.F. (Eds.), Uncertainty in Artificial Intelligence, v. 5, North-Holland, Amsterdam, p. 295-308.

Straczec, J.A., and Srikant, B., 1967. The geology of Zawar zinc-lead area, Rajasthan, India. Memoir Geological Survey of India, v. 92, Geological Survey of India Press, Calcutta India, 85 pp.

Sugden, T.J., Deb, M., and Windley, B.F., 1990. The tectonic setting of mineralization in the Proterozoic Aravalli-Delhi orogenic belt, NW India. In: Naqvi, S.M. (Ed.), Precambrian Continental Crust and its Economic Resources, Elsevier, Amsterdam, p. 367-390.

Sugeno, M., and Kang, G.T., 1988. Structure identification of fuzzy model. Fuzzy Sets and Systems, v. 28, p. 12-33.

Sugeno, M., and Tanaka, K., 1991. Successive identification of a fuzzy model and its application to prediction of complex systems. Fuzzy Sets and Systems, v. 42, p. 315-334.

Suzuki, J., 1996. A construction of Bayesian networks from databases based on an MDL scheme. In: Heckerman, D., and Mamdani, A. (Eds.), Proceedings of the Ninth Conference on Uncertainty in Artificial Intelligence, p. 266-273.

Swain, C.J., 1976. A Fortran IV program for interpolating irregularly spaced data using differential equations for minimum curvature. Computers and Geosciences, v. 1, p. 231-240.

Takagi, T., and Sugeno, M., 1985. Fuzzy identification of systems and its applications to modelling and control: IEEE Transactions on Systems, Man and Cybernetics, v. 15(1), p. 116-132.

Tewari, H.C., Divakar Rao, V., Narayan, B.L., Dixit, M.M., Madhav Rao, N., Murthy, A.N.S., Rajendra Prasad, B., Reddy, P.R., Venkateswarlu, N., Vijaya Rao, V., Mishra, D.C., and

269

Gupta, S.R., 1998. Nagaur-Jhalawar geotransect across the Delhi/Aravalli fold belt in NW India. Journal of the Geological Society of India, v. 52, p. 153-161.

Tewari, H.C., Dixit, M.M., Madhav Rao, N., Venkateshwarlu, N., and Vijaya Rao, V., 1997a. Crustal thickening under the Palaeo/ Mesoproterozoic Delhi fold belt in northwestern India: evidence from deep reflection profiling. Geophysical Journal International, v. 129, p. 657-668.

Tewari, H.C., Rajendra Prasad, B., Vijaya Rao, V., Reddy, P.R., Dixit, M.M., and Madhav Rao, 1997b. Crustal reflectivity parameter for deciphering the evolutionary processes across the Palaeaoproterozoic Aravalli-Delhi fold belt. Journal of the Geological Society of India, v. 50, p. 779-785.

Tewari, H.C., Vijaya Rao, V., Dixit, M.M., Rajendra Prasad, B., Rao, N.M., Venkateswarlu, N., Khare, P., Keshav Rao, G., Raju, S., and Kaila, K.L., 1995. Deep reflection studies across the Delhi-Aravalli fold belt: results from the northwestern part. In: Sinha-Roy, S., Gupta, K.R. (Eds.), Continental crust of northwestern and central India. Memoir Geological Society of India, v. 31, p. 382-402.

Tewari, H.C., Vijaya Rao, V., and Rajendra Prasad, B., 2000. Tectonic significance of seismic reflectivity pattern: a study from the NW Indian shield. In: Deb, M. (Ed.), Crustal Evolution and Metallogeny in the Northwestern Indian Shield. Narosa Publishing House, New Delhi, India, p. 189-202.

Thole, U., Zimmermann, H.J., and Zysno, P., 1979. On the suitability of minimum and product operators for intersection of fuzzy sets. Fuzzy Sets and Systems, v. 2, p. 167-180.

Torkkola, K., and Kohonen, T., 1995. Speech Recognition: A Hybrid Approach. The Handbook of Brain Theory and Neural Networks, The MIT Press, p. 907-910.

Tsopanoglou, A., and Mourjopoulos, J., 1994. Adaptation of an isolated word speech recognition system to continuous speech using multisection LVQ codebook modification and prosodic parameter transformation. Speech Communication, v. 15(1), p. 1-20.

270

Tsukamoto, Y., 1979, An approach to fuzzy reasoning method. In: Gupta, M.M., Ragade, R.K. and Yager, R.R., (Eds.), Advances in Fuzzy Set Theory and Applications, North-Holland, Amsterdam, p. 137-149.

Upadhyaya, R., Sharma, B.L., Sharma, B.L. (Jr.), Roy, A.B., 1992. Remnant of greenstone sequence from the Archaean rocks of Rajasthan. Current Science, v. 63, p. 87-92.

Vearncombe, J., and Vearncombe, S., 1999. The spatial distribution of mineralization: application of Fry analysis. Economic Geology, v. 94, p. 475-486.

Vijaya Rao, V., Rajendra Prasad, B., Reddy, P.R., Tewari, H.C., 2000. Evolution of Proterozoic Aravalli Delhi Fold Belt in the northwestern Indian Shield from seismic studies. Tectonophysics, v. 327, p. 109-130.

Vinogradov, A.P., Tugarinov, A.I., Zhykov, C., Stapnikova, N., Bibikova, E., and Khorre, K., 1964. Geochronology of the Indian Precambrian. Report of 22nd Internation Geological Congress, v. 10, p. 553-567.

Waibel, A., and Lee, K.-F., 1990. Readings in Speech Recognition, Morgan Kaufmann, San Mateo, CA, 680 pp.

Wang, C., Venkatesh, S.S., and Judd, J.S., 1994, Optimal stopping and effective machine complexity in learning. In Cowan, J.D., Tesauro, G., and Alspector, J., (Eds.), Advances in Neural Information Processing Systems: Morgan Kaufmann, San Francisco, p. 303-310.

Weidenbeck, M., and Goswami, J.N., 1994. An ion-probe zircon 207Pb/206Pb age of Mewar gneiss at Jhamarkotra, Rajasthan. Geochemica et Cosmochemica Acta, v. 58, p. 2135-2141.

Weidenbeck, M., Goswami, J.N., and Roy, A.B., 1996. Stabilization of the Aravalli craton of northwestern India at 2.4 Ga: an ion microprobe study. Chemical Geology, v. 129, p. 325-340.

Werbos, P., 1974. Beyond Regression: New Tools for Prediction and Analysis in the Behavioral Sciences. Ph.D. Dissertation, Committee on Applied Mathematics, Harvard University, Cambridge, MA, 61 pp.

Wermuth, N., and Lauritzen, S., 1983. Graphical and recursive models for contingency tables. Biometrika, v. 72, p. 537-552.

Wilks, S. S., 1962. Mathematical Statistics, John Wiley & Sons, New York, 644 pp.

Wright, D.F., and Bonham-Carter, G.F., 1996. VHMS favorability mapping with GIS-based integration models, Chisel-Andersen Lake area. Geological Survey of Canada, Bulletin, v. 426, p. 339-376.

Zadeh, L.A., 1965. Fuzzy sets. IEEE Information and Control, v. 8, p. 338-353.

Zadeh, L.A., 1971. Similarity relations and fuzzy orderings. Information Science, v. 3, p. 177-206.

Zadeh, L.A., 1973. Outline of a new approach to the analysis of complex systems and decision process. IEEE Transactions on Systems, Man and Cybernetics, v. 3, p. 28-44.

Zimmermann, H.J., 1991. Fuzzy Set Theory - and Its Applications, Kluwer Academic Publishing, Dordrecht, 399 pp.

Zimmermann, H.J., and Zysno, P., 1980. Latent connectives in human decision making. Fuzzy Sets and Systems, v. 4, p. 37-51.

Zuqiang Zhao, 1992. Integration of Neural Networks and Hidden Markov Models for Continuous Speech Recognition Artificial Neural Networks, 2, Vol. I, North-Holland, pp. 779-782.

Summary

Porwal, A., 2006, Mineral Potential Mapping with Mathematical Geological Models. Ph.D. Thesis, University of Utrecht, The Netherlands, 289 pp.

Mathematical geological models are being increasingly used by natural resources delineation and planning agencies for mapping areas of mineral potential in order to optimize land use in accordance with socio-economic needs of the society. However, a key problem in spatial-mathematical-model-based mineral potential mapping is the selection of appropriate functions that can effectively approximate the complex relationship between target mineral deposits and recognition criteria. This research evaluates a series of mathematical geological models based on different linear and non-linear functions by applying them to base-metal potential mapping of the Aravalli province, western India, where several significant base-metal deposits are already known.

Linear models applied in this research are an extended weights-of-evidence model and a hybrid fuzzy weights-of-evidence model, while non-linear models are knowledge and data-driven fuzzy models, a neural network model, a hybrid neuro-fuzzy model and an augmented naive Bayesian classifier model. From a conceptual model of base-metal metallogenesis in the study area, host rock lithology, stratigraphic position, (palaeo-)sedimentary environment, association of mafic volcanic rocks and proximity to favorable structures are identified as recognition criteria for base-metal mineralization and, in the form of predictor maps, constitute the input for the models. The parameters of the knowledge-driven fuzzy model are estimated from the expert knowledge, while those of the neural network and Bayesian classifier model are estimated from the data. The two hybrid models use both expert knowledge and data for parameter estimation.

As compared to the linear models, the non-linear models generally perform better in predicting the known base-metal deposits in the study area, including the known deposits that are characterized by unusual geological settings. This is attributed to the ability of non-linear functions to (a) better approximate the relation between mineral

deposits and recognition criteria and (b) recognize and account for possible dependencies amongst recognition criteria. Although the linear models do not fit the data as efficiently as the non-linear models, they are easier to implement using basic GIS functionalities and their parameters are more amenable to geoscientific interpretation. In addition, the linear models are less susceptible to the curse of dimensionality as compared to non-linear models, which makes them more suitable for applications to mineral potential mapping of the areas where there is a paucity of training mineral deposits. The hybrid models that conjunctively use both knowledge and data for parameter estimation generally perform better than purely knowledge-driven or purely data-driven models. This is attributed to the capability of the hybrid models to cross-compensate the deficiencies in either the knowledge-base or in the database.

The output of various mathematical geological models indicate that about 10% of the study area has potential for base-metal deposits. The high-favorability zones tend to reflect a strong lithostratigraphic control on base-metal mineralization in the study area and the importance of crustal-scale faults in spatial localization of base-metal mineralizations in the study area. The low proportion of base-metal potential area delineated and the high prediction rates, which vary from 83% to 96% depending on the model applied, indicate not only (a) the efficiency of the mathematical geological models in capturing the complex relationship between the target mineral deposits and the deposit recognition criteria, but also (b) usefulness of the favorability maps as inputs to natural resources planning for optimizing land use in the study area.

Samenvatting

Ruimtelijke wiskundige modellen worden in toenemende mate gebruikt voor het in kaart brengen van het mogelijk voorkomen van erts. Met name instanties die zich bezig houden met het managen en plannen van het gebruik van natuurlijke hulpbronnen vinden daar baat bij. Het uiteindelijke doel hiervan is om het landgebruik te optimaliseren en in overeenstemming te brengen met de socio-economische behoefte van de samenleving. Een belangrijk onderdeel van deze vorm van modelleren is de selectie van passende functies om de complexe relatie tussen het voorkomen van erts en de herkenningscriteria daarvoor te benaderen. In dit onderzoek wordt een aantal ruimtelijke wiskundige modellen gevalueerd. Al deze modellen zijn gebaseerd op verschillende lineaire en niet-lineaire functies. Ze worden toegepast op het in kaart brengen van het mogelijke voorkomen van *base-metal* in de Aravalli provincie in West India.

Lineaire modellen die in dit onderzoek worden gebruikt zijn een uitgebreide *weights-of-evidence* model en een hybride *fuzzy weights-of-evidence* model. Niet-lineaire modellen zijn zowel op kennis als op data gebaseerde modellen, te weten een neuraal netwerk model, een hybride *neuro-fuzzy* model en een *augmented naive* Bayesiaans classificatie model. Met behulp van een conceptueel model voor metalogenese van *base-metal* in het studie gebied is een aantal herkenningscriteria voor *base-metal* mineralisatie aangeduid. In de vorm van voorspellingskaarten zijn deze ingevoerd worden in de verschillende modellen. We onderscheiden het type nevengesteente, de stratigrafische positie, het (paleo-) sedimentaire milieu, de samenhang met mafische vulkanische gesteentes en de nabijheid van gunstige structuren. De parameters van het *fuzzy* model dat op kennis is gebaseerd zijn geschat op basis van expert kennis, terwijl die van het neurale netwerk en het Bayesiaanse classificatie model geschat zijn met behulp van gegevens. Voor het schatten van parameters van de twee hybride modellen zijn zowel expert kennis als data gebruikt.

Vergeleken met de lineaire modellen voorspellen de niet-lineaire modellen het reeds

275

bekende voorkomen *base-metal* in het studie gebied beter, inclusief dat in ongewone geologische formaties. Dit komt omdat niet-lineaire functies (a) de relatie tussen het voorkomen van erts en de herkenningscriteria beter benaderen en (b) rekening houden met mogelijke onderlinge afhankelijkheid tussen de criteria.

Hoewel de lineaire modellen niet zo goed passen bij de gegevens, zijn ze wel eenvoudiger te implementeren met behulp van basale GIS functionaliteit. Hun parameters zijn ook beter op een geowetenschappelijke manier te interpreteren. Verder zijn lineaire modellen minder vatbaar voor problemen ten gevolge van dimensionaliteit. Dit maakt ze beter toepasbaar om het mogelijke voorkomen van erts in gebieden met onvoldoende trainingsvoorkomens in kaart te brengen. De hybride modellen die zowel kennis als gegevens gebruiken voor het schatten van de parameters werken over het algemeen beter dan modellen die enkel op kennis of op gegevens zijn gebaseerd. De reden hiervoor is dat hybride modellen de tekortkomingen compenseren met gegevens uit de kennis- of de database.

De resultaten, gegenereerd met de verschillende ruimtelijke wiskundige modellen, laten zien dat ongeveer 10% van het studiegebied mogelijk *base-metals* bevat. Er is een sterke lithostratigrafische en een regionaal-structurele invloed op het voorkomen van *base-metal* in het studiegebied. Het relatief kleine gebied met grote waarschijnlijkheid op het voorkomen van erts en met een groot aantal correcte voorspellingen hiervoor, afhankelijk van het gekozen model varirend van 83% tot 96%, laat twee zaken zien. In de eerste plaats toont het de effectiviteit van de wiskundige modellen in het bepalen van de complexe relaties tussen ertsvoorkomens en hun herkenningscriteria. In de tweede plaats toont het de bruikbaarheid van voorspellingskaarten van mogelijk voorkomen van erts bij het plannen en optimaliseren van landgebruik en het beheren van natuurlijke hulpbronnen in het studiegebied.

Curriculum Vitae

ALOK PORWAL was born on 30 June 1964 in the city of Udaipur (Rajasthan), India. He completed his secondary education from Sainik School, Chittaurgarh (Rajasthan), affiliated to the central Board of Secondary Education, New Delhi, in 1981. He received his Bachelor of Science in Geology, Mathematics and Chemistry in 1984 from ML Sukhadia University, India, with distinctions in Geology and Mathematics. In 1986, he received his Master of Science in Geology from Rajasthan University, India, with distinctions in Stratigraphy, Sedimentology and Photogeology and a gold medal for standing first in the order of merit at the university. In the same year, he began his career as an exploration and mining geologist with an iron ore mining company in Goa, India, where he carried out detailed exploration for iron-ore in Vagurem prospect. In 1991, he was appointed Lecturer in the post-graduate department of geology, Government College, Didwana (Rajasthan), where he taught Economic Geology and Applied Geology. In 1993, he joined the State Department of Mines and Geology, Government of Rajasthan, where he continues to work on applications of remote sensing and GIS to mineral exploration. He was awarded the Netherlands Government's NFP fellowship for carrying out PhD research at ITC in 1998 and started his PhD research the next year. During his doctoral research, he published seven papers in peer-reviewed international journals and two papers in conference proceedings. He participated and presented his work in four international conferences/symposia and chaired a technical session in the 'VII International Symposium on Mineral Exploration (ISME): Application of Neural Networks to Earth Sciences' held at NASA Moffett Field, California, from 21 to 22 August 2003. He also reviewed two scientific papers that were submitted for publication in Computers and Geosciences and Mathematical Geology. He will defend his thesis on 1 February 2005.

List of ITC PhD Dissertations

1. Akinyede (1990), Highway cost modelling and route selection using a geotechnical information system

2. Pan He Ping (1990), 90-9003-757-8, Spatial structure theory in machine vision and applications to structural and textural analysis of remotely sensed images

3. Bocco Verdinelli, G. (1990), Gully erosion analysis using remote sensing and geographic information systems: a case study in Central Mexico

4. Sharif, M. (1991), Composite sampling optimization for DTM in the context of GIS

5. Drummond, J. (1991), Determining and processing quality parameters in geographic information systems

6. Groten, S. (1991), Satellite monitoring of agro-ecosystems in the Sahel

7. Sharifi, A. (1991), 90-6164-074-1, Development of an appropriate resource information system to support agricultural management at farm enterprise level

8. Zee, D. van der (1991), 90-6164-075-X, Recreation studied from above: Air photo interpretation as input into land evaluation for recreation

9. Mannaerts, C. (1991), 90-6164-085-7, Assessment of the transferability of laboratory rainfall-runoff and rainfall soil loss relationships to field and catchment scales: a study in the Cape Verde Islands

10. Ze Shen Wang (1991), 90-393-0333-9, An expert system for cartographic symbol design

279

11. Zhou Yunxian (1991), 90-6164-081-4, Application of Radon transforms to the processing of airborne geophysical data

12. Zuviria, M. de (1992), 90-6164-077-6, Mapping agro-topoclimates by integrating topographic, meteorological and land ecological data in a geographic information system: a case study of the Lom Sak area, North Central Thailand

13. Westen, C. van (1993), 90-6164-078-4, Application of Geographic Information Systems to landslide hazard zonation

14. Shi Wenzhong (1994), 90-6164-099-7, Modelling positional and thematic uncertainties in integration of remote sensing and geographic information systems

15. Javelosa, R. (1994), 90-6164-086-5, Active Quaternary environments in the Philippine mobile belt

16. Lo King-Chang (1994), 90-9006526-1, High Quality Automatic DEM, Digital Elevation Model Generation from Multiple Imagery

17. Wokabi, S. (1994), 90-6164-102-0, Quantified land evaluation for maize yield gap analysis at three sites on the eastern slope of Mt. Kenya

18. Rodriguez, O. (1995), Land Use conflicts and planning strategies in urban fringes: a case study of Western Caracas, Venezuela

19. Meer, F. van der (1995), 90-5485-385-9, Imaging spectrometry & the Ronda peridotites

20. Kufoniyi, O. (1995), 90-6164-105-5, Spatial coincidence: automated database updating and data consistency in vector GIS

21. Zambezi, P. (1995), Geochemistry of the Nkombwa Hill carbonatite complex of Isoka District, north-east Zambia, with special emphasis on economic minerals

22. Woldai, T. (1995), The application of remote sensing to the study of the geology and structure of the Carboniferous in the Calaas area, pyrite belt, SW Spain

23. Verweij, P. (1995), 90-6164-109-8, Spatial and temporal modelling of vegetation patterns: burning and grazing in the Paramo of Los Nevados National Park, Colombia

24. Pohl, C. (1996), 90-6164-121-7, Geometric Aspects of Multisensor Image Fusion for Topographic Map Updating in the Humid Tropics

25. Jiang Bin (1996), 90-6266-128-9, Fuzzy overlay analysis and visualization in GIS

26. Metternicht, G. (1996), 90-6164-118-7, Detecting and monitoring land degradation features and processes in the Cochabamba Valleys, Bolivia. A synergistic approach

27. Hoanh Chu Thai (1996), 90-6164-120-9, Development of a Computerized Aid to Integrated Land Use Planning (CAILUP) at regional level in irrigated areas: a case study for the Quan Lo Phung Hiep region in the Mekong Delta, Vietnam

28. Roshannejad, A. (1996), 90-9009284-6, The management of spatio-temporal data in a national geographic information system

29. Terlien, M. (1996), 90-6164-115-2, Modelling Spatial and Temporal Variations in Rainfall-Triggered Landslides: the integration of hydrologic models, slope stability models and GIS for the hazard zonation of rainfall-triggered landslides with examples from Manizales, Colombia

30. Mahavir, J. (1996), 90-6164-117-9, Modelling settlement patterns for metropolitan regions: inputs from remote sensing

31. Al-Amir, S. (1996), 90-6164-116-0, Modern spatial planning practice as supported by the multi-applicable tools of remote sensing and GIS: the Syrian case

32. Pilouk, M. (1996), 90-6164-122-5, Integrated modelling for 3D GIS

33. Duan Zengshan (1996), 90-6164-123-3, Optimization modelling of a river-aquifer system with technical interventions: a case study for the Huangshui river and the coastal aquifer, Shandong, China

34. Man, W.H. de (1996), 90-9009-775-9, Surveys: informatie als norm: een verkenning van de institutionalisering van dorp - surveys in Thailand en op de Filippijnen

35. Vekerdy, Z. (1996), 90-6164-119-5, GIS-based hydrological modelling of alluvial regions: using the example of the Kisafld, Hungary

36. Pereira, Luisa (1996), 90-407-1385-5, A Robust and Adaptive Matching Procedure for Automatic Modelling of Terrain Relief

37. Fandino Lozano, M. (1996), 90-6164-129-2, A Framework of Ecological Evaluation oriented at the Establishment and Management of Protected Areas: a case study of the Santuario de Iguaque, Colombia

38. Toxopeus, B. (1996), 90-6164-126-8, ISM: an Interactive Spatial and temporal Modelling system as a tool in ecosystem management: with two case studies: Cibodas biosphere reserve, West Java Indonesia: Amboseli biosphere reserve, Kajiado district, Central Southern Kenya

39. Wang Yiman (1997), 90-6164-131-4, Satellite SAR imagery for topographic mapping of tidal flat areas in the Dutch Wadden Sea

40. Saldana-Lopez, Asuncin (1997), 90-6164-133-0, Complexity of soils and Soilscape patterns on the southern slopes of the Ayllon Range, central Spain: a GIS assisted modelling approach

41. Ceccarelli, T. (1997), 90-6164-135-7, Towards a planning support system for communal areas in the Zambezi valley, Zimbabwe; a multi-criteria evaluation linking farm household analysis, land evaluation and geographic information systems

42. Peng Wanning (1997), 90-6164-134-9, Automated generalization in GIS

43. Lawas, C. (1997), 90-6164-137-3, The Resource Users' Knowledge, the neglected input in Land resource management: the case of the Kankanaey farmers in Benguet, Philippines

44. Bijker, W. (1997), 90-6164-139-X, Radar for rain forest: A monitoring system for land cover Change in the Colombian Amazon

45. Farshad, A. (1997), 90-6164-142-X, Analysis of integrated land and water management practices within different agricultural systems under semi-arid conditions of Iran and evaluation of their sustainability

46. Orlic, B. (1997), 90-6164-140-3, Predicting subsurface conditions for geotechnical modelling

47. Bishr, Y. (1997), 90-6164-141-1, Semantic Aspects of Interoperable GIS

48. Zhang Xiangmin (1998), 90-6164-144-6, Coal fires in Northwest China: detection, monitoring and prediction using remote sensing data

49. Gens, R. (1998), 90-6164-155-1, Quality assessment of SAR interferometric data

50. Turkstra, J. (1998), 90-6164-147-0, Urban development and geographical information: spatial and temporal patterns of urban development and land values using integrated geo-data, Villaviciencia, Colombia

51. Cassells, C. (1998), 90-6164-234-5, Thermal modelling of underground coal fires in northern China

52. Naseri, M. (1998), 90-6164-195-0, Characterization of Salt-affected Soils for Modelling Sustainable Land Management in Semi-arid Environment: a case study in the Gorgan Region, Northeast, Iran

53. Gorte B.G.H. (1998), 90-6164-157-8, Probabilistic Segmentation of Remotely Sensed Images

54. Tegaye, Tenalem Ayenew (1998), 90-6164-158-6, The hydrological system of the lake district basin, central main Ethiopian rift

55. Wang Donggen (1998), 90-6864-551-7, Conjoint approaches to developing activity-based models

56. Bastidas de Calderon, M. (1998), 90-6164-193-4, Environmental fragility and vulnerability of Amazonian landscapes and ecosystems in the middle Orinoco river basin, Venezuela

57. Moameni, A. (1999), Soil quality changes under long-term wheat cultivation in the Marvdasht plain, South-Central Iran

58. Groenigen, J.W. van (1999), 90-6164-156-X, Constrained optimisation of spatial sampling: a geostatistical approach

59. Cheng Tao (1999), 90-6164-164-0, A process-oriented data model for fuzzy spatial objects

60. Wolski, Piotr (1999), 90-6164-165-9, Application of reservoir modelling to hydrotopes identified by remote sensing

61. Acharya, B. (1999), 90-6164-168-3, Forest biodiversity assessment: A spatial analysis of tree species diversity in Nepal

62. Akbar Abkar, Ali (1999), 90-6164-169-1, Likelihood-based segmentation and classification of remotely sensed images

63. Yanuariadi, T. (1999), 90-5808-082-X, Sustainable Land Allocation: GIS-based decision support for industrial forest plantation development in Indonesia

64. Abu Bakr, Mohamed (1999), 90-6164-170-5, An Integrated Agro-Economic and Agro-Ecological Framework for Land Use Planning and Policy Analysis

65. Eleveld, M. (1999), 90-6461-166-7, Exploring coastal morphodynamics of Ameland (The Netherlands) with remote sensing monitoring techniques and dynamic modelling in GIS

66. Yang Hong (1999), 90-6164-172-1, Imaging Spectrometry for Hydrocarbon Microseepage

67. Mainam, Flix (1999), 90-6164-179-9, Modelling soil erodibility in the semiarid zone of Cameroon

68. Bakr, Mahmoud (2000), 90-6164-176-4, A Stochastic Inverse-Management Approach to Groundwater Quality

69. Zlatanova, Z. (2000), 90-6164-178-0, 3D GIS for Urban Development

70. Ottichilo, Wilber K. (2000), 90-5808-197-4, Wildlife Dynamics: An Analysis of Change in the Masai Mara Ecosystem

71. Kaymakci, Nuri (2000), 90-6164-181-0, Tectono-stratigraphical Evolution of the Cankori Basin (Central Anatolia, Turkey)

72. Gonzalez, Rhodora (2000), 90-5808-246-6, Platforms and Terraces: Bridging participation and GIS in joint-learning for watershed management with the Ifugaos of the Philippines

73. Schetselaar, Ernst (2000), 90-6164-180-2, Integrated analyses of granite-gneiss terrain from field and multisource remotely sensed data. A case study from the Canadian Shield

74. Mesgari, Saadi (2000), 90-3651-511-4, Topological Cell-Tuple Structure for Three-Dimensional Spatial Data

75. Bie, Cees A.J.M. de (2000), 90-5808-253-9, Comparative Performance Analysis of Agro-Ecosystems

76. Khaemba, Wilson M. (2000), 90-5808-280-6, Spatial Statistics for Natural Resource Management

77. 77. Shrestha, Dhruba (2000), 90-6164-189-6, Aspects of erosion and sedimentation in the Nepalese Himalaya: highland-lowland relations

78. Asadi Haroni, Hooshang (2000), 90-6164-185-3, The Zarshuran Gold Deposit Model Applied in a Mineral Exploration GIS in Iran

79. Raza, Ale (2001), 90-3651-540-8, Object-oriented Temporal GIS for Urban Applications

80. Farah, Hussein (2001), 90-5808-331-4, Estimation of regional evaporation under different weather conditions from satellite and meteorological data. A case study in the Naivasha Basin, Kenya

81. Zheng, Ding (2001), 90-6164-190-X, A Neural - Fuzzy Approach to Linguistic Knowledge Acquisition and Assessment in Spatial Decision Making

82. Sahu, B.K. (2001), Aeromagnetics of continental areas flanking the Indian Ocean; with implications for geological correlation and reassembly of Central Gondwana

83. Alfestawi, Y. (2001), 90-6164-198-5, The structural, paleogeographical and hydrocarbon systems analysis of the Ghadamis and Murzuq Basins, West Libya, with emphasis on their relation to the intervening Al Qarqaf Arch

84. Liu, Xuehua (2001), 90-5808-496-5, Mapping and Modelling the Habitat of Giant Pandas in Foping Nature Reserve, China

85. Oindo, Boniface Oluoch (2001), 90-5808-495-7, Spatial Patterns of Species Diversity in Kenya

86. Carranza, Emmanuel John (2002), 90-6164-203-5, Geologically-constrained Mineral Potential Mapping

87. Rugege, Denis (2002), 90-5808-584-8, Regional Analysis of Maize-Based Land Use Systems for Early Warning Applications

88. Liu, Yaolin (2002), 90-5808-648-8, Categorical Database Generalization in GIS

89. Ogao, Patrick (2002), 90-6164-206-X, Exploratory Visualization of Temporal Geospatial Data using Animation

90. Abadi, Abdulbaset M. (2002), 90-6164-205-1, Tectonics of the Sirt Basin - Inferences from tectonic subsidence analysis, stress inversion and gravity modelling

91. Geneletti, Davide (2002), 90-5383-831-7, Ecological Evaluation for Environmental Impact Assessment

92. Sedogo, Laurent G. (2002), 90-5808-751-4, Integration of Participatory Local and Regional Planning for Resources Management using Remote Sensing and GIS

93. Montoya, Lorena (2002), 90-6164-208-6, Urban Disaster Management: a case study of earthquake risk assessment in Carthago, Costa Rica

94. Ahmad, Mobin-ud-Din (2002), 90-5808-761-1, Estimation of Net Groundwater Use in Irrigated River Basins using Geo-information Techniques: A case study in Rechna Doab, Pakistan

95. Said, Mohammed Yahya (2003), 90-5808-794-8, Multiscale perspectives of species richness in East Africa

96. Schmidt, Karin (2003), 90-5808-830-8, Hyperspectral Remote Sensing of Vegetation Species Distribution in a Saltmarsh

97. Lopez Binnquist, Citlalli (2003), 90-3651-900-4, The Endurance of Mexican Amate Paper: Exploring Additional Dimensions to the Sustainable Development Concept

98. Huang, Zhengdong (2003), 90-6164-211-6, Data Integration for Urban Transport Planning

99. Cheng, Jianquan (2003), 90-6164-212-4, Modelling Spatial and Temporal Urban Growth

286

100. Campos dos Santos, Jose Laurindo (2003), 90-6164-214-0, A Biodiversity Information System in an Open Data/Metadatabase Architecture

101. Hengl, Tomislav (2003), 90-5808-896-0, PEDOMETRIC MAPPING, Bridging the gaps between conventional and pedometric approaches

102. Barrera Bassols, Narciso (2003), 90-6164-217-5, Symbolism, Knowledge and management of Soil and Land Resources in Indigenous Communities: Ethnopedology at Global, Regional and Local Scales

103. Zhan, Qingming (2003), 90-5808-917-7, A Hierarchical Object-Based Approach for Urban Land-Use Classification from Remote Sensing Data

104. Daag, Arturo S. (2003), 90-6164-218-3, Modelling the Erosion of Pyroclastic Flow Deposits and the Occurrences of Lahars at Mt. Pinatubo, Philippines

105. Bacic, Ivan (2003), 90-5808-902-9, Demand-driven Land Evaluation with case studies in Santa Catarina, Brazil

106. Murwira, Amon (2003), 90-5808-951-7, Scale matters! A new approach to quantify spatial heterogeneity for predicting the distribution of wildlife

107. Mazvimavi, Dominic (2003), 90-5808-950-9, Estimation of Flow Characteristics of Ungauged Catchments. A case study in Zimbabwe

108. Tang, Xinming (2004), 90-6164-220-5, Spatial Object Modelling in Fuzzy Topological Spaces with Applications to Land Cover Change

109. Kariuki, Patrick (2004), 90-6164-221-3, Spectroscopy and Swelling Soils; an integrated approach

110. Morales, Javier (2004), 90-6164-222-1, Model Driven Methodology for the Design of Geo-information Services

111. Mutanga, Onisimo (2004), 90-5808-981-9, Hyperspectral Remote Sensing of Tropical Grass Quality and Quantity

112. liuas, Ricardas V. (2004), 90-6164-223-X, Managing Informal Settlements: a study using geo-information in Dar es Salaam, Tanzania

113. Lucieer, Arko (2004), 90-6164-225-6, Uncertainties in Segmentation and their Visualisation

114. Corsi, Fabio (2004), 90-8504-090-6, Applications of existing biodiversity information: Capacity to support decision-making

115. Tuladhar, Arbind (2004), 90-6164-224-8, Parcel-based Geo-information System: Concepts and Guidelines

116. Elzakker, Corn van (2004), 90-6809-365-7, The use of maps in the exploration of geographic data

117. Nidumolu, Uday Bhaskar (2004), 90-8504-138-4, Integrating Geo-information models with participatory approaches: applications in land use analysis

118. Koua, Etien L. (2005), 90-6164-229-9, Computational and Visual Support for Exploratory Geovisualization and Knowledge Construction

119. Blok, Connie A. (2005), Dynamic visualization variables in animation to support monitoring of spatial phenomena

120. Meratnia, Nirvana (2005), 90-365-2152-1, Towards Database Support for Moving Object Data

121. Yemefack, Martin (2005), 90-6164-233-7, Modelling and monitoring Soil and Land Use Dynamics within Shifting Agricultural Landscape Mosaic Systems

122. Kheirkhah, Masoud (2005), 90-8504-256-9, Decision support system for floodwater spreading site selection in Iran

123. Nangendo, Grace (2005), 90-8504-200-3, Changing forest-woodland-savanna mosaics in Uganda: with implications for conservation

124. Mohamed, Yasir Abbas (2005), 04-15-38483-4, The Nile Hydroclimatology: impact of the Sudd wetland (Distinction)

125. Duker, Alfred, A. (2005), 90-8504-243-7, Spatial analysis of factors implicated in mycobacterium ulcerans infection in Ghana

126. Ferwerda, Jelle, G., (2005), 90-8504-209-7, Charting the Quality of Forage: Measuring and mapping the variation of chemical components in foliage with hyperspectral remote sensing

127. Martinez, Javier (2005), 90-6164-235-3, Monitoring intra-urban inequalities with GIS-based indicators. With a case study in Rosario, Argentina

128. Saavedra, Carlos (2005), 90-8504-289-5, Estimating spatial patterns of soil erosion and deposition in the Andean region using Geo-information techniques. A case study in Cochabamba, Bolivia

129. Vaiphasa, Chaichoke (2006), 90-8504-353-0, Remote Sensing Techniques for Mangrove Mapping